



uOttawa

L'Université canadienne
Canada's university

Numerical computations of action potentials for the
heart-torso coupling problem.

Myriam Rioux

Thesis submitted to the Faculty of Graduate and Postdoctoral Studies
in partial fulfillment of the requirements for the degree of Doctor of Philosophy in
Mathematics ¹

Department of Mathematics and Statistics
Faculty of Science
University of Ottawa

© Myriam Rioux, Ottawa, Canada, 2011

¹The Ph.D. program is a joint program with Carleton University, administered by the Ottawa-Carleton Institute of Mathematics and Statistics

Abstract

The work developed in this thesis focusses on the electrical activity of the heart, from the modeling of the action potential originating from cardiac cells and propagating through the heart, as well as its electrical manifestation at the body surface. The study is divided in two main parts: modeling the action potential, and numerical simulations.

For modeling the action potential a dimensional and asymptotic analysis is done. The key advance in this part of the work is that this analysis gives the steps to reliably control the action potential. It allows predicting the time/space scales and speed of any action potential that is to say the shape of the action potential and its propagation. This can be done as the explicit relations on all the physiological constants are defined precisely. This method facilitates the integrative modeling of a complete human heart with tissue-specific ionic models. It even proves that using a single model for the cardiac action potential is enough in many situations.

For efficient numerical simulations, a numerical method for solving the heart-torso coupling problem is explored according to a level set description of the domains. This is done in the perspective of using directly medical images for building computational domains. A finite element method is then developed to manage meshes not adapted to internal interfaces. Finally, an anisotropic adaptive remeshing methods for unstructured finite element meshes is used to efficiently capture propagating action potentials within complex, realistic two dimensional geometries.

Résumé

Le travail développé dans cette thèse s'intéresse à l'activité électrique du cœur, en passant par la modélisation du potentiel d'action des cellules cardiaques, sa propagation dans les tissus, jusqu'à sa manifestation électrique à la surface du corps. L'étude se divise principalement en deux parties: la modélisation du potentiel d'action et les simulations numériques.

Afin de modéliser le potentiel d'action, une analyse asymptotique et dimensionnelle est effectuée. Une avancée remarquable de cet aspect du travail est que cette analyse donne les étapes précises pour contrôler efficacement le potentiel d'action. Cette méthode permet donc de prédire les échelles de temps et d'espace de n'importe quel potentiel d'action, c'est-à-dire son profil et sa propagation. Cela est rendu possible grâce à la définition précise de relations explicites dépendant de toutes les constantes physiologiques impliquées dans le modèle. Cette méthode facilite la modélisation d'un cœur humain avec des modèles ioniques spécifiques aux différents tissus. Cela prouve également que l'utilisation d'un seul modèle ionique est suffisante dans plusieurs situations pour modéliser le potentiel d'action cardiaque.

Pour des simulations précises et efficaces, une méthode numérique pour résoudre le problème de couplage cœur-thorax est explorée. Cette méthode est basée sur une description des domaines par ensembles de niveau dans la perspective d'utiliser directement les images médicales segmentées pour construire les domaines de calcul. Une méthode par éléments finis est aussi développée pour calculer sur des maillages

non adaptés aux interfaces internes. Finalement, une stratégie d'adaptation de maillage anisotrope est utilisée pour capturer efficacement les variations rapides de la solution dans des géométries complexes et réalistes en deux dimensions.

Acknowledgements

Je remercie tout d'abord mon directeur de thèse Yves Bourgault pour m'avoir proposé ce sujet de thèse passionnant. Je le remercie particulièrement pour son encadrement que je considère exceptionnel. Il a su me diriger dans un tout nouveau domaine de recherche dans un programme différent de ma formation antérieure. Nous avons eu plusieurs discussions très animées, en personne ou à distance, dont je garde de bons souvenirs, et où Yves n'a pas manqué de me rappeler l'importance de la rigueur en mathématiques.

Je tiens aussi à remercier tous ceux avec qui j'ai pu collaborer de près ou de loin, particulièrement Youssef Belhamadia à l'Université de l'Alberta pour nos discussions sur l'adaptation de maillage, l'équipe multidisciplinaire du GIREF à l'Université Laval qui m'a offert un soutien précieux en modélisation et programmation, et aussi Yves Coudière à l'Université de Nantes, avec qui j'ai entamé une collaboration qui se poursuivra durant mon post-doc.

Je remercie certains collègues de classe et de bureau dont quelques-uns m'ont franchement aidé à passer au travers de mes examens de compréhension en analyse, tout particulièrement Olivier Rousseau qui m'a également fourni un soutien moral à l'occasion. Je remercie ma famille, mes amis autant à Ottawa qu'à Québec pour avoir agrémenté ma vie tout au long de ce projet.

Je remercie aussi l'énergie solaire qui alimente présentement mon ordinateur portable. Cette énergie solaire provient du système électrique de notre chalet que

nous avons construit mon conjoint et moi ces 3 dernières années. C'est là où j'y ai passé presque toutes mes fins de semaine, et où j'ai pu déconnecter, déstresser et finalement m'inspirer dans l'écriture de cette thèse.

Enfin, je te remercie Éric pour ta persévérance et ta patience. Notre vie à distance ne nous a pas empêché de réaliser de beaux projets et de grandir dans notre amour.

Dedication

À Éric

Contents

List of Figures	xii
List of Tables	xxi
1 Introduction	1
1.1 The heart at the cell level	2
1.1.1 The cell membrane	2
1.1.2 Excitability and action potential	7
1.1.3 Modeling the action potential	9
1.2 The heart at the organ level	10
1.2.1 Modeling propagation - The bidomain model	10
1.2.2 The monodomain model	15
1.2.3 Heart tissue and fiber arrangement	16
1.2.4 The conduction system	17
1.3 Perspective of heart simulation	19
1.3.1 Computational cardiac electrophysiology	20
1.3.2 Geometrical model of the heart and level sets	21
1.3.3 Finite element method	26
1.4 The scope of this thesis	33

2	A predictive method allowing the use of a single ionic model in numerical cardiac electrophysiology	35
2.1	Introduction	35
2.2	Ionic models	37
2.2.1	FitzHugh-Nagumo model[32, 59]	38
2.2.2	Fenton-Karma model	38
2.2.3	Mitchell-Shaeffer model	41
2.2.4	Modeling realistic APs	46
2.3	Nondimensionalization	46
2.3.1	A nondimensionalization specific to the asymptotic analysis	51
2.4	Asymptotic analysis	52
2.4.1	Definitions	53
2.4.2	Analysis of the phase space	54
2.4.3	Asymptotic characterization of the depolarization front . . .	61
2.4.4	Overall characterization of the asymptotic solution	68
2.4.5	Using the asymptotic solution to predict the numerical solution	77
2.4.6	Periodic excitations	83
2.4.7	Predicting the restitution curves	86
2.5	Modeling physiological AP propagating in various tissues of the heart	86
2.5.1	Ventricle	89
2.5.2	Purkinje fibers	89
2.5.3	Considerations to take for a narrower upstroke	91
2.6	Existence and uniqueness of a traveling wave for the asymptotic solution	92

3	Influence of discretization	100
3.1	Stability of the time integration scheme	100
3.2	General influence of the time/space discretization	109
4	On the convergence of the heart-torso coupling problem using non-body fitted meshes.	119
4.1	Introduction	119
4.2	Convergence of the diffusion problem	121
4.2.1	Definition of the problem	121
4.2.2	Review of finite element methods for problems with internal interfaces and fixed meshes.	123
4.2.3	Two finite element methods for the use of non body-fitted meshes	126
4.2.4	Order of convergence of the methods	131
4.3	Convergence of the heart-torso coupling problem	139
4.3.1	Variational formulation and resolution with a finite element method	139
4.3.2	Resolution technique using a level set description of the domains and non body-fitted meshes	140
4.3.3	Order of convergence for a simple test case	141
4.4	2D simulation using realistic patient data	147
5	Mesh Adaptation	157
5.1	Introduction: the need for mesh adaptation	157
5.2	Overview of techniques and algorithms used in mesh adaptation	159
5.2.1	Metric error estimation	159
5.2.2	Pre-intersection of metrics	161
5.2.3	Error estimation for piecewise continuous functions	163

5.3	Numerical results in 2D with mesh adaptation	163
5.3.1	Pseudo-code for the resolution-adaptation loop	163
5.3.2	Using level sets and fiber arrangement in a resolution-adaptation loop	170
5.3.3	Calculating isochrons in a resolution-adaptation loop	171
5.3.4	Refining the mesh near the internal interfaces	173
5.3.5	First numerical solutions with mesh adaptation	173
5.3.6	Optimization of the adaptation-resolution loop	177
5.4	Simulating the movement of the heart embedded in the torso	185
5.4.1	Deforming the heart geometry using small/large deforma- tions	185
5.4.2	Deforming the heart geometry using non-body fitted meshes and level sets	186
A	Solving the Neumann problem with a finite element method	198
A.0.3	Other ways to solve the Neumann problem [10]	202
B	Complement on the Conjugate Gradient (CG)	205
C	Definitions and theorems [20]	208

List of Figures

1.1	An electrical circuit model of the cell membrane.	5
1.2	The cardiac action potential.	9
1.3	Geometrical considerations for the homogenization process used to derive the bidomain model.	11
1.4	The heart H embedded in the extracardiac domain T	15
1.5	The cardiac conduction system with the shapes of the action potentials in different tissues of a human heart. Source: [68].	18
1.6	2D iterative segmentation of the heart from a CT scan image. (a) The image to be segmented, (b) the result of the first application of the Chan-Vese model using the original image, (c)-(e) second step, obtained using a blurred versions of the image (a), (f) the final segmentation of the heart muscle over the 2D image. Source: Olivier Rousseau [74].	23
1.7	3D segmentation of the human heart ventricles from a 3D CT image. (a)-(b) Different views of the segmentation, (c) a view of the segmented exterior surface over the original image, (d) a view of the segmented ventricles together with the atria cavities and the aorte. Source: Olivier Rousseau [74].	24

1.8	The level set method can manage topology changes. Slices are shown at different times for illustrating the curve evolution process. Remark that $\varphi < 0$ inside the cones, $\varphi = 0$ at the surface of the cones and $\varphi > 0$ outside the cones.	26
1.9	Domains for the elliptic problem (1.3.3).	28
1.10	Lagrange FE basis functions in P_1	31
2.1	AP of the FHN model.	39
2.2	AP for the FK model.	41
2.3	AP of the original MS model.	42
2.4	The smoothed step function $s(u, \kappa, u_{gate})$ for different values of κ and $u_{gate} = 0.13$	45
2.5	Numerical simulation of the electrical activity of a single cell using various versions of the MS model. With the characteristic time $T = 1$ ms, all simulations use the non dimensional parameters $\tau_{in} = 0.3$, $\tau_{out} = 6$, $\tau_{open} = 130$ and $u_{gate} = 0.13$	56
2.6	The phase space for both the MS and modified MS models. Numerical simulations are performed with $T = 0.001$ s, $\tau_{in} = 0.3$ (ms), $\tau_{out} = 6$ (ms), $\tau_{open} = 130$ (ms), $\tau_{close} = 150$ (ms) and $u_{gate} = 0.13$. See text for definitions of curves, points, etc identified.	57
2.7	0D and 1D solutions in the phase space of the phase space of the 0D system.	60
2.8	Upstroke duration versus $\frac{\sigma}{C_m \chi}$ for the MS model. The asymptotic prediction is detailed in section 2.4.5.	66
2.9	Upstroke length (a) and speed (b) versus $\frac{\sigma}{C_m \chi}$ for the MS model. The asymptotic prediction is detailed in section 2.4.5.	67
2.10	The three proposed ways of estimating the asymptotic upstroke duration.	71

2.11 Asymptotic approximations of the durations $(k_{AB}\widehat{T}_{up}, k_{CD}\widehat{T}_{down})$ versus (τ_{in}, τ_{out}) for $v_- = 1$, $k_{AB} = 2.15$ and $k_{CD} = 0.45$. Level sets for \widehat{T}_{up} are rather vertical (plain labels) and level sets for \widehat{T}_{down} are horizontal (boxed labels). 79

2.12 1D numerical solution. (T_{up}, T_{down}) versus (τ_{in}, τ_{out}) for $v_- = 1$, $\tau_{open} = 130$ ms, $\tau_{close} = 150$ ms. Level sets for \widehat{T}_{up} are rather vertical (plain labels) and level sets for \widehat{T}_{down} are rather horizontal (boxed labels). Note that the ranges for the τ_{in} and τ_{out} axis are not the same as in figure 2.11. 80

2.13 Asymptotic approximations of the durations $(\widehat{T}_{AP}, \widehat{T}_{peak})$ versus $(\tau_{fclose}, \tau_{sclose})$ for $v_- = 1$. Level sets for \widehat{T}_{peak} are rather vertical (plain labels) and level sets for \widehat{T}_{AP} are horizontal (boxed labels). 81

2.14 1D numerical solution. (T_{AP}, T_{peak}) versus $(\tau_{fclose}, \tau_{sclose})$ for $v_- = 1$, $\tau_{open} = 130$ ms, $\tau_{close} = 150$ ms. Level sets for \widehat{T}_{peak} are rather vertical (plain labels) and level sets for \widehat{T}_{AP} are rather horizontal (boxed labels). 81

2.15 The simulations are calculated over 5000 ms. The dimensionless number is that of Adim3. 84

2.16 Asymptotic predictions (continuous line) of numerical AP's features (dots) of waves trains paced at v_- 85

2.17 Asymptotic restitution curves predicting the numerical restitution curves. 87

2.18 Phase planes for both MS and modified MS models. The equilibrium points in the phase I (see on the ν -axis) are denoted $\nu_{1,2,3}^*$ on figure a) and ν^* on figure b). The solutions plotted for both models use the physiological parameters indicated in the second column of the table 2.3 together with the dimensioning parameters $L = 0.001$ m and $T = 0.001$ s, i.e. with $N = 0.10212$. The nullclines and the vector field are for $v_- = 0.99$. Solutions for the indicated values of c are plotted in black. The nullclines and the vector fields vary with c but as c varies only slightly, they appear to be superposed. 94

2.19 Real part of the eigenvalues of the equilibrium points in the phase I for the MS ionic model. We take $c = 0.6$ because the dimensional speed (in m/s) is already close to the physiological speed of the depolarization front in the ventricle (around 0.5 m/s). An isolated traveling wave is considered so $v_- = 1$ 96

2.20 Value of the speed where there is a transition from an unstable focus to an unstable node. The threshold $4\tau_{in}/\tau_{out}$ for the existence of the transition comes from the threshold for the existence of the third equilibrium point $\nu_3^* = h_3(v_-) = 1/2 + 1/2\sqrt{1 - 4\tau_{in}/\tau_{out}v_-}$ 97

2.21 Schematic representation of what happen when the speed is augmented progressively. In order to see details that are not distinguishable in the real phase space (figure 2.18), this is a modified version of the real phase space, 98

3.1 Transmembrane potential u and the recovery variable v for the FHN model on $\Omega \times [0, t_{max}] = [0, 200] \times [0, 500]$ and the MS model on $\Omega \times [0, t_{max}] = [0, 1000] \times [0, 1000]$. Remark that the FHN features the hyperpolarization after the wave, contrary to the MS models. The waves move from right to left. 111

4.1	Body fitted meshes vs a non body fitted mesh. The internal interface between subdomains is in red.	120
4.2	Preliminary steps of a realistic simulation with non body fitted mesh. From a medical image (a), a segmentation (b) is done to capture the complicated internal interfaces between the heart and the torso. A simple (non body fitted) mesh (c) is built on the whole image. . . .	120
4.3	Left: The heart domain defined by a level set is in red. Right: The heart domain defined as the largest set of elements inside the level set description of Ω^-	128
4.4	Bad approximation of the normal vector for a coarse non-body fitted mesh.	129
4.5	Domains for the elliptic problem with $\Omega = [-100, 100] \times [-100, 100] = \Omega^- \cup \Omega^+ \cup \Gamma$ with $\Omega^- = [-50, 50] \times [-50, 50]$	133
4.6	Error on the solution as a function of the mesh size h for the diffusion problem with Neumann boundary conditions on body fitted meshes compared to non-body fitted meshes with the conductivity defined by level sets. Remark that n refers to the order of convergence. Results for the Dirichlet boundary conditions are very similar. . . .	136
4.7	Error on the solution as a function of the mesh size h for the diffusion problem on non-body fitted meshes and with Neumann boundary conditions. Remark that n refers to the order of convergence. Results for the Dirichlet boundary conditions are very similar. . . .	137
4.8	Difference between the non body fitted solution (using quadratic elements on mesh $\mathcal{T}_{NB,2}$) and the exact solution of the diffusion problem with discontinuous conductivities defined by level sets. . . .	137
4.9	The exact solution (in black) and the non body fitted solution (in red) (using quadratic elements on mesh $\mathcal{T}_{NB,2}$) of the diffusion problem with discontinuous conductivities defined by level sets.	138

4.10 L_2 -norm of the error versus the jump of conductivities σ on Γ	138
4.11 Domain used for the simulations of the heart-torso coupling problem. The red region is depolarized at the initial time.	141
4.12 Difference between the isochrons of depolarization for the body vs non-body fitted meshes. There is a maximal difference of 10 ms for a depolarization time of 200 ms near the heart surface (5% of error).	144
4.13 The isochrons of depolarization for a simulation using non body fit- ted mesh (black isochrons) versus body fitted mesh (colored isochrons).	144
4.14 Error on the isochrons as a function of the mesh size h for non body- fitted meshes and a level set description of the domains. The order of convergence obtained with a linear fit is given by n	146
4.15 Computational domain of the heart-torso coupling problem with lungs and heart cavities. Activation zones are shown in black. The ECG can be plotted using probes $V1$ to $V6$	148
4.16 Isochrons of depolarization of an isolated human heart, based on measurements at 870 electrodes[27].	148
4.17 Isochrons of depolarization and repolarization.	149
4.18 The transmembrane potential u , the recovery variable v and the ex- tracellular/extracardiac potential u_w at selected time steps. Figures (a) to (i) show the depolarization phase, and figures (j) to (l) show the repolarization phase.	150
4.19 Zoom of the solution to see that the mesh does not capture very well the depolarization front. The region illustrated shows in grey the bottom of the left cavity.	151

<p>4.20 The solutions u, v and u_w for all time steps at a given point of the septum. The small oscillations observed on the solution on both sides of the depolarisation front are likely coming from the fact that the time step 0.3 used in this simulation is too close to the critical time step for stability. This is an illustration of the loss of monotonicity of the solution discussed in section 3.1 for time steps just below the critical value.</p>	<p>152</p>
<p>4.21 Isochrons of depolarization for the body fitted mesh. Contours are separated by 10 ms. There is a maximal difference of 3 ms between the geometry containing the heart, the lungs, the heart cavities and the torso (black contours) and the heart and the torso only (red contours).</p>	<p>153</p>
<p>4.22 Isochrons of depolarization for the non-body fitted mesh. Contours are separated by 10 ms. There is a maximal difference of 3 ms between the geometry containing the heart, the lungs, the heart cavities and the torso (blue contours) and the heart and the torso only (green contours).</p>	<p>153</p>
<p>4.23 Isochrons of depolarization of the geometry containing the heart, the lungs, the heart cavities and the torso. Contours are separated by 10 ms. There is a maximal difference of 10 ms between the body and the non body fitted meshes (black and blue contours, resp.). . .</p>	<p>154</p>
<p>4.24 Isochrons of depolarization of the geometry containing the heart and the torso only. Contours are separated by 10 ms. There is a maximal difference of 5 ms between the body and the non body fitted meshes (red and green contours, resp.).</p>	<p>154</p>

4.25 ECG with probes $V1$ to $V6$ (illustrated in figure 4.15). Blue: Heart-torso with a body fitted mesh. Green dash-dot: Heart-torso with a non body fitted mesh. Red dash: Heart-lungs-cavities-torso with a body fitted mesh.	155
5.1 Problems in reinterpolating a vector field.	170
5.2 The transmembrane potential propagating through the myocardium with a fiber arrangement. The notches (in boxes) appearing the depolarization front (figure 5.2(a)) caused by the error introduced by the reinterpolation of fibers vector field are attenuated when reinterpolating the conductivity tensor (figure 5.2(b)).	171
5.3 Background mesh used to calculate the isochrons. The figure is zoomed near the smallest cavity of the heart.	172
5.4 The solution at selected times for the non body fitted simulation with the adaptive strategy.	174
5.5 The adapted mesh at selected times for the non body fitted simulation. During the repolarization (d), solution variations are smoother than in depolarization (a), (b) and (c). The mesh is refined where the solution gradient is high, i.e. in the depolarization front.	175
5.6 The anisotropic mesh is refined near internal interfaces. The red curve represents the level set $\varphi = 0$ of the distance function φ from the surface of the heart. The domain of the heart (colored in blue) is defined as the largest set of elements completely inside $\varphi \leq 0$. This figure shows a portion of the heart cavity with the largest interface curvature.	176

5.7	Body fitted mesh at time 80 ms using different adaptation strategies: (a) refining along the internal interfaces, and (b) not refining along the internal interfaces. Isovalue $u = 0.13$ at $t=80$ ms are shown in (c) for both adaptation strategies (a) and (b). The isovalue for the strategy without adaptation along the internal interfaces is ahead with about 0.5 ms compared to the isovalue for the strategy with adaptation along the internal interfaces.	178
5.8	Zoom of the adapted meshes along an internal interface. The region illustrated is near the bottom of the heart. Meshes at time $t = 62$ ms with a number of nodes limited to 5,000 (a), 10,000 (b) and 20,000 (c). The background color is the magnitude of u with $u = 1$ in red and $u = 0$ in dark blue.	184
5.9	The data coming from a segmented CT scan used to build the ficti- tious moving heart.	187
5.10	Comparison of experimental measures and our model for the relation between the transmembrane potential and the force of contraction.	189
5.11	The transmembrane potential u calculated on an adapted non body fitted mesh of a moving level set based geometry.	190
5.12	The recovery variable v of the MS model calculated on an adapted non body fitted mesh of a moving level set based geometry.	191
5.13	The extracellular/extracardiac potential u_w calculated on an adapted non body fitted mesh of a moving level set based geometry.	192
5.14	The non body fitted mesh adapted every 1 ms (every 10 time steps) of a moving level set based geometry.	193
5.15	For inward displacements (a), a part of the solution may be lost. For outward displacements (b), the solution may be misdiplaced with a projection (e.g. x_1 to x'_1). It should have to be displaced with \vec{d} (e.g. x_2 to x'_2).	195

List of Tables

1.1	Typical values for intracellular and extracellular ionic concentrations and resting potentials for human cardiac cells. Source: [29].	3
2.1	FK parameters proposed in [83].	40
2.2	Speeds and recovery duration are taken in [47] where the heart cycle is of 700 ms. Similar values for speed can also be found in [1].	47
2.3	Parameters of the bidomain model for a human heart. Three different dimensional scalings are proposed. Adim1: based on the transmembrane potential upstroke. Adim2: based on the action potential duration and width. Adim3: based on convenient units. The values are taken from [81], [21] and [68].	50
2.4	Model's parameters for a physiological ventricle to get the asymptotic \sim -quantities.	90
2.5	MS and bidomain model's parameters for a physiological Purkinje system to get the asymptotic \sim -quantities. The numerical solution is performed on a domain of 2000 mm-long and of 1000 ms. Discretization: Forward Euler time scheme with 100,000 time steps and 8,000 degrees of freedom.	90

2.6	MS and bidomain model's parameters for a physiological Purkinje system to get the asymptotic \sim -quantities for a very steep upstroke. The numerical solution is performed on a domain of 1000 mm-long and of 1000 ms.	91
3.1	Monodomain model with FHN ionic model and the forward Euler time-stepping scheme: convergence study. The shadowed rows are close to the limit of stability. Reference solution's features are $T_{up,ref} = 29.9$, $T_{AP,ref} = 69.5$ and $c_{ref} = 0.32$ calculated with 4,000 nodes and 1,000,000 time steps.	113
3.2	Monodomain model with FHN ionic model and the Gear time-stepping scheme: convergence study. The limit of stability is experimentally about $n_t > 40$, or $\Delta t < 12$. Reference solution's features are $T_{up,ref} = 29.9$, $T_{AP,ref} = 69.5$ and $c_{ref} = 0.32$ calculated with 4,000 nodes and 1,000,000 time steps.	114
3.3	Monodomain model with the original MS ionic model: convergence study with forward Euler time-stepping scheme. The shadowed rows are close to the limit of stability.	115
3.4	Monodomain model with the original MS ionic model: convergence study with Gear time-stepping scheme. The shadowed rows are close to the limit of stability.	116
3.5	Features of the converged solution of the ionic models under study. .	116
3.6	Number of nodes required on a heart to have the prescribed relative error (1st column to 3rd column) on the upstroke duration, excited phase duration and speed. These results are calculated for simulations of 1000 ms and 8000 time steps with a Gear time-stepping scheme.	118
4.1	Theoretical order of convergence of $\ u - u_h\ _{0,\Omega}$. The domain $\Omega \subset \mathbb{R}^2$.	132

4.2	Statistics for the body fitted meshes.	135
4.3	Statistics for the non body fitted meshes.	135
4.4	Degrees of freedom for the body fitted meshes.	142
4.5	Degrees of freedom for the non body fitted meshes.	142
4.6	Parameters of the bidomain model for a human heart.	147
5.1	Wall clock (WC) and CPU times (s) for a typical iteration of Loop 2 for simulations with various time steps during the depolarization. .	179
5.2	Accuracy of the solution during the depolarization.	180
5.3	Accuracy of the solution during the repolarization.	181
5.4	Wall clock (WC) and CPU times (s) for a typical iteration of Loop 2 for simulations with various number of nodes (imposed at the adaptation step) during the depolarization. The time step is 0.1 ms.	182

Chapter 1

Introduction

The heart is a vital organ responsible for pumping blood throughout the body by rhythmic cycles of contractions and relaxations. Every day, the human heart can pump about 8,000 liters of blood with up to 100,000 heart beats[81]. The pumping function of the heart relies on the collective coordinated action and reaction of billions of cells, in order to ensure that each part of the heart contracts at the correct time. Heart failure is one of the most important causes of death in Canada. This is a great motivation for heart related research as an improved understanding of heart functions may lead to new treatments and diagnostic techniques. There exists a remarkable amount of knowledge about the mechanisms at the cellular and organ levels, where there is a complex interaction between a wide variety of phenomena:

- The electrochemical phenomena, where ion exchanges at the cell level are translated at the organ level by the propagation of a potential wave (cardiac action potential).
- The mechanical phenomena, which are initiated by the electrical activity and are affected by the blood pressure.
- The blood flow in heart cavities (blood propelled by the heart) and blood flow

in the myocardium vessels (blood supplying the heart). For example, ischemia or restriction in blood supply to a portion of the heart, can lead to conduction abnormalities and stimulus current pathologies.

Although a relatively complete understanding of separate small-scale processes can be obtained, it is very hard to understand the details of how these processes interact to form the functioning organ. Moreover, the behavior of the heart under pathological conditions is even more difficult to understand.

The electrocardiogram (ECG) is still the most widely used tool for heart diagnosis. ECG is a very powerful tool having the benefit of being non-invasive, but which is unfortunately not able to reveal all the detailed functions and dysfunctions of the heart. In fact, there remain many unresolved questions. For example, the understanding of defibrillation and its onset is still limited, for instance the application of a large electrical shock ends the ventricular fibrillation (rapid irregular contractions) with a high success rate, but the way the electrical current gets into the heart is not really known. As a consequence, there is a great need to refine existing techniques as well as developing new ones for the examination of the heart and the analysis of the heart functions.

1.1 The heart at the cell level

1.1.1 The cell membrane

The cell membrane provides a boundary separating the intracellular and extracellular environment. It consists of a bilayer of phospholipids with water-filled pores and protein-lined pores, called channels, which allow the passage of specific molecules. Typical values of ionic concentrations are given in Table 1.1.

Table 1.1: Typical values for intracellular and extracellular ionic concentrations and resting potentials for human cardiac cells. Source: [29].

Ion	Intracellular concentration (mmol/L)	Extracellular concentration (mmol/L)	Equilibrium potential (mV)
Na^+	10	135 - 145	72
K^+	155	3.5 - 5.0	-95
Ca^{2+}	10^{-4}	2	134

Ion transport

Osmosis is a passive process by which water is transported through a semipermeable membrane to balance the osmotic pressure, which is the hydrostatic pressure due to a difference in the concentrations of solute from one side to the other side of the membrane. Diffusion accounts for the passage of small molecules through pores and of lipid soluble molecules through the bilipid layer. For example, sodium and potassium ions pass through their specific channels and the process is driven by diffusion and electrical forces.

Concentration differences are maintained by active mechanisms, e.g. pumping ions against their concentration gradient, which require the expenditure of energy. For example, the $\text{Na}^+ - \text{K}^+$ pump, which uses the energy stored in ATP to pump three Na^+ out of the cell and two K^+ in, resulting a high intracellular K^+ concentration and a low intracellular Na^+ concentration. This pump regulates the cell volume and maintains an intra/extracellular difference of potential.

Another example of an important type of pump is the $\text{Na}^+ - \text{Ca}^{2+}$ exchanger, which uses the energy inherent in the concentration gradient of one ion to pump the other ion against its concentration gradient. This pump removes Ca^{2+} from the cell at the expense of Na^+ entry.

The transmembrane potential

It is a consequence of the control of the cell volume that the cell develops a potential difference across its membrane. In this thesis, we follow the standard convention for the transmembrane potential, which is given by

$$u = u_i - u_e \quad (1.1.1)$$

i.e. the intracellular minus the extracellular potential.

For a given ion, say S , the equilibrium is reached when the electric field exactly balances the diffusion of that ion. At equilibrium, the current must be zero and the potential difference across the membrane is given by the Nernst potential for ion S ,

$$u_S = -\frac{kT}{eq} \ln \left(\frac{[S]_e}{[S]_i} \right) \quad (1.1.2)$$

where T is the temperature, k is the Boltzmann's constant, e is the charge of an electron, q is the valence of the ion S , and $[S]$ denotes the concentration of ion S . The Nernst potential is independent of how the ions move across the membrane and is dependent only on the concentration difference. It is in a sense a universal law and it can be derived from many different principles[43].

Although the current is zero when a single ion species is considered, it is much more complicated when more than one ion can move through the membrane. In this case, the transmembrane potential that generates zero total current does not necessarily have no net current for each ion.

Electrical circuit model of the cell membrane and the voltage-current relation

The basis for many of the theoretical models in electrophysiology is derived from Kirchhoff's laws of electrical circuits. An example of a simple electrical circuit used

to model the cell membrane is shown in figure 1.1, where I_{ion} is the sum of all ionic currents. The cell membrane acts as a capacitor. Although many processes make

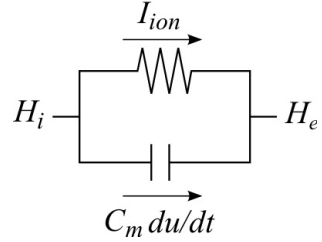


Figure 1.1: An electrical circuit model of the cell membrane.

the ions cross the membrane causing an electrical potential to develop, the medium on both sides of the membrane remains electrically neutral to a good approximation. Only a small amount of ions cross the membrane and the excess of charge accumulates near the interface. For an isolated cell not subject to any external stimuli, there is no production of charge on either sides of the membrane so the sum of the currents at one or the other side (outside or inside) of the membrane is zero. With the net transmembrane current $I_{ion} = \sum_S I_S$, we have

$$C_m \frac{du}{dt} + I_{ion} = 0. \quad (1.1.3)$$

The typical value of the capacitance of a cell membrane is $C_m = 1.0 \mu F/cm^2$.

At equilibrium the potential difference due to the difference of concentration for a given ion S is given by the Nernst potential u_S (eq. (1.1.2)). The net current flow due to the potential difference follows Ohm's law

$$I_S = g(u - u_S), \quad (1.1.4)$$

where I_S is the transmembrane current for ion S , g is the conductance of the "ohmic" channel and u is a potential resulting from all ions of the system. This linear current-voltage relation is also called the linear $I - u$ curve. Note that g is usually non

constant since the ability of cells to generate an electrical signal results from voltage and time dependence of the conductance.

Finally, remark that $I_{ion} = 0$ at equilibrium but each of the ionic current I_S is not necessarily null, meaning that u is not necessarily equal to u_S for all ions S .

Membrane Ion Channels

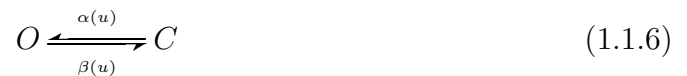
There are mainly two steps to simulate current in ionic channels. First, one needs to properly model the voltage-current relation to describe how the ions flow through *open* channels. Secondly, one needs to model the kinetics of channel gating, describing how the channels open or close in response to a change of voltage.

An open channel can be modeled as a sequence of binding sites, separated by barriers of potential: the passage of an ion through the channel is determined by the “probability” to go from one binding site to an other. The rate at which ions traverse the channel depends on both transmembrane potential and channel type (various heights of barriers and deepness of sites along the channel).

The opening and closing of ionic channels in response to changes in the transmembrane potential is the basis for electrical excitability. The current through a population of channels depends on the $I - u$ curve $\phi(u)$ (equation (1.1.4)) of a single open channel and on the fraction $\chi(u, t)$ of open channels.

$$I = \chi(u, t) \phi(u) \tag{1.1.5}$$

Let us present the simplest gating model for an ion channel. Suppose the channel can only take two states, either open, O , or close, C , and that the rates of conversion from one state to the other ($\alpha(u)$ and $\beta(u)$) are voltage dependent.



The rate of change of χ can be written as follows

$$\frac{d\chi}{dt} = \alpha(u)(1 - \chi) - \beta(u)\chi, \quad (1.1.7)$$

where the fraction of closed channels is $1 - \chi$ because of conservation. Under voltage clamp conditions (see Remark 1 below), $\alpha(u)$ and $\beta(u)$ are constants and then we can solve for χ as a function of time. It is convenient to write (1.1.7) as

$$\tau_\chi(u) \frac{d\chi}{dt} = \chi_\infty(u) - \chi \quad (1.1.8)$$

where $\chi_\infty(u) = \frac{\alpha}{\alpha+\beta}$ is the steady state of χ and $\tau_\chi(u) = \frac{1}{\alpha+\beta}$ is the characteristic time to approach the steady state. As there are many channels, the average rates $\alpha(u)$ and $\beta(u)$ can be determined from experimental data. However, this model is not enough representative of experimental data[43]. The analysis can then be extended to the case of channels with multiple sites where ions can be bound. More possible channel states than open O and closed C have to be considered. The sodium and potassium conductances in the Hodgkin-Huxley model are of that kind. The sites can be of different type and the rates of conversion from one state to another differ.

Remark 1 (Voltage Clamp) *The voltage clamp technique is used experimentally to measure the ion currents across a cell membrane. It operates by negative feedback holding the membrane voltage at a set level. It allows the membrane voltage to be manipulated independently of the ionic currents, allowing the voltage-current relation of channels to be studied.*

1.1.2 Excitability and action potential

For electrically excitable cells, an action potential (AP) is a biological manifestation described by a fast rise (depolarization) and fall (repolarization) of the transmembrane

potential. The AP of a cell is the result of the movement of ions through the cell membrane (passive transport and active transport e.g. voltage-gated channels), and this electrical activity is triggered typically by the electrical activity of adjacent cells. The propagation of the AP in the heart stimulates the myocardium and subsequently follows the contraction, allowing blood to be pumped throughout the body. An efficient contraction is ensured by a well-regulated stimulation, hence it is crucial to understand the inherent physiology.

If a heart beat results from the complex interaction of different APs in different portions of the heart, the model of the ventricular AP reveals far enough to have a good overall understanding of the cardiac AP. Here is a brief description (see [16]) of the ventricular AP featuring the most important four phases. Figure 1.2 shows a typical ventricular AP separated in phases and the relative ion flows with an example of a concurrent electrocardiogram.

Phase I: Transmembrane potential upstroke or depolarization (short time scale)

The transmembrane potential is initially at its resting state ($V_{rest} \simeq -85$ mV), where all the fast Na^+ channels are closed. A partial depolarization opens these channels causing a large influx of Na^+ ions, further increasing the depolarization. The cell gets positively charged ($V_{max} \simeq 40$ mV) or depolarized.

Phase II: Excited phase (long time scale) An outward current of potassium ions

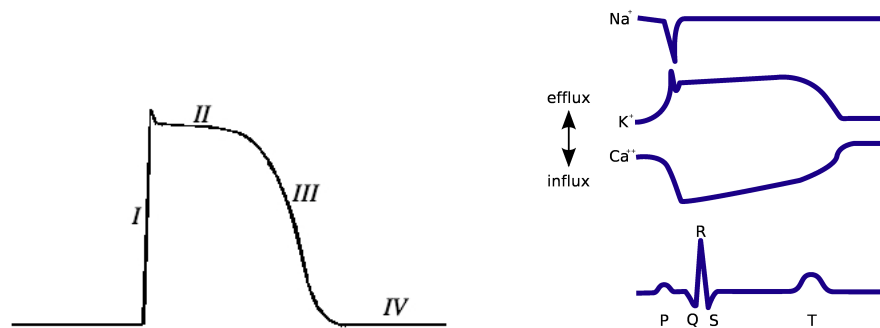
is balanced by an inward movement of calcium ions, causing a plateau. Sodium ions are still flooding in and just about keep pace. The transmembrane potential falls slowly. Note: The transient net outward current causing the small downward deflection (such an overshoot is observed for some cardiomyocyte) is, among others, due to the movement of K^+ ions.

Phase III: Downstroke or repolarization (short time scale) The calcium chan-

nels close while potassium channels are still open. The net outward positive

current causes the cell to repolarize until the transmembrane potential is restored to about -85 mV. The cell may pass its equilibrium polarization, and becomes hyperpolarized.

Phase IV: Refractory period (long time scale) Most of the sodium channels are inactive, and need time to recover before they can open again. The cell has already recovered its polarization but is nevertheless not susceptible to react to any external stimulus.



(a) The transmembrane potential versus time with the four main phases of the cardiac AP. This is the typical shape of a ventricular AP.

(b) Relative ion flows (three curves at top) and the concurrent electrocardiogram (bottom curve).

Figure 1.2: The cardiac action potential.

1.1.3 Modeling the action potential

A first crucial step in setting simulations in cardiac electrophysiology consists in choosing the ionic model, which are systems of ODEs able to reproduce the shape of the AP through time. The ionic models available (see www.cellML.org) are numerous and it is important to understand the benefits and the limitations of each model so that an appropriate choice can be made [22]. They can be classified in two types respective to the way these models are constructed. Accordingly, they are intended to simulate different phenomena.

Physiological cell ionic models give a detailed description of ions currents, ion channels and pumps because they are aimed to reproduce experimental data (Luo-Rudy [54], Beeler-Reuter [5], Hodgkin-Huxley [41, 63], Ten Tusscher [46], etc.). They are usually stiff, and their numerical solutions are time-consuming because of the necessity of using many descriptive variables and very short time scales.

A second class of ionic models contains the **phenomenological models** (FitzHugh-Nagumo (FHN) [33, 58], Aliev-Panfilov [4], Mitchell-Schaeffer [83, 56], etc.). The set of variables is usually reduced to two: one describes the activation and the other the recovery (u and v in the text). For the sake of simplicity the specific behavior of channels and ions currents are ignored, hence the phenomenological models are rather used to determine general propagation profiles. The number of unknowns and parameters is small, and the computational cost is appreciably reduced. This advantage is exploited for example in patient-specific modeling [71, 72] where multiple parameters adjustments are required and numerical solutions have to be readily obtained.

1.2 The heart at the organ level

1.2.1 Modeling propagation - The bidomain model

The most accepted model in the literature for cardiac AP propagation is the bidomain model (see [43, 81] and references therein). This mathematical model for cardiac tissues is based on volume averaging, the cardiac cells being too numerous to be modeled individually. To combine the effects of the potential difference through the cell membrane, the tissue is divided in two domains, which are the **intracellular** and the **extracellular** media (H_i and H_e resp.). A surface Γ_m separates these two domains. The presence of gap junctions (non selective channels that form direct intracellular connections) is taken into account and the intracellular domain is considered connected (see figure 1.3(a)).

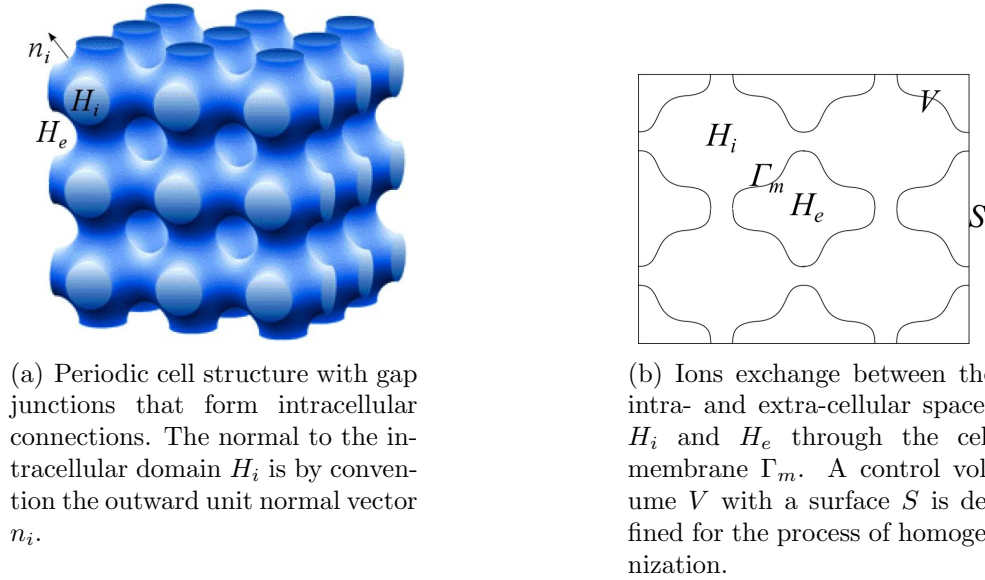


Figure 1.3: Geometrical considerations for the homogenization process used to derive the bidomain model.

Both domains are considered as passive conductors at the quasistatic state (time scales in electrophysiology are of the order of the ms and are way larger than time scales in electromagnetism), so that the potentials and the volume current densities can be related by Ohm's law:

$$J_{i,e} = -\sigma_{i,e} \nabla u_{i,e},$$

where σ_i and σ_e , assumed space dependent, are the conductivity tensors of intra and extracellular domains, respectively. There is no charge source and sink inside H_i or H_e and the ion dynamics occurs at the membrane to a good approximation. The transmembrane current density I_T is introduced and quantifies the ionic surface current flowing through the membrane by the following equation

$$I_T = J_i \cdot n_i = -J_e \cdot n_e,$$

representing a charge conservation (the ions leaving the intracellular domain go necessarily in the extracellular domain). As seen in section 1.1.1, the cell membrane that separates both media is considered as a electrical insulator (capacitive behavior) with channels specific to the passage of ions (resistive behavior). The total transmembrane current is then the sum of the capacitive and ionic currents:

$$I_T = C_m \frac{\partial u}{\partial t} + I_{ion} = -\sigma_i \nabla u_i \cdot n_i,$$

where u is the transmembrane potential (equation (1.1.1)).

Let us now derive the bidomain equations according to heuristic arguments. Details of a rigorous proof are given in [60]. We consider a volume V with a surface S containing a large number of cells. The volume V could be the "cube" illustrated in figure 1.3(a). On the one hand we have that

$$-\int_{V \cap \Gamma_m} (\sigma_i \nabla u_i) \cdot n_i dS = -\int_{(V \cap \Gamma_m) \cup S} (\sigma_i \nabla u_i) \cdot n_i dS$$

because of charge conservation in H_i , and

$$-\int_{V \cap \Gamma_m} (\sigma_i \nabla u_i) \cdot n_i dS = \int_{V \cap \Gamma_m} C_m \frac{\partial u}{\partial t} + I_{ion} dS.$$

We now define $S_i = V \cap \Gamma_m \cup S$ and $V_i = V \cap H_i$. On the other hand we have that

$$-\int_{S_i} (\sigma_i \nabla u_i) \cdot n_i dS = \int_{V_i} \nabla \cdot (\sigma_i \nabla u_i) dV$$

using the divergence theorem. All the variables are averaged over the volume V_i to get the variables denoted with a prime:

$$|V_i| \nabla \cdot (\sigma_i \nabla u'_i) = |S_i| \left(C_m \frac{\partial u'}{\partial t} + I'_{ion} \right).$$

For the charge conservation, an averaged result is also obtained

$$\nabla \cdot (\sigma_i \nabla u'_i) + \nabla \cdot (\sigma_e \nabla u'_e) = 0.$$

From an homogenization argument, the intra and extracellular domains are considered continuous and cover the whole cardiac muscle ($H = H_i = H_e$). To each point x in the heart H are associated intracellular and extracellular potentials, respectively u_i and u_e . For more details on the homogenization for the derivation of the bidomain model, see [36]. For the boundary conditions, we assumed that the heart is electrically insulated if the bidomain model is solved for the heart only. The bidomain model for an isolated heart consists in finding (u, v, u_e) such that

$$\frac{\partial v}{\partial t} = g(u, v) \quad \text{in } H, \quad (1.2.1)$$

$$\chi \left(C_m \frac{\partial u}{\partial t} + I_{ion}(u, v) \right) = \nabla \cdot (\sigma_i \nabla u) + \nabla \cdot (\sigma_e \nabla u_e) \quad \text{in } H, \quad (1.2.2)$$

$$\nabla \cdot (\sigma_i \nabla u) + \nabla \cdot ((\sigma_i + \sigma_e) \nabla u_e) = 0 \quad \text{in } H, \quad (1.2.3)$$

$$n_H \cdot (\sigma_i \nabla u + (\sigma_i + \sigma_e) \nabla u_e) = n_H \cdot (\sigma_T \nabla u_T) \quad \text{on } \partial H, \quad (1.2.4)$$

$$n_H \cdot (\sigma_i \nabla u_i) = 0 \quad \text{on } \partial H \quad (1.2.5)$$

with v the vector of variables for the ionic model, χ is the cell membrane surface to volume ratio $|S_i|/|V_i|$ and C_m is the specific capacitance per unit area of the cell membrane. The last equation comes from the assumption that the intracellular domain is isolated from the extracardiac domain.

The first equation represents the system of equations of the ionic model, which is coupled with the bidomain model via the current I_{ion} . For a simple 2-variable phenomenological model, the reaction term I_{ion} is expressed as an algebraic function $F(u, v)$. The vector function $G(u, v)$ is used for modeling the dynamics of every variable v_i , component of the vector v .

If the bidomain model is solved over the heart and the torso, we assume continuity of potentials between the extracellular domain and the extracardiac domain T (see figure 1.4)

$$u_e = u_T, \quad \text{on } \partial H,$$

where u_T is the potential in the extracardiac domain. We assume moreover that the intracellular domain is isolated from the extracardiac domain

$$n_H \cdot (\sigma_i \nabla u_i) = 0, \quad \text{on } \partial H,$$

and finally that the extracellular and the extracardiac domains are in direct contact

$$n_H \cdot (\sigma_e \nabla u_e) = n_H \cdot (\sigma_T \nabla u_T), \quad \text{on } \partial H,$$

where n_H is the outward unit normal to the heart and σ_T is the conductivity tensor of the extracardiac domain. The bidomain model for the heart-torso coupling problem consists in finding (u, v, u_e, u_T) such that

$$\frac{\partial v}{\partial t} = g(u, v) \quad \text{in } H, \quad (1.2.6)$$

$$\chi \left(C_m \frac{\partial u}{\partial t} + I_{ion}(u, v) \right) = \nabla \cdot (\sigma_i \nabla u) + \nabla \cdot (\sigma_i \nabla u_e) \quad \text{in } H, \quad (1.2.7)$$

$$\nabla \cdot (\sigma_i \nabla u) + \nabla \cdot ((\sigma_i + \sigma_e) \nabla u_e) = 0 \quad \text{in } H, \quad (1.2.8)$$

$$n_H \cdot (\sigma_i \nabla u + (\sigma_i + \sigma_e) \nabla u_e) = n_H \cdot (\sigma_T \nabla u_T) \quad \text{on } \partial H, \quad (1.2.9)$$

$$n_H \cdot (\sigma_i \nabla u_i) = 0 \quad \text{on } \partial H, \quad (1.2.10)$$

$$\nabla \cdot (\sigma_T \nabla u_T) = 0 \quad \text{in } T, \quad (1.2.11)$$

$$n_T \cdot (\sigma_T \nabla u_T) = 0 \quad \text{on } \partial T, \quad (1.2.12)$$

where we consider the extracardiac domain T as a passive conductor insulated, hence the two last equations.

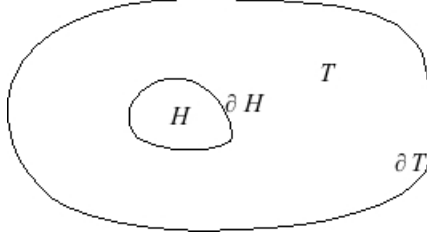


Figure 1.4: The heart H embedded in the extracardiac domain T .

1.2.2 The monodomain model

In the attempt of reducing the computational burden, the variable u_e can be eliminated for the one dimensional bidomain model for the isolated heart problem. This can be done by combining equations (1.2.2) and (1.2.3). The following model is equivalent to the bidomain model in 1D: finding (u, v) in $[0, x_{max}]$ such that

$$\chi \left(C_m \frac{\partial u}{\partial t} + I_{ion}(u, v) \right) = \sigma_{harm} \frac{\partial^2 u}{\partial x^2}, \quad (1.2.13)$$

$$\frac{\partial v}{\partial t} = g(u, v), \quad (1.2.14)$$

with $\sigma_{harm} = (\sigma_i^{-1} + \sigma_e^{-1})^{-1}$ is the harmonic average of the intra and extracellular conductivities in the x -direction. As the monodomain model is defined on the isolated heart only, a homogeneous Neumann boundary condition is applied on u .

The monodomain model can be seen as an extension of equations (1.2.13)-(1.2.14) in more than one dimension, and reads as

$$\chi \left(C_m \frac{\partial u}{\partial t} + I_{ion}(u, v) \right) = \nabla \cdot \sigma_{mono} \nabla(u), \quad (1.2.15)$$

$$\frac{\partial v}{\partial t} = g(u, v), \quad (1.2.16)$$

with σ_{mono} the conductivity tensor of the monodomain model.

In the particular case of equal anisotropy ratios between intra and extracellular media, that is $\sigma_e(x) = k\sigma_i(x)$ for all $x \in H$ and for $k > 0$, then $\sigma_{mono} = \frac{k}{k+1}\sigma_i$ and

the equations (1.2.15)-(1.2.16) are called the monodomain equations.

The monodomain model cannot be applied in all situations because it does not permit currents in the extracellular domain to influence the transmembrane potential u and ionic currents [70]. This influence has to be taken into account when there are applied currents due to pacing or defibrillation[28, 88].

But even when there are no applied currents, the heart-torso coupling problem turns out to be an example where the monodomain model is not suitable. Indeed, the current flow through the extracellular and extracardiac domains may influence cardiac sources in a way that can only be represented by a bidomain model (see for instance [92]). Finally, there exist models for the heart-torso coupling problem using the monodomain model, and where solutions are comparable to the bidomain solution in some specific situations[9].

1.2.3 Heart tissue and fiber arrangement

As mentioned above, the conductivity values in both the bidomain and monodomain models are represented at each point in space by a tensor σ , which is justified by the anisotropic conductivity properties of the heart tissue. The anisotropy comes from the fact that the heart muscle is composed of fibers. The conductivity is higher in the fiber direction while it is lower in the cross-fiber direction. The muscle fibers are arranged in sheets, which leads to the introduction of three different eigendirections for the conductivity tensor: along the fibers (longitudinal direction a_l), perpendicular to the fibers but along the sheet (transverse direction a_t) and perpendicular to the sheet (normal direction a_n). The local conductivity tensor σ expressed in this eigenbasis

(of unit vectors a_l , a_t and a_n) is diagonal:

$$\bar{\sigma} = \begin{pmatrix} \sigma_l & 0 & 0 \\ 0 & \sigma_t & 0 \\ 0 & 0 & \sigma_n \end{pmatrix}.$$

Values of the conductivities eigenvalues σ_l , σ_t and σ_n for different media (intracellular, extracellular media, and any other extracardiac media) can be found in the literature (see section 2.3). Let A be a local orthogonal matrix having the vectors a_l , a_t and a_n as columns. Then the intracellular and extracellular conductivity tensors can be written as

$$\sigma_{i,e} = A\bar{\sigma}_{i,e}A^T \quad (1.2.17)$$

in the Cartesian coordinate system.

1.2.4 The conduction system

The electrical basis of the heart provides rhythmicity to cause the mechanical functioning of the heart. Figure 1.5 shows what is known as the conduction system. The conduction system constitutes only a small part of the total mass of the myocardium. Therefore, the myocardial cells of the atria and ventricles provide a larger electrical signal than the whole of the specialized conduction tissue.

The sequence of excitation starts at the sinoatrial node which is the physiological pacemaker of the heart. From the sinoatrial node, excitation spreads through both atria to the atrioventricular node, then, via the bundle of His and its two branches which carries the impulse to the ventricular muscle through a specialized collection of fibers called the Purkinje fibers. Activation of the ventricular muscle takes place from endocardium (internal surface) to epicardium (external surface) and from the apex (lowest part of the heart) of the ventricles to the base (up to the atrial)[43].

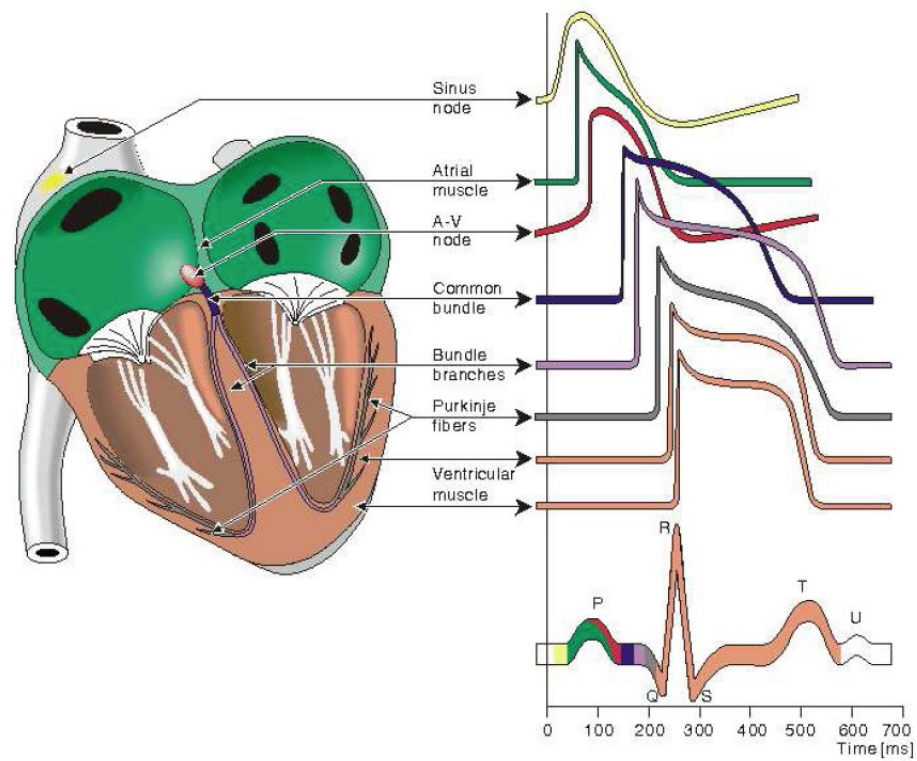


Figure 1.5: The cardiac conduction system with the shapes of the action potentials in different tissues of a human heart. Source: [68].

1.3 Perspective of heart simulation

The quest for knowledge in this field inspires many researchers interacting in many domains: physicians, physiologists, specialists in functional imaging, physicists, mathematicians, etc. In the current biomedical research, numerical simulations are a powerful tool in helping scientists solve complex cardiac problems. The use of computer simulations based on mathematical modeling in physiology is a very active field of research. Advanced simulations can be used to study detailed heart functions over long time periods. Interconnected and multiscale models are implemented including biomechanics, electrophysiology, and the underlying mechanisms of cardiac cells. With appropriate combinations of mathematical models, it is possible to perform simulations that not only reproduce data from experiments, but that also have a predictive power. In fact, there is a growing need for patient-specific and complete modeling of the heart to support comprehensive disease assessment and therapy planning[85].

Personalization is a key aspect of biophysical models in order to impact clinical practice like therapy planning[24]. A complete description of the heart includes both physiological and anatomical data, and numerical simulations must be performed with such data in order to get realistic results. Realistic modeling remains a great challenge, just considering a priori the complex anatomy of the heart circulatory system (including valves, blood vessels), the muscle (including fiber arrangement, heterogeneous mechanical properties of the myocardium), the conducting system, etc. Experimental data are essential to integrate within models but they are difficult to obtain. They are even more difficult to integrate in a whole patient specific model, because of the variability between individuals. The development of experimental techniques provides more and more information, leading to the development of increasingly sophisticated models. It drives continuously research advances because of the strong and continuous interaction with modeling.

Finally, performing realistic simulations does not depend only on setting up accu-

rate models with suitable data. It also depends on the ability to solve accurately and efficiently the resulting equations using numerical techniques. The multiscale aspects of the equations makes it very challenging to solve, and the numerical techniques employed are still a very debated issue.

1.3.1 Computational cardiac electrophysiology

The cardiac electrical activity results of small-scale processes and transports information at the organ level, where the overall forms a complex heterogeneous system for conduction and contraction. There are many ways to take advantage of the numerical simulations for a better understanding of the heart functions and dysfunctions from the electrical point of view. Numerical cardiac electrophysiology can be divided in two main classes of problems: the direct problem and the inverse problem.

Direct (forward) problem: The forward problem of cardiac electrophysiology consists in studying the electrical activity of the heart, from the description of cardiac activity from sub-cellular and cellular level to the level of the whole organ, and finally to the non-invasive recording of this activity at the body surface[52]. Despite the conceptual simplicity of the problem, the task is far from trivial, and to date we still cannot consider this problem to be solved in any true meaning of the word. An example of application of the direct problem is in therapy planning, where the location of the ablation site of an infarct scar can be confirmed to be successful or not[85]. This modeling framework also allows to carefully examine the effects of cellular level activity on the recorded ECGs.

Inverse problem: The inverse problem of cardiac electrophysiology can be summarized as the computation of the cause at the cellular level and/or at the organ level (e.g. location of an infarct) of a given measured effect (e.g. ECG)[81]. A great difficulty of inverse problems is that the same set of non-invasive measurements could

result from more than one source configuration. Hence the inverse problems are often ill-posed, i.e. fail to satisfy at least one of the following solution conditions (in the sense of Hadamard): existence, uniqueness and continuous dependence on the data.

Remark 2 *In many cases, the cause we want to identify is the set of parameters of the model equations from measurements of the solution of the associated direct problem. This situation refers as the parameter identification problem[12], and a variant of this type of problem will be treated in chapter 2.*

1.3.2 Geometrical model of the heart and level sets

Simulations in cardiac electrophysiology are often made using the finite difference, the finite element or the finite volume methods. These methods require a mesh of the computational domain. Two types of geometrical models are typically used: models of simplified representation of cardiac geometry[87, 62], and high-resolution image-based models of cardiac structure and geometry[89]. A simplified geometry enables propagation to be studied in the absence of anatomical detail, whereas more detailed geometrical models with high spatial resolution enable the role of anatomical structures to be evaluated[21].

As the computational domain of a realistic human heart has a complex geometry, most computations are made on meshes of simplified geometries. The mesh can also be deformed to fit a medical image with increasingly refined models where a fiber mapping is involved[84, 88]. Though these methods are very robust, they rely on a standard mean shape of the heart, hence the complex details of the geometry can be lost (see [93] for an overview of model-to-image adaptation techniques).

It is important to build accurate geometrical models of the heart for understanding phenomena like defibrillation and the study of an infarcted heart, as these phenomena are highly influenced by the propagation through fine anatomical structures. Realistic geometrical models of the heart containing fine anatomical features

can be obtained directly from segmentations of medical images (e.g. CT scan, MRI, echocardiography, Visible Human Project). The finite element simulations presented in this thesis use precise human heart segmentations based on an original method developed by Olivier Rousseau[74]. His work had allowed to achieve the construction of two and three dimensional geometrical models (figures 1.6 for a 2D model and figure 1.7 for a 3D model) of the human heart using an iterative Chan-Vese model. It is publicly available to the scientific community[73]. The segmentation process developed provides a level set description of the heart (see next section), a framework allowing the possibility of dealing with moving geometry and facilitating the integration of patient-specific cardiac geometries. In the lack of data time series, we restrained our analysis to fixed geometries but the extension to a realistic time deforming geometry would be natural.

Level set method

The level set method devised by Sethian and Osher [65] gives tools for computing and analyzing the motion of an interface Γ in two or three dimensions. In the context of describing the heart H embedded in the extracardiac domain T as in section 1.2.1, the interface of the heart is $\Gamma = \partial H$, where the whole domain $\Omega = H \cup \partial H \cup T$. The idea is to define a continuous function $\varphi : \Omega \rightarrow \mathbb{R}$ with

$$\varphi(x) \begin{cases} < 0 & \text{for } x \in H, \\ = 0 & \text{for } x \text{ on } \partial H, \\ > 0 & \text{otherwise,} \end{cases} \quad (1.3.1)$$

with $x \in \Omega \subset \mathbb{R}^2$ or \mathbb{R}^3 . The level curve $\varphi = 0$ represents the interface ∂H . For $\rho > 0$, we denote by

$$N(\Gamma, \rho) = \{x \in \Omega : \text{dist}(x, \Gamma) < \rho\}$$

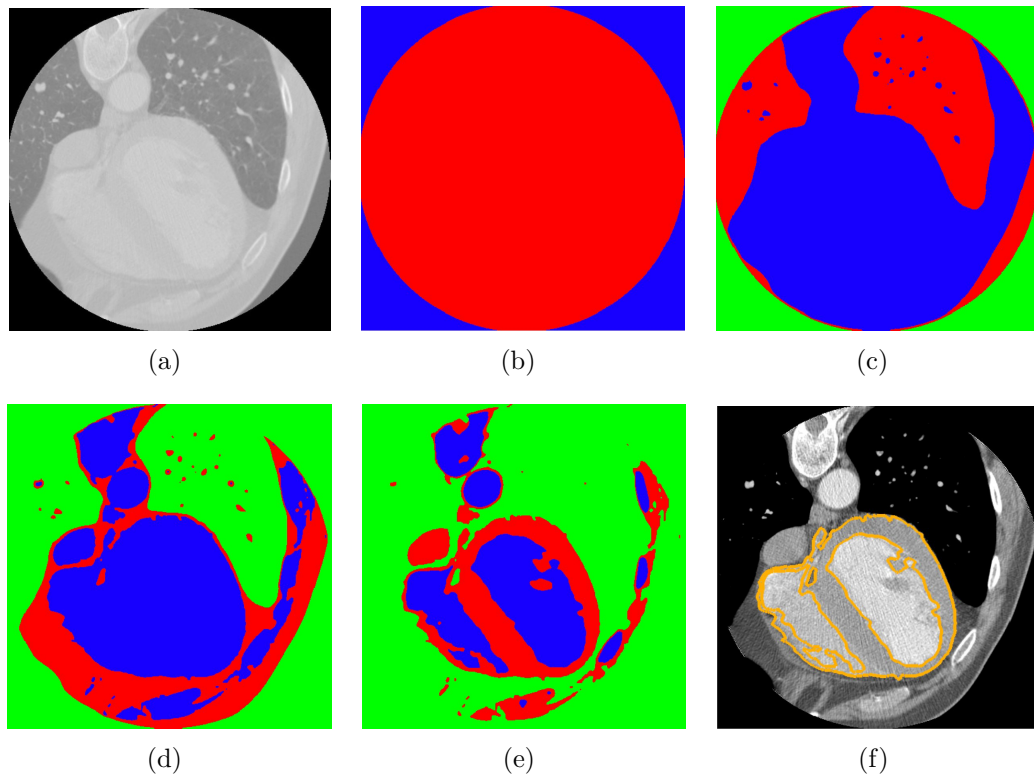


Figure 1.6: 2D iterative segmentation of the heart from a CT scan image. (a) The image to be segmented, (b) the result of the first application of the Chan-Vese model using the original image, (c)-(e) second step, obtained using a blurred versions of the image (a), (f) the final segmentation of the heart muscle over the 2D image. Source: Olivier Rousseau [74].

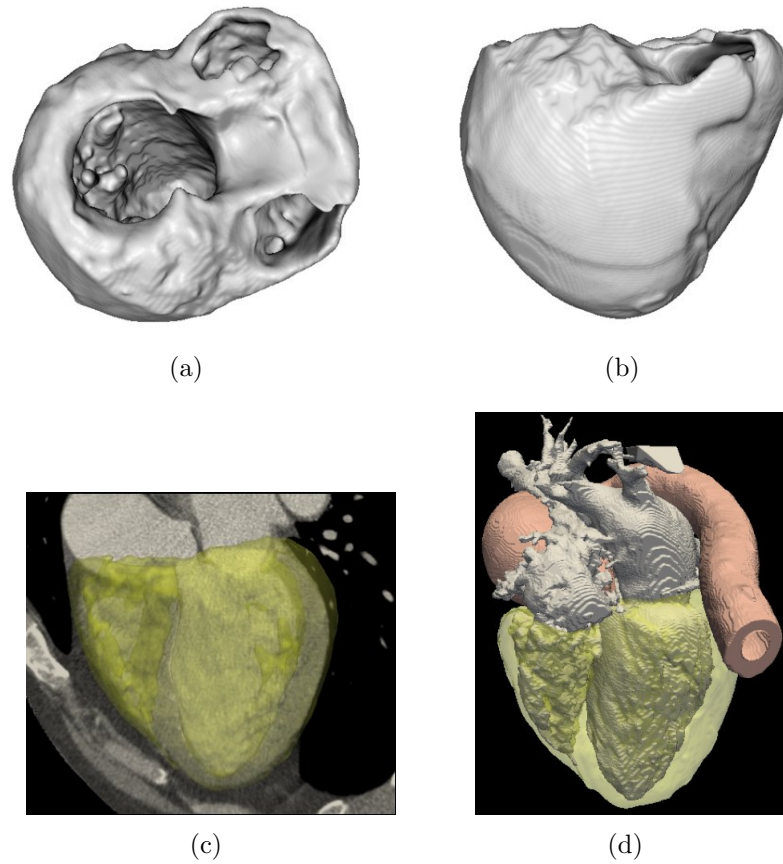


Figure 1.7: 3D segmentation of the human heart ventricles from a 3D CT image. (a)-(b) Different views of the segmentation, (c) a view of the segmented exterior surface over the original image, (d) a view of the segmented ventricles together with the atria cavities and the aorta. Source: Olivier Rousseau [74].

the ρ -neighborhood of Γ , where $\text{dist}(x, \Gamma)$ is the distance between x and Γ , i.e. the shortest distance between x and all $x_\Gamma \in \Gamma$. Suppose that it exists a ρ_0 such that $\overline{N(\partial H, \rho_0)} \subset \Omega$, φ is a regular function and $|\nabla\varphi| > 0$ in $N(\partial H, \rho_0)$. The normal vector n pointing outward H is given by

$$n = \frac{\nabla\varphi}{|\nabla\varphi|}.$$

The signed distance function

$$\varphi(x) = \begin{cases} -\text{dist}(x, \partial H) & \text{for } x \in H, \\ 0 & \text{for } x \text{ on } \partial H, \\ \text{dist}(x, \partial H) & \text{otherwise.} \end{cases} \quad (1.3.2)$$

is a typical function which satisfies the hypothesis for the definition of a level set function.

An important advantage of describing the heart dynamics in the level-set framework is the possibility of automatically dealing with moving and deforming walls. Thus, the interface is captured for all time t , by locating the set $\{x \in \Omega | \varphi(x, t) = 0\}$. This also allows for automatic integration of patient-specific cardiac segmentations when time series of medical images are available.

Topology changes like merging and breaking do not require special care using level set functions (figure 1.8). They occur naturally as nothing special happens to the level set function when the topology of its level sets changes. As a comparison the active contour approach (energy-minimizing spline guided by external constraint forces and influenced by image forces that pull it toward features such as lines and edges[42]) handles topology changes with difficulty.

Finally, level set methods have achieved success in the recent years in dealing with computations of free surface fluid dynamics[34], deforming objects and liquids,

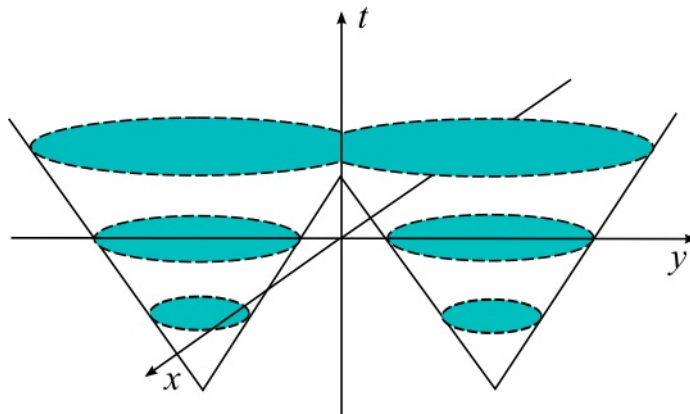


Figure 1.8: The level set method can manage topology changes. Slices are shown at different times for illustrating the curve evolution process. Remark that $\varphi < 0$ inside the cones, $\varphi = 0$ at the surface of the cones and $\varphi > 0$ outside the cones.

and even blood fluid dynamics from four-dimensional cardiac CT images[55]. We finally suggest that level set methods could be also applied to other types of problems in numerical simulations of the heart like in electrophysiology and electromechanical coupling.

1.3.3 Finite element method

The literature in cardiac numerical electrophysiology is vast. The numerical methods employed with their numerous variants go in all directions. The finite difference method, the finite volume method and the finite element method are the most commonly applied techniques to discretize spatially the monodomain or bidomain equations. Other methods have also been used like the boundary element method, mesh free methods, spectral methods, etc (see [21] and references therein). Let us first depict a general portrait of the most commonly used numerical methods with their advantages and disadvantages.

The finite difference method uses finite difference formula to discretize derivatives in order to approximate the solutions of differential equations (see [70] for applica-

tions in electrophysiology). The spatial mesh has to be usually structured though this approach can be generalised for grids with irregular spacing (see [86]). The advantage of the finite difference method is the straightforward implementation of the method. The disadvantage is that it is difficult to describe smooth curved surfaces, so that it becomes difficult to implement boundary conditions[21]. For the finite volume method, volume integrals in a PDE involving a divergence component are converted to surface integrals applying the divergence theorem. Finite volumes schemes exhibit good stability properties with regard to the sharpness of the reaction terms in bidomain modeling[23]. The finite volume is conservative and can be formulated to allow for unstructured meshes. Finally, the finite element method seeks the approximate solution of partial differential equations using its weak form discretized in a finite dimensional space. It is widely used for solving differential equations over complex, curved geometries, see for example [89]. Let us see the details of how the standard finite element method is applied to a simplified problem.

Definition of a simplified problem and weak formulation

In this section, we focus on the finite element method for solving Poisson's equation, as the monodomain (equations (1.2.15)-(1.2.16)) and bidomain (equations (1.2.1)-(1.2.5)) models are based on Ohmic law and Poisson's equation for stationary electrical currents. This approach allows for a description of the anisotropic electrical properties of cardiac tissue by studying a diffusion problem with subregions of different conductivities.

Let $\Omega = \Omega^- \cup \Omega^+ \cup \Gamma$ be a domain with subdomains Ω^- and Ω^+ (see figure 1.9). The domain Ω^- is embedded in the domain Ω^+ (see figure 1.9). Note that $\Gamma \cap \partial\Omega = \emptyset$ and the specific shape illustrated in figure 1.9 has no importance in this section. The internal interface Γ separates the two subdomains that have a different conductivity constant σ .

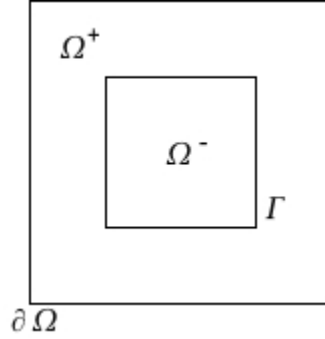


Figure 1.9: Domains for the elliptic problem (1.3.3).

The problem consists of finding u such that

$$\begin{aligned} -\nabla \cdot (\sigma^- \nabla u) &= f \quad \text{in } \Omega^-, \\ -\nabla \cdot (\sigma^+ \nabla u) &= f \quad \text{in } \Omega^+, \end{aligned} \tag{1.3.3}$$

with the following transmission conditions on Γ , namely the continuity on u

$$[u]_{\Gamma} = 0, \tag{1.3.4}$$

where $[u]_{\Gamma}$ denotes the jump of u on Γ , and the continuity on the normal flux of u

$$[\sigma \nabla u \cdot n]_{\Gamma} = 0, \tag{1.3.5}$$

and finally the boundary conditions on $\partial\Omega$, which could be either of Dirichlet ($u = g$) or Neumann type ($\sigma^+ \nabla u \cdot n = 0$ in the homogeneous case).

The diffusion problem in its weak form consists in finding u in the appropriate function space $V \in H^1(\Omega)$ such that

$$\int_{\Omega} \sigma \nabla u \cdot \nabla \phi = \int_{\Omega} f \phi, \quad \forall \phi \in V_0 \tag{1.3.6}$$

with

$$\sigma = \begin{cases} \sigma^+ & \text{in } \Omega^+ \\ \sigma^- & \text{in } \Omega^-. \end{cases}$$

Let $f \in L^2(\Omega)$ and $\sigma \in L^\infty(\Omega)$ with the ellipticity condition $\sigma(x) \geq \sigma_0 > 0$. Then the problem has a unique solution u in $H^1(\Omega)$. Precisely, let $\tilde{V} = \{v \text{ s.t. } v|_{\Omega^-} \equiv u^- \in H^1(\Omega^-), v|_{\Omega^+} \equiv u^+ \in H^1(\Omega^+), u^-|_\Gamma = u^+|_\Gamma\}$. For Dirichlet boundary conditions on $\partial\Omega$, u is found in $V = \{v \in \tilde{V} \text{ s.t. } v|_\Gamma = u_{exact}\}$. For Neumann boundary conditions, u is found in $V = \tilde{V}/\mathbb{R}$ and $V \equiv V_0$ in the homogeneous case.

The exact and the approximate problems

Consider the following linear abstract variational problem: find u in V such that:

$$a(u, \phi) = (f, \phi), \quad \forall \phi \in V. \quad (1.3.7)$$

This abstract problem represents the problem (1.3.6), with $a(u, \phi) = \int_\Omega \sigma \nabla u \cdot \nabla \phi$ and $(f, \phi) = \int_\Omega f \phi$. When one attempts to solve such a problem with the finite element method, one rather writes an approximated formulation of the problem (1.3.7) for finding an approximate solution.

The finite element approach relies on a discretization of the continuous domain into discrete subdomains, called elements and usually denoted by K [20]. The set of all the elements is called the mesh, denoted by \mathcal{T} . As the calculations are done on a mesh \mathcal{T}_h with a mesh size h , one expects to find formulations that allow the convergence of the approximate solution u_h towards the exact solution u as $h \rightarrow 0$. With any finite dimensional subspace V_h of V , the approximate (discrete) problem associated to (1.3.7) reads as: find u_h in V_h such that

$$a_h(u_h, \phi_h) = (f, \phi_h), \quad \forall \phi_h \in V_{0h}. \quad (1.3.8)$$

Definition 1.3.1 *Approximating the solution of problem (1.3.7) by defining a similar problem in a finite dimensional subspace of V refers to the **Galerkin method**. The approximate space V_h is said **conforming** if V_h is a subspace of the space V . Otherwise, V_h is said **non conforming**.*

Let us examine how the discrete problem (1.3.8) is solved in practice. Let $(w_k)_{k=1}^M$ be a basis in the space V_h . Then the solution $u_h = \sum_{k=1}^M u_k w_k$ of problem (1.3.8) is such that the coefficients u_k are solutions of the linear system

$$\sum_{k=1}^M a(w_k, w_l) u_k = (f, w_l), \quad 1 \leq l \leq M.$$

Definition 1.3.2 (Finite element [20]) *A finite element is a triple (K, P, Σ) where*

1. K is a closed subset of \mathbb{R}^n with a non empty interior and a Lipschitz-continuous boundary,
2. P is a space of real-valued functions (usually called the basis functions of the finite element) defined over the set K ,
3. Σ is a finite set of linearly independent linear forms ϕ_i , $i = 1 \leq i \leq M$ (usually called the degrees of freedom of the finite element) defined over the set P . It is assumed that there exists functions $p_i \in P$, $i = 1 \leq i \leq M$ which satisfy $\phi_j(p_i) = \delta_{ij}$, $i = 1 \leq i \leq M$ so that we have $p = \sum_{i=1}^M \phi_i(p) p_i$.

The finite elements most commonly used by engineers are Lagrange finite elements, where the degrees of freedom are point values, i.e. $u_i = u(x_i)$. The basic idea is to use polynomial approximations. Let us denote by $P_k(K)$ the space of all polynomials $p : x \in K \rightarrow p(x)$ of degree $\leq k$. Then the finite element space must be built such that the restriction of the solution on each element K satisfies $u_i = \sum_{j=1 \leq i \leq M} u_j p_j(x_i) = u(x_i)$. In order to give a very simple example in 1D, the

piecewise linear Lagrange polynomial (in P_1) associated to a given node x_i is the hat function illustrated in figure 1.10.

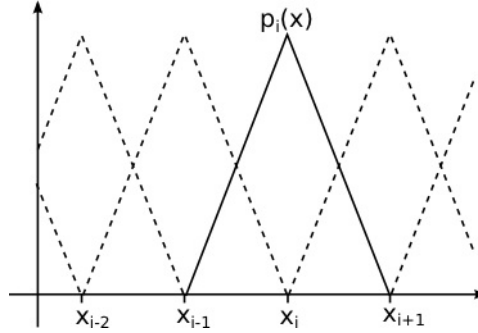


Figure 1.10: Lagrange FE basis functions in P_1 .

The next step consists in computing the bilinear form $a(\cdot, \cdot)$ which is now a matrix with entries $a(w_k, w_l)$. Referring to the problem (1.3.6) discretized with Lagrange finite elements, the values of entries $a(w_k, w_l) = \sum_{K \in \mathcal{T}} \int_K \sigma \nabla w_k \cdot \nabla w_l$ can be computed using a Gauss quadrature to give the result $a_h(w_k, w_l)$. If the numerical result of the integral is exact, then $a_h(\cdot, \cdot) = a(\cdot, \cdot)$ and the method is said consistent. The consistency can also be obtained asymptotically as $h \rightarrow 0$.

Theoretical order of convergence

Depending on the finite element formulation, some theoretical results exist [20], [49], [51], [53], [67], even about the order of convergence with discontinuous coefficients. If the exact solution of the problem is known, a finite element method is said to converge with order p in the norm of the space V if the following error estimate holds

$$\|u - u_h\|_{V, \Omega} \leq Ch^p$$

. The order of convergence is then a measure of how the error $e_h = u - u_h$ tends to zero with the mesh size h .

From the theorems C.0.1 and C.0.2, one can deduce the optimal order of convergence in the H^1 and the L^2 norms, respectively, when the mesh is adapted to the piecewise linear internal interface and the domain is polygonal. The solution of problem (1.3.6) with a standard Galerkin FE formulation and P_k basis functions converges with order k in the H^1 -norm [20] if u is sufficiently smooth. It converges with order $k + 1$ in the L^2 -norm for the same regularity condition on u , i.e. u in $H^{k+1}(\Omega)$. If a finite element method is endowed with one of these orders of convergence, we say that the method is *optimal* in the respective norm.

Finally, remark that when the domain has a curved boundary, isoparametric finite element methods are optimal, and the order of convergence is limited to $3/2$ in the H^1 -norm[79].

Time discretization and stability

Most finite element methods use finite difference schemes for time discretization. Explicit, implicit, and semi-implicit methods can be used to solve the equations describing the time dependence of action potential propagation. The choice of numerical method influences the stability, computational cost and the accuracy of the implemented model. Explicit methods can be used (for instance in [84, 90]), because they are easy to implement. However, even though the computational cost for each time step is low in an explicit method, the time step may need to be small to guarantee stability. Implicit and semi-implicit schemes can be stable with larger time steps[15], but are more computationally expensive. Semi-implicit methods turn out to be a good compromise as their stability does not depend on the mesh size unlike the explicit methods. In addition, they do not require the resolution of a system of nonlinear equations unlike the implicit methods[30]. We consider only two methods in this thesis:

Definition 1.3.3 (Euler and Gear time-stepping schemes) *The following dif-*

ferential equation

$$\frac{du}{dt} = f(u, t),$$

is discretized with the forward Euler time integration scheme as

$$\frac{u_{t+\Delta t} - u_t}{\Delta t} = f(u_t, t)$$

and with the implicit Gear time integration scheme as

$$\frac{3u_{t+\Delta t} - 4u_t + u_{t-\Delta t}}{2\Delta t} = f(u_{t+\Delta t}, t + \Delta t).$$

1.4 The scope of this thesis

The work developed in this thesis focusses on the electrical activity of the heart, from the modeling of the action potential originating from cardiac cells and propagating through the heart, as well as its electrical manifestation at the body surface (electrocardiogram). The study is divided in two main parts: modeling the action potential, and numerical simulations. It addresses the three following problems in an original way.

1. **Problem:** One of the current debates about simulating the electrical activity in the heart is the following: Using a realistic anatomical setting, i.e. realistic geometries, fibers orientations, etc., is it enough to use a simplified 2-variable phenomenological model to reproduce almost all cardiac electrical propagation behaviors, and in what sense is that sufficient?

Solution: A dimensional asymptotic analysis is developed in order to predict the time/space scales and speed of an action potential wave simulated with a selected ionic model. It allows to control the solution in a region of constant conductivity. This is made possible as explicit relations on all the physiological constants are obtained.

2. **Problem:** Time and space discretization is difficult to manage when several models are coupled together, not to mention when realistic patient data are considered and model parameters have to be modified in order to reproduce the most exactly an experimental sequence of data.

Solution: We explore the influence of the space and time discretization on a 1D finite elements (FE) solution of selected ionic models. Theoretical stability conditions are derived for a selection of time integration schemes, and are verified numerically. Stability conditions are derived in such a way that any model parameter dependence is revealed explicitly.

3. **Problem:** For the last decade, there is a clear trend of using as much experimental data (e.g. medical images) as possible in numerical cardiac electrophysiology. Patient specific simulations is a very popular concept but simulations are often performed on the same geometrical models. There is a need in adapting numerical methods to the data available from the geometrical models (e.g. level sets from segmentations of medical images).

Solution: A numerical method for solving the heart-torso coupling problem is explored according to a level set description of the domains coming from segmented medical images. Mesh adaptation is used to improve the accuracy and the efficiency of the numerical method developed.

Chapter 2

A predictive method allowing the use of a single ionic model in numerical cardiac electrophysiology

2.1 Introduction

For the last decade there is an increasingly popular trend to patient-specific modeling, where the predictions in clinical applications rely on the personalization of cardiac electrophysiology models. There is great need in developing prediction tools that could be used for example to improve therapy planning. For instance, mapping models are used in [71, 72] to estimate the model parameters, resulting in model predictions similar to the actual clinical data.

These applications require doing realistic numerical simulations, which imply playing with space/time varying parameters. These parameters are either associated with models at the cell scale (the ionic models) or associated with models at the

myocardium scale (models for propagation, e.g. the monodomain or bidomain model). The problem arises mainly when one wants to incorporate ionic models in the model of propagation: the time and space scales have to match and some parameters have to be tuned properly. The ionic models are systems of ODEs that are particularly sensitive to the variation of the parameters. It is hard to change the parameters in the equations so that the whole system of differential equations reacts with the right time and space scales. As a result, doing realistic simulations implies that the influence of every single involved parameter has to be well understood.

This overall understanding is hard to achieve and to address this difficulty we propose to reduce the set of parameters in the equations. First of all, a non dimensionalization is performed and much less parameters are necessary that is to say *a single* nondimensional number replaces all parameters related to the propagation of the potential. Second, the Mitchell-Schaeffer phenomenological ionic model is used to reproduce the action potential dynamics. See section 2.2.3 for the justification of this choice. Using an asymptotic analysis, a bijective relation between the set of the ionic model parameters and the set of solution features is built. The combination of the dimensional analysis and the asymptotic analysis makes possible to fix precisely the parameters of the ionic model and the bidomain model.

Aside from its theoretical interest, this work gives the steps to control the wave's shape and its propagation in a local region of constant conductivity. This is a huge step towards the inverse problem (introduced section 1.3.1) because it removes many unknowns in the system. If the use of the Mitchell-Schaeffer model turns out to be sufficient, every model parameter and numerical scheme can be chosen properly by virtue of the knowledge of the resulting solution. The approach is then predictive. Remark that a similar approach could probably be successfully applied to another ionic model.

As a last comment, this work results from a combination of methods that have been used extensively. In previous works in this domain, e.g. [43, 16] for ODE models

and [56, 75, 76] for mapping models, the results of the analysis portrays a general behavior of the solution features. It gives some dependences on some parameters of the model, but not all possibly influent parameters. Our analysis allows to reliably predict a desired solution with explicit dependences on *all* model parameters and *all* the physiological constants. Our approach is not only able to deal with isolated as well as sequences APs, but it also can be used to precisely shape *propagated* APs. This approach is then suitable for predictions and the results could also be extended in mapping models.

2.2 Ionic models

Within the framework of fully integrative modeling, as much knowledge as possible is integrated at each level of organization. Many submodels are then coupled together, their complexities making each of them hard to handle (adjustments of parameters, different time/space scales) among others submodels within the whole model. For most applications, it may not be necessary to construct a highly detailed and expensive to compute physiological ionic model [22]. Phenomenological models become worthy in this situation (see section 1.1.3) and it turns out that this is our choice of framework. This section reviews a selection of phenomenological models, some are introduced for completing the understanding, the others are used in numerical simulations under various contexts treated throughout the whole thesis. Note that in this section, ODE models are presented in order to analyze the behavior of a single cell only. This is the phenomena at the membrane that are described here, hence there is no need for considering variables such as u_i or u_e .

More precisely, two well-known phenomenological models are used in this thesis: the FitzHugh-Nagumo (FHN) model and a modified Mitchell-Schaeffer (MS) model. The FHN model, with all its limitations, is introduced for comparison only because it is the most known and pedagogical model. The Fenton-Karma model is introduced

as it is from where the MS is derived. It is the goal of this chapter to provide a justification for using the MS model within the framework of realistic modeling and patient-specific modeling. It will be used for most subsequent analysis and numerical simulations.

2.2.1 FitzHugh-Nagumo model[32, 59]

The FHN model is a simplified version of the Hodgkin-Huxley model that was originally developed to reproduce the AP in squid giant axons. A wave resembling a cardiac AP (figure 2.1) can be obtained when other parameters than the original model are used. The model equations in 0D are given by

$$\frac{du}{dt} + f(u, v) = 0, \quad \text{where } f(u, v) = f_0 u(u - \alpha)(u - 1) + v \quad (2.2.1)$$

$$\frac{dv}{dt} = g(u, v), \quad \text{where } g(u, v) = \epsilon(\gamma u - \beta v), \quad (2.2.2)$$

where $f_0 = 1$, $\beta = 1$, $\gamma = 0.16875$, $\epsilon = 0.01$ and $\alpha = 0.25$ (parameters taken from [7]). Remark that the transmembrane potential u joins two equilibrium states 0 and 1, hence u is without dimension.

2.2.2 Fenton-Karma model

The version of the model presented here is a slightly modified version proposed in [83] that originates from the model of [31]. The Fenton-Karma model is a three variable ionic model where the nondimensionalized transmembrane potential u is coupled with a fast gating variable v_f and a slow gating variable v_s . The voltage changes in response to the ionic currents according to

$$\frac{du}{dt} + (I_{fast} + I_{slow} + I_{ung} + I_{stim}) = 0,$$

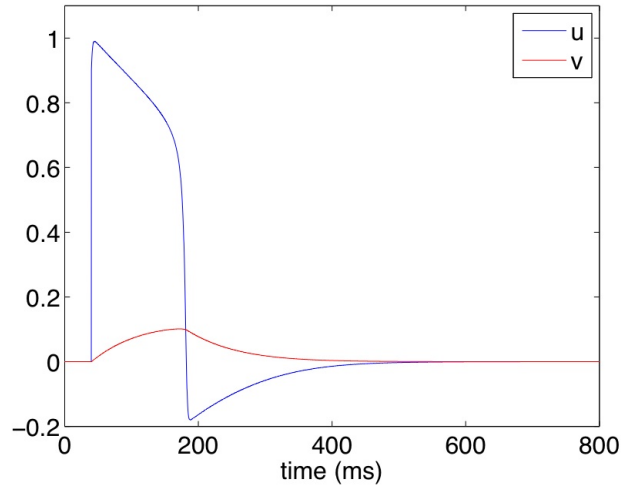


Figure 2.1: AP of the FHN model.

where the fast inward current is

$$I_{fast} = \begin{cases} -\frac{1}{\tau_{fast}} v_f (u - u_{crit})(1 - u) & \text{if } u > u_{crit}, \\ 0 & \text{otherwise.} \end{cases}$$

and τ_{fast} is a characteristic time for the current I_{fast} . The fast gating variable v_f is given by

$$\frac{dv_f}{dt} = \frac{v_{f,\infty} - v_f}{\tau_f(u)},$$

where

$$\begin{cases} v_{f,\infty} = 0 \text{ and } \tau_f(u) = \tau_{fclose} & \text{if } u < u_{fgate}, \\ v_{f,\infty} = 1 \text{ and } \tau_f(u) = \tau_{fopen} & \text{otherwise.} \end{cases}$$

The slow inward current has the following sigmoid form

$$I_{slow} = -v_s \frac{1}{\tau_{slow}} \frac{1}{2} [1 + \tanh(\kappa(u - u_{sig}))]$$

and the gate variable v_s is governed by

$$\frac{dv_s}{dt} = \frac{v_{s,\infty} - v_s}{\tau_s(u)},$$

where

$$\begin{cases} v_{s,\infty} = 1 \text{ and } \tau_f(u) = \tau_{s\text{close}} & \text{if } u > u_{sgate}, \\ v_{s,\infty} = 0 \text{ and } \tau_f(u) = \tau_{s\text{open}} & \text{otherwise.} \end{cases}$$

The ungated current I_{ung} is defined by

$$I_{ung} = \begin{cases} \frac{1}{\tau_{ung}} & \text{if } u > u_{out} \\ \frac{1}{\tau_{ung}} \frac{u}{u_{out}} & \text{otherwise.} \end{cases}$$

The stimulus current I_{stim} is an external current applied by the experimenter. Typically, I_{stim} consists of a periodic train of brief pulses (e.g. with duration of 1 ms), each of approximately twice the strength required to excite fully recovered tissue[83]. The currents I_{fast} , I_{slow} , and I_{ung} may be identified with sodium, calcium, and potassium currents, respectively. Table 2.1 lists the values of the parameters used in the 0D simulation illustrated in figure 2.2.

Table 2.1: FK parameters proposed in [83].

Parameters	Values	Parameters	Values
τ_{fast}	0.25	u_{crit}	0.13
τ_{slow}	127	u_{sig}	0.85
τ_{ung}	130	u_{out}	0.1
$\tau_{f\text{close}}$	10	$u_{f\text{gate}}$	u_{crit}
$\tau_{f\text{open}}$	18	$u_{s\text{gate}}$	u_{crit}
$\tau_{s\text{close}}$	1000	κ	10
$\tau_{s\text{open}}$	80		

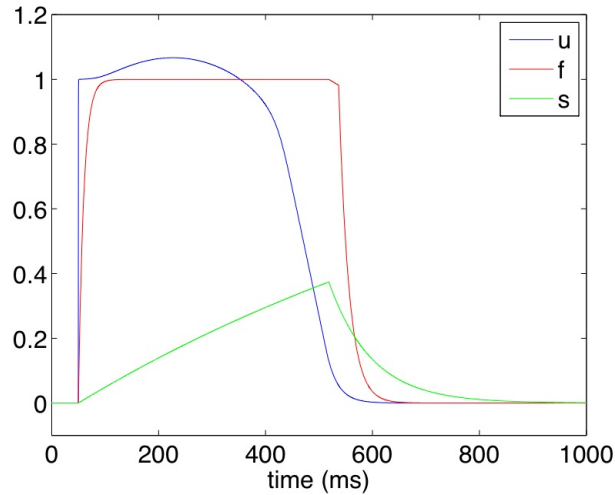


Figure 2.2: AP for the FK model.

2.2.3 Mitchell-Shaeffer model

The Mitchell-Shaeffer (MS) model was first introduced in [83]. This 2-variable phenomenological model has several qualities that makes it a candidate of choice for achieving our goal of matching several AP features (conduction speed, time scales, restitution) with the simplest possible model. First of all, because it is derived from the Fenton-Karma ionic model, it has benefits of an ionic model though it is a phenomenological model. Moreover, many authors have used the MS model for realistic clinical applications. In order to simulate a right bundle-branch block Boulakia and al. [11] used the MS model on the one hand to keep as low as possible the complexity of the model and on the other hand to model as accurately as possible the physical phenomena. As an other example, mapping models for predictions of the excited phase duration and the recovery duration (derived in [83, 56]) were proved to be efficient for cardiac model personalization using real patient data in [71, 72]. For these reasons, the MS model will be used for all subsequent analysis and numerical simulations.

The original MS model reads as

$$\frac{du}{dt} + f(u, v) = 0, \quad \text{where } f(u, v) = \frac{1}{\tau_{in}}vu^2(u - 1) + \frac{1}{\tau_{out}}u, \quad (2.2.3)$$

$$\frac{dv}{dt} = g(u, v), \quad \text{where } g(u, v) \begin{cases} \frac{1}{\tau_{open}}(1 - v) & \text{for } u < u_{gate}, \\ -\frac{1}{\tau_{close}}v & \text{for } u \geq u_{gate}, \end{cases} \quad (2.2.4)$$

with $\tau_{in} = 0.3$ ms, $\tau_{out} = 6$ ms, $\tau_{open} = 120$ ms, $\tau_{close} = 150$ ms and $u_{gate} = 0.13$, a set of parameter values proposed in [56]. The AP with this set of parameters is illustrated in figure 2.3.

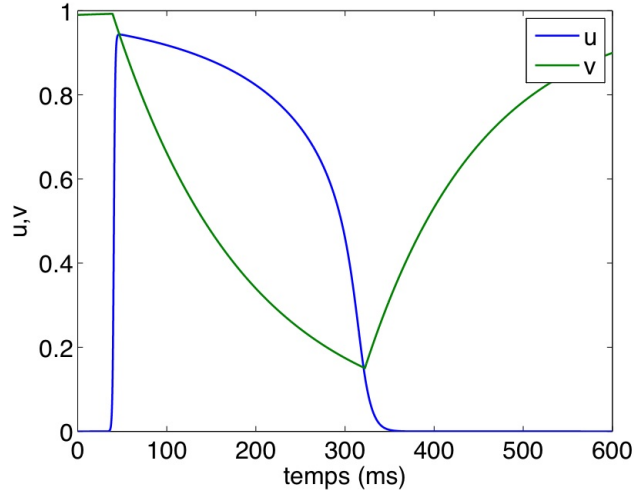


Figure 2.3: AP of the original MS model.

Note that the 0D MS model solution presented in figure 2.3 varies between the rest state at $u = 0$ and the excited state at $u = 1$. The original MS model found in the literature is then partly nondimensional, i.e. it has nondimensional variables u and v but dimensional parameters τ . Without considering any dimension or units aspect, the source term $f(u, v)$ represents the ionic transmembrane current as I_{ion} does in equation (1.1.3).

Several modified versions of the MS model are brought in the literature (see for example [44, 26, 75, 76]). The following text outlines the subtleties of the different versions of the reaction terms.

Keener presents a continuous version in [44] where the source term $g(u, v)$ is smoothed with a $\tanh()$ function:

$$g(u, v) = \frac{1}{\tau_u} [(1 - s(u, \kappa, u_{gate})) (1 - v) - s(u, \kappa, u_{gate})v] \quad (2.2.5)$$

with

$$\tau_u = \tau_{open} + (\tau_{close} - \tau_{open})s(u, \kappa, u_{gate})$$

and

$$s(u, \kappa, u_{gate}) = \frac{1}{2} (1 + \tanh(\kappa(u - u_{gate}))).$$

An other variant of the MS model is presented in [26]. A noticeable difference between the original MS and this modified version is the introduction of the parameter a in $f(u, v)$

$$f(u, v) = \frac{1}{\tau_{in}} v(u + a)^2(u - 1) + \frac{1}{\tau_{out}} u, \quad (2.2.6)$$

where $a = 0.02$ is suggested. It can be used to control the excitability and mimic a pacemaker activity. Sorine et al. [26] also use a regularization of the step in $g(u, v)$ and their whole model is continuously differentiable. The property of continuous differentiability is preferable when an algorithm like Newton's method is required to linearize the equation before solving them. That being said, both smoothed version in [44] and [26] have a new parameter κ that has to be fixed. This parameter tunes the width of the smoothed jump in $g(u, v)$. We briefly discuss how its value could be determined.

The smooth function $s(u, \kappa, u_{gate})$ replaces a step function, where an increasing κ sharpens the smoothed jump. This step function also indicates a change in time scales from τ_{open} to τ_{close} and vice-versa that reflects a state change in the wave, respectively

from the recovery phase to the excited phase and vice-versa. In the original MS model the parameters τ_{in} , τ_{out} , τ_{open} and τ_{close} are meaningful time parameters reflecting time scales in the solution. The state change has to be similar to the one in the original MS model. If not, the correspondence between these time parameters and solution time scales will be lost. First of all, the state change in the MS model is instantaneous. As a consequence, $s(u, \kappa, u_{gate})$ has to be sharp enough so that the excited phase duration and the recovery duration are not affected.

Figure 2.4 illustrates the possible overlaps. The excited phase occurs chronologically for values of u between 1 (end of the depolarization) and 0.5 (beginning of the repolarization). If the smoothed jump overlaps this interval, it means that the transition between the times scales τ_{open} to τ_{close} is not completed. The excited phase duration T_{AP} could be modified considerably, only because this period depends mainly on τ_{close} [83]. Similarly, there could be an overlap during the recovery phase which occurs in the neighborhood of $u = 0$. If $s(0, \kappa, u_{gate})$ is not sufficiently close to zero, then the recovery time T_{rec} will be different than for the original model. This is because this period depends mainly on τ_{open} . Remark that in [26], simulations are performed with $\kappa = 1000$.

Schaeffer and al. [75, 76] brought an extension to the original MS model. The new model has three variables, where the third variable is concentration-like and acts as a memory variable. It also helps the charge balance through time. This model improves predictions where rate dependence and accommodation are involved. Besides this, a relevant change is brought to the source term $g(u, v)$ upon what the solution features the overshoot after the depolarization as illustrated in figure 1.2(a).

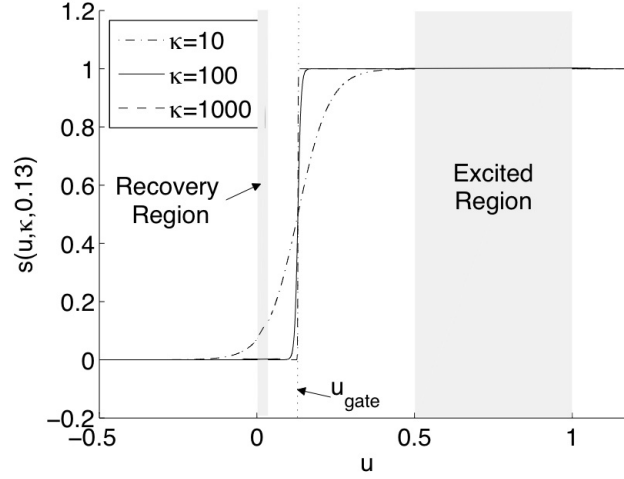


Figure 2.4: The smoothed step function $s(u, \kappa, u_{gate})$ for different values of κ and $u_{gate} = 0.13$.

The closing rate τ_{close} becomes voltage-dependent and reads as

$$\frac{1}{\tau_{close}(u)} = \begin{cases} \frac{1}{\tau_{fclose}} - \left(\frac{1}{\tau_{fclose}} - \frac{1}{\tau_{sclose}} \right) \frac{1-u}{1-u_{sldn}} & \text{if } u > u_{sldn}, \\ \frac{1}{\tau_{sclose}} & \text{otherwise,} \end{cases} \quad (2.2.7)$$

where τ_{fclose} and τ_{sclose} are time scale parameters referring, respectively, to a fast and slow closing rate. Right after the depolarization, the closing rate slows down progressively until $u = u_{sldn}$ where the rest of the phase II happens similarly as in the original MS model. In [76], the following set of parameters $\{\tau_{in} = 0.28, \tau_{out} = 3.2, u_{gate} = 0.13, u_{sldn} = 0.89, \tau_{open} = 500, \tau_{sclose} = 22, \tau_{fclose} = 320\}$ is proposed.

In the text, what is called the modified MS model has the reaction terms $f(u, v)$ of equation (2.2.6) and $g(u, v)$ of equation (2.2.4) with the associated time scale $\tau_{close}(u)$ of equation (2.2.7). Suppose that the overshoot is considered useless in some simulations for any reason. One can set $\tau_{close}(u) = \tau_{sclose}$ and then the system degenerates to the original MS model if $a = 0$.

2.2.4 Modeling realistic APs

Now that ionic models are available, we want to reproduce AP measured experimentally using these models. The very first step is gathering experimental data (measures of AP, anatomical data, etc.) from many sources. Collecting information can become a huge task just to characterize a healthy human heart not to mention when heart abnormalities are studied [81, 43]. Moreover, depending in which tissue the AP is propagated, the cells are different and so are the features of the AP (see table 2.2). The AP is a phenomenon that exists in every single excitable cell. It can be measured and through time, it has the shape of a pulse, as illustrated in figure 1.2a. We attempt to reproduce the most exactly the AP shape by adjusting the parameters of the ionic models and the bidomain model.

One way of setting this parameter identification problem (see section 1.3.1) is by defining quantities that describe the AP wave measured experimentally. These quantities can also describe the numerical AP obtained with the ionic model. In this case, these quantities depend on the model parameters. Throughout the text, the term *solution feature* is any quantity characterizing the solution. For instance the duration of every phase and the speed of the propagated potential wavefront are solution features that are going to be studied.

2.3 Nondimensionalization

In the sequel, we start with all the dimensional parameters to keep in sight their influence and we perform a dimensional analysis of the bidomain model coupled with any nondimensional ionic model. One of the usual ways found in the literature of writing the source terms describing the transmembrane current of a specific ion is

$$I_{ion} = \frac{hp(u, v)}{\tau}, \quad (2.3.1)$$

Table 2.2: Speeds and recovery duration are taken in [47] where the heart cycle is of 700 ms. Similar values for speed can also be found in [1].

Tissue	Speed cm/s	Phase I ms	Phase II ms	Phase IV ms
Ventricle	35-55	1-3	150-200	255-275
Atria	60			250-270
SA node	5			430
AV node	5			300
Bundle of His	170			210
Bundle Branches	200			270-310
Purkinje fibers	180			320

where h is a gating variable, $p(u, v)$ is a function of the transmembrane potential and τ is the time scale of this charge flow. As $p(u, v)$ can be any function (combination of exponentials, polynomials, etc.), h , u and v are often taken dimensionless and τ dimensional (in seconds) in order to preserve the balance of the units in the equations. As a consequence of using nondimensional potentials, the source terms proposed in the literature have most of the time the units s^{-1} to match the units of the terms $\partial v/\partial t$ or $\partial u/\partial t$.

Let us perform the usual steps of a nondimensionalization and start from the unit-balancing dimensional bidomain model for an isolated heart (1.2.1)-(1.2.5). We define nondimensional variables and nondimensional parameters, denoted with a \sim . The dimensional transmembrane potential u is rescaled using $u = V_m \tilde{u} + V_{rest}$ with $V_m = V_{max} - V_{rest}$, where V_m , V_{max} and V_{rest} are, respectively, the characteristic action potential amplitude, the maximal potential attained once the cell is depolarized and the resting potential. The extra-cellular potential is also rescaled with $u_e = V_m \tilde{u}_e + V_{rest}$. For the independent variables, the time is rescaled with $t = \tilde{t}T$ and the space with $x = \tilde{x}L$. The eigenvalues of the conductivity tensor are rescaled with $\sigma_\alpha = \sigma \tilde{\sigma}_\alpha$, with indices $\alpha = (i, l), (i, t), (e, l), (e, t)$, where i and e refer to the intracellular and the extracellular medium, respectively, the indices t and l refer to the

transverse and the longitudinal eigendirections, both related to the fiber arrangement of the myocardium. Finally, v is already taken nondimensional, in order to use directly the source terms given in the literature.

The following equations form the nondimensional version of the bidomain model coupled with any nondimensional ionic model with source terms of the form (2.3.1), written with the explicit dependence on the time parameters τ .

$$\frac{\partial v}{\partial \tilde{t}} = \tilde{g}(\tilde{u}, v) \quad \text{in } H, \quad (2.3.2)$$

$$\frac{\partial \tilde{u}}{\partial \tilde{t}} + \tilde{I}_{ion}(\tilde{u}, v) = N \tilde{\nabla} \cdot \left(\tilde{\sigma}_i \tilde{\nabla} (\tilde{u} + \tilde{u}_e) \right) \quad \text{in } H, \quad (2.3.3)$$

$$\tilde{\nabla} \cdot \left(\tilde{\sigma}_i \tilde{\nabla} \tilde{u} \right) + \tilde{\nabla} \cdot \left((\tilde{\sigma}_i + \tilde{\sigma}_e) \tilde{\nabla} \tilde{u}_e \right) = 0 \quad \text{in } H, \quad (2.3.4)$$

$$n_H \cdot \left(\tilde{\sigma}_i \tilde{\nabla} \tilde{u} + (\tilde{\sigma}_i + \tilde{\sigma}_e) \tilde{\nabla} \tilde{u}_e \right) = n_H \cdot \left(\tilde{\sigma}_T \tilde{\nabla} \tilde{u}_T \right) \quad \text{on } \partial H, \quad (2.3.5)$$

$$n_H \cdot \left(\tilde{\sigma}_i \tilde{\nabla} \tilde{u}_i \right) = 0 \quad \text{on } \partial H, \quad (2.3.6)$$

$$\tilde{\nabla} \cdot \left(\tilde{\sigma}_T \tilde{\nabla} \tilde{u}_T \right) = 0 \quad \text{in } T, \quad (2.3.7)$$

$$n_T \cdot \left(\tilde{\sigma}_T \tilde{\nabla} \tilde{u}_T \right) = 0 \quad \text{on } \partial T. \quad (2.3.8)$$

with $N = T\sigma/C_m\chi L^2$. Note that $\tilde{I}_{ion}(u, v) = \frac{T}{C_m V} I_{ion}(u, v)$ and $\tilde{g}(u, v) = \frac{T}{V} g(u, v)$. In general, the explicit versions of I_{ion} and g of equations (1.2.6)-(1.2.12) are useless because most of the phenomenological models are already written for nondimensional potentials. For the MS model or for any model with source terms of the form (2.3.1), note that $\frac{1}{T} \tilde{I}_{ion}(\tilde{u}, v) = f(\tilde{u}, v)$ with f of equation (2.2.3), and $\frac{1}{T} \tilde{g}(\tilde{u}, v) = g(\tilde{u}, v)$ with g of equation (2.2.4).

The dimensionless number N can also be found with the Buckingham Π -theorem (see for example [57]). We have 5 physical variables T , C_m , V_m , σ/χ and L expressible in terms of 4 independent fundamental units seconds s , Amperes A , Volts V and meters m . The theorem says that the physically meaningful equation $\zeta(t, C_m, V_m, \sigma/\chi, L) = 0$ is equivalent to an equation involving a single ($\#$ variables - $\#$ units = 1) dimensionless variable N constructed from the original variables. We equivalently have

$\zeta(N) = 0$ with $N = T^{n_1} C_m^{n_2} V_m^{n_3} (\sigma/\chi)^{n_4} L^{n_5}$. Written in terms of fundamental units, the equation becomes

$$1 = (s)^{n_1} (As/(Vm^2))^{n_2} (V)^{n_3} (A/V)^{n_4} (m)^{n_5}.$$

The remaining problem consists in solving a homogeneous linear system of dimension 5 and as all the units are useful, the rank of the matrix involved is 4. The dimension of the kernel of this matrix is the number of nondimensional numbers prescribed by the theorem (a single number here). Choosing one basis vector in the kernel, one gets the dimensionless number N given in the text.

One is then left with a single nondimensional number N , and finding a value for it. The parameters C_m , V_m , χ and σ are fixed, but the time scale T and the space scale L are still free. Fixing these is not necessarily obvious, especially because each phase (described in section 2.2.4) has its own time and space scales. Any choice made for T and L in a dimensional scaling specific to a phase is justified by the fact that it is preferable to have a maximal value for $D_{\tilde{t}}\tilde{u}$ and $D_{\tilde{x}}\tilde{u}$ of about 1 during this phase. This way, it is easier to compare the contribution of every term in the differential equations during this phase.

In the following, we propose values for the time and the space scales based on what is observed for a healthy human heart. The parameters defined for three different dimensional scalings and the parameters of the model are given in Table 2.3. A typical AP upstroke (depolarization) of a ventricle is used to scale the time and space for the first proposed dimensional scaling Adim1. The excited phase duration and width are used to scale for the second dimensional scaling Adim2. The last dimensional scaling Adim3 is not justified by any physiological manifestation but is practical in terms of units (time measured in *ms* and space in *mm*).

Table 2.3: Parameters of the bidomain model for a human heart. Three different dimensional scalings are proposed. Adim1: based on the transmembrane potential upstroke. Adim2: based on the action potential duration and width. Adim3: based on convenient units. The values are taken from [81], [21] and [68].

Description	Param.	Values Adim1	Values Adim2	Values Adim3	Units
Threshold potential	V_{th}		-0.065		V
Maximum potential	V_{max}		0.040		V
Resting potential	V_{rest}		-0.085		V
Characteristic potential	V_m		0.125		V
Cell surface to volume ratio	χ		$2 \cdot 10^5$		m^{-1}
Transmembrane specific capacitance	C_m		$1 \cdot 10^{-2}$		F/m^2
Characteristic conductivity	σ		$1 \cdot 10^{-1}$		S/m
Intracellular conductivity	$\tilde{\sigma}_{i,l}$		1.741		-
	$\tilde{\sigma}_{i,n}$		0.1934		-
	$\tilde{\sigma}_{e,l}$		3.906		-
Extracellular conductivity	$\tilde{\sigma}_{e,l}$		3.906		-
	$\tilde{\sigma}_{e,n}$		1.970		-
Characteristic time	T	$1 \cdot 10^{-3}$	0.2	$1 \cdot 10^{-3}$	s
Characteristic length	L	$5 \cdot 10^{-4}$	0.1	$1 \cdot 10^{-3}$	m
Nondimensional number	N	0.2	$1 \cdot 10^{-3}$	$5 \cdot 10^{-2}$	-

2.3.1 A nondimensionalization specific to the asymptotic analysis

The estimation of the magnitude of every term is crucial in the asymptotic analysis of section 2.4. To achieve this comparison for the MS model, the time scales T_f and T_g , associated respectively with sources terms f and g , are introduced. The resulting time parameters are not only dimensionless, but of order one as they are rescaled with $\tau_{in,out} = \tilde{\tau}_{in,out}T_f$ and $\tau_{open,close} = \tilde{\tau}_{in,out}T_g$. Note that this method is general enough that it is applicable for any ionic model constructed with source terms of the form (2.3.1). From the equations (2.2.3)-(2.2.4), T_f (resp. T_g) depends only on τ_{in} and τ_{out} (resp. τ_{open} and τ_{close}). From the values proposed for the parameters τ 's, T_f is necessarily a short time scale and T_g is a long time scale. The following nondimensionalization of the conduction model with MS, using these two new time scales, is brought in order to facilitate the asymptotic analysis.

$$\frac{\partial v}{\partial \tilde{t}} = \frac{T}{T_g} \tilde{g}(\tilde{u}, v) \quad \text{in } H \quad (2.3.9)$$

$$\frac{\partial \tilde{u}}{\partial \tilde{t}} + \frac{T}{T_f} \tilde{f}(\tilde{u}, v) = N \tilde{\nabla} \cdot \left(\tilde{\sigma}_i \tilde{\nabla} (\tilde{u} + \tilde{u}_e) \right) \quad \text{in } H \quad (2.3.10)$$

Remark that when numerical simulations are performed with nondimensional equations, it is neither useful nor practical to find values for the time scales T_f and T_g . Absorbing T/T_f (resp. T/T_g) in \tilde{f} (resp. in \tilde{g}) is a better choice in this circumstance, where the only relevant non dimensional number is N and the only parameters that remain to be fixed are T and L . This is why there is a factor T/T_f (resp. T/T_g) between the \tilde{f} (resp. in \tilde{g}) of equations (2.3.9)-(2.3.10) and equations (2.3.2)-(2.3.3).

2.4 Asymptotic analysis

This section is devoted to the analysis of the solution's features via an asymptotic analysis. The choice of the phenomenological models to describe the ionic activity becomes obvious here, as their 0D (resp. the 1D) solutions can be readily analyzed in the (u, v) phase space (resp. the (u_x, u, v) phase space). This is done for instance in [43] and [16] for the FHN equations using the singular perturbation theory. The latter reference uses the smallness of a parameter ϵ , which is related to ratios of time and space scales, but which has nothing to do with physical parameters (conductivity σ , cell surface to volume ratio χ , membrane specific capacitance C_m). They even prove the convergence in terms of the parameter ϵ of the numerical solutions with diffusion to the asymptotic solution.

Our approach is different because the equations are all set with their physiological parameters (see section 2.3). The smallness of some terms compared to others allows to simplify the equations and get the asymptotic 1D model and solutions. There is no convergence result because varying the parameters is not an option. The problem is addressed that way in the hope of finding as many relations as possible between the parameters of the equations and the features of the solution.

This is also why the MS model is chosen. There exists already many results in the literature allowing to characterize the solution of the MS model in terms of the model parameters. In [83], Mitchell and Schaeffer first characterized the 0D solution by giving mappings predicting for instance the next APD according to the last APD, diastolic interval and pacing interval. Schaeffer and al. [75, 76] refined the MS model and the associated prediction mappings. Starting from these valuable results, the analysis is pushed further and leads to the achievement of this chapter: being able to control locally a propagated AP by controlling the model parameters (see section 2.5).

2.4.1 Definitions

To allow a clear description of the AP, we define the following time scales, quantifying each specific phases. During the depolarization (phase I), the AP can be characterized with its upstroke duration T_{up} . T_{AP} is defined to measure the duration of the excitation phase (phase II) and it is commonly called the AP duration (APD) in the literature. Though it seems to be of less importance in the literature, the phase III has to be somehow measured so the downstroke duration T_{down} is defined to characterize the repolarization. Finally, the recovery duration T_{rec} characterizes the period during which the cell remains repolarized but is not responsive to any further electrical stimuli (phase IV).

Every temporal manifestation occurring in the AP is propagated in the tissue. The propagation of the AP in a tissue due to the conductive properties of the media adds a spatial dimension to the phenomenon. Hence the AP has to be quantified in terms of space scales considering the propagation at a given speed c . For the overall description of the propagated AP, we define also the upstroke length L_{up} , the excited phase length L_{AP} , the downstroke length L_{down} and the recovery length L_{rec} . These spatial scales are going to be used in the dimensional analysis in order to compare the magnitude of phenomena, as well as in the asymptotic analysis in order to allow a spatial description of the propagated AP.

Remark 3 *The depolarization can be characterized also with the maximum rate of depolarization of the cells dV/dt_{max} . This way of measuring the depolarization is not going to be used.*

The time of depolarization (resp. repolarization), which is the time taken for the depolarization (resp. repolarization) front to sweep the heart, is commonly used to describe the dynamic associated with the propagation. These values can be recovered with the speed of propagation and the size of the heart. ■

2.4.2 Analysis of the phase space

We start analyzing the 0D system in order to understand the behavior of an isolated cardiac cell. For the MS model, as for any 2 variable models, the work relies on the analysis of a 2D phase space. The nullclines and the equilibrium points are defined so that the four phases appear by themselves.

First of all, when there is no propagation involved, the nondimensional equations (2.3.2)-(2.3.8) reduce to the simple system

$$\frac{\partial \tilde{u}}{\partial \tilde{t}} + \frac{T}{T_f} \tilde{f}(\tilde{u}, v) = 0, \quad (2.4.1)$$

$$\frac{\partial v}{\partial \tilde{t}} = \frac{T}{T_g} \tilde{g}(\tilde{u}, v). \quad (2.4.2)$$

The modified MS model retained is endowed with the following nondimensional source terms:

$$\tilde{f}(\tilde{u}, v) = \frac{1}{\tilde{\tau}_{in}} v (\tilde{u} + a)^2 (\tilde{u} - 1) + \frac{1}{\tilde{\tau}_{out}} \tilde{u},$$

$$\tilde{g}(\tilde{u}, v) = \begin{cases} \frac{1}{\tilde{\tau}_{open}} (1 - v) & \text{for } \tilde{u} < \tilde{u}_{gate}, \\ -\frac{1}{\tilde{\tau}_{close}} v & \text{for } \tilde{u} \geq \tilde{u}_{gate} \end{cases}$$

where the time scale $\tilde{\tau}$ are nondimensionalized with T_f and T_g , and τ_{close} equals $\tau_{close}(\tilde{u})$ of equation (2.2.7). In the following the \sim are removed for the sake of convenience. Remark that the source terms given in [83, 75, 76], referring to $f(u, v)$ of equation (2.2.6) and $g(u, v)$ of equation (2.2.4), are partially nondimensionalized. On the one hand, the time scales are dimensional (e.g. $\tau_{in} = 0.3$ ms, $\tau_{out} = 6$ ms, $\tau_{open} = 130$ ms, etc.). On the other hand, u and v are nondimensional (e.g. $u_{gate} = 0.13$) because they both vary within the interval $[0, 1]$ given standard initial conditions $(u(0), v(0)) \in (0, 1) \times (0, 1)$.

In the MS model, the transmembrane potential u is considered as the fast variable and the recovery variable v is considered as the slow variable. The solutions of the original MS model and modified MS models are illustrated in figure 2.5. Their respective phase spaces are illustrated with the four phases in figures 2.6. The phase spaces are going to be thoroughly described for a better understanding of the asymptotic analysis.

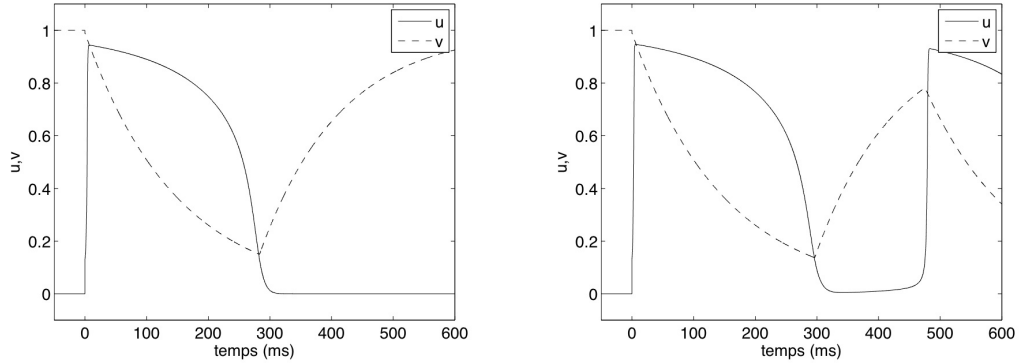
Remark 4 *The analysis of the modified version of the MS model featuring the overshoot is very similar to that of the original MS model when $u_{gate} < u_{sldn}$; the nullclines are the same though the vector field is different in the half-plane $u > u_{sldn}$.* ■

For the original MS model (see figure 2.6(a)), there is a local minimum on the nullcline $f(u, v) = 0$ at $(u_*, v_*) = (1/2, 4\tau_{in}/\tau_{out})$. Note that the point at which this minimum occurs is not on the solution curve $(u(v), v)$ with the initial condition $(u(0), v(0)) = (0.13, 0.99)$. This local minimum separates the nullcline in 2 branches: the left-hand side branch is denoted $u = h_2(v)$ and the right-hand side branch $u = h_3(v)$ with

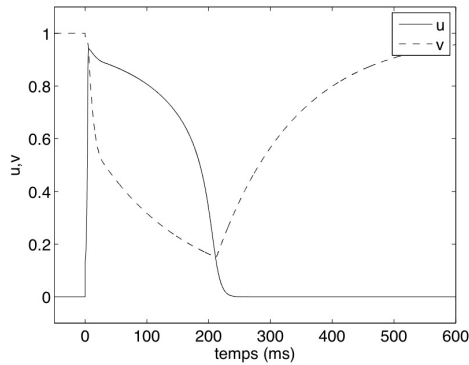
$$u = h_{2,3}(v) = \frac{1}{2} \mp \frac{1}{2} \sqrt{1 - 4 \frac{\tau_{in}}{\tau_{out} v}}. \quad (2.4.3)$$

There are 3 equilibrium points, $(0, 1)$, $(h_2(1), 1)$ and one on the line $u = u_{gate}$, precisely the point $(u_{gate}, \tau_{in}/[\tau_{out}u_{gate}(1 - u_{gate})])$. For the set of parameters given above, the equilibria $(0, 1)$ and $(h_2(1), 1)$ are saddle points. Their stability can be studied with a standard analysis of the linearized version of system (2.4.1)-(2.4.2). The third equilibrium $(u_{gate}, h_2(v))$ is an unstable focus, which can be seen by inspection of the vector

field in the phase plane. During phase I the solution starts at the initial condition point A to reach quickly the point B while the recovery variable v barely varies. Phase II is characterized by a solution following very closely the branch $u = h_3(v)$ of the

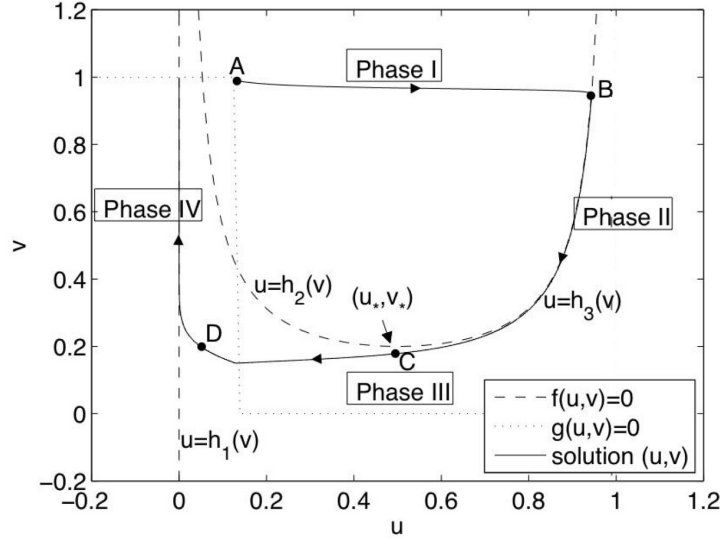


(a) Original MS model ($a = 0$ and $\tau_{close} = \tau_{sclose}$).
 (b) Modified MS model illustrating an auto-excitability behavior ($a = 0.02$ and $\tau_{close} = \tau_{sclose}$).

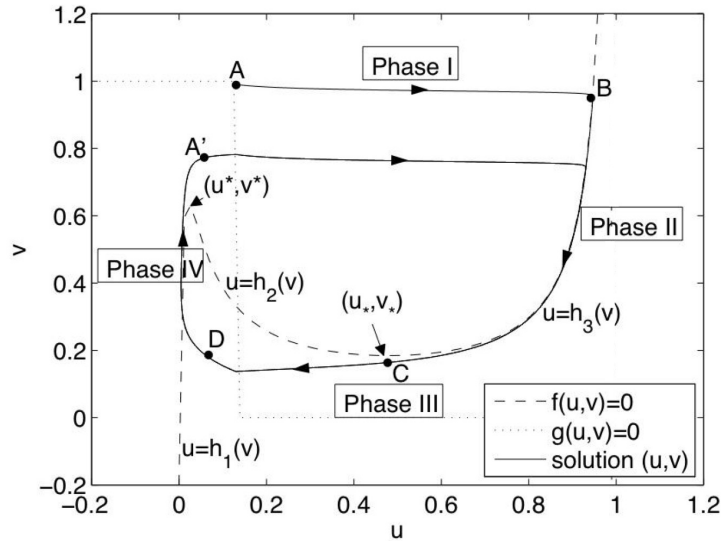


(c) Modified MS model illustrating the overshoot after the depolarization (with non dimensional parameters $a = 0$, $u_{sldn} = 0.89$, $\tau_{sclose} = 150$, $\tau_{fclose} = 10$ and $\tau_{close}(u)$ is given by equation (2.2.7)).

Figure 2.5: Numerical simulation of the electrical activity of a single cell using various versions of the MS model. With the characteristic time $T = 1$ ms, all simulations use the non dimensional parameters $\tau_{in} = 0.3$, $\tau_{out} = 6$, $\tau_{open} = 130$ and $u_{gate} = 0.13$.



(a) The phase plane for 0D original MS model with a numerical solution.



(b) The phase plane for 0D modified MS model with a numerical solution for $a = 0.02$.

Figure 2.6: The phase space for both the MS and modified MS models. Numerical simulations are performed with $T = 0.001$ s, $\tau_{in} = 0.3$ (ms), $\tau_{out} = 6$ (ms), $\tau_{open} = 130$ (ms), $\tau_{close} = 150$ (ms) and $u_{gate} = 0.13$. See text for definitions of curves, points, etc identified.

nullcline $f(u, v) = 0$, i.e. from point B to C . During phase III, the solution leaves the nullcline $f(u, v) = 0$ at the point C , u goes fast to zero while v varies only slightly. In phase IV the solution goes along the nullcline $u = 0$ from the point D while v increases slowly. The solution reaches asymptotically the equilibrium point $(0, 1)$.

For the modified MS model (see figure 2.6(b)), the nullcline $f(u, v) = 0$ has a local minimum at (u_*, v_*) with $u_* = 1/4 (1 - \sqrt{1 - 8a})$ and a local maximum at (u^*, v^*) with $u^* = 1/4 (1 + \sqrt{1 - 8a})$. These local extrema separate the nullcline in 3 branches denoted by $u = h_1(v)$, $u = h_2(v)$ and $u = h_3(v)$ with $h_1(v) \leq h_2(v) \leq h_3(v)$. The solution starts at the initial condition point A and follows a trajectory close to that of the original MS model until phase IV, where the solution goes along $u = h_1(v) \equiv 0$ from the point D while v increases slowly. The solution eventually leaves the nullcline near the point (u^*, v^*) . Finally, the solution goes again by itself in the phase I (from point A') after a complete heart cycle. This model is clearly suitable for auto-excitable cells because of the repeating cycles. There is no assumption here about the periodicity of the solution.

Following the same idea as in [43] for the FHN model, a similar asymptotic analysis could be done for the MS model by regarding the 0D solution separately in its phases I, II, III and IV. In both models phases I and III are characterized by a time scale that is so short for the slow variable v that it remains almost constant during these periods. The solution moves along the nullclines during phases II and IV. Each part of the solution can be approximated with a simplified trajectory (moving along a nullcline or at a constant v). We define the 0D asymptotic solution by connecting these simplified trajectories together.

We are rather interested in an asymptotic analysis of the 1D solution, so let us now explore the phenomenological MS model coupled with a 1D model of propagation. Using the nondimensional 1D bidomain model (\sim are removed for simplicity) with a

constant conductivity, the problem consists in finding (u, u_e, v) in $[0, x_{max}]$ such that

$$\begin{aligned} \frac{\partial u}{\partial t} + \frac{T}{T_f} f(u, v) &= N_i \frac{\partial^2(u + u_e)}{\partial x^2}, \\ \sigma_i \frac{\partial^2 u}{\partial x^2} + (\sigma_i + \sigma_e) \frac{\partial^2 u_e}{\partial x^2} &= 0, \\ \frac{\partial v}{\partial t} &= \frac{T}{T_g} g(u, v, t), \end{aligned}$$

with $N_i = T\sigma_i/C_m\chi L^2$ the nondimensional number associated to the intracellular medium of conductivity σ_i . On the boundaries $x = 0$ and $x = x_{max}$, homogeneous Neumann boundary conditions are applied for both u and u_e . A zero mean condition can be applied on the potential u_e so that the degeneracy is removed.

The following monodomain model is equivalent to the bidomain model in 1D: finding (u, v) in $[0, x_{max}]$ such that

$$\frac{\partial u}{\partial t} + \frac{T}{T_f} f(u, v) = N_{harm} \frac{\partial^2 u}{\partial x^2}, \quad (2.4.4)$$

$$\frac{\partial v}{\partial t} = \frac{T}{T_g} g(u, v, t), \quad (2.4.5)$$

with $N_{harm} = T\sigma_{harm}/C_m\chi L^2$ and $\sigma_{harm} = (\sigma_i^{-1} + \sigma_e^{-1})^{-1}$ is the harmonic average of the intra and extracellular conductivities in the x -direction. As the analysis is done in 1D, the monodomain model is used because of its low computational cost and because it gives exactly the same solution as the bidomain model.

The next step is to verify that under physiologically plausible conditions, the MS model with spatial propagation is suitable for an asymptotic analysis. A 1D solution is computed beforehand with the parameters of the third column of table 2.3 together with the dimensioning parameters $L = 0.001$ m, $T = 0.001$ s and $N_{harm} = 0.05$. The domain is the interval $[0, 600]$ and the simulation is performed over the time interval

$[0, 1000]$. The initial condition is given by

$$u(0) = \begin{cases} 0 & \text{for } x \in [0, 570) \\ 0.8 & \text{otherwise} \end{cases}$$

and $v(0) = 0.99$.

At one coordinate point ($x = 300$), the solution is plotted in the phase space of the 0D model, with its corresponding nullclines (see figure 2.7). There are obvious similarities between the solution of the system with diffusion in 1D and the solution of the equations for an isolated cell in 0D (see figure 2.7).

Again, it follows that the solution can be separated in four parts respect to the four phases. The solution parts are matched together to give the so-called asymptotic 1D solution.

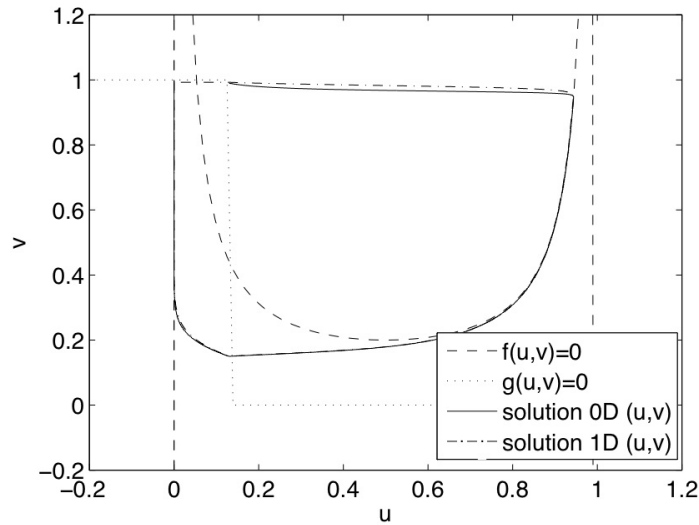


Figure 2.7: 0D and 1D solutions in the phase space of the phase space of the 0D system.

The time and space scales of the asymptotical solution are defined (as it is done in section 2.4.1, e.g. T_{up} and L_{up} were defined) and they are denoted with a hat ($\hat{\cdot}$).

For instance, the asymptotic upstroke duration is denoted by \widehat{T}_{up} , the asymptotic upstroke width by \widehat{L}_{up} , etc.

2.4.3 Asymptotic characterization of the depolarization front

In order to find the asymptotic regime of the depolarization, the magnitude of each term in the equations (2.4.4)-(2.4.5) is estimated in phase I. The leading terms will form the equations to solve for the asymptotic solution in phase I. Known values for the depolarization duration and width can be used (see table 2.3) for this purpose. For example, the ventricle characteristic depolarization duration is about 1 ms and the speed of the wave is about 0.5 m/s. Using $T = 1$ ms and $L = 0.5$ mm, the terms in the equations are of order one and they are weighted by the nondimensional numbers multiplying them. Because $T/T_f \sim 1$, $N_{harm} = N_{up} = 0.2$ and $T/T_g \sim 7 \times 10^{-3}$, the term $T/T_g g(u, v)$ is considered as negligible compared to the other terms. The system to solve for the asymptotic solution in phase I becomes: find (u, v) in $[0, x_{max}] \times [0, t_{max}]$ such that

$$\frac{\partial u}{\partial t} + \frac{T}{T_f} f(u, v_-) = N_{up} \frac{\partial^2 u}{\partial x^2} \quad \text{with } u(t = 0) = u_0, \quad (2.4.6)$$

$$\frac{\partial v}{\partial t} = 0 \quad \Leftrightarrow v = v(t = 0) = v_-, \quad (2.4.7)$$

with the domain and initial conditions given in section 2.4.2. The fact that the transmembrane potential u has a depolarization occurring at a nearly constant v is then justifiable with simple arguments of magnitude analysis. The value of v at which phase I occurs will be called v_- , where v_- can be interpreted as the value of v facing the arrival of the wave. As the wave can be paced at almost any value of v , v_- is not specified unless an isolated wave is analyzed. In this case, $v_- = 1$, i.e. the value at the equilibrium.

Now that the system to solve for the asymptotic solution in phase I is known, we now change voluntarily the parameters T and L so that the asymptotic upstroke has a duration of 1 and a width of 1 in the nondimensional frame. The appropriate choice for the nondimensionalization is then to use $T = \widehat{T}_{up}$ and $L = \widehat{L}_{up}$. Doing this allows to do the same analysis whatever the choice of the parameters of the models (ionic and propagation). The system then reduces to

$$\frac{\partial u}{\partial t} + \frac{\widehat{T}_{up}}{T_f} f(u, v_-) = N_{up} \frac{\partial^2 u}{\partial x^2}, \quad (2.4.8)$$

where the solution u goes from $u(0)$ to $h_3(v_-)$.

It is known that under appropriate assumptions, reaction-diffusion equations such as equation (2.4.8) have travelling wave solutions, i.e. solutions of the form $u(x, t) = \nu(x + ct)$, propagating at the speed c in the direction of decreasing x if $c > 0$. As a simple and well-known example, for $f(u, v_-) = -\alpha u$, the existence of a planar travelling wave solution can be easily proved in a constructive way (see [16]). This wave is asymptotically stable, with wave speeds approaching the constant value c as $t \rightarrow \infty$ for any initial solution that leads to the asymptotic state. However, for more complicated ionic models, the proof of existence of travelling waves requires care as it is highly dependent on the form of the ionic terms. For instance, the 1D travelling solution of the FHN model is thoroughly analyzed in [40, 25] including the existence of different modes. For the MS model, we are not aware of any published proof of existence for travelling waves but we present a detailed argument for the existence of such wave in section 2.6.

We summarize the argument and clarify notations here for the sequel of the text. The necessary conditions for the existence of travelling wave can be studied by analyzing the (ν, ν') -phase plane. The speed c must be properly set, say to c^* , so that a travelling wave exists, which amounts to the existence of a heteroclinic connection of the equilibrium points $(\nu, \nu') = (0, 0)$ and $(\nu, \nu') = (h_3(v_-), 0)$. It is

easy to show that non-monotonous orbits starting at $\nu = 0$ and reaching $\nu = h_3(v_-)$ are impossible. By monotonicity, the heteroclinic orbit is attained in a unique way referring to a specific speed c^* , where the uniqueness holds for any fixed value of v_- . If a bounded positive speed for the monotonous orbit can be found, the necessary conditions for the existence of such heteroclinic orbit are going to be all satisfied (see section 2.6 for more details). The next step concerns the computation of that unique and bounded speed.

Speed of the asymptotic traveling wave solution

Using similar arguments as in [43] and [16], the propagation speed will be found by analyzing the formation of a traveling wave in 1D. The traveling wave is formed in the phase I, so the speed is that of the depolarization front. Remark that $c = \widehat{L}_{up}/\widehat{T}_{up}$ and nondimensional speed is equal to 1 in the nondimensional frame.

The asymptotic traveling wave solution $u(x, t) = \nu(x + ct) = \nu(s)$ solves the equation (2.4.8) so

$$c\nu' + \frac{T}{T_f}f(\nu, v_-) = N\nu'' \tag{2.4.9}$$

The matching condition to find the speed, referring to $c = c^*$, where the heteroclinic orbit connects the points $\nu = 0$ and $\nu = h_3(v_-)$ as $s \rightarrow \mp\infty$, respectively, reads as the following integral

$$c^* \int_{-\infty}^{+\infty} \nu'(s)^2 ds = -\frac{T}{T_f} \int_0^{h_3(v_-)} f(\nu, v_-) d\nu.$$

The dimensional asymptotic speed \widehat{c} is then

$$\widehat{c} = \frac{L}{T}c^* = -L \frac{F_{AB}(v_-)}{\int_{-\infty}^{+\infty} \nu'(s)^2 ds} \tag{2.4.10}$$

with

$$\begin{aligned}
 F_{AB}(v_-) &\equiv \frac{1}{T_f} \int_0^{h_3(v_-)} f(\nu, v_-) d\nu \\
 &= \left[\frac{v_-}{\tau_{in}} \left(\frac{h_3(v_-)^4}{4} - \frac{h_3(v_-)^3}{3} \right) + \frac{1}{2} \frac{h_3(v_-)^2}{\tau_{out}} \right].
 \end{aligned}$$

For $v_- \in (4\tau_{in}/\tau_{out}, 1]$, $F_{AB}(v_-)$ (in s^{-1} ; recall that the τ 's are nondimensionalized with T_f) is well defined and negative as $f(\nu, v_-) < 0$ during phase I.

As $L = \widehat{L}_{up}$ and $T = \widehat{T}_{up}$ are used to nondimensionalize the equations in this section, the dimensionless speed c^* is equal to 1. The consequence is that the dimensional asymptotic upstroke duration can be written as

$$\widehat{T}_{up} = -\frac{1}{F_{AB}(v_-)} \int_{-\infty}^{+\infty} \nu'(s)^2 ds. \tag{2.4.11}$$

The expression (2.4.10) for the asymptotic speed is a known result derived for instance in [43] while analyzing the FHN model. It cannot be used directly to predict the speed of the travelling wave because the value of the integral $\int_{-\infty}^{+\infty} \nu'(s)^2 ds$ is not known so far. With the analysis of Sections 2.4.3 and 2.4.4, this integral will be estimated in terms of the parameters of the equations.

Calculation of the speed using an ansatz

In this section, an approximation of the traveling wave solution is constructed especially for the phase I. At the very beginning of the formation of the wave, the rise of the potential is assumed to occur exponentially. The ansatz then reads as

$$\nu(s) = u_{gate} e^{s/\delta}, \tag{2.4.12}$$

where δ is nondimensional and is chosen to be

$$\delta = \frac{1}{\ln \left(\frac{h_3(v_-)}{u_{gate}} \right)}$$

for the upstroke to be between u_{gate} and $h_3(v_-)$ and have a width of 1 in the nondimensional frame (because nondimensionalization uses $L = \widehat{L}_{up}$ and $T = \widehat{T}_{up}$).

In the same spirit as collocation methods, we want the ansatz (2.4.12) to solve the equation (2.4.9) at a given point, say at the location where $\nu = u_{gate}$. Other collocation points could be chosen and one would end up with similar results. The choice of the point with $\nu = u_{gate}$ seems to be the most appropriate since this is where the solution resemble the most an exponential. Substituting $e^{s/\delta}$ in equation (2.4.9) gives

$$\frac{c^{**}}{\delta} + \psi(u_{gate}, v_-) = \frac{N}{\delta^2}$$

at $s = 0$, where

$$\psi(u_{gate}, v_-) = \frac{1}{\tau_{in}} v_- u_{gate} (u_{gate} - 1) + \frac{1}{\tau_{out}}$$

and c^{**} is the dimensionless speed of a travelling wave of this shape. As $L = \widehat{L}_{up}$ and $T = \widehat{T}_{up}$, the dimensionless speed c^{**} is again equal to 1, then

$$\frac{\delta^2}{\widehat{T}_{up}} \psi(u_{gate}, v_-) + \frac{\delta}{\widehat{T}_{up}} = \frac{\sigma}{C_m \chi \widehat{L}_{up}^2}. \quad (2.4.13)$$

The next discussion is about general dependences between the solution features and the model parameters using equation (2.4.13). First of all, the shape of the wave is something dictated by the behavior of the cells, mathematically dictated by ionic models. If a cell is excited by an external stimulus, it reacts with certain time delays which have nothing to do with the properties of the surrounding media, e.g. its conductivity. Intuitively, the nondimensional integral $\int_{-\infty}^{+\infty} \nu'(s)^2 ds$ does not depend on the group $\sigma/(C_m \chi)$. In addition, F_{AB} (equation (2.4.3)) depends only on the parameters of the ionic model, so does T_{up} . Extracting the time scales of the 0D solution to predict those of the 1D solution is expected to be fruitful according to this last qualitative argument, and figure 2.8 is the confirmation.

The left hand side of equation (2.4.13) is constant for given values of τ 's, u_{gate}

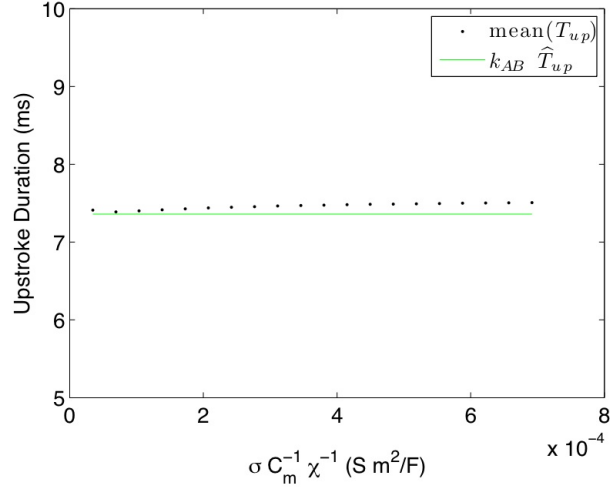
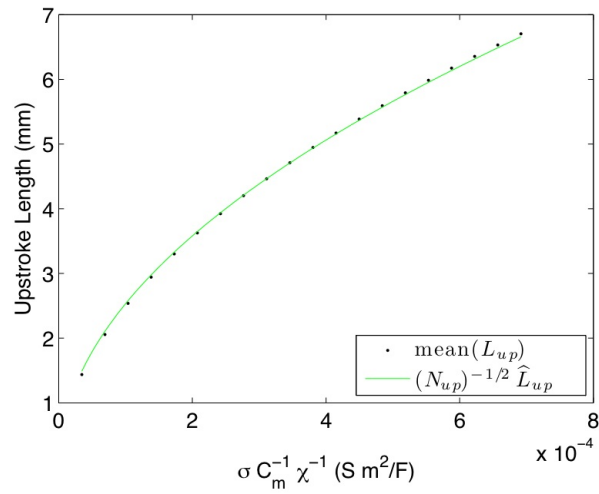


Figure 2.8: Upstroke duration versus $\frac{\sigma}{C_m \chi}$ for the MS model. The asymptotic prediction is detailed in section 2.4.5.

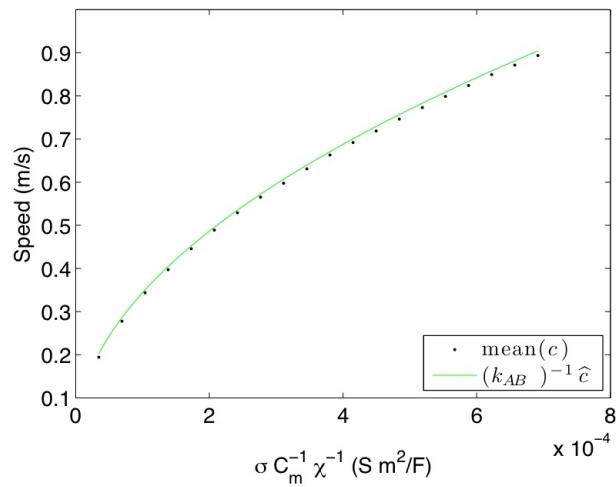
and v_- , as the dimensional asymptotic upstroke duration does not depend on the group $\sigma/(C_m \chi)$. Consequently, \hat{L}_{up} behaves as $\sqrt{\sigma/(C_m \chi)}$, and as $\hat{c} = \hat{L}_{up}/\hat{T}_{up}$, \hat{c} behaves as $\sqrt{\sigma/(C_m \chi)}$ too. The asymptotic behaviors of the travelling wave speed and upstroke width can be verified numerically as shown on figure 2.9.

In summary, the characterization of the depolarization front rises the following important facts, for given values of τ 's, u_{gate} and v_- .

1. The asymptotic upstroke duration \hat{T}_{up} is independant of the group $\sigma/(C_m \chi)$.
2. The asymptotic upstroke width \hat{L}_{up} behaves as $\sqrt{\sigma/(C_m \chi)}$. This holds also for the numerical solution.
3. The asymptotic speed \hat{c} behaves as $\sqrt{\sigma/(C_m \chi)}$. This holds also for the numerical solution.
4. The dimensionless number \hat{N}_{up} calculated using the length and time scales of the upstroke phase is constant with respect to the group $\sigma/(C_m \chi)$.



(a) Upstroke length.



(b) Speed.

Figure 2.9: Upstroke length (a) and speed (b) versus $\frac{\sigma}{C_m \chi}$ for the MS model. The asymptotic prediction is detailed in section 2.4.5.

2.4.4 Overall characterization of the asymptotic solution

In this section, the features of the asymptotic solution are studied. With a judicious combination of assumptions, algebraic expressions for short time scale features (durations) are derived, followed by long time scale features and finally, spatial features (length and speed). These expressions depend on the parameters of the model, and describe the asymptotic solution. In section 2.4.5, these results are used to predict the numerical solution of the action potential.

The asymptotic short time scales: Phases I and III

In order to find an expression for the nondimensional asymptotic upstroke duration \widehat{T}_{up} , the remaining integral in equation (2.4.11) has to be somehow estimated. To do so, a linear rise of u is assumed during the upstroke and

$$v' \simeq \begin{cases} h_3(v_-) & \text{for } 0 \leq s \leq 1, \\ 0 & \text{otherwise,} \end{cases} \quad (2.4.14)$$

The asymptotic upstroke duration is then deduced with simple calculation

$$\widehat{T}_{up} = -\frac{1}{F_{AB}(v_-)} h_3(v_-)^2. \quad (2.4.15)$$

Note that the asymptotic upstroke duration depends nonlinearly on the following set parameters τ_{in} , τ_{out} , v_- and u_{gate} . If the action potential pulse is considered as isolated the solution before and after the pulse goes towards the equilibrium point $(u, v) = (0, 1)$. In this case, using $v_- = 1$ gives a very good estimate.

Finally, it is impossible to measure the upstroke duration of a numerical simulation using the depolarization threshold $u = 0$, with $u = v$ in the depolarization phase. The following two remarks bring alternative ways of measuring and predicting the upstroke duration.

Remark 5 *Justified by the ansatz (2.4.12), an exponential rise of u is assumed during the asymptotic upstroke and*

$$v' \simeq \begin{cases} \frac{u_{gate}}{\delta} e^{s/\delta} & \text{for } 0 \leq s \leq 1, \\ 0 & \text{otherwise.} \end{cases}$$

The upstroke needs to be measured between $u = u_{gate}$ (at $s = 0$) and $h_3(v_-)$ (at $s = 1$). Consequently, the integral in F_{AB} is rather estimated using

$$\begin{aligned} F_{AB}(v_-) &\equiv \frac{1}{T_f} \int_{u_{gate}}^{h_3(v_-)} f(v, v_-) dv \\ &= \left[\frac{v_-}{\tau_{in}} \left(\frac{h_3(v_-)^4}{4} - \frac{h_3(v_-)^3}{3} \right) + \frac{1}{2} \frac{h_3(v_-)^2}{\tau_{out}} \right] \\ &\quad - \left[\frac{v_-}{\tau_{in}} \left(\frac{u_{gate}^4}{4} - \frac{u_{gate}^3}{3} \right) + \frac{1}{2} \frac{u_{gate}^2}{\tau_{out}} \right] \end{aligned}$$

and the asymptotic upstroke duration becomes

$$\widehat{T}_{up} = -\frac{u_{gate}}{2\delta F_{AB}(v_-)} (h_3^2(v_-) - u_{gate}^2).$$

■

Remark 6 *If a linear rise between $u = u_{gate}$ and $h_3(v_-)$ is assumed during the asymptotic upstroke,*

$$v' \simeq \begin{cases} h_3(v_-) - u_{gate} & \text{for } 0 \leq s \leq 1, \\ 0 & \text{otherwise,} \end{cases}$$

and the asymptotic upstroke duration becomes

$$\widehat{T}_{up} = -\frac{1}{F_{AB}(v_-)} (h_3(v_-) - u_{gate})^2,$$

using $F_{AB}(v_-)$ of Remark 5. ■

If τ_{in} and τ_{out} vary, the behaviors of the three ways of estimating the asymptotic upstroke duration are very similar (see figure 2.10). One or the other way of estimating the asymptotic upstroke duration is then equivalent. The approach of Remark 6 is going to be used in the following.

Remark 7 *To find a relation for \widehat{T}_{up} , either the whole integral*

$$\int_{-\infty}^{+\infty} \nu'(s)^2 ds$$

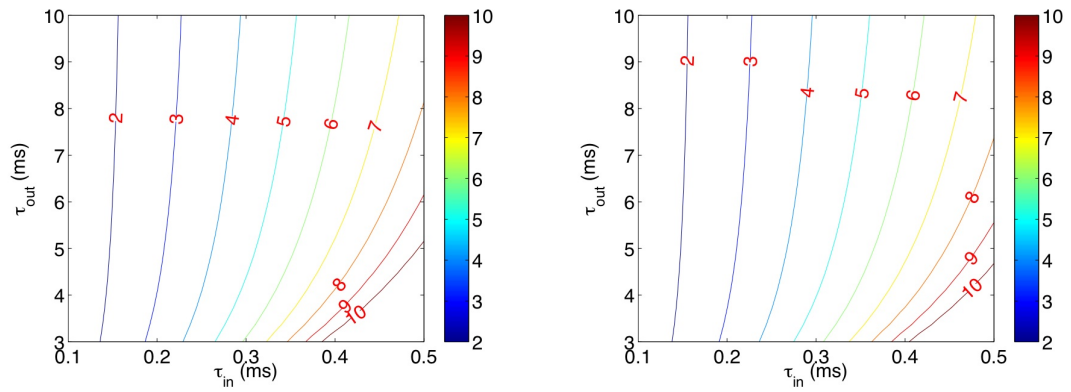
or $\nu'(s)$ has to be estimated. In equation (2.4.14), $\nu'(s)$ during the upstroke is estimated as if the upstroke of u was piecewise linear. Equivalently, this is the average speed of depolarization.

To estimate the integral directly, remark first that

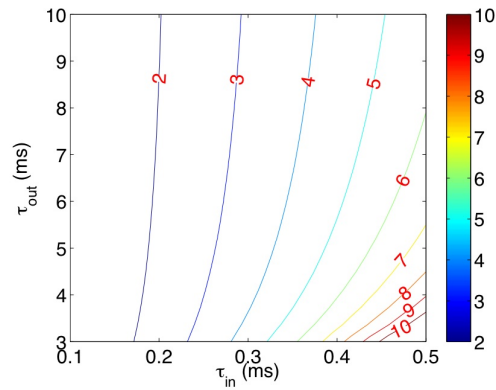
$$\int_{-\infty}^{+\infty} \nu'(s)^2 ds \geq \int_0^1 \nu'(s)^2 ds. \tag{2.4.16}$$

The transmembrane potential crosses the excitation threshold u_{gate} at $x = 0$ when $L = \widehat{L}_{up}$ and $T = \widehat{T}_{up}$ are used in the nondimensionalization. Note that both integrals are constants in this nondimensional frame.

This estimate, which is actually a lower bound, can be found formally since $\nu'(s)$



(a) Asymptotic upstroke duration using a linear rise between 0 and $h_3(v_-)$. (b) Asymptotic upstroke duration using an exponential rise between u_{gate} and $h_3(v_-)$.



(c) Asymptotic upstroke duration using a linear rise between u_{gate} and $h_3(v_-)$.

Figure 2.10: The three proposed ways of estimating the asymptotic upstroke duration.

is a non negative real valued Lebesgue integrable function. Jensen's inequality

$$\varphi \left(\int_0^1 \nu'(s) ds \right) \leq \int_0^1 \varphi(\nu'(s)) ds$$

can be used with $\varphi(s) = s^2$, a convex function on the real line, hence

$$\int_0^1 \nu'(s)^2 ds \geq \left[\int_0^1 \nu'(s) ds \right]^2 = (h_3(v_-) - u_{gate})^2. \quad (2.4.17)$$

The estimation of \widehat{T}_{up} proposed in Remark 6 is then a lower bound. ■

For a stable travelling wave the repolarization speed is the same as the depolarization speed and one has that $c^* = \widehat{L}_{down}/\widehat{T}_{down}$. In phase III, the asymptotic solution consists in a trajectory connecting $(u_*, v_*) = (1/2, 4\tau_{in}/\tau_{out})$ and $(0, v_*) = (0, 4\tau_{in}/\tau_{out})$. Estimating that the decay of u is linear, the dimensional asymptotic downstroke duration reads now as

$$\widehat{T}_{down} = -\frac{u_*^2}{F_{CD}} = -\frac{1}{4F_{CD}}$$

with

$$\begin{aligned} F_{CD} &\equiv -\frac{1}{T_f} \int_{1/2}^0 f(\nu, 4\tau_{in}/\tau_{out}) d\nu \\ &= \frac{4}{\tau_{out}} \left(\frac{(1/2)^4}{4} - \frac{(1/2)^3}{3} \right) + \frac{1}{2} \frac{(1/2)^2}{\tau_{out}} \\ &= \frac{1}{48\tau_{out}}. \end{aligned} \quad (2.4.18)$$

The asymptotic long time scales: Phases II and IV

In phase II, the nondimensional equations (2.4.4)-(2.4.5) are used in order to find the asymptotic action potential duration \widehat{T}_{AP} . The time scale of phase II has to characterize the period of excitation so $T = \widehat{T}_{AP}$ can be chosen. However, \widehat{T}_{AP} is not known yet in terms of the parameters of the equations. Let $T = T_g$ so that T is a long time scale and depends on τ_{open} and τ_{close} , which is enough to allow the comparison between the magnitude of the terms in the equations and furthermore gives an estimate of how good is the asymptotic approximation. Recall that T_f depends on τ_{in} and τ_{out} , time scales of f , so it is a short time scale (that now can be taken equal to the predicted value of T_{up}). Now that $\partial u/\partial t$ and $\partial^2 u/dx^2$ are of order one in magnitude, one gets $T_g/T_f = T_{AP}/T_{up} \sim 100$ and $(\sigma_{harm}T)/(\chi C_m L^2) = 1 \times 10^{-3}$.

Remark 8 *In the asymptotic analysis of the FHN model done in [43], T_f/T_g can be compared to the parameter ϵ .* ■

Because the coefficients of the nondimensionalized model $(\sigma_{harm}T_f)/(\chi C_m L^2)$ and 1 are negligible compared to T_g/T_f , we expect the solution to stay within the neighborhood $\{(u, v) \mid |f(u, v)| \lesssim 10^{-2}\}$ but we are going to assume that the solution goes along the nullcline $f(u, v) = 0$ during this phase. In other words, the equation (2.4.4) becomes $f(u, v) = 0$ (or equivalently $u = h_3(v)$) to leading order. Matching the solution with that of phase I, the recovery variable is described using

$$\frac{\partial v}{\partial t} = \frac{T}{T_g} g(h_3(v), v) \quad \text{with } v(0) = v_-,$$

where v_- is the (given) value of v facing the arrival of the wave ($v_- = 1$ for a isolated wave). The trajectory goes along the branch $u = h_3(v)$ because it follows $f(u, v) = 0$

and v decreases until it reaches v_* beyond $h_3(v)$ ceases to exist. The dimensional time taken for this phase is

$$\widehat{T}_{AP} = T_g \int_{v_-}^{v_*} \frac{1}{g(h_3(v), v)} dv$$

where $g(h_3(v), v)$ has nondimensional parameters and variables.

During this phase, $u_{gate} < u_* = 1/2$ and then $g(h_3(v), v)/T_g = -v/\tau_{close}$ so

$$\widehat{T}_{AP} = - \int_{v_-}^{4\frac{\tau_{in}}{\tau_{out}}} \frac{\tau_{close}}{v} dv = \tau_{close} \ln \left(\frac{\tau_{out} v_-}{4\tau_{in}} \right) \quad (2.4.19)$$

This is a well established result first published in [56]. With the dimensional values of τ and $v_- = 1$, one gets $\widehat{T}_{AP} \approx 241$ ms for the MS model (2.2.3)-(2.2.4).

Remark 9 (Characterization of the overshoot) *The overshoot duration and height can be characterized as for the AP duration. The overshoot is a part of the phase II because the trajectory is along the branch $u = h_3(v)$ even if the time scale is temporarily shortened with $\tau_{close}(u)$. The overshoot features a peak of height given by $h_3(v_-) - u_{sldn}$ and duration given by the following integral*

$$\widehat{T}_{peak} = T_g \int_{h_3(v_-)}^{u_{sldn}} \frac{1}{g(u, h_3^{-1}(u))} \frac{dv}{du} du$$

with $v = h_3^{-1}(u) = \tau_{in}/[\tau_{out}u(1-u)]$. As $1/\tau_{close}(u) = m(u+b)$ with $m = (1/\tau_{fclose} - 1/\tau_{sfclose})/(1-u_{sldn})$ and $b = (1-u_{sldn})/(1-\tau_{fclose}/\tau_{sfclose}) - 1$ the integral becomes

$$= -\frac{1}{m} \int_{h_3(v_-)}^{u_{sldn}} \frac{2u-1}{(u+b)u(u-1)} du.$$

The latter integral is easily computed and the result gives

$$\widehat{T}_{peak} = -\frac{1}{m} \left[-\frac{2b+1}{b(b+1)} \ln(u+b) + \frac{1}{b} \ln(u) + \frac{1}{b+1} \ln(u-1) \right]_{h_3(v_-)}^{u_{sldn}}.$$

The asymptotic AP duration is now slightly modified as

$$\begin{aligned}\widehat{T}_{AP} &= \widehat{T}_{peak} + \tau_{sclose} \ln \left(\frac{\tau_{out} h_3^{-1}(u_{sldn})}{4\tau_{in}} \right) \\ &= \widehat{T}_{peak} - \tau_{sclose} \ln (4u_{sldn}(1 - u_{sldn})).\end{aligned}$$

■

In phase IV, the asymptotic recovery duration and length can be derived with assumptions very similar as for phase II. The dimensional scaling is based on the refractory period, then $T = T_g$, and again the equation (2.4.5) reduces to $f(u, v) = 0$ to the leading order.

The system for the recovery variable reads as

$$\frac{\partial v}{\partial t} = \frac{T}{T_g} g(h_1(v), v) \Leftrightarrow v(0) = v_*,$$

with $u = h_1(v)$ for the asymptotic solution to be continuous (matching condition with phase III). For the original MS model, v increases and the solution goes to the stable point $(0, 1)$ so the time to reach this equilibrium is infinitely long. If a region of the domain is paced at a certain value of v , say v_{pace} , the recovery time for the MS model can be approximated by

$$\widehat{T}_{rec} = \tau_{open} \ln \left(\frac{\frac{4\tau_{in}}{\tau_{out}} - 1}{v_{pace} - 1} \right). \quad (2.4.20)$$

The last expression is obtained using similar arguments than those used in the phase II.

When $a \neq 0$, the upper bound for v in this phase cannot be found exactly unless an analysis of the periodic solution is performed. This is not going to be done just because doing such a laborious analysis is pointless considering the objective: evaluating the following time scale

$$\widehat{T}_{rec,a} = \int_{v_*}^{v_{up,periodic}} \frac{1}{g(h_1(v), v)} dv,$$

where $v_{up,periodic}$ is the value of v during the upstroke of an asymptotic periodic solution, i.e. a wave train in dimension one.

One can however estimate an upper bound with v going from v^* to 0.8 (values suggested from numerical simulations). The dimensional time taken for this phase is then

$$\int_{v_*}^{v^*} \frac{1-v}{\tau_{open}} dv \lesssim T_{rec,a} \lesssim \int_{v_*}^{0.8} \frac{1-v}{\tau_{open}} dv.$$

as for the modified MS model, $u < u_{gate}$ and then $g(h_1(v), v) = (1-v)/\tau_{open}$. With the dimensional values of τ , the recovery time can be estimated with $122 \lesssim T_{rec,a} \lesssim 211$ ms.

The asymptotic space scales and speed

Now that it is known that \widehat{T}_{up} does not depend on the group $\sigma/(C_m\chi)$ for a chosen set of parameters τ 's (see section 2.4.3, equation (2.4.15)), it is possible to find an expression for the asymptotic upstroke width \widehat{L}_{up} with equation (2.4.13).

$$\widehat{L}_{up} = k_{up} \sqrt{\widehat{T}_{up}} \sqrt{\frac{\sigma}{C_m\chi}}.$$

In the right hand side, the factor $k_{up} \sqrt{\widehat{T}_{up}}$ does not depend on the group $\sigma/(C_m\chi)$. It depends only on the parameters of the ionic model. The remaining factor depends only on the parameters of the propagation (monodomain or bidomain) model.

Using equation (2.4.10) with $L = \widehat{L}_{up}$, one has

$$\widehat{c} = -\frac{F_{AB}\widehat{L}_{up}}{(h_3(v_-) - u_{gate})^2}, \quad (2.4.21)$$

Similarly, the other asymptotic widths are all given by

$$\widehat{L}_{down,AP,rec} = k_{down,AP,rec} \sqrt{\frac{\widehat{T}_{down,AP,rec}\sigma}{C_m\chi}}.$$

2.4.5 Using the asymptotic solution to predict the numerical solution

The first aim of this section is estimating the time required for the rise of the numerical solution u from u_{gate} to $h_3(v_-)$, which is by definition the upstroke time T_{up} . The asymptotic upstroke time \widehat{T}_{up} is suggested as an approximation of the numerical upstroke time T_{up} and it turns out that this approximation is good enough to be used for the prediction of T_{up} in the heart (see section 2.5).

The asymptotic upstroke duration \widehat{T}_{up} (equation (2.4.15)) involves the assumption that the upstroke occurs linearly and at a constant $v = v_-$. This approximation makes the values of \widehat{T}_{up} a bit off the values of T_{up} though the behavior with respect to the parameters remains satisfactory. For \widehat{T}_{up} to be convenient to estimate T_{up} , it can be scaled with a constant $k_{AB} > 0$ as

$$T_{up} \simeq k_{AB}\widehat{T}_{up} = k_{AB} \frac{h_3^2(v_-)}{|F_{AB}(v_-)|}, \quad (2.4.22)$$

and the constant k_{AB} can be found using a single numerical simulation for a given set of data $\{\tau_{in}, \tau_{out}\}$. An exponential upstroke for the traveling wave, as proposed in section 2.4.3, could be an other choice. At the end, another constant like k_{AB} would be needed to compensate for this other approximation of \widehat{T}_{up} . For the sake of

simplicity, it turns out that the linear rise is a good choice: simple calculations and satisfactory predictions.

In a certain neighborhood of the data set $\{\tau_{in}, \tau_{out}\}_0$ initially used for a 1D simulation, if $\{\tau_{in}, \tau_{out}\}$ changes for any reason (for example, from one tissue of the heart to another, where the AP is different), one could assume that k_{AB} remains the same as the one calculated with $\{\tau_{in}, \tau_{out}\}_0$. This assumption can be explained by the fact that k_{AB} compensates for an integral of the upstroke's profile (the integral of the square of the upstroke slope), which remains nearly the same: if $\{\tau_{in}, \tau_{out}\}$ change, \widehat{T}_{up} and \widehat{L}_{up} changes so impact the nondimensionalization of the phase I. The new profile is simply a scaling with the new \widehat{T}_{up} and \widehat{L}_{up} . As a result, the approximation (2.4.14) used to estimate the upstroke is scaled in the same way.

For simulations with spatial propagation, the constant k_{AB} can be fixed from a single simulation in 1D. We will see later that this way of estimating T_{up} works in a reliable way, as long as u_{gate} remains the same. Changing the value of u_{gate} is equivalent to change the threshold of the upstroke. Consequently, it could modify considerably the upstroke profile, then the integral of its derivative and so the scaling factor k_{AB} (see section 2.5 for examples where k_{AB} has to be recalculated).

The dimensional downstroke duration can also be predicted with

$$T_{down} \simeq k_{CD} \widehat{T}_{down} = 12k_{CD} \tau_{out}, \quad (2.4.23)$$

where the constant $k_{CD} > 0$ emerges from the same arguments as for k_{AB} . Assuming that the phase III occurs for a constant $v = v_*$ is not as nearly true as for the upstroke. However, the scaling constant k_{CD} is enough to compensate for the approximations used to find \widehat{T}_{down} .

The extracted information in these phases gives a relation ξ between model's

parameters and the asymptotic solution's features:

$$\xi : (\tau_{in}, \tau_{out}) \rightarrow (k_{AB}\widehat{T}_{up}, k_{CD}\widehat{T}_{down}).$$

For solution's features T_{up} and T_{down} of physiological relevance, it turns out that ξ is bijective. The asymptotic 1D solution is then controllable, giving a reasonably good handleability of the solution (figures 2.11 and 2.12).

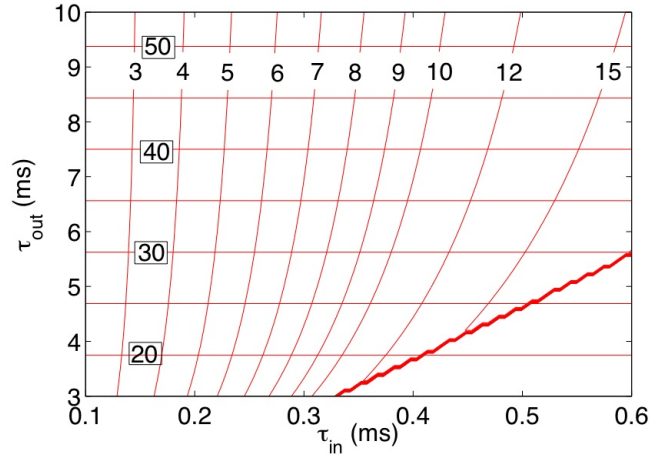


Figure 2.11: Asymptotic approximations of the durations $(k_{AB}\widehat{T}_{up}, k_{CD}\widehat{T}_{down})$ versus (τ_{in}, τ_{out}) for $v_- = 1$, $k_{AB} = 2.15$ and $k_{CD} = 0.45$. Level sets for \widehat{T}_{up} are rather vertical (plain labels) and level sets for \widehat{T}_{down} are horizontal (boxed labels).

In phase II, the goal is again to find an approximation of the action potential duration T_{AP} using the behavior of the asymptotic 1D solution. Contrary to equations for \widehat{T}_{up} and \widehat{T}_{down} , \widehat{T}_{AP} needs not to be scaled

$$T_{AP} \approx \widehat{T}_{AP}, \tag{2.4.24}$$

and this is simply because the asymptotic approximation is better (asymptotic and numerical solution both go very closely along the nullcline $f(u, v) = 0$) and no assumption is done on the shape of this part of the wave. Remark that one also have

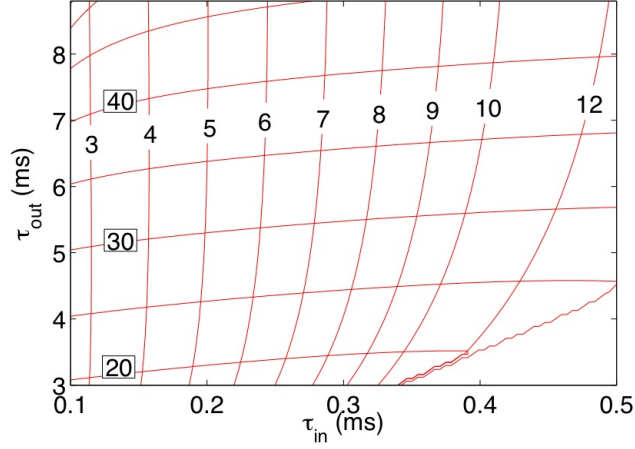


Figure 2.12: 1D numerical solution. (T_{up}, T_{down}) versus (τ_{in}, τ_{out}) for $v_- = 1$, $\tau_{open} = 130$ ms, $\tau_{close} = 150$ ms. Level sets for \hat{T}_{up} are rather vertical (plain labels) and level sets for \hat{T}_{down} are rather horizontal (boxed labels). Note that the ranges for the τ_{in} and τ_{out} axis are not the same as in figure 2.11.

$$T_{peak} \approx \hat{T}_{peak}.$$

In phase IV, the recovery duration can be predicted as long as the next wave is paced at a given value v_{pace} and $T_{rec} \approx \hat{T}_{rec}$ with equation (2.4.20). For waves paced at various values of v_{pace} , the asymptotic analysis is as well predictive (see section 2.4.6).

The numerical upstroke length is predicted using

$$L_{up} \simeq \sqrt{k_{AB} \hat{L}_{up}} = k_{up} \sqrt{\frac{T_{up} \sigma}{C_m \chi}}. \quad (2.4.25)$$

If one assumes that (2.4.25) holds for any values of model's parameters, this means that k_{up} has the same value whatever the values of the model's parameters. In other words, the nondimensional number associated with the phase I $N_{up} = \sigma T_{up} / (C_m \chi L_{up}^2) = 1/k_{up}^2$ is assumed to be a constant.

The numerical results predicted by equation (2.4.25) are illustrated in figure

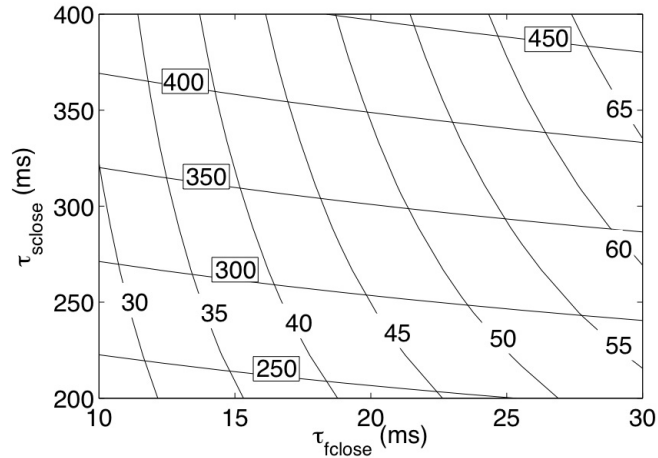


Figure 2.13: Asymptotic approximations of the durations $(\hat{T}_{AP}, \hat{T}_{peak})$ versus $(\tau_{fclose}, \tau_{sclose})$ for $v_- = 1$. Level sets for \hat{T}_{peak} are rather vertical (plain labels) and level sets for \hat{T}_{AP} are horizontal (boxed labels).

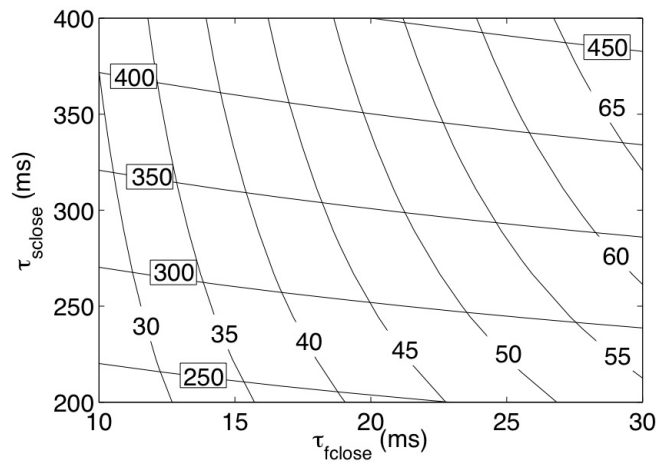


Figure 2.14: 1D numerical solution. (T_{AP}, T_{peak}) versus $(\tau_{fclose}, \tau_{sclose})$ for $v_- = 1$, $\tau_{open} = 130$ ms, $\tau_{close} = 150$ ms. Level sets for \hat{T}_{peak} are rather vertical (plain labels) and level sets for \hat{T}_{AP} are rather horizontal (boxed labels).

2.9(a). To fit the asymptotic behavior to the data (see figure 2.9(a)), the nondimensional number was $N_{up} = 0.1149$. The numerical speed can be predicted as well with the asymptotic speed as

$$c = \frac{L_{up}}{T_{up}} \simeq \frac{\sqrt{K_{AB}} \widehat{L}_{up}}{K_{AB} \widehat{T}_{up}} = \frac{1}{\sqrt{K_{AB}}} \widehat{c} \quad (2.4.26)$$

and the numerical results predicted are illustrated in figure 2.9(b), still with $N_{up} = 0.1149$.

Remark 10 (Precisions about the numerical simulations) *The numerical values T_{up} and L_{up} are averaged over the total time of the simulation. The time and space discretization was precise enough that the solution was converged in time and space (less than 1% of variation on T_{up} , L_{up} , T_{AP} , L_{AP} and speed compared to an abusively precise solution).* ■

Similarly, the value of the nondimensional number $N_{down} = (T_{down}\sigma)/(C_m\chi L_{down}^2)$ associated with the phase III can be found using the same 1D simulation as it is assumed to be a constant. The downstroke width can be estimated as well using equation (2.4.23) and

$$L_{down} \simeq \sqrt{k_{CD} \widehat{L}_{down}} = \frac{1}{\sqrt{N_{down}}} \sqrt{\frac{k_{CD} \widehat{T}_{down} \sigma}{C_m \chi}}. \quad (2.4.27)$$

The validity of the approximation is striking. Using the same 1D simulation, one gets $k_{CD} = 0.45$ and $N_{down} = 0.02601$. T_{down} and L_{down} could be plotted versus $\sigma/(C_m\chi)$. The figure is very similar than figure 2.9 and will not be showed to avoid redundancy.

The behavior of the AP length is asymptotically of the form

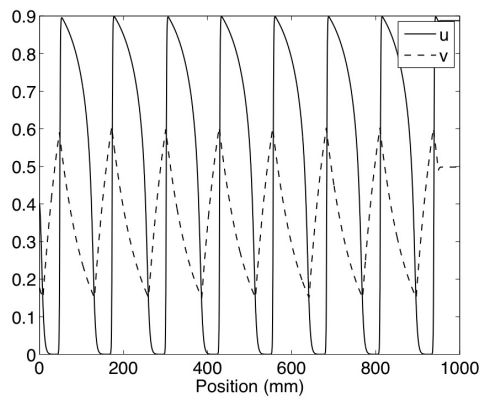
$$L_{AP} \simeq \frac{1}{\sqrt{N_{AP}}} \sqrt{\frac{\widehat{T}_{AP} \sigma}{C_m \chi}}.$$

The nondimensional number associated to the phase II is $N_{AP} = 3.3029 \times 10^{-3}$ and is found using the same 1D numerical simulation than the one used to fit the upstroke length. Again, the behavior of the action potential duration and width can be predicted accurately. Finally, the recovery length can be found by fixing the nondimensional number for this phase (using again the same simulation than the one used to fit the upstroke width). Again, the asymptotic results fit almost perfectly the numerical solutions (as illustrated in figure 2.9).

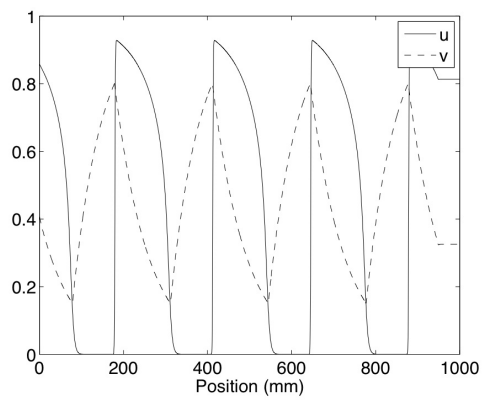
2.4.6 Periodic excitations

The asymptotic speed (equations (2.4.21)) as well as the asymptotic upstroke duration (equation (2.4.15)) depend on the state v_- . This dependence has a considerable impact on the solutions if the waves are very close to each other. For instance, when waves are paced at a high frequency, v_- does not have a chance to reach the equilibrium $v = 1$ between each pacing. Consequently, the action potential considerably changes. This kind of phenomenon can occur in real life in pathological situations like arrhythmia and fibrillation. The last example is often modeled with spiral waves (e.g. see [46]), where the wave fronts propagate side by side very closely. In the following, relations obtained from the asymptotic analysis are going to be used to predict what happen to the solution of the MS model when there is a periodic pacing.

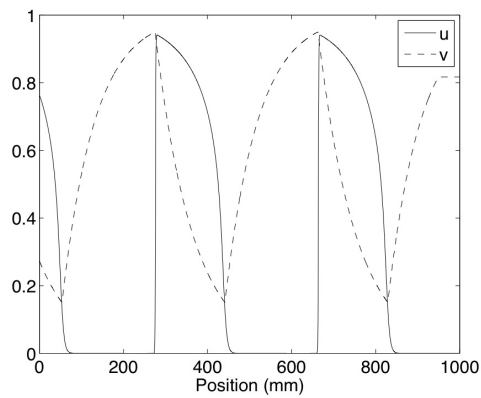
In the numerical simulations used to illustrate our results, a new wave is started in a pacing region any time the recovery variable v is equal to a prescribed $v_{pace} = v_-$ in that region. A sequence of waves is thus generated. They are constrained to move together, pushed in the back by a following wave. In the long run, the wave train is stable, i.e. all the waves have the same speed, action potential duration, recovery time, etc. To get values of these wave features depending on v_- , it suffices to excite the new wave at that v_- . The dependences are analyzed once a stable wave train is obtained (figure 2.15).



(a) Wave train paced at $v_- = 0.6$.

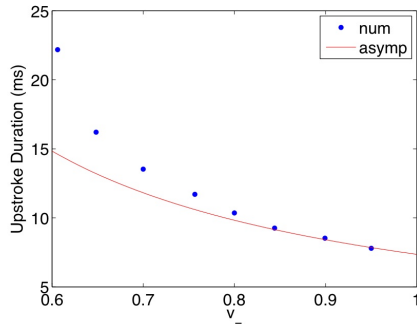


(b) Wave train paced at $v_- = 0.8$.

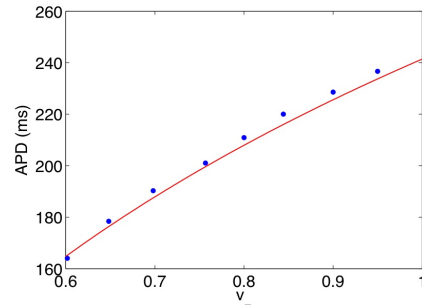


(c) Wave train paced at $v_- = 0.95$.

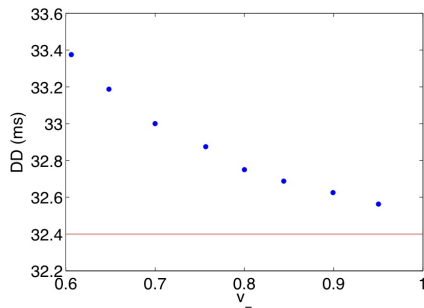
Figure 2.15: The simulations are calculated over 5000 ms. The dimensionless number is that of Adim3.



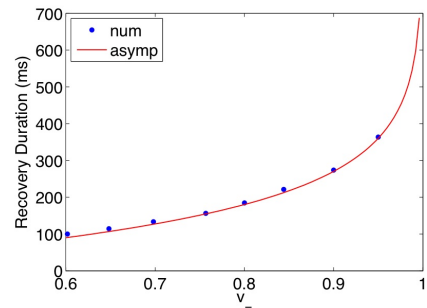
(a) Upstroke duration of a wave train paced at v_- .



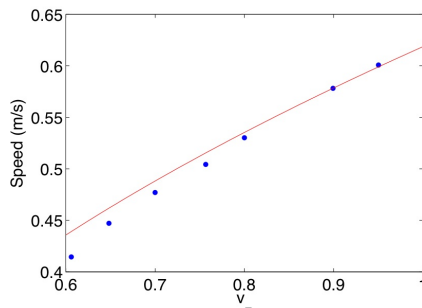
(b) Action potential duration of a wave train paced at v_- .



(c) Downstroke duration of a wave train paced at v_- .



(d) Recovery duration of a wave train paced at v_- .



(e) Speed of a wave train paced at v_- .

Figure 2.16: Asymptotic predictions (continuous line) of numerical AP's features (dots) of waves trains paced at v_- .

Figure 2.16 shows that the asymptotic analysis is still very reliable to predict T_{AP} and T_{rec} . Predicting T_{up} for wave trains is more difficult because the approximation of the integral (see remark 7) with the corresponding scaling k_{AB} for $v_- = 1$ no longer holds when v_- varies. The approximation \widehat{T}_{up} is as bad as 35% off T_{up} when $v_- = 0.6$. The approximation for the speed \widehat{c} is also affected by the approximation of the integral. It is nonetheless reliable since in the worst case ($v_- = 0.6$), \widehat{c} is less than 6% off c . The approximation for T_{down} seems to be very poor because \widehat{T}_{down} does not depend on v_- . It is not the case because T_{down} varies less than 4% from $v_- = 0.6$ to $v_- = 1$. The asymptotic approximation describing the behavior of wave trains is finally very good as long as the prediction of the upstroke duration is.

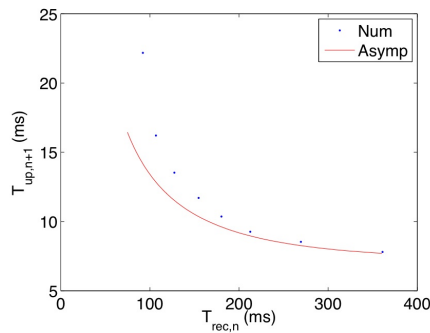
2.4.7 Predicting the restitution curves

Using equation 2.4.20, the restitution curves can be plotted (figure 2.17) for the upstroke duration, the action potential, the downstroke duration and the speed.

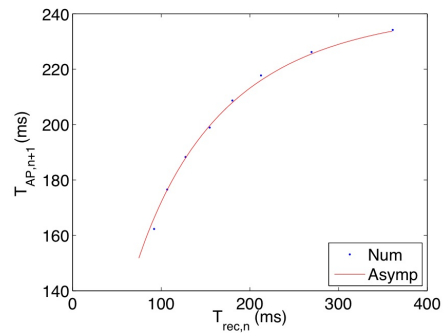
2.5 Modeling physiological AP propagating in various tissues of the heart

This section is devoted to the application of the asymptotic analysis to model various APs. In the human heart, there are different tissues with different APs (figure 1.5) propagating at different speeds. In the same perspective than in integrative modeling, a Purkinje fibers AP as well as a ventricle AP of a healthy human heart are going to be modeled in order to prove the efficiency of our asymptotic analysis.

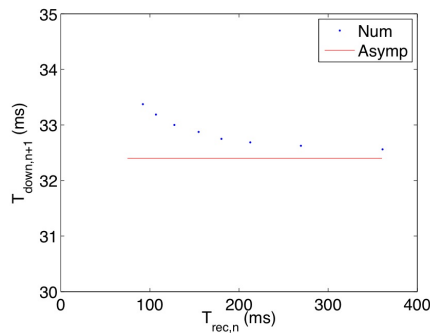
The very first step is to simulate one AP in 1D using a given set of parameters $\{u_{gate}, \tau_{in}, \tau_{out}, \tau_{open}, \tau_{close}\}$. Note here that the same u_{gate} has to be used for every simulation unless a new 1D simulation is computed any time u_{gate} changes. Using the results of the 1D simulation, the constants k_{AB} and k_{CD} can be fixed to match the



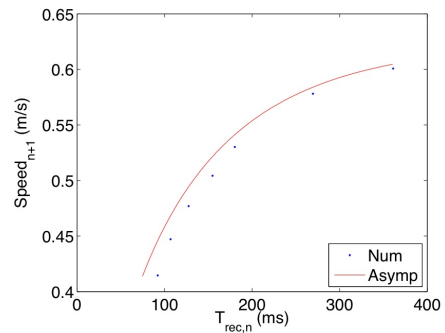
(a) Upstroke duration $T_{up,n+1}$ of a wave following a recovery duration of $T_{rec,n}$.



(b) Action potential duration $T_{AP,n+1}$ of a wave following a recovery duration of $T_{rec,n}$.



(c) Downstroke duration $T_{down,n+1}$ of a wave following a recovery duration of $T_{rec,n}$.



(d) Speed c_{n+1} of a wave following a recovery duration of $T_{rec,n}$.

Figure 2.17: Asymptotic restitution curves predicting the numerical restitution curves.

asymptotic predictions at such u_{gate} .

The second step is to impose the desired time scales of the AP. From equations (2.4.15), (2.4.19), (2.4.23) and (2.4.20), the relations are summed up as

$$\begin{aligned} T_{up} &\simeq \widehat{T}_{up}(\tau_{in}, \tau_{out}) \\ T_{AP} &\simeq \widehat{T}_{AP}(\tau_{close}, \tau_{in}, \tau_{out}) \\ T_{down} &\simeq \widehat{T}_{down}(\tau_{out}) \\ T_{rec} &\simeq \widehat{T}_{rec}(\tau_{open}, \tau_{in}, \tau_{out}) \end{aligned}$$

and the order in which the parameters of the MS model have to be fixed is obvious: τ_{out} from \widehat{T}_{down} followed by τ_{in} from \widehat{T}_{up} followed by τ_{open} and τ_{close} from \widehat{T}_{rec} and \widehat{T}_{AP} , respectively. If for any reason the overshoot is important in the simulation, one more relation is considered

$$T_{peak} \simeq \widehat{T}_{peak}(u_{sldn}, \tau_{in}, \tau_{out}, \tau_{fclose}, \tau_{sclose}),$$

and the parameters are fixed in the following order: u_{sldn} from the overshoot height, followed by the same steps as without the overshoot and finally, τ_{fclose} from the overshoot duration.

The third step is to impose the speed of propagation by fixing the group of parameters $\sigma/(C_m\chi)$ in the bidomain model using equation (2.4.21). Using the results of the 1D simulation, the nondimensional numbers N_{up} , N_{down} , N_{AP} and N_{rec} are automatically set. The space scales L_{up} , L_{down} , L_{AP} and L_{rec} are thus deduced.

Finally, the characteristic potential V_m is fixed so that the AP sweeps an appropriate range in Volts. Any characteristic time T and length L can be chosen as long as the domain is already scaled in the right way. For instance, if a numerical simulation is done on a mesh of a human heart, L has to be fixed so that the heart have an appropriate dimension and T can be chosen arbitrarily. The nondimensional values of τ 's in the MS model will have to be adjusted consequently because the original MS

model is designed for $T = 1$ ms.

2.5.1 Ventricle

In the intent of reproducing the ventricle's AP, which is the most representative AP of the heart, the first numerical simulation uses parameters such that the AP is physiological, i.e. has time scales and speed of real patient data.

In order to see the entire cycle with the four phases in the numerical simulation, the interval $[0, t_{max}]$ over which the simulation is done is chosen such that $t_{max} > \widehat{T}_{up} + \widehat{T}_{AP} + \widehat{T}_{down} + \widehat{T}_{rec}$. The size of the domain has to be larger than $\widehat{c}t_{max}$.

The numerical solution is performed on a domain of 1000 mm-long and of 1000 ms. A forward Euler time scheme is used with 80,000 time steps and a finite difference method is used with 4,000 degrees of freedom. A characteristic time $T = 1$ ms and length $L = 1$ mm are used for the nondimensionalization. $u_{gate} = 0.13$ and the scaling constants k_{AB} , k_{CD} as well as the nondimensional numbers of every phase are the same as those used in section 2.4.5. The results of the asymptotic predictions are presented in table 2.4 and the numerical simulation gives a solution with no more than 5 % off the predicted time scales. Note that c is 12.6% off its asymptotic prediction. As $c = \sqrt{N}$, the number N is readily adjustable so that the desired speed is exactly obtained.

2.5.2 Purkinje fibers

This is an example where the AP has time scales of the order of magnitude of those of the ventricle's AP. However, the speed of propagation is way larger. The scaling constants k_{AB} , k_{CD} as well as the nondimensional numbers of every phase are the same as those used for the simulation of the ventricle's AP. The results of the asymptotic predictions are presented in table 2.5 and the numerical simulation gives a solution with no more than 10 % off the predicted time scales and speed.

Table 2.4: Model's parameters for a physiological ventricle to get the asymptotic \sim -quantities.

Phase	Duration	\widehat{T} (ms)	MS parameters (ms)		T (ms)	$ \widehat{T} - T /\widehat{T}$ (%)
I	Upstroke	8	τ_{in}	0.3150	7.9750	0.313
II	AP	250	τ_{close}	168.50	260.93	4.38
III	Downstroke	30	τ_{out}	5.5556	31.196	4.00
IV	Recovery	260	τ_{open}	94.942	257.41	0.996
Phase	Speed	\widehat{c} (m/s)	Bidomain parameter (nondimensional)		c (m/s)	$ \widehat{c} - c /\widehat{c}$ (%)
I		0.5	N	1.8508e-04	0.4368	12.6

Table 2.5: MS and bidomain model's parameters for a physiological Purkinje system to get the asymptotic \sim -quantities. The numerical solution is performed on a domain of 2000 mm-long and of 1000 ms. Discretization: Forward Euler time scheme with 100,000 time steps and 8,000 degrees of freedom.

Phase	Duration	\widehat{T} (ms)	MS parameters (ms)		T (ms)	$ \widehat{T} - T /\widehat{T}$ (%)
I	Upstroke	8	τ_{in}	0.3590	8.77	9.7
II	AP	380	τ_{close}	178.73	401.12	5.6
III	Downstroke	65	τ_{out}	12.037	61.54	5.4
IV	Recovery	320	τ_{open}	111.55	305.29	4.6
Phase	Speed	\widehat{c} (m/s)	Bidomain parameter (nondimensional)		c (m/s)	$ \widehat{c} - c /\widehat{c}$ (%)
I		1.8	N	0.0024	1.65	8.4

Table 2.6: MS and bidomain model’s parameters for a physiological Purkinje system to get the asymptotic \hat{T} -quantities for a very steep upstroke. The numerical solution is performed on a domain of 1000 mm-long and of 1000 ms.

Phase	Duration	\hat{T} (ms)	MS parameters (ms)		T (ms)	$ \hat{T} - T /\hat{T}$ (%)
I	Upstroke	1	τ_{in}	0.02	0.9554	4.46
II	AP	380	τ_{close}	71.026	407.68	7.28
III	Downstroke	65	τ_{out}	16.852	58.940	9.32
IV	Recovery	320	τ_{open}	106.989	360.05	12.52
Phase	Speed	\hat{c} (m/s)	Bidomain parameter (nondimensional)		c (m/s)	$ \hat{c} - c /\hat{c}$ (%)
I		1.8	N	1.6175e-04	1.7975	0.03

2.5.3 Considerations to take for a narrower upstroke

For a very steep upstroke of 1 ms-long, τ_{in} has to be reduced to 0.0827. This affects considerably the phase space. For a complete cycle to occur during the simulation, u_{gate} has to be reduced otherwise the domain gets re-depolarized prematurely. This example of simulation uses $u_{gate} = 0.005$, with 100,000 time steps and 4,000 degrees of freedom. The scaling constants k_{AB} , k_{CD} had to be re-calculated. The τ 's are obtained using the results of a numerical simulation with the \hat{T} calculated with the constants k_{AB} and k_{CD} of $u_{gate} = 0.13$. Obviously this preliminary 1D simulation gives wrong results in time scales and speed, but it is essential to find k_{AB} , k_{CD} as well as the nondimensional numbers of every phase associated with $u_{gate} = 0.005$. Once these constants are found, a new numerical simulation is performed. The results of the asymptotic predictions for a Purkinje fiber are presented in table 2.6 and the numerical simulation gives a solution with no more than 13 % off the predicted long time scales and no more than 10 % off the predicted short time scales. The speed is perfectly predicted.

2.6 Existence and uniqueness of a traveling wave for the asymptotic solution

The conditions establishing the existence of travelling wave solutions for the reaction-diffusion equation (2.4.8) have been studied thoroughly in [91] for a general source term f . The properties of the source term determine the existence of waves, their number, their kind (monotone, non monotone, periodic), and their stability. For 2-variable models, the analysis is done in a two- or three-dimensional phase space, often resulting in simpler existence proofs (at least in comparison with higher dimensional space). In [25] and [40], the existence of many types of travelling waves is proven for the FHN model. The argument is relatively difficult given the several travelling modes.

In the following we will see that the source term of the MS model is constructed so that under certain conditions the travelling wave is unique. We are going to establish the necessary conditions for the existence of this wave.

Remark 11 *In this section, $N = N_{harm}$ and the value of N represents that of phase I e.g. $N = N_{up} = 0.2$ as in table 2.3.* ■

With the equation (2.4.8), one gets that the traveling wave solution $u(x, t) = \nu(x + ct)$ solves the equation (2.4.9)

$$c\nu' + f(\nu, v_-) = N\nu''.$$

Let $\eta = \nu'$ and the last equation can be written as a system of two ordinary differential

equations.

$$\begin{aligned} \nu' &= \eta \\ \eta' &= \frac{1}{N}f(\nu, v_-) + \frac{c}{N}\eta \end{aligned} \tag{2.6.1}$$

For the original MS model the system of ODEs has three equilibrium points, and for the modified MS with $a \neq 0$ there is only a single equilibrium point. The vector fields and the equilibrium points for the reduced systems (2.6.1) for both the MS and modified MS models are illustrated in figure 2.18.

For the MS model, a traveling wave corresponds to an orbit connecting the equilibrium points $(\nu_1^*, \eta_1^*) = (0, 0)$ and $(\nu_3^*, \eta_3^*) = (h_3(v_-), 0)$ (i.e. a heteroclinic orbit) such that

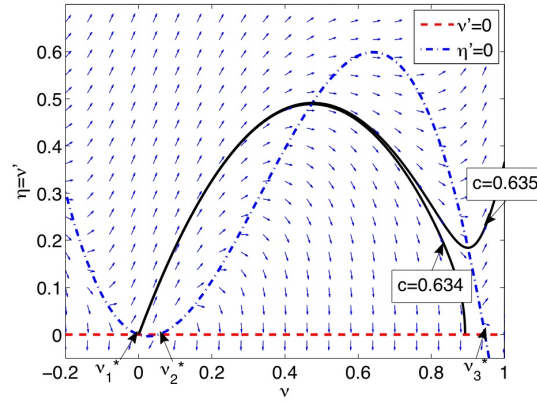
$$\lim_{s \rightarrow -\infty} (\nu(s), \eta(s)) = (0, 0) \quad \text{and} \quad \lim_{s \rightarrow +\infty} (\nu(s), \eta(s)) = (h_3(v_-), 0).$$

A heteroclinic orbit cannot be found for the modified MS model (single equilibrium point). In the sequel we are going to focus on the traveling waves for the MS model only.

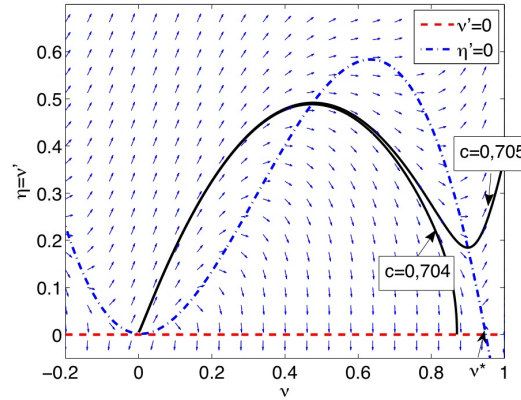
The existence of a heteroclinic orbit depends on f . In fact, the local stability of an equilibrium point depends on the eigenvalues of the Jacobian matrix of the right hand side of (2.6.1) evaluated at equilibrium points as long as no eigenvalue is null (see [19] and [80]). The Jacobian matrix is

$$J(\nu, \eta) = \begin{pmatrix} 0 & 1 \\ \frac{1}{N} \frac{\partial f(\nu, v_-)}{\partial \nu} & \frac{c}{N} \end{pmatrix}.$$

Computing the eigenvalues of $J(0, 0)$ for $c \in [0, 1]$ (note that this remains true for all $c > 0$), one finds that $(0, 0)$ is a saddle point (see figure 2.19). The equilibrium $(\nu_2^*, 0)$ is either an unstable focus (eigenvalues with non zero imaginary parts and positive real parts) or an unstable node. The transition between the two states of



(a) MS ionic model: 3 equilibrium points $(\nu_1^* = 0, 0)$, $(\nu_2^* = h_2(v_-), 0)$ and $(\nu_3^* = h_3(v_-), 0)$ depending on v_- .



(b) Modified MS ionic model with $a = 0.02$.

Figure 2.18: Phase planes for both MS and modified MS models. The equilibrium points in the phase I (see on the $\nu - axis$) are denoted $\nu_{1,2,3}^*$ on figure a) and ν^* on figure b). The solutions plotted for both models use the physiological parameters indicated in the second column of the table 2.3 together with the dimensioning parameters $L = 0.001$ m and $T = 0.001$ s, i.e. with $N = 0.10212$. The nullclines and the vector field are for $v_- = 0.99$. Solutions for the indicated values of c are plotted in black. The nullclines and the vector fields vary with c but as c varies only slightly, they appear to be superposed.

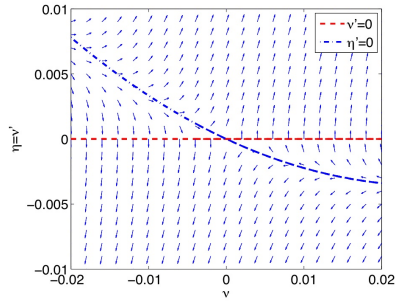
stability depends on where the wave starts in the phase plane (depends on v_-). The eigenvalues are plotted in figure 2.19(d), showing clearly the transition. It looks like a bifurcation but it is not because of the absence stability change. The value of the speed at which the transition occurs depends on v_- (see figure 2.20). The third equilibrium $(\nu_3^*, 0)$ is a saddle point. We are interested in finding a heteroclinic orbit between the equilibrium points $(\nu_1^*, 0)$ and $(\nu_3^*, 0)$.

In [91] traveling waves are studied for a scalar (monostable and bistable) equation of the form:

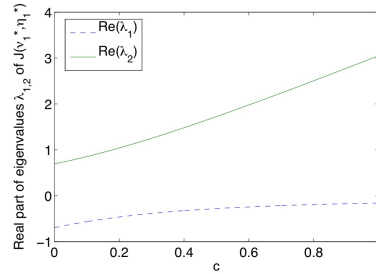
$$\frac{\partial u}{\partial t} = \frac{\partial^2 u}{\partial x^2} + F(u).$$

A key criteria for uniqueness of a heteroclinic orbit relies on the *monotonicity* of the trajectory[91]. Let us show that the asymptotic wave is monotonous, provided the value of v_- is fixed. First of all, the last equation is general enough so that it applies exactly in our case, where $F(u) = f(u, v_-)$ and $N = 1$ can be obtained without loss of generality as long as the domain and the duration of the simulation are rescaled. Both $(\nu_1^*, 0)$ and $(\nu_3^*, 0)$ are saddle points. For the upstroke to be monotonous, the heteroclinic orbit connecting $(\nu_1^*, 0)$ to $(\nu_3^*, 0)$ has to stay in the half-plane $\nu' = \eta \geq 0$. In this half-plane and for $u \in [\nu_1^*, \nu_3^*]$ an unstable manifold crosses ν_1^* and a stable manifold crosses ν_3^* . In fact, $f(\nu, v_-) \geq 0$ in this region, suggesting a global behavior for this heteroclinic orbit. From figure 2.21 the possible behaviors of trajectories in the phase plane can be explained for various speeds c , at a given $v_- > 4\tau_{in}/\tau_{out}$ for definiteness of ν_3^* . We are going to show that non-monotonous orbits starting at ν_1^* and reaching ν_3^* are impossible. As a consequence, the orbit is unique for a fixed v_- .

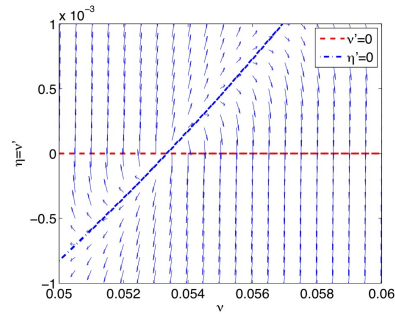
Let us suppose that one has a solution with an initial condition in the neighborhood of ν_1^* in the half-plane $\nu' \geq 0$. Suppose also that the speed $c < c^*$ is such that the solution crosses $\nu' = 0$ from above between the points $(\nu_2^*, 0)$ and $(\nu_3^*, 0)$ (see figure 2.21(a)). In other words, the solution misses the point $(\nu_3^*, 0)$ (like the solution for $c = 0.634$ in the figure 2.18, the kick given by c is not enough to reach $(\nu_3^*, 0)$).



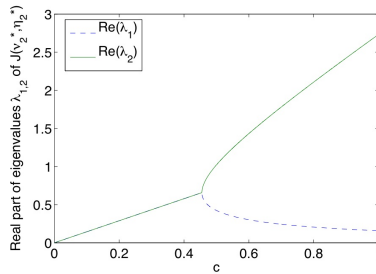
(a) Vector field around (ν_1^*, η_1^*) , a saddle point. $c = 0.6$.



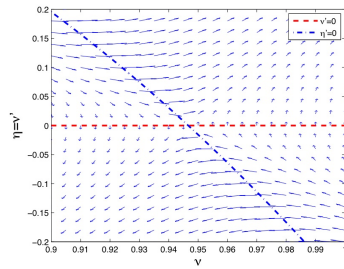
(b) Eigenvalues of $J(\nu_1^*, \eta_1^*)$ as a function of the speed c .



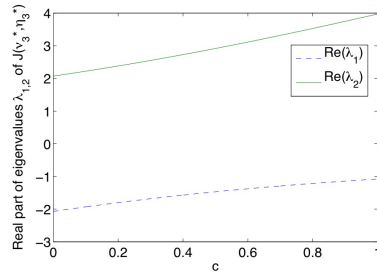
(c) Vector field around (ν_2^*, η_2^*) , an unstable focus. $c = 0.6$.



(d) Real part of the eigenvalues of $J(\nu_2^*, \eta_2^*)$ as a function of the speed c .



(e) Vector field around (ν_3^*, η_3^*) , a saddle point. $c = 0.6$.



(f) Eigenvalues of $J(\nu_3^*, \eta_3^*)$ as a function of the speed c .

Figure 2.19: Real part of the eigenvalues of the equilibrium points in the phase I for the MS ionic model. We take $c = 0.6$ because the dimensional speed (in m/s) is already close to the physiological speed of the depolarization front in the ventricle (around 0.5 m/s). An isolated traveling wave is considered so $v_- = 1$.

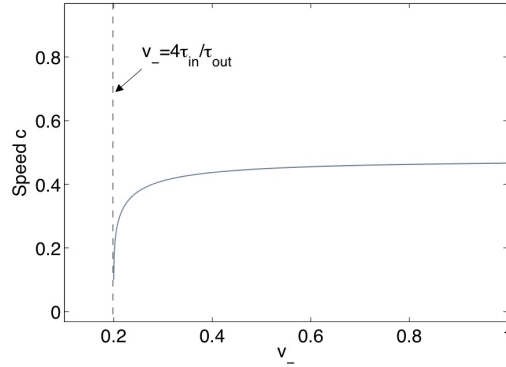
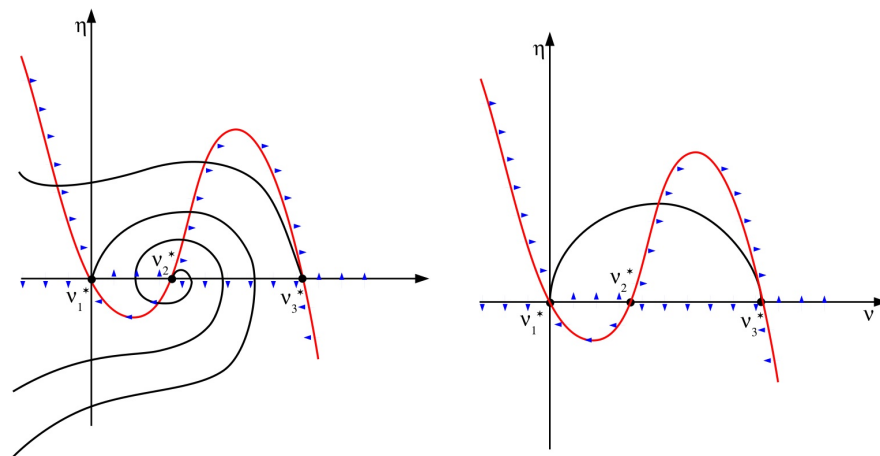


Figure 2.20: Value of the speed where there is a transition from an unstable focus to an unstable node. The threshold $4\tau_{in}/\tau_{out}$ for the existence of the transition comes from the threshold for the existence of the third equilibrium point $\nu_3^* = h_3(v_-) = 1/2 + 1/2\sqrt{1 - 4\tau_{in}/\tau_{out}v_-}$.

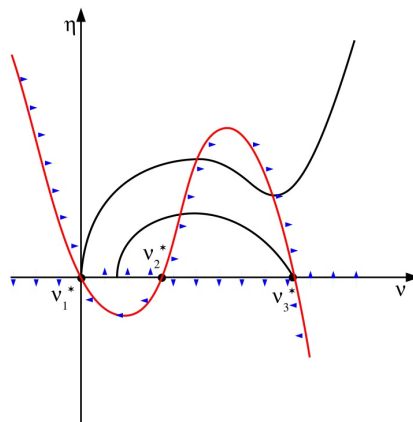
We wonder if it could reach $(\nu_3^*, 0)$ in another way than directly and monotonically from $(\nu_1^*, 0)$. It means that ν would need to increase again or equivalently that the solution returns to the half-plane $\nu' \geq 0$.

When the solution is in the half-plane $\nu' < 0$, the only leak possible to reach again the half-plane $\nu' \geq 0$ would be between the points $(\nu_1^*, 0)$ and $(\nu_2^*, 0)$. The interval $[\nu_1^*, \nu_2^*]$ is actually the only region on the ν -axis where the vector field points upward. If it does cross again $\nu' = 0$ between the points $(\nu_1^*, 0)$ and $(\nu_2^*, 0)$, it is impossible that the solution hits $(\nu_3^*, 0)$ without crossing its own trajectory, which is forbidden by the uniqueness of the solution. Hence the non-monotonous orbit joining ν_1 and ν_3 does not exist. In conclusion the heteroclinic orbit has to reach ν_3^* without leaving the half-plane $\nu' \geq 0$.

We emphasize that in equation (2.4.9), as well as in the equations (2.6.1), the speed c must be properly set say to c^* so that a traveling wave exists, which amounts to the existence of a heteroclinic connection for these ODEs. The monotonous orbits coming from $(\nu_1^*, 0)$ either reach $(\nu_3^*, 0)$ or go to the infinity (like the solution for $c > c^*$ in the figure 2.21(c)). By monotonicity, the heteroclinic orbit is attained in a unique way referring to a specific speed c^* . Remark that this uniqueness is achieved



(a) $c < c^*$, the orbit starting at ν_1^* misses ν_3^* . (b) $c = c^*$, the orbit starting at ν_1^* reaches ν_3^* .



(c) $c > c^*$, the orbit starting at ν_1^* passes ν_3^* .

Figure 2.21: Schematic representation of what happens when the speed is augmented progressively. In order to see details that are not distinguishable in the real phase space (figure 2.18), this is a modified version of the real phase space, .

only for a fixed value of v_- . Recall that section 2.4.4 concerns the computation of that unique and bounded speed.

Chapter 3

Influence of discretization

This chapter deals with the important question of choosing the right temporal/spatial discretization when modeling phenomena in cardiac electrophysiology. There are generally two effects that are related to a coarse discretization: numerical instability and errors affecting the action potential wave form and speed propagation. This chapter analyzes both phenomena.

Section 3.1 discusses the problem of numerical stability, starting from a standard finite element formulation of the bidomain model. The goal of this section is to provide a ground for choosing the time step and mesh size on a quantitative basis, i.e. from a criteria directly based on the model parameters. Section 3.2 describes how the discretization affects the action potential shape and propagation in one dimension.

3.1 Stability of the time integration scheme

In chapter 2 an asymptotic analysis is made in order to find the parameters of the MS model coupled with a 1D monodomain model for almost any desired AP (realistic or not). Because of very small scale phenomena, time-stepping schemes for solving these equations are numerically unstable unless the time step is taken to be extremely

small. The aim of this section is to show how critical is the choice of the time step with respect to the space discretization and model parameters to preserve stability. Based on the arguments developed in [30], [14] and [13], stability conditions depending on all possible parameters are derived for the Gear and the forward Euler time-stepping schemes (see section 1.3.3 for definitions) for the FHN and the MS ionic models.

First, the bidomain equations in the isolated heart (equations (1.2.1)-(1.2.5)) are discretized in space with a finite element method. Assuming that the solution is smooth enough, the variational formulation of these equations is

$$\begin{aligned} \int_H \frac{\partial u}{\partial t} \phi_u + \int_H N_i \nabla(u + u_e) \cdot \nabla \phi_u + \int_H f(u, v) \phi_u &= \int_{\partial H} N_i \nabla(u + u_e) \cdot n_H \phi_u = 0 \\ \int_H \sigma_i \nabla u \cdot \nabla \phi_w + \int_H (\sigma_i + \sigma_e) \nabla u_e \cdot \nabla \phi_w &= \int_{\partial H} (\sigma_i \nabla u + (\sigma_i + \sigma_e) \nabla u_e) \cdot n_H \phi_w = 0 \\ \int_H \frac{\partial v}{\partial t} \phi_v + \int_H g(u, v) \phi_v &= 0, \end{aligned}$$

for all ϕ_u, ϕ_v, ϕ_w in appropriate test functions spaces, resp. $H^1(H), L^2(H), H^1(H)$, and with $N_i = \sigma_i T / (C_m \chi L^2)$. The first two equations have null right hand side terms because of the homogeneous Neumann boundary conditions in the isolated heart.

Provided the test functions $\phi_u = u(t), \phi_w = u_e(t)$ and $\phi_v = v(t)$ in these three variational equations, respectively, we have first for the Gear time-stepping scheme that

$$\begin{aligned} \int_H \left[\frac{3u^{n+1} - 4u^n + u^{n-1}}{2\Delta t} \right] u^{n+1} &= - \int_H f(u^{n+1}, v^{n+1}) u^{n+1} \\ &\quad - \int_H N_i \nabla(u^{n+1} + u_e^{n+1}) \cdot \nabla u^{n+1} \end{aligned} \quad (3.1.1)$$

$$\int_H \sigma_i \nabla u^{n+1} \cdot \nabla u_e^{n+1} + \int_H (\sigma_i + \sigma_e) \nabla u_e^{n+1} \cdot \nabla u_e^{n+1} = 0 \quad (3.1.2)$$

$$\int_H \left[\frac{3v^{n+1} - 4v^n + v^{n-1}}{2\Delta t} \right] v^{n+1} = \int_H g(u^{n+1}, v^{n+1}) v^{n+1} \quad (3.1.3)$$

For the sake of self-consistency the most relevant theorems and steps of the

stability analysis are going to be integrally transcribed from [30]. Using the following lower bound for the diffusive terms

$$\int_{\Omega} (\sigma_i \nabla (u + u_e)) \cdot \nabla (u + u_e) + \int_{\Omega} (\sigma_e \nabla u_e) \cdot \nabla u_e \geq m_i |u + u_e|_1^2 + m_e |u_e|_1^2 \geq \bar{m} (|u|_1^2 + |u_e|_1^2)$$

with $m_{i,e} = \inf_{\Omega} \{ \sigma_{(i,e),l}, \sigma_{(i,e),n}, \sigma_{(i,e),t} \}$ and

$$\bar{m} = \frac{1}{2} \left(2m_i + m_e - \sqrt{4m_i^2 + m_e^2} \right),$$

as well as the identity

$$2(3a^{n+1} - 4a^n + a^{n-1})a^{n+1} = (a^{n+1})^2 + (2a^{n+1} - a^n)^2 - (a^n)^2 - (2a^n - a^{n-1})^2 + (\delta_{tt}a^{n+1})^2$$

with $\delta_{tt}a^{n+1} = a^{n+1} - 2a^n + a^{n-1}$, one can get the following inequality by summing the equations (3.1.1)-(3.1.3)

$$\begin{aligned} & \|u^{n+1}\|_0^2 + \|2u^{n+1} - u^n\|_0^2 - \|u^n\|_0^2 - \|2u^n - u^{n-1}\|_0^2 + \|v^{n+1}\|_0^2 \\ & + \|2v^{n+1} - v^n\|_0^2 - \|v^n\|_0^2 - \|2v^n - v^{n-1}\|_0^2 + 4\Delta t \bar{m} (|u^{n+1}|_1^2 + |u_e^{n+1}|_1^2) \\ & \leq -4\Delta t \int_{\Omega} f(u^{n+1}, v^{n+1})u^{n+1} + 4\Delta t \int_{\Omega} g(u^{n+1}, v^{n+1})v^{n+1}. \end{aligned} \quad (3.1.4)$$

Remark 12 *The value of \bar{m} is obtained considering that $m_i|x + y|^2 + m_e|y|^2 = m_i|x|^2 + 2m_i\langle x, y \rangle + (m_i + m_e)|y|^2$ is a quadratic form that can be written in the following way*

$$\begin{pmatrix} x & y \end{pmatrix} \begin{pmatrix} m_i & m_i \\ m_i & m_i + m_e \end{pmatrix} \begin{pmatrix} x \\ y \end{pmatrix} \geq \bar{m}(|x|^2 + |y|^2),$$

with $\bar{m} > 0$ the smallest eigenvalue of the above matrix.

The crucial step (useful for any implicit time integration scheme) is getting a

bound for the ionic terms:

$$\begin{aligned}
-\int_{\Omega} f(u, v)u + \int_{\Omega} g(u, v)v &= f_0 \int_{\Omega} (-u^4 + (1 + \alpha)u^3 - \alpha u^2) + \int_{\Omega} (\epsilon\gamma - 1)uv - \epsilon\beta v^2 \\
&\leq f_0 \int_{\Omega} (-au^4 + bu^2) - f_0\alpha\|u\|_0^2 + \frac{|\epsilon\gamma - 1|}{2k}\|u\|_0^2 + \frac{|\epsilon\gamma - 1|}{2}k\|v\|_0^2 - \epsilon\beta\|v\|_0^2 \\
&\leq C_{FHN, Gear} (\|u\|_0^2 + \|v\|_0^2).
\end{aligned} \tag{3.1.5}$$

where

$$C_{FHN, Gear} = \inf_{\substack{b \geq (1+\alpha)^2/4 \\ k > 0}} \max \left\{ f_0(b - \alpha) + \frac{|\epsilon\gamma - 1|}{2k}, \frac{|\epsilon\gamma - 1|k}{2} - \epsilon\beta \right\}.$$

Note that for $k > 0$, we have $xy \leq x^2/2k + y^2k/2$ for $x, y \in \mathbb{R}$. Also, we have used that

$$u^4 - (1 + \alpha)u^3 \geq au^4 - bu^2 \text{ if } a \leq 1 - (1 + \alpha)^2/4b \text{ and } b \geq (1 + \alpha)^2/4.$$

Remark that taking the infimum allows to get a constant $C_{FHN, Gear}$ independent of b and k . The requirement that $C_{FHN, Gear}$ be positive is satisfied as the infimum is taken over two quantities with one always positive. In fact, by analyzing the phase space one can show that $f_0(b - \alpha) + |\epsilon\gamma - 1|/2k$ is bounded uniformly away from zero. First of all, we have $\epsilon\gamma = 1$ in the worst case, and $\alpha > 0$ for having the equilibrium state at $(u, v) = (0, 0)$. In addition, the u -nullcline has a local maximum (u^*, v^*) located between two zeros $u = \alpha$ and $u = 1$, hence $\alpha < u^* < 1$. Finally, the value of f_0 can be viewed as a time scale that can be fixed to a strictly positive value without loss of generality.

The equation (3.1.4) is combined with (3.1.5) and the sum of the resulting in-

equalities when n varies from 0 to $m - 1$ gives

$$\begin{aligned} & (1 - 4\Delta t C_{FHN,Gear}) [\|u^m\|_0^2 + \|v^m\|_0^2] + 4\Delta t \bar{m} \sum_{n=1}^m (|u^n|_1^2 + |u_e^n|_1^2) \\ & \leq 2 (\|u^0\|_0^2 + \|v^0\|_0^2) + 4\Delta t C_{FHN,Gear} \sum_{n=0}^{m-1} (\|u^n\|_0^2 + \|v^n\|_0^2), \end{aligned} \quad (3.1.6)$$

where m is an integer between 1 and M , the index of the final time step. Choosing the time step such that $\Delta t < \frac{1}{4C_{FHN,Gear}}$, the following estimate is derived

$$\|u^m\|_0^2 + \|v^m\|_0^2 \leq \frac{2}{1 - 4\Delta t C_{FHN,Gear}} (\|u^0\|_0^2 + \|v^0\|_0^2) + \frac{4\Delta t C_{FHN,Gear}}{1 - 4\Delta t C_{FHN,Gear}} \sum_{n=0}^{m-1} (\|u^n\|_0^2 + \|v^n\|_0^2) \quad (3.1.7)$$

The next step uses the following discrete version of the Gronwall lemma (see for example [19]).

Lemma 3.1.1 (Discrete Gronwall) *Let $\{k_n\}$ and $\{p_n\}$ be to sequences of non-negative real numbers, φ^m a discrete real-valued function and g_0 a non-negative real number such that $\varphi^0 \leq g_0$. Also suppose that $\forall m \geq 1$,*

$$\varphi^m \leq g_0 + \sum_{n=0}^{m-1} p_n + \sum_{n=0}^{m-1} k_n \varphi^n.$$

Then the following estimate is true

$$\varphi^m \leq \left(g_0 + \sum_{n=0}^{m-1} p_n \right) e^{\sum_{n=0}^{m-1} k_n}.$$

■

The application of lemma 3.1.1 to equation (3.1.7) yields for any $n = 1, \dots, M$

$$\|u^n\|_0^2 + \|v^n\|_0^2 \leq \frac{2}{1 - 4\Delta t C_{FHN,Gear}} (\|u^0\|_0^2 + \|v^0\|_0^2) e^{4t_n C_{FHN,Gear}/(1-4\Delta t C_{FHN,Gear})}.$$

The (non-dimensional) stability condition for the Gear time-stepping scheme (depending only on the parameters of the problem) is then simply given by $\Delta t < \frac{1}{4C_{FHN,Gear}}$.

With the FHN model's parameters given in section 2.2, the stability condition is $\Delta t < 0.5946$ while it is $\Delta t \lesssim 5$ numerically. The energy method used above gives a critical time step that is sufficient for stability, while larger time steps can often be used in numerical simulations. Moreover the critical time step for stability is difficult to identify in practice as higher order time-stepping schemes often give rise to non-monotone solutions for time steps just below the critical value. This loss of monotonicity is seen as oscillations near regions with sharp gradients, such as the depolarization front, which oscillations do not grow with time and eventually disappear at larger times. This loss of monotonicity may easily be confused with an unstable numerical solution that eventually blows up after a finite but large number of time steps.

From [13] and [26], a physiological stability condition can be derived for the MS ionic model presented in the section 2.2.3. Defining $\Omega_g = \{x \in \Omega | u(x) \geq u_{gate}\}$ and rewriting for convenience (similarly as in equation (2.2.4)) the source term $g(u, v)$ as

$$g(u, v) = \frac{1}{\tau_u} [(1 - s_\infty(u, u_{gate})) (1 - v) - s_\infty(u, u_{gate})v]$$

with

$$\tau_u = \tau_{open} + (\tau_{close} - \tau_{open})s_\infty(u, u_{gate})$$

and

$$s_\infty(u, u_{gate}) = \frac{1}{2}(1 + \text{sgn}(u - u_{gate})),$$

one gets the following bound for the ionic terms (see also equation (2.2.3) for the source term $f(u, v)$)

$$\begin{aligned} & - \int_{\Omega} f(u, v)u + \int_{\Omega} g(u, v)v = \dots \\ = & \int_{\Omega} \frac{v}{\tilde{\tau}_{in}}(-u^4 + u^3) - \frac{1}{\tilde{\tau}_{out}}u^2 + \int_{\Omega} \frac{1}{\tilde{\tau}_u} [(1 - s_\infty(u, u_{gate}))(v - v^2) - s_\infty(u, u_{gate})v^2] \leq \dots \\ & \leq \int_{\Omega} \frac{v}{\tilde{\tau}_{in}}(-au^4 + bu^2) - \frac{1}{\tilde{\tau}_{out}}u^2 + \frac{1}{\tilde{\tau}_{open}} \int_{\Omega \setminus \Omega_g} (v - v^2) - \frac{1}{\tilde{\tau}_{close}} \int_{\Omega_g} v^2 \leq \dots \\ & \leq \left(\frac{v_{max}}{\tilde{\tau}_{in}}b - \frac{1}{\tilde{\tau}_{out}} \right) \|u\|_{L^2(\Omega)}^2 + \frac{1}{\tilde{\tau}_{open}} \int_{\Omega} (v + v^2) + \frac{1}{\tilde{\tau}_{close}} \int_{\Omega} v^2 \leq \dots \\ & \leq \left(\frac{v_{max}}{\tilde{\tau}_{in}}b - \frac{1}{\tilde{\tau}_{out}} \right) \|u\|_{L^2(\Omega)}^2 + \frac{1}{\tilde{\tau}_{open}} \|v\|_{L^1(\Omega)} + \left(\frac{1}{\tilde{\tau}_{open}} + \frac{1}{\tilde{\tau}_{close}} \right) \|v\|_{L^2(\Omega)}^2 \leq \dots \\ & \leq \left(\frac{v_{max}}{\tilde{\tau}_{in}}b - \frac{1}{\tilde{\tau}_{out}} \right) \|u\|_{L^2(\Omega)}^2 + \frac{1}{2k\tilde{\tau}_{open}} |\Omega| + \left(\frac{k}{2\tilde{\tau}_{open}} + \frac{1}{\tilde{\tau}_{open}} + \frac{1}{\tilde{\tau}_{close}} \right) \|v\|_{L^2(\Omega)}^2 = \dots \end{aligned}$$

with $a > 0$ and $b > 1/4$. It can be proved [13] that $v_{max} = 1$. Remark that the last inequality is obtained with the Cauchy-Schwarz inequality, followed with the application of the identity $xy \leq x^2/2k + y^2k/2$ that holds for $x, y \in \mathbb{R}$ and any $k > 0$. Hence

$$- \int_{\Omega} f(u, v)u + \int_{\Omega} g(u, v)v \leq \frac{1}{2k\tilde{\tau}_{open}} |\Omega| + C_{MS,Gear} (\|u\|_0^2 + \|v\|_0^2),$$

where the stability constant is

$$C_{MS,Gear} = \inf_{\substack{b > 1/4 \\ k > 0}} \max \left\{ \frac{v_{max}}{\tilde{\tau}_{in}}b - \frac{1}{\tilde{\tau}_{out}}, \frac{1}{\tilde{\tau}_{open}} \left(\frac{k}{2} + 1 \right) + \frac{1}{\tilde{\tau}_{close}} \right\}.$$

The term $|\Omega|/(2k\tilde{\tau}_{open})$ is kept aside as it is taken into account in the terms p_n in the

Gronwall lemma, which gives

$$\|u^n\|_0^2 + \|v^n\|_0^2 \leq \frac{1}{1 - 4\Delta t C_{MS,Gear}} \left[2 (\|u^0\|_0^2 + \|v^0\|_0^2) + 4 \frac{t_n k |\Omega|}{2\tau_{open}} \right] e^{4t_n C_{MS,Gear}/(1-4\Delta t C_{MS,Gear})}.$$

Remark that as $\tilde{\tau}_{in,out}$ are small time scales and $\tilde{\tau}_{open,close}$ are large scale. In addition, if k is taken small enough, the stability constant is given by

$$C_{MS,Gear} = \frac{v_{max}}{4\tilde{\tau}_{in}} - \frac{1}{\tilde{\tau}_{out}} > 0,$$

meaning that the stability condition $\Delta t < 1/(4C_{MS,Gear})$ is controlled by the smallest time scales of the ionic model. We recall that the existence of two distinct nullcline branches in the phase space requires that $1/4\tau_{in} - 1/\tau_{out} > 0$ (see equation 2.4.3). This explains why $C_{MS,Gear} > 0$ provided $v_{max} = 1$. Finally, the condition on the values of k

$$0 < k < 2 \left[\tau_{open} \left(\frac{1}{4\tau_{in}} - \frac{1}{\tau_{out}} - \frac{1}{\tau_{close}} \right) - 1 \right]$$

only imposes a gap between small scales and large scales.

Recalling the following asymptotic dependences (see equations (2.4.15) and (2.4.23)),

$$T_{up} \simeq \hat{T}_{up}(\tau_{in}, \tau_{out})$$

$$T_{down} \simeq \hat{T}_{down}(\tau_{out})$$

this can also be viewed as a stability condition depending on the AP upstroke and downstroke durations. With parameters given in section 2.2.3 and also in Table 2.3 with Adim3 the stability condition is $\Delta t < 0.25$ (ms). The stability condition has not been fully explored numerically but at $\Delta t = 0.5$ (ms), the solution is still stable.

It is proved in [30] that the forward Euler scheme has a stability constant that is independent of the ionic source terms. For completeness, we repeat the result which holds for any ionic model.

If a forward Euler scheme is used, the stability criteria is

$$\Delta t \leq C_{FE} h^2$$

where

$$C_{FE} = \frac{2\chi C_m L^2 \bar{m}}{TC^2 M_i \left(1 + \frac{M_i}{(m_i + m_e)}\right)^2} = \frac{2\bar{m}}{N_{sup,i} C^2 \left(1 + \frac{M_i}{(m_i + m_e)}\right)^2},$$

with $M_{i,e} = \sup_{\Omega} \{\sigma_{(i,e),l}, \sigma_{(i,e),n}, \sigma_{(i,e),t}\}$, $N_{sup,i} = \frac{TM_i}{C_m \chi L^2}$, $C = 2\sqrt{3}$ in 1D, $C = 6\sqrt{2}$ in 2D. The inverse inequality C.0.3 presented in Appendix C is used.

In conclusion, the ionic model itself and the non dimensional number N affects the stability of the time-stepping scheme. The explicit dependences on all implied parameters are given and this reflects the fact that the sharpness of the upstroke as well as the speed of the wave are of first importance when a simulation is performed. Precisely, when an implicit Gear time-stepping scheme is used with the MS model the stability constant depends only on the parameters controlling the small time scales of the AP, i.e. the upstroke and the downstroke durations. In contrast with the implicit Gear time-stepping scheme, the forward Euler time-stepping scheme has a stability constant which depends only on the non dimensional number N , a criteria in relation with the propagation speed of the AP.

In a physiological simulation the upstroke can be very steep and the propagation speed very high, depending on which tissue is simulated. These stability conditions are very useful to assess discretization requirements and obtain a numerical solution with the least computational resources possible. A time step near the critical value for stability is usually not sufficient for obtaining an accurate solution. In some situations, getting a solution is a first step which is not necessarily easy when using

new sets of parameters. Having these stability conditions ensures to have a solution, and then an analysis of the convergence of the solution with respect to the time and space discretization can be done. A precise numerical solution can finally be obtained for the new set of parameters.

3.2 General influence of the time/space discretization

The numerical results presented in [30] (with the bidomain model and the FitzHugh-Nagumo ionic model) clearly show that one cannot reliably compute waves if the spatial grid is too coarse and the time steps are too large, irrespective of the time-stepping scheme used. This means that to test the parameters of any ionic model i.e. to see the effect of their variations on the solution, the time and space discretizations have to be such that the solution is converged. Furthermore, it is said, again in [30], that higher order methods are necessary to solve the bidomain model, second order methods being in fact the optimal choice in terms of accuracy and computational cost. Remark that higher order methods are not the optimal choice in the special case where they are used with linear or quadratic finite elements. Many aspects of the discretization are thus important, from the choice of the discretization scheme with its associated order of convergence, to the number of spatial and temporal degrees of freedom.

This section presents unidimensional numerical simulations for the FHN and the MS models in order to evaluate the effects of the discretization. The goal is to see how the use of the MS model, set so that scales of the AP are properly represented, influence the numerical accuracy in comparison to the FHN model that was used in [30] to do such a numerical study. For the MS model (equations (2.2.3) and (2.2.4)), the simulations are done with the dimensional scaling Adim3 presented in the table

2.3. The domain is $l_{max} = 600$ mm-long, and the final time is $t_{max} = 1000$ ms. The domain is larger than a human heart (around 70 mm) and the simulation longer than a heart beat (around 600 ms) to see the propagation of the wave over a large time. The MS model parameters are those presented in Table 2.4 and for the monodomain model, we take the nondimensional number $N = 0.3$.

For the FHN model (equations (2.2.1) and (2.2.2)), no dimensional scaling is specified and the monodomain model with $N = 1$ together with the parameters given in section 2.2.1 are used. The domain is of $l_{max} = 200$ space units, and the final time is of $t_{max} = 500$ time units.

Note that the following results hold also for the unidimensional bidomain model. In 1D, the monodomain model with the harmonic approximation of the conductivity tensor, i.e. $\sigma_{harm} = (\sigma_i^{-1} + \sigma_e^{-1})^{-1}$, gives a system of PDEs which is equivalent to the bidomain model (see section 2.4.2). The results for the monodomain model only are presented, but the correspondence with the bidomain numerical solutions has been verified.

The problem consists in finding (u, v) in $[0, l_{max}] \times [0, t_{max}]$ such that

$$\begin{aligned} \frac{\partial u}{\partial t} + f(u, v) &= N_{harm} \frac{\partial^2 u}{\partial x^2}, \\ \frac{\partial v}{\partial t} &= g(u, v, t). \end{aligned}$$

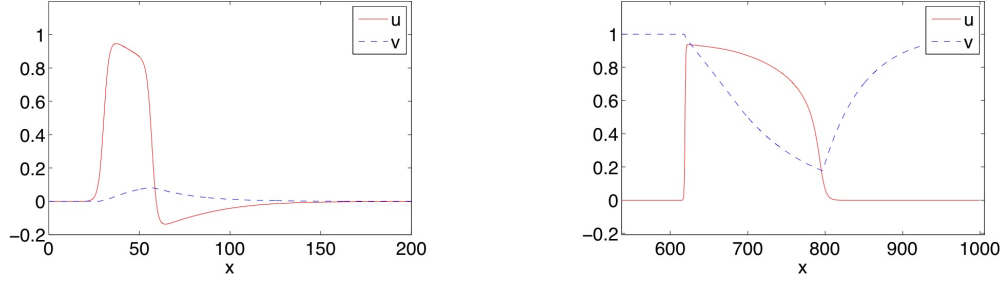
The initial conditions for the MS model are given by

$$u(x, 0) = \begin{cases} 0.8 & \text{for } x \in (0, 0.95l_{max}), \\ 0 & \text{for } x \in [0.95l_{max}, l_{max}), \end{cases}$$

and

$$v(x, 0) = 1 \quad \forall x \in (0, l_{max}).$$

Homogeneous Neumann boundary condition is applied for u . Figure 3.1 shows the spatial profile of the APs for both ionic models.



(a) FHN, Solution at $t=500$ ms. Time step: 0.25 time units, Mesh size: 0.005 space units.

(b) Original MS [56], Solution at $t=500$ ms. Time step: 0.075 ms, Mesh size: 0.0125 mm.

Figure 3.1: Transmembrane potential u and the recovery variable v for the FHN model on $\Omega \times [0, t_{max}] = [0, 200] \times [0, 500]$ and the MS model on $\Omega \times [0, t_{max}] = [0, 1000] \times [0, 1000]$. Remark that the FHN features the hyperpolarization after the wave, contrary to the MS models. The waves move from right to left.

For the time discretization a forward Euler (explicit first order) and a Gear (implicit second order) time integration schemes are used (see section 1.3.3 for definitions). For the space discretization a second order finite difference method is used, which is equivalent in 1D to P_1 finite elements over a uniform grid. With a constant conductivity, the diffusion operator is simply a second derivative discretized as

$$\frac{\partial^2 u}{\partial x^2}(x) \approx \frac{u(x+h) - 2u(x) + u(x-h)}{h^2},$$

where h is the mesh size. For a comparison with the finite element, the variational formulation is presented in section 1.3.3.

For both ionic models, the convergence of the solution with respect to the time and the space discretization is verified. It is already known that many features of the solutions are affected by the discretization. In [69], the influence of the discretization on the speed of the depolarization front is analyzed. Here, the influence on the

excited phase duration T_{AP} (a long time scale) and the upstroke duration T_{up} (short time scale) is also analyzed.

In order to analyze the solutions, four types of isochrons are calculated. The first are the isochrons of depolarization iso_{depol} , which are updated at each time step. iso_{depol} has a value on every degree of freedom in the domain and is defined as the first time the given degrees of freedom x_i is depolarized i.e the transmembrane potential u crosses from below a threshold u_{th} . We compute $iso_{depol}(x_i)$ as follows:

Initialize with $iso_{depol}(x_i, 0) = -1$, and set at time t

$$iso_{depol}(x_i, t) = t \text{ if } u(x_i, t) \geq u_{th} \text{ and } iso_{depol}(x_i, t - \Delta t) < 0. \quad (3.2.1)$$

Here u_{th} was set to 0.13 or -68.75 mV. The value 0.1 is suggested in [56] as the usual experimental way to measure the APD. However, in their own ionic model, they use $u_{gate}=0.13$ as the threshold for the APD (see section 2.2.3). Colli Franzone et al. [37] use 0.2. This threshold is also used for the FHN model.

The three other types of isochrons are iso_{max} , iso_{repol} and iso_{rec} that are defined similarly with $iso_{depol} < iso_{max} < iso_{repol} < iso_{rec}$ and with the thresholds $0.95 \max_{\Omega}(u)$, 0.5 and $0.05 \max_{\Omega}(u)$ for the last three of these, respectively. These thresholds are justified in chapter 2 by the asymptotic analysis of the MS model .

The excited phase duration T_{AP} is calculated at every time step by performing $iso_{repol} - iso_{max}$. We avoid considering the early time steps where the wave is not completely formed and where solution's features are not yet stabilized. The upstroke duration T_{up} is also calculated at every time step by performing $iso_{max} - iso_{depol}$. The speed of the depolarization front c is the inverse of the slope of iso_{depol} for the last time steps. The slope is calculated with a least square fit of an affine function on the last time steps data. Tables 3.1 to 3.4 show how the time and space discretization can affect the solution features T_{up} , T_{AP} and c .

Reference values are presented in table 3.5. For the FHN model, the reference

solution is calculated with 4,000 nodes and 1,000,000 time steps using a forward Euler time-stepping scheme. To give an idea of how the solution is converged, the difference between the two most precise solution (two last rows of Table 3.1) is less than 0.4 % for T_{up} , less than 0.15 % for T_{AP} and less than 0.7 % for c . For the MS model, the reference solution is calculated with 8,000 nodes and 32,000 time steps using a Gear time-stepping scheme. To give an idea of how the solution is converged, the difference between the two most precise solution (Table 3.4) is less than 0.7 % for T_{up} , less than 0.04 % for T_{AP} and less than 0.02 % for c .

Table 3.1: Monodomain model with FHN ionic model and the forward Euler time-stepping scheme: convergence study. The shadowed rows are close to the limit of stability. Reference solution's features are $T_{up,ref} = 29.9$, $T_{AP,ref} = 69.5$ and $c_{ref} = 0.32$ calculated with 4,000 nodes and 1,000,000 time steps.

n_x	n_t	T_{up}	T_{AP}	c
200	1200	28.533221	68.391026	0.317878
200	2,000	28.579392	68.269231	0.319834
200	5,000	28.625503	68.061832	0.321946
200	10,000	28.634564	68.026718	0.322845
200	100,000	28.646577	67.988321	0.323671
200	1,000,000	28.647674	67.984908	0.323772
400	4200	29.214286	68.972026	0.318298
400	10,000	29.232167	68.916540	0.319095
400	100,000	29.243405	68.879829	0.319657
400	1,000,000	29.244638	68.876029	0.319720
800	16200	29.580103	69.277707	0.319299
800	100,000	29.586567	69.236638	0.319745
800	1,000,000	29.587695	69.232934	0.319802
1600	65000	29.768536	69.431666	0.321612
1600	100,000	29.769179	69.429422	0.321715
1600	1,000,000	29.770309	69.425768	0.321775
4000	1,000,000	29.883481	69.528513	0.320456

Table 3.2: Monodomain model with FHN ionic model and the Gear time-stepping scheme: convergence study. The limit of stability is experimentally about $n_t > 40$, or $\Delta t < 12$. Reference solution's features are $T_{up,ref} = 29.9$, $T_{AP,ref} = 69.5$ and $c_{ref} = 0.32$ calculated with 4,000 nodes and 1,000,000 time steps.

n_x	n_t	T_{up}	T_{AP}	c
200	100	30.000000	64.871795	0.312657
200	500	28.702703	67.969231	0.323652
200	1000	28.674497	67.946565	0.322461
200	5000	28.651007	67.982443	0.323911
200	10000	28.648658	67.982061	0.323853
200	100000	28.647886	67.984618	0.323797
400	100	30.000000	70.000000	0.309531
400	500	29.324415	67.737255	0.319453
400	1000	29.261667	68.847909	0.318883
400	5000	29.246179	68.872243	0.319742
400	10000	29.244186	68.875475	0.319766
400	100000	29.244651	68.875760	0.319754
800	100	30.000000	72.142857	0.313340
800	500	29.785075	66.583333	0.319049
800	1000	29.605482	68.246589	0.318946
800	5000	29.588226	69.252372	0.319808
800	10000	29.587811	69.233049	0.319863
800	100000	29.587894	69.232547	0.319819
1600	100	30.000000	68.750000	0.310783
1600	500	29.993103	64.111111	0.321064
1600	1000	29.824888	66.636445	0.320576
1600	5000	29.771310	69.423886	0.321934
1600	10000	29.770813	69.424408	0.321864
1600	100000	29.770431	69.425346	0.321804

Table 3.3: Monodomain model with the original MS ionic model: convergence study with forward Euler time-stepping scheme. The shadowed rows are close to the limit of stability.

n_x	n_t	T_{up}	T_{AP}	c
1000	2800	8.032230	260.118652	0.500255
1000	4000	7.948399	260.269386	0.515709
1000	8000	7.933046	260.361111	0.532357
1000	16000	7.926342	260.395994	0.543236
1000	32000	7.928356	260.412452	0.550199
2000	7800	7.995490	260.875114	0.540193
2000	8000	7.970268	260.900115	0.541443
2000	16000	7.978101	260.917566	0.552278
2000	32000	7.985711	260.923050	0.553882
2000	64000	7.983088	260.931875	0.556807
4000	28000	8.065232	261.116004	0.556341
4000	60000	8.066963	261.121130	0.560039
4000	120000	8.067838	261.123158	0.559651
4000	240000	8.067376	261.124901	0.560555
8000	110000	8.121066	261.204277	0.560166
8000	200000	8.121770	261.205022	0.561118
8000	400000	8.121628	261.205844	0.560930
8000	800000	8.121635	261.206181	0.561807

Table 3.4: Monodomain model with the original MS ionic model: convergence study with Gear time-stepping scheme. The shadowed rows are close to the limit of stability.

n_x	n_t	T_{up}	T_{AP}	c
1000	600	6.656687	262.058824	0.656523
1000	1000	6.636073	261.888252	0.584623
1000	2000	7.823626	260.552395	0.558457
1000	4000	7.911863	260.457326	0.549307
1000	8000	7.912917	260.445537	0.550212
1000	16000	7.914931	260.443835	0.549338
1000	32000	7.919444	260.439911	0.548990
2000	600	6.661836	262.903226	0.664927
2000	1000	6.987469	261.933544	0.590235
2000	2000	7.848862	261.072009	0.565129
2000	4000	7.948389	260.975074	0.558741
2000	8000	7.968084	260.954732	0.557799
2000	16000	7.975964	260.944765	0.560978
2000	32000	7.987162	260.934519	0.560243
4000	600	6.658076	262.988506	0.664674
4000	1000	6.967033	262.060606	0.591367
4000	2000	8.000000	261.375000	0.567278
4000	4000	7.996979	261.195962	0.561705
4000	8000	8.075776	261.119200	0.560944
4000	16000	8.061053	261.131452	0.562256
4000	32000	8.066731	261.126601	0.561865
8000	600	6.662447	263.181818	0.665761
8000	1000	6.666667	262.192308	0.591777
8000	2000	8.000000	261.345420	0.567332
8000	4000	8.000263	261.215900	0.562645
8000	8000	8.105303	261.225033	0.561984
8000	16000	8.117320	261.210756	0.561333
8000	32000	8.121670	261.206815	0.561942

Table 3.5: Features of the converged solution of the ionic models under study.

Ionic Model	T_{up}	T_{AP}	c	L_{up}	L_{AP}
FHN	29.9	69.5	0.320	9.58	22.28
MS	8.1	261.2	0.562	4.55	146.8

General behaviors of the effect of the discretization on the solution features can be extracted. For the FHN ionic model with both the forward Euler and the Gear time-stepping schemes, the solution's features are very stable or very close to their converged values even when the time step is close to the critical value for instability.

For the MS model with the forward Euler scheme, one can observe that for a number of nodes n_x fixed, if the number n_t of time steps is increased, the speed of the depolarization front increases, the upstroke duration slightly decreases and the excited phase duration is stable. One can also observe that if the number n_x of nodes is increased, the speed of the depolarization front increases, the upstroke duration and the excited phase duration slightly increase.

For the MS model with the Gear scheme, one can observe that for a number of nodes n_x fixed, if the number n_t of time steps is increased,

- the speed of the depolarization front c decreases (e.g. from the limit of stability to convergence, c decreases by 5%),
- the upstroke duration T_{up} increases (e.g. from the limit of stability to convergence, T_{up} increases by 12%),
- the upstroke length L_{up} increases (e.g. from the limit of stability to convergence, L_{up} increases by 7%),
- the excited phase duration T_{AP} is stable (e.g. from the limit of stability to convergence, less than 0.4% of variation) and
- the excited phase length L_{AP} decreases (by about 5%).

One can also observe that for a number of time steps n_t fixed, if the number n_x of nodes is increased,

- the speed of the depolarization front c increases,

- the upstroke duration T_{up} increases,
- the upstroke length L_{up} is increases,
- the excited phase duration T_{AP} is stable and
- the excited phase length L_{AP} increases.

Estimate of requirements in 2D and 3D Table 3.6 summarizes the number of nodes required for a simulation with the MS model ionic model for different level of numerical error on the solution. The area of the 2D myocardium (third column) is the area of our 2D realistic model used for numerical simulations in chapter 4. The volume of the 3D myocardium (last column) is taken from 3D echocardiography measurements[48]. The reference solution is calculated in 1D with 8000 nodes and 32000 time steps on a domain of [600 mm]×[1000 ms] using a Gear time-stepping scheme. Finally, the number of nodes is estimated by assuming that the 1D nodes are equally spaced, as well as the 2D and 3D meshes are uniform.

Table 3.6: Number of nodes required on a heart to have the prescribed relative error (1st column to 3rd column) on the upstroke duration, excited phase duration and speed. These results are calculated for simulations of 1000 ms and 8000 time steps with a Gear time-stepping scheme.

Relative error (%) on			Number of nodes suggested			Δt (ms)
T_{up}	T_{AP}	c	1D (10 cm)	2D (48 cm ²)	3D (174 cm ³)	
2.6	0.29	2.1	166	13,300	800,000	0.125
1.9	2.8	2.3	333	53,300	6,500,000	0.125
0.57	0.03	0.18	666	213,300	51,500,000	0.125
18.3	0.26	4.0	166	13,300	800,000	1

Chapter 4

On the convergence of the heart-torso coupling problem using non-body fitted meshes.

4.1 Introduction

The aim of this chapter is to demonstrate numerically the accuracy and the order of convergence of an algorithm solving the heart-torso coupling problem, using a level set description of the domains (see section 1.3.2) and using non-body fitted meshes (see figure 4.1). The goal of choosing this way of tackling the problem is to be able to use realistic geometries coming from segmented medical images (see figure 4.2) while keeping the code implementation as minimal as possible.

In this chapter a diffusion problem with subdomains of different conductivities is first studied in section 4.2. In fact, the last five equations of the heart-torso coupling problem (1.2.6)-(1.2.12) can be viewed as a diffusion problem with discontinuous conductivities. Moreover, this type of problem is well documented in the literature (see section 1.3.3). Numerical methods for dealing with complex geometries and

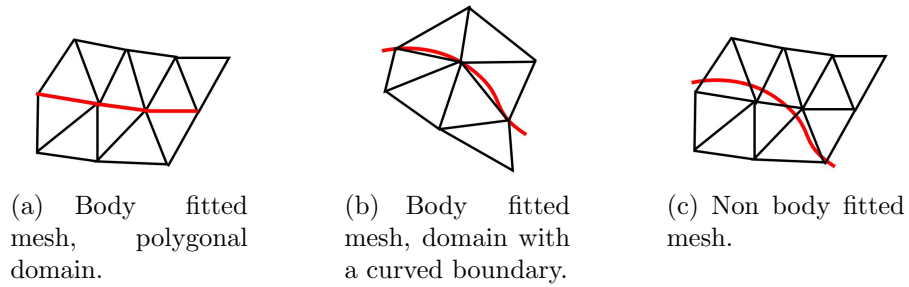


Figure 4.1: Body fitted meshes vs a non body fitted mesh. The internal interface between subdomains is in red.

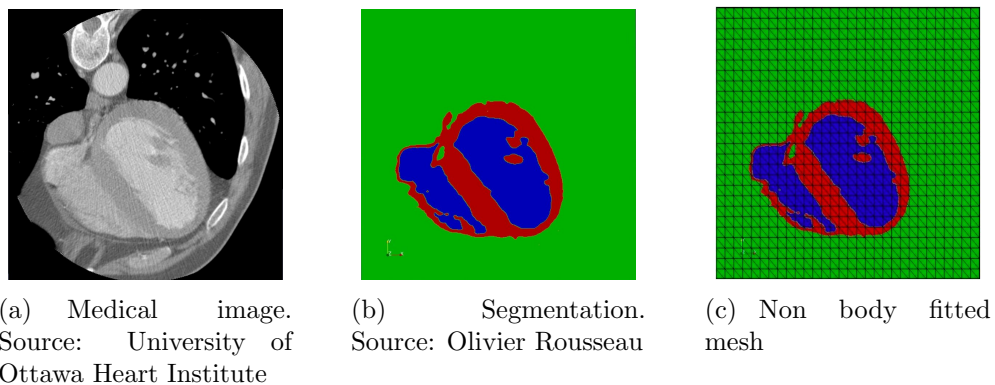


Figure 4.2: Preliminary steps of a realistic simulation with non body fitted mesh. From a medical image (a), a segmentation (b) is done to capture the complicated internal interfaces between the heart and the torso. A simple (non body fitted) mesh (c) is built on the whole image.

jumps in the conductivities are one of our first concern. A review of finite element methods for complex geometries and fixed meshes is done in section 4.2.2 and the analysis of the method is done for a diffusion problem. In section 4.2.3, we describe two original finite element method which use a level set description of the domain and a non-body fitted meshes. We then quantify numerically in section 4.2.4 what is the loss in precision and the loss in the order of convergence for a diffusion problem.

In section 4.3, we quantify what is the loss in precision and the loss in the order of convergence for the heart-torso coupling problem. Finally, the heart-torso coupling problem is solved in section 4.4 using 2D realistic patient data. The method is obviously not optimal in terms of order of convergence (see section 1.3.3). We will see in chapter 5 that mesh adaptation can be used to improve the accuracy of the method.

4.2 Convergence of the diffusion problem

The bidomain model will be reformulated below in the way that there will be a diffusion equation with discontinuous coefficients. We are interested in the order of convergence of the whole heart-torso coupling problem, but studying first the diffusion problem with discontinuous coefficients is very important for instance to see the limitation of the numerical method. The diffusion problem is also well documented in the literature (see for instance [20],[49],[51],[53],[67]).

4.2.1 Definition of the problem

We recall and generalized the Poisson elliptic problem or diffusion problem with interface presented in section 1.3.3: Find u such that:

$$-\nabla \cdot (\sigma^- \nabla u) = f \quad \text{in } \Omega^-, \tag{4.2.1a}$$

$$-\nabla \cdot (\sigma^+ \nabla u) = f \quad \text{in } \Omega^+, \quad (4.2.1b)$$

$$[u]_\Gamma = w, \quad (4.2.1c)$$

$$[\sigma \nabla u \cdot n]_\Gamma = Q, \quad (4.2.1d)$$

$$u = g \quad \text{on } \partial\Omega \quad (4.2.1e)$$

where

$$\sigma = \begin{cases} \sigma^+ & \text{if } x \in \Omega^+, \\ \sigma^- & \text{if } x \in \Omega^- \end{cases}$$

with n the normal outward vector of Ω^- , w is the value of the jump of the solution on Γ and Q is the value of the normal flux jump on Γ .

In reference to the bidomain model, u is the extracellular and extracardiac potentials and σ the conductivity. If Γ separates two different media (like the heart, the torso, the lungs, the heart cavities, etc), the conductivity σ may be discontinuous. Physically the potential is continuous, which could be translated into $[u]_\Gamma = u_\Gamma^+ - u_\Gamma^- = 0$, i.e. the jump of u is null at the interface. If the source term $f(x)$ is continuous, then $[\sigma \nabla u \cdot n]_\Gamma = 0$, that is to say the normal flux $\sigma \nabla u \cdot n$ is continuous, but $\nabla u \cdot n$ is in general discontinuous, because of the jump on σ .

The diffusion problem (1.3.3) with the transmission conditions (1.3.4)-(1.3.5) is a special case of the problem (4.2.1). Note that the weak form of the simplified problem (1.3.3) is written in section 1.3.3. Theoretical results of convergence for the simplified problem (1.3.3) are given in section 1.3.3. We also analyze the order of convergence in practice by solving this problem in section 4.2.4 using the finite element code MEF++ [2]. The problem (4.2.1) is used in section 4.2.2 for a review of existing finite element methods with internal interfaces.

4.2.2 Review of finite element methods for problems with internal interfaces and fixed meshes.

This section depicts some finite elements (FE) methods that have all something in common: they can be used for solving problems with discontinuous coefficients and domains with irregular interfaces described with level sets. FE methods with optimal order of convergence are preferable. As there exists many FE methods and variants, optimal or not, the interest will be focussed on four methods applied on the elliptic problem (4.2.1) in Ω .

IIFEM: Immersed-Interface Finite-Element Methods

The method called IIFEM was developed by Z. Li and al. [49, 51, 39] for solving elliptic problems on regular grids with non homogeneous jumps on internal interfaces. The interfaces are allowed to cut the elements of the mesh so that it is a non-body-fitted mesh. With a finite element formulation using level sets, an “extension” function \tilde{w} is built in order to satisfy the non homogeneous jump conditions on the interfaces. With such an extension function jumps on solution and fluxes are removed. An elliptic problem is then obtained with homogeneous jumps on interfaces. This problem is equivalent to the simplified problem (1.3.3). A special finite element basis is built for elements near the interface which provides a way to represent solutions with homogeneous jumps. The resulting linear system is symmetric positive definite. Optimal convergence rates are attained, i.e. similar to those for methods with interfaces passing through the mesh nodes (see section 1.3.3).

Fictitious domain methods

Fictitious domain methods constitute a whole class of methods for efficiently solving problems with complex external boundaries. The first step consists in embedding the domain with a complex or moving boundary in a “fictitious” domain with a simple

and fixed boundary, e.g. a square. In a method developed by Glowinski and al.[38] a Lagrange multiplier is used to impose the boundary conditions at the complex boundary. This method allows for solving the problem without having to cut the mesh at the interface.

The problem consists in finding the solution in Ω^- with Dirichlet boundary conditions $u = u_g$ on Γ . The solution u is calculated in all Ω with a mixed variational formulation which imposes transmission conditions at the interface like the Dirichlet boundary conditions on Γ . For the fictitious domain formulation, we define the Lagrangian $\mathcal{L} : V \times H^{-1/2}(\Gamma) \rightarrow \mathbb{R}$ by

$$\mathcal{L}(v, \mu) = \frac{1}{2} \int_{\Omega} \sigma |\nabla v|^2 - \int_{\Omega} f v - \langle \mu, v - u_g \rangle,$$

where $\langle \cdot, \cdot \rangle$ indicates here the duality between $H^{-1/2}(\Gamma)$ and $H^{1/2}(\Gamma)$, and V is an appropriate subspace of $H^1(\Omega)$. The first order optimality condition gives the following saddle-point problem: find $\{u, \chi\} \in V \times H^{-1/2}(\Gamma)$ such that:

$$\begin{aligned} a_{\Omega}(u, v) &= \int_{\Omega} f v + \langle \chi, v \rangle \quad \forall v \in V, \\ \langle \mu, u - u_g \rangle &= 0 \quad \forall \mu \in H^{-1/2}(\Gamma). \end{aligned}$$

In [38] an appropriate choice of finite element spaces is done and the linear system is solved with a preconditioned conjugate gradient method. The convergence of the approximate solution u_h to the solution u is demonstrated for $u_g = 0$.

A non-conforming FE approximation with a Lagrange multiplier

This method was developed by Peichl and Touzani [67] for the resolution of the simplified elliptic problem (1.3.3) with discontinuous coefficients and homogeneous jumps (problem (4.2.1) with $w = 0$ and $Q = 0$). This method is designed to solve more elaborate problems like time dependent problems on fixed meshes, e.g. where the interface

Γ moves, and nonlinear problems. In fact, this finite element method starts from a fixed cartesian grid with a complex interface intersecting the mesh edges. A preliminary step consists in cutting the interface elements in three sub-elements. Then the linear finite element basis functions on the original mesh is enriched with linear basis functions on the sub-elements. The added degrees of freedom have local supports and then yield a non-conforming finite element method. A Lagrange multiplier removes this non-conformity and ensures an optimal convergence rate, if the exact solution u and the mesh satisfy certain regularity conditions. The following saddle point problem indicates that the continuity of u across the edges e of \mathcal{E}_h , which designates the set of all the edges of the sub-elements, is enforced by a Lagrange multiplier technique.

$$\begin{aligned} \mathcal{A}(u, v) - \mathcal{B}(\chi, v) &= (f, v) \quad \forall v \in V_h, \\ \mathcal{B}(\mu, u) &= 0 \quad \forall \mu \in Q_h. \end{aligned}$$

where

$$\begin{aligned} \mathcal{A}(u, v) &= \int \sigma_h \nabla u \cdot \nabla v, \\ \mathcal{B}(v, \mu) &= \sum_{e \in \mathcal{E}_h} \int_e \mu [v] \end{aligned}$$

and where σ_h is the piecewise linear interpolant of σ on the set of all the elements and sub-elements obtained from cutting at the interface, V_h is the space with the enriched basis and Q_h is the space of the Lagrange multiplier. Remark that in [67], the Lagrange multiplier is taken constant along the edges $e \in \mathcal{E}_h$ and the system is solved with iterative process like the Uzawa method. In such situations, each iteration step consists in solving an elliptic problem with a given χ . In this method, the interface supports the added degrees of freedom but the Lagrange multipliers are defined on the edges intersected by the interface and thus serve to compensate the nonconformity of the finite element space rather than enforcing interface conditions,

which are being naturally ensured by the variational formulation.

Regularizing methods for discontinuous coefficients

A simple approach is to smoothen jumps on the coefficient σ . The expression of the interface through a level set description makes the regularizing methods simpler for 2D and 3D problems[65, 64]. The solutions are also smoothen at the interface. This method has been implemented for finite difference simulations as well as for finite element simulations (see for instance [82] and [34]).

An other method used with finite difference methods is the harmonic average technique[50]. This method is of second order for particular problems in 1D, but generally is not for 2D and 3D problems. In order to guarantee a second order of convergence, it is necessary to precisely compute the integral for the harmonic average. This integral is not necessarily easy to calculate precisely, especially near discontinuities. The second order of convergence may be lost in case of an inaccurate computation of the integral, unless the interface is aligned with the mesh nodes.

4.2.3 Two finite element methods for the use of non body-fitted meshes

A drawback of using finite element methods described in the previous section is that these techniques require elaborate techniques like element cutting, modifying the finite element basis for the set of elements intersected at the interface, or the introduction of a Lagrange multiplier. The choice of the enriched basis having for support the intersected elements, or the choice of the discretization space of the Lagrange multiplier is a delicate issue.

In order to keep the code implementation as minimal as possible, two simple finite element methods are implemented for the use of non-body fitted meshes. Both methods use the same finite element formulation as the one used for body fitted

meshes (section 1.3.3) and the names of the methods refer to the way the conductivity tensor is handled.

By level set

The first method consists in defining the conductivity constant with the use of a level set function. Precisely, if Ω^- is described with a level set function $\varphi(x)$ as it is explained in section 1.3.2 for the domain H , then

$$\sigma(x) = \begin{cases} \sigma^- & \text{for } x \text{ such that } \varphi(x) \leq 0, \\ \sigma^+ & \text{for } x \text{ such that } \varphi(x) > 0. \end{cases} \quad (4.2.2)$$

We recall here the finite element formulation: find u_h in V_h such that

$$a(u_h, \phi_h) = (f, \phi_h), \quad \forall \phi_h \in V_h. \quad (4.2.3)$$

with $a(u_h, \phi) = \int_{\Omega} \sigma \nabla u_h \cdot \nabla \phi$, $(f, \phi_h) = \int_{\Omega} f \phi_h$. Let $(w_k)_{k=1}^M$ be a basis in the space V_h . Then the solution $u_h = \sum_{k=1}^M u_k w_k$ of problem (4.2.3) is such that the coefficients u_k are solutions of the linear system

$$\sum_{k=1}^M a(w_k, w_l) u_k = (f, w_l), \quad 1 \leq l \leq M.$$

In practice, we use Lagrange polynomials for basis functions (see section 1.3.3 for more details) and u_k are nodal values of the approximate solution u_h . The next step consists in computing integrals for evaluating the elementary matrix with entry $A_{lk} = a(w_k, w_l)$. This is done with a n -point Gaussian quadrature

$$\int \sigma \nabla w_k \cdot \nabla w_l = \sum_{i=1}^n \omega_i \sigma(x_i) \nabla w_k(x_i) \cdot \nabla w_l(x_i),$$

where ω_i is a weight associated to the quadrature point x_i . Finally, we use equation (4.2.2) and

$$A_{lk} = \sum_{i|\varphi(x_i)\leq 0} \omega_i \sigma^- \nabla w_k(x_i) \cdot \nabla w_l(x_i) + \sum_{i|\varphi(x_i)>0} \omega_i \sigma^+ \nabla w_k(x_i) \cdot \nabla w_l(x_i).$$

By element

An other simple way to tackle the problem consists in defining Ω^- as the largest set of elements which are completely inside the level set description of Ω^- (figure 4.3).

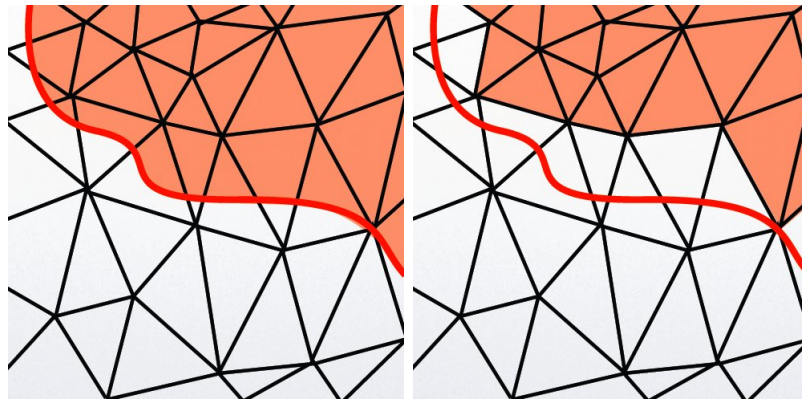


Figure 4.3: Left: The heart domain defined by a level set is in red. Right: The heart domain defined as the largest set of elements inside the level set description of Ω^- .

For a non-body fitted mesh, denoted by \mathcal{T}_{NB} , over a polygonal domain Ω we define

$$\Omega_{NB}^- = \bigcup_{\substack{K \in \mathcal{T}_{NB} \\ \varphi(x) \leq 0, \forall x \in K}} K$$

and denote its boundary by

$$\Gamma_{NB} = \partial \Omega_{NB}^-.$$

The problem (4.2.3) allows to satisfy naturally the transmission conditions $[\sigma \nabla u \cdot n]_{\Gamma} = 0$, at least for the continuous problem before discretization (see Remark 13). However, this is the following discrete variational form that is solved for u_h

$$a_h(u_h, \phi_h) = \sum_{K \in \Omega_{NB}^-} \int_K \sigma^- \nabla u_h \cdot \nabla \phi_h + \sum_{K \in \Omega_{NB}^+} \int_K \sigma^+ \nabla u_h \cdot \nabla \phi_h = \int_{\Omega} f \phi_h = f(\phi_h), \forall \phi_h \in V_h.$$

The method is non conformal as the bilinear form $a_h(\cdot, \cdot)$, built with the discrete domain $\Omega_{NB} = \Omega_{NB}^- \cup \Omega_{NB}^+$, replaces the bilinear form $a(\cdot, \cdot)$ built with the exact domain $\Omega = \Omega^- \cup \Omega^+$. By refining the mesh, $a_h(\cdot, \cdot)$ approaches $a(\cdot, \cdot)$ as $h \rightarrow 0$. When the problem is solved on a non body fitted mesh the transmission condition is satisfied on Γ_{NB} , not on Γ . In the worst case, $\Gamma_{NB} \cap \Gamma = \emptyset$. In addition, there could be a bad approximation of the normal vector when the mesh is coarse (figure 4.4).

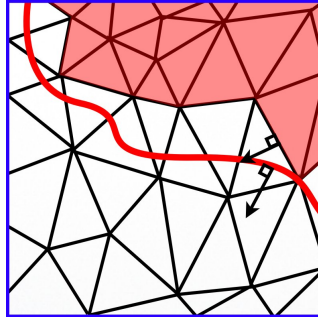


Figure 4.4: Bad approximation of the normal vector for a coarse non-body fitted mesh.

Remark 13 (Satisfaction of the transmission conditions) *Suppose that u is a sufficiently regular solution (except maybe on Γ where only continuity on u is enforced) of the following variational equation:*

$$\int_{\Omega^-} \sigma^- \nabla u \cdot \nabla v + \int_{\Omega^+} \sigma^+ \nabla u \cdot \nabla v = \int_{\Omega} f v$$

Applying one of the Green's identities over each subdomain Ω^+ or Ω^- , provided n_{Γ} is

the outward normal vector to Ω^- , gives

$$-\int_{\Omega^-} v \nabla \cdot \sigma^- \nabla u - \int_{\Omega^+} v \nabla \cdot \sigma^+ \nabla u + \int_{\Gamma} v \sigma^- \nabla u \cdot n_{\Gamma} - \int_{\Gamma} v \sigma^+ \nabla u \cdot n_{\Gamma} + \int_{\partial\Omega} v \sigma^+ \nabla u \cdot n = \int_{\Omega} f v, \quad \forall v \in V.$$

We first assume the following regularity properties: $u|_{\Omega^-} \in H^2(\Omega^-)$ and $u|_{\Omega^+} \in H^2(\Omega^+)$. As the last equation holds for all v in V , consider the three following special cases.

1. Take $v \in H_0^1(\Omega^-)$ and $v|_{\Omega^+} = 0$, and then

$$-\int_{\Omega^-} v \nabla \cdot \sigma^- \nabla u = \int_{\Omega^-} f v.$$

Then u is the solution of the partial differential equation $\nabla \cdot \sigma^- \nabla u = f$ in Ω^- .

2. Take $v \in H_0^1(\Omega^+)$ and $v|_{\Omega^-} = 0$, and then

$$-\int_{\Omega^+} v \nabla \cdot \sigma^+ \nabla u = \int_{\Omega^+} f v.$$

Then u is the solution of the partial differential equation $\nabla \cdot \sigma^+ \nabla u = f$ in Ω^+ .

3. Take $v \in H_0^1(\Omega)$, and then

$$-\int_{\Omega^-} v \nabla \cdot \sigma^- \nabla u - \int_{\Omega^+} v \nabla \cdot \sigma^+ \nabla u + \int_{\Gamma} v \sigma^- \nabla u \cdot n_{\Gamma} - \int_{\Gamma} v \sigma^+ \nabla u \cdot n_{\Gamma} = \int_{\Omega} f v.$$

As $\int_{\Omega} f v = \int_{\Omega^+} f v + \int_{\Omega^-} f v$, one gets

$$-\int_{\Omega^-} v (\nabla \cdot \sigma^- \nabla u + f) - \int_{\Omega^+} v (\nabla \cdot \sigma^+ \nabla u + f) + \int_{\Gamma} v \sigma^- \nabla u \cdot n_{\Gamma} - \int_{\Gamma} v \sigma^+ \nabla u \cdot n_{\Gamma} = 0.$$

By virtue of 1. and 2. the two first terms cancel, then

$$\int_{\Gamma} v (\sigma^{-} \nabla u \cdot n_{\Gamma} - \sigma^{+} \nabla u \cdot n_{\Gamma}) = 0$$

for $v \neq 0$ on Γ so the transmission condition $\sigma^{-} \nabla u \cdot n_{\Gamma} = \sigma^{+} \nabla u \cdot n_{\Gamma}$ is satisfied on Γ .

Finally, assuming that the transmission condition is satisfied on Γ and taking $v \in H^1(\Omega)$ gives

$$-\int_{\Omega^{-}} v \nabla \cdot \sigma^{-} \nabla u - \int_{\Omega^{+}} v \nabla \cdot \sigma^{+} \nabla u + \int_{\partial\Omega} v \sigma^{+} \nabla u \cdot n = \int_{\Omega} f v.$$

Performing similar steps as above shows that the boundary condition $\sigma^{+} \nabla u \cdot n = 0$ is satisfied on $\partial\Omega$. ■

The next section is devoted to the estimates of the order of convergence for these two methods specially designed for non-body fitted meshes. We name the methods by the way the conductivity tensor is defined: by level sets, or by element. Building a reference solution with an algebraic expression, the error can be computed and the order of convergence can be estimated from numerical computations.

4.2.4 Order of convergence of the methods

Meshing complicated geometries coming from segmented medical images or moving geometries is not necessarily obvious, especially when combined with mesh adaptation strategies. As an alternative, the problem can be solved with interfaces which do not pass on the nodes of a fixed mesh, called a *non-body fitted mesh* (see figure 4.1). A standard FE formulation of such a problem does not converge generally at the optimal order in the $H^1(\Omega)$ norm. However, it is well known that the solution of the

same problem with a mesh adapted to the interface (*body fitted mesh*) and a standard Galerkin FE formulation with P_k basis functions converges at the order k [20] if u is sufficiently smooth (in $H^{k+1}(\Omega)$). For a domain that has a curved boundary, the error can be estimated for linear and quadratic finite elements. In [79], the result is derived only in 2D, but could be easily extended in 3D. For either Dirichlet or Neumann problems, homogeneous or inhomogeneous, the geometrical error induced by the change of domain is $O(h^{3/2})$ in the energy norm (i.e. the H^1 semi-norm). The approximation error is still $O(h^k)$ [20] in the H^1 semi-norm. The inequality $\|u - u_h\|_{0,\Omega} \leq Ch\|u - u_h\|_{1,\Omega}$ is obtained with the Aubin-Nitsche lemma, and the order of convergence in the L^2 -norm are deduced. Table 4.1 summarizes the optimal order of convergence in the L^2 -norm that are discussed in section 1.3.3. Remark that with quadratic finite elements basis functions, the error is dominated by the change of domain and half of an order of convergence is lost.

Table 4.1: Theoretical order of convergence of $\|u - u_h\|_{0,\Omega}$. The domain $\Omega \subset \mathbb{R}^2$.

Test space	Body fitted mesh Polygonal domain	Body fitted mesh Curved boundary	Non body fitted mesh
P_1	$O(h^2)$	$O(h^2)$	unknown
P_2	$O(h^3)$	$O(h^{5/2})$	unknown

These theoretical results of convergence are confirmed for body fitted meshes in the following. The orders of convergence for non body fitted meshes are also estimated with computations. To this end, a test problem is built with the diffusion problem (1.3.3) on the square domain $\Omega = [-L, L] \times [-L, L] = \Omega^- \cup \Omega^+ \cup \Gamma$ with the square subdomain $\Omega^- = [-L/2, L/2] \times [-L/2, L/2]$ (see figure 4.5). The exact solution of

problem is given by the following function

$$u_{exact} = \begin{cases} \frac{\sigma^-}{\sigma^+} \cos\left(\frac{\pi}{L}x\right) \cos\left(\frac{\pi}{L}y\right) & \text{in } \Omega^+ \\ \cos\left(\frac{\pi}{L}x\right) \cos\left(\frac{\pi}{L}y\right) & \text{in } \Omega^-. \end{cases}$$

The source term f (continuously differentiable), obtained by applying the Laplacian to u_{exact} , is then

$$f(x, y) = 2\sigma^- \left(\frac{\pi}{L}\right)^2 \cos\left(\frac{\pi}{L}x\right) \cos\left(\frac{\pi}{L}y\right).$$

The computational domain used in our simulations is dimensioned with $L = 100$.

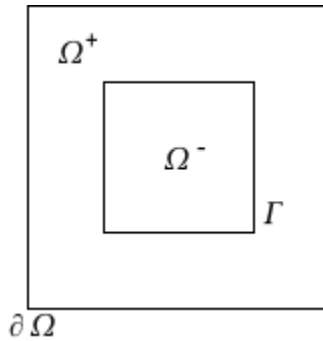


Figure 4.5: Domains for the elliptic problem with $\Omega = [-100, 100] \times [-100, 100] = \Omega^- \cup \Omega^+ \cup \Gamma$ with $\Omega^- = [-50, 50] \times [-50, 50]$.

We can easily see that the exact solution satisfies the transmission conditions (note that u is zero on Γ). There may be a loss of precision near the corners of Ω^- as the normal derivative is not even defined at the corners of Ω^- and transmission condition are ill-defined. Note that u_{exact} given above is a C^∞ function with a gradient vanishing at the corners of Ω^- .

The order of convergence is calculated both for the Dirichlet and Neumann boundary conditions. We use the analytical solution u_{exact} evaluated on $\partial\Omega$ to impose the boundary conditions for the Dirichlet problem. For the Neumann problem, we impose homogeneous boundary conditions on $\partial\Omega$. Remark that this problem satisfies

the compatibility condition, i.e.

$$\int_{\Omega} f = \int_{\partial\Omega} n \cdot \sigma^+ \nabla u,$$

with n the outward normal to Ω . Precisely, f has a null average for homogeneous Neumann boundary conditions. The choice of the resolution technique to solve the Neumann problem can be tricky as it leads to a singular problem. Various numerical method were tested for the Neumann problem and they are discussed in the appendix A and B. We finally decided to remove the singularity by perturbing the matrix, but not the residual. This is made by adding a mass matrix of order ϵ with ϵ small, and we solve the linear system by the iterative correction method. Let $u = u_0 + \delta u$ with u_0 the initial guess and δu the correction. The new approximate problem becomes:

Find $\delta u \in P_k$ such that

$$A\delta u + M\delta u = F - Au_0,$$

where

$$A_{ij} = \sum_K \int_K \nabla \phi_j \cdot \nabla \phi_i,$$

$$M_{ij} = \epsilon \sum_K \int_K \phi_j \phi_i$$

with $\delta u = \sum \delta u_j \phi_i$, ϕ_i are basis functions, namely piecewise polynomials of degree k on elements K of the mesh. The iterative correction method requires that we solve for δu and update u_0 until the right hand side becomes zero. Once converged, the residual of the non modified approximate problem (without the mass matrix) is zero and we have a solution of $Au = F$. We used body fitted meshes described in Table 4.2 and non-body fitted meshes described in Table 4.3 for the analysis of the error and convergence.

We first confirmed the theoretical order of convergence in the L^2 -norm (table

Table 4.2: Statistics for the body fitted meshes.

Mesh	# Elmts	# dofs in P_1	# dofs in P_2	h/L (adim.)
$\mathcal{T}_{B,1}$	760	419	1,597	0.1
$\mathcal{T}_{B,2}$	3,040	1,597	6,233	0.05
$\mathcal{T}_{B,3}$	12,160	6,233	24,625	0.025
$\mathcal{T}_{B,4}$	194,560	97,889	390,337	0.00625
$\mathcal{T}_{B,5}$	778,240	390,337	1,558,913	0.003125

Table 4.3: Statistics for the non body fitted meshes.

Mesh	# Elmts	# dofs in P_1	# dofs in P_2	h/L (adim.)
$\mathcal{T}_{NB,1}$	204	121	445	0.2
$\mathcal{T}_{NB,2}$	812	445	1,701	0.1
$\mathcal{T}_{NB,3}$	3,338	1,748	6,833	0.05
$\mathcal{T}_{NB,4}$	13,154	6,735	26,625	0.025
$\mathcal{T}_{NB,5}$	52,756	26,687	106,139	0.0125
$\mathcal{T}_{NB,6}$	212,062	106,670	425,401	0.00625

4.1) when the mesh is body fitted and the conductivity coefficient is

$$\sigma(x) = \begin{cases} 1 & \text{for } \varphi(x) \leq 0 \\ 2 & \text{otherwise.} \end{cases}$$

when defined by level set and

$$\sigma(x) = \begin{cases} 1 & \text{for } x \in \Omega_{NB}^- \\ 2 & \text{otherwise.} \end{cases}$$

when defined by element. Again, the finite element code MEF++ [2] is used and the numerical results are presented in figure 4.6. After, we calculated what was the order of convergence when we have non-body fitted meshes and the conductivity constant is defined either by level set or by element. Figure 4.7 shows that using P_1 or P_2 finite element basis, and whatever the way the conductivity is defined, the order of convergence is around one. However, the error can be ten times smaller for the

method by level sets compared to the method by element, e.g. for P_2 basis functions. The method by level set is better than the method by elements, and using P_2 basis functions instead of P_1 basis functions improves the accuracy of the solution.

Also, the map of the difference between the exact solution and the solution on the non body fitted mesh (figure 4.8) shows that the error is concentrated in the internal domain Ω^- and especially near the interface Γ . For the method defining the conductivity by element, one can explain this error distribution with the fact that the transmission condition is not satisfied at Γ but at Γ_{NB} . For the method defining the conductivity by level set, figure 4.9 illustrates that error in the transmission condition can introduce a shift of the solution inside Ω^- . Finally, we experimented the effect of the magnitude of the conductivity jump on Γ . Figure 4.10 indicates that the higher is the jump the higher is error on the solution in the L^2 -norm.

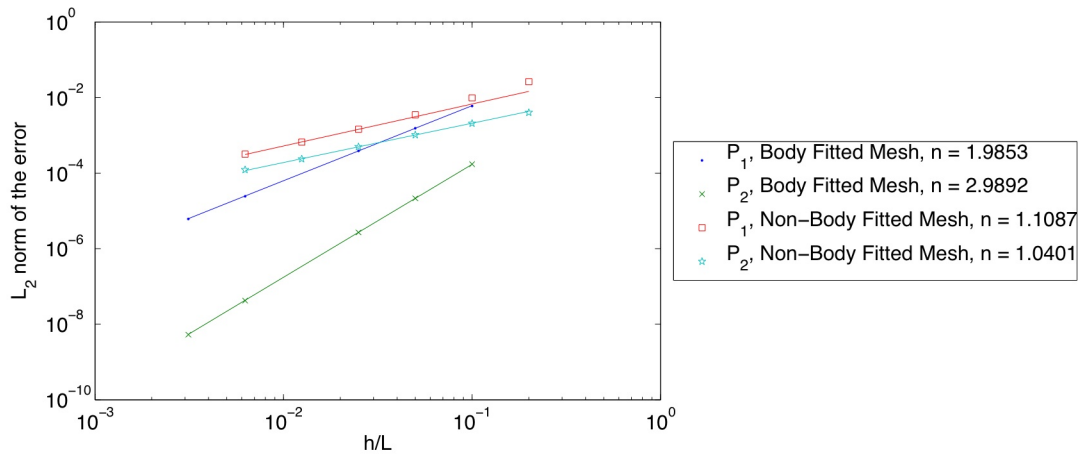


Figure 4.6: Error on the solution as a function of the mesh size h for the diffusion problem with Neumann boundary conditions on body fitted meshes compared to non-body fitted meshes with the conductivity defined by level sets. Remark that n refers to the order of convergence. Results for the Dirichlet boundary conditions are very similar.

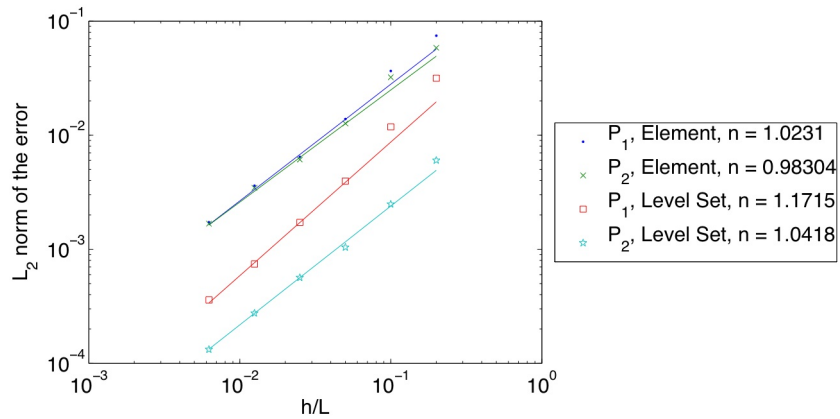


Figure 4.7: Error on the solution as a function of the mesh size h for the diffusion problem on non-body fitted meshes and with Neumann boundary conditions. Remark that n refers to the order of convergence. Results for the Dirichlet boundary conditions are very similar.

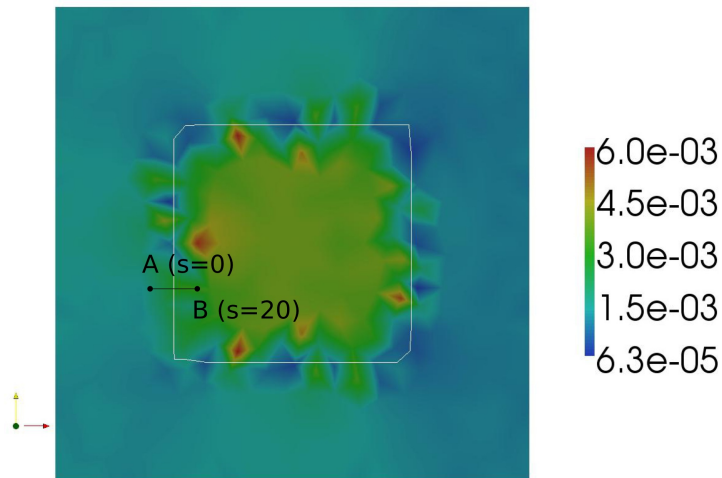


Figure 4.8: Difference between the non body fitted solution (using quadratic elements on mesh $\mathcal{T}_{NB,2}$) and the exact solution of the diffusion problem with discontinuous conductivities defined by level sets.

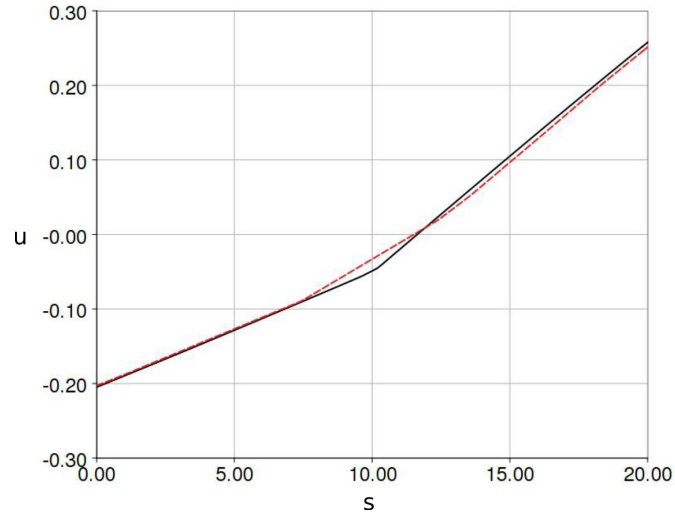


Figure 4.9: The exact solution (in black) and the non body fitted solution (in red) (using quadratic elements on mesh $\mathcal{T}_{NB,2}$) of the diffusion problem with discontinuous conductivities defined by level sets.

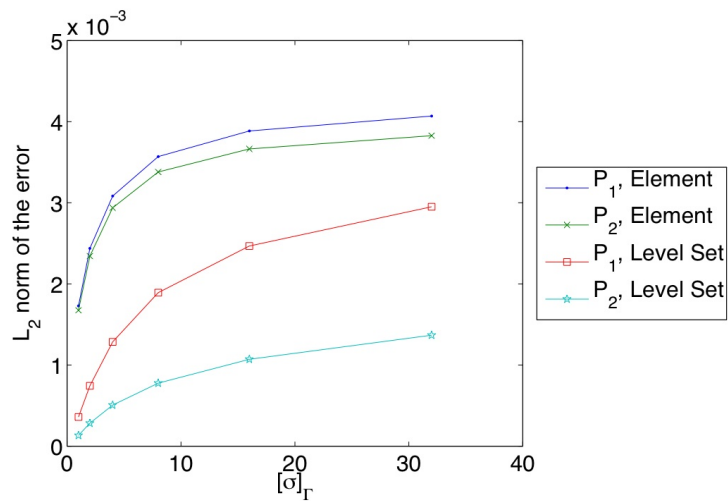


Figure 4.10: L_2 -norm of the error versus the jump of conductivities σ on Γ .

4.3 Convergence of the heart-torso coupling problem

4.3.1 Variational formulation and resolution with a finite element method

The version of the heart-torso coupling problem which was used is given by the equations (1.2.6)-(1.2.12)) with the ionic model given by (2.2.1)-(2.2.2). Assuming that the strong solution of these equations is enough smooth, the brute variational formulation of these equations is

$$\int_H \frac{dv}{dt} \phi_v + \int_H g(u, v) \phi_v = 0$$

$$\chi C_m \int_H \frac{du}{dt} \phi_u + \int_H \sigma_i \nabla u_e \cdot \nabla \phi_u + \int_H \sigma_i \nabla u \cdot \nabla \phi_u + \chi \int_H f(u, v) \phi_u = \int_{\partial H} (\sigma_i \nabla (u + u_e)) \cdot n_H \phi_u$$

$$\int_H \sigma_i \nabla u \cdot \nabla \phi_w + \int_H (\sigma_i + \sigma_e) \nabla u_e \cdot \nabla \phi_w = \int_{\partial H} (\sigma_i \nabla u + (\sigma_i + \sigma_e) \nabla u_e) \cdot n_H \phi_w$$

$$\int_T \sigma_T \nabla u_T \cdot \nabla \phi_w = \int_{\partial T \cap \partial H} \sigma_T \nabla u_T \cdot n_T \phi_w + \int_{\partial T - \partial T \cap \partial H} \sigma_T \nabla u_T \cdot n_T \phi_w,$$

for all $\phi_u \in H^1(H)$, $\phi_v \in L^2(H)$ and $\phi_w \in H^1(H \cup T)$.

Using the boundary conditions and defining these following new quantities

$$\sigma_w = \begin{cases} \sigma_i + \sigma_e & \text{in } H \\ \sigma_T & \text{in } T \end{cases}$$

$$\tilde{\sigma}_i = \begin{cases} \sigma_i & \text{in } H \\ 0 & \text{in } T \end{cases}$$

$$u_w = \begin{cases} u_e & \text{in } H \\ u_T & \text{in } T, \end{cases}$$

we get the variational formulation that we discretize and solve with Newton's method.

$$\int_H \frac{dv}{dt} \phi_v + \int_H g(u, v) \phi_v = 0 \quad (4.3.1)$$

$$\chi C_m \int_H \frac{du}{dt} \phi_u + \int_H \sigma_i \nabla(u_w|_H) \cdot \nabla \phi_u + \int_H \sigma_i \nabla u \cdot \nabla \phi_u + \chi \int_H f(u, v) \phi_u = 0 \quad (4.3.2)$$

$$\int_{H \cup T} \tilde{\sigma}_i \nabla u \cdot \nabla \phi_w + \int_{H \cup T} \sigma_w \nabla u_w \cdot \nabla \phi_w = 0 \quad (4.3.3)$$

The spaces in which we seek the weak solutions are

$$v \in L^2([0, t_{max}]; L^2(H)),$$

$$u \in L^2([0, t_{max}]; H^1(H)),$$

$$u_w \in \{v \text{ s.t. } v|_H \in L^2([0, t_{max}]; H^1(H)), v|_T \in L^2([0, t_{max}]; H^1(T)), u_e|_{\partial H} = u_T|_{\partial H}\} / \mathbb{R}.$$

Note that the equation $n_H \cdot (\sigma_i \nabla u + (\sigma_i + \sigma_e) \nabla u_e) = n_H \cdot (\sigma_T \nabla u_T)$ is naturally satisfied on ∂H by the variational formulation (see Remark 13 above for a similar derivation). The functional spaces are chosen according to [13] and [14]. This choice of functional spaces is appropriate for proving the existence of a solution for the coupled variational problem. Higher regularity on the exact solution is needed to ensure the convergence of the numerical solution to the exact solution.

4.3.2 Resolution technique using a level set description of the domains and non body-fitted meshes

The time scheme chosen is an implicit Gear scheme (justified in [30] and [6]), so the time discretization was of order 2 whatever the order of the space discretization. We

did not investigate more about the time discretization, but we rather focussed on the space discretization. We already calculated what was the order of convergence and the behavior of the error on the solution for the diffusion problem. In fact, the equation (4.3.3) is a diffusion problem with discontinuous coefficients. The expectations are an order of less than one for the convergence on the isochrons of depolarization.

Now, the problem is slightly more complex. We have different domains with different equations. We still have jumps on the conductivities. We have the equations (4.3.1)-(4.3.2) defined only in the heart (H), and the equation (4.3.3) defined everywhere ($H \cup T$). We would like to solve this problem with a level set description of the domains and a non body-fitted mesh.

4.3.3 Order of convergence for a simple test case

The problem solved on a geometry illustrated in figure 4.11. A circular disc defining the heart is embedded in a square, which defines the thorax. The total domain $\bar{\Omega}$ is the square $[-100, 100] \times [-100, 100]$ and $H = D((0, 0); 30)$, i.e. an open disc of radius 30 centered at $(0, 0)$. The activation zone is $A = D((0, -30); 10) \cap H$ and the initial

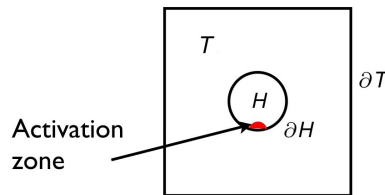


Figure 4.11: Domain used for the simulations of the heart-torso coupling problem. The red region is depolarized at the initial time.

conditions are

$$u(x, 0) = \begin{cases} 1 & \text{for } x \in A, \\ 0 & \text{otherwise,} \end{cases}$$

$$u_w(x, 0) = \begin{cases} -0.5 & \text{for } x \in A, \\ 0 & \text{otherwise} \end{cases}$$

and for the ionic variable $s(x, 0) = v(x, 0) \equiv 0$ on all Ω . The reference solution is calculated with quadratic finite elements on a body-fitted mesh, i.e. a mesh with nodes on the boundary of the interior disc H . The number of degrees of freedom and the corresponding mesh size h for this reference solution are indicated in the shadowed cells in the table 4.4. The mesh for this reference solution is fine enough so that the solution is converged with respect to the space discretization. The criteria for convergence consists in requiring a difference of less than 1% between the reference isochrons of depolarization for a mesh size h and the isochrons of depolarization for a mesh size $2h$.

Table 4.4: Degrees of freedom for the body fitted meshes.

# Elmts	# dofs in P_1	# dofs in P_2	h (adim.)
3,338	1,748	6,833	5
13,154	6,736	26,625	2.5
52,756	26,697	106,149	1.25
212,062	106,670	425,401	0.625

Table 4.5: Degrees of freedom for the non body fitted meshes.

# Elmts	# dofs in P_1	# dofs in P_2	h (adim.)
3,648	1,897	7,741	5
14,592	7,441	29,473	2.5
58,368	29,473	117,313	1.25
233,472	117,313	468,097	0.625

As the problem is time dependent, we have to find a way to compare time dependent solutions. It is done via the isochrons of depolarization iso_{depol} , which are updated at each time step. We refer the reader to section 3.2 for the definition of the isochrons iso_{depol} and the other isochrons iso_{max} , iso_{repol} and iso_{rec} , as well as T_{up} , T_{AP} are measured on the numerical solution.

To draw the contours, iso_{depol} is interpolated linearly on every element K . For example, the contour associated to the time τ is

$$x_\tau = \{x \in \Omega \text{ s.t. } iso_{depol} = \tau\}$$

while it should be

$$x_\tau = \{x \in \Omega \text{ s.t. } u(x, \tau) = u_{th}\}.$$

The error between the two last quantities is always less than the mesh size h as long as the contour where $u(x, \tau) = u_{th}$ does not cross a whole element during a single time step. In our simulations, the time step and the speed of the action potential are such that this condition is satisfied. Because of time discretization an error of at most $c\Delta t$ can be expected between the two contours defined above. As the wavefront propagates at a nearly constant speed c , this can be seen as a shift introduced by time discretization.

The order of convergence for both methods for non-body fitted meshes is $n \simeq 1$ when solving a simple elliptic problem. We expect a lower order of convergence for the heart-torso coupling problem. There are several sources of error that could be responsible for this limited order of convergence:

1. The problem is solved on an approximate domain (non conformity of the method).
2. The error is calculated on the isochrons of depolarization $iso_{depol}(x_i)$, not on the solution. The isochrons are linearly interpolated.
3. The value of $iso_{depol}(x_i)$ for a given mesh node x_i is not even the exact time the solution u crossed u_{th} at x_i because of the time discretization.

For a bad approximation of the domain by a coarse non body fitted mesh, as illustrated in figure 4.4, the propagation of the AP is spoiled near the internal interface ∂H . In figure 4.12(b), the difference between the isochrons of depolarization

is shown near the interface ∂H . The level set description of the heart ($\varphi = 0$) is represented by a circular arc (in black). The body fitted mesh edges are drawn in black (it is a mesh with 194,560 elements) and the values of the difference between the isochrons are showed only in the subdomain Ω_{NB}^- . To visualize how deformed are the isochrons, figure 4.13 shows a series of contours at various times. The isochrons are well calculated (error of 5%) even if the non body fitted mesh has an irregular boundary that could lead to spurious propagation. This is however an encouraging result. Remark that the non body fitted mesh covers the surface area of the domain H with an error of at most 3% in this case.

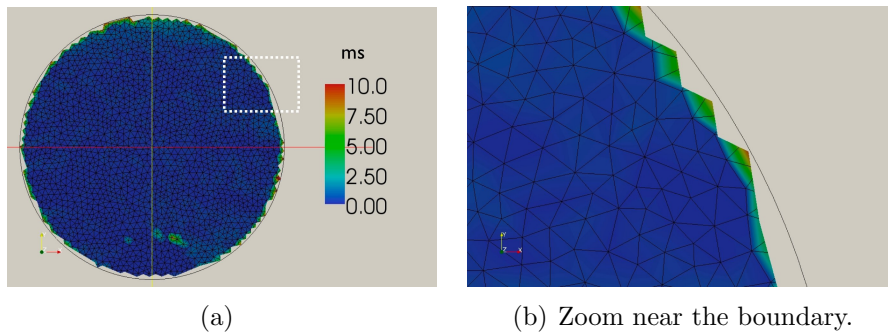


Figure 4.12: Difference between the isochrons of depolarization for the body vs non-body fitted meshes. There is a maximal difference of 10 ms for a depolarization time of 200 ms near the heart surface (5% of error).

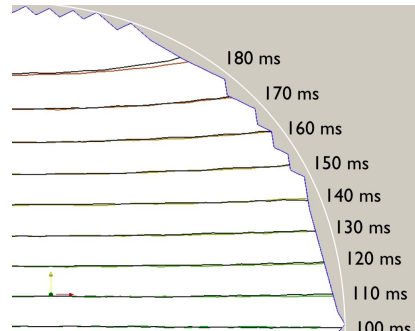


Figure 4.13: The isochrons of depolarization for a simulation using non body fitted mesh (black isochrons) versus body fitted mesh (colored isochrons).

Figure 4.14 shows the orders of convergence of the finite element methods when using body fitted and non body fitted meshes with conductivity defined by level set. The error is calculated on normalized isochrons of depolarization. i.e. $0 \leq iso_{depol}(x) / \max_x(iso_{depol}(x)) \leq 1$, on the non body fitted subdomain $H = \Omega_{NB}^-$. When using body or non body fitted meshes for computing the heart-torso coupling problem, it turns out that the order of convergence for the isochrons is about 0.5. The level of error is lower for quadratic finite elements on body fitted meshes, than for the three other methods. For non body fitted meshes, linear finite elements have the highest order of convergence and the lowest level of error asymptotically. We expect from these results that the method used to compute the isochrons is more critical than the selection of a body vs non body fitted finite element method to solve the bidomain model, at least to control the level of error on the isochrons. Indeed a possible reason why figure 4.6 shows higher orders of convergence than figure 4.14 is that in the latter case the error is calculated on a derived variable, the isochrons, while in the former case the error is calculated directly on the solution. Of course, this conclusion must be tempered by the fact that we are comparing the solution of a simple linear diffusion problem with the nonlinear propagation of cardiac potential waves.

Finally, the fact that P_1 finite elements are better for the level of error than P_2 finite elements came as a surprise. We hypothesize that this behavior may come from an inappropriate combination of interpolation and resolution methods: linear interpolation of isochrons computed from a solution calculated with a quadratic finite element method on non body fitted meshes that use a piecewise linear level set description of domains.

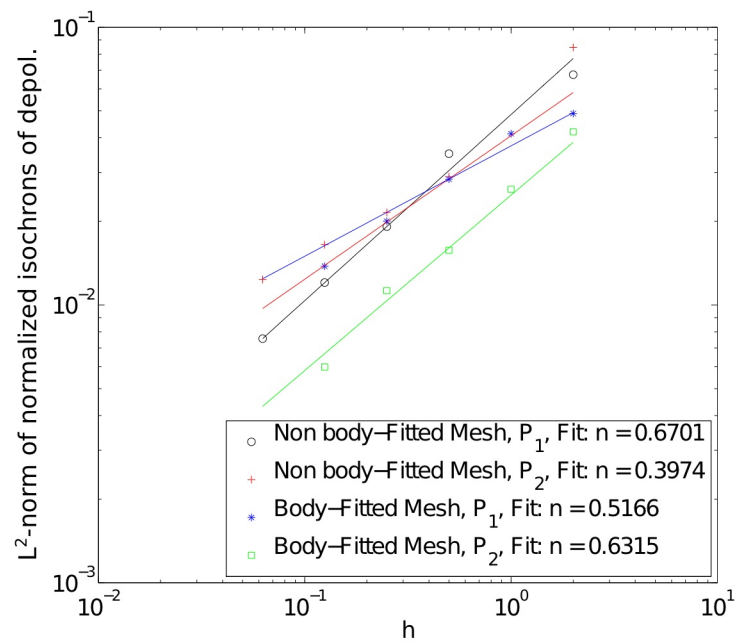


Figure 4.14: Error on the isochrons as a function of the mesh size h for non body-fitted meshes and a level set description of the domains. The order of convergence obtained with a linear fit is given by n .

4.4 2D simulation using realistic patient data

The problem is solved on a geometry based on the segmented medical image of figure 4.2(b). The segmentation process gives the level set description of the heart, the heart cavities and the lungs. The whole domain is shaped to resemble a torso, where the heart is embedded. The conductivity tensors are defined with the eigenvalues given in table 4.6. The non dimensional number N and the parameters of the MS model are calculated as it is done in section 2.5.1.

Table 4.6: Parameters of the bidomain model for a human heart.

Description	Param.	Value	Units
Characteristic conductivity	σ	$1 \cdot 10^{-1}$	S/m
Intracellular conductivity	$\tilde{\sigma}_{i,l}$	1.741	-
	$\tilde{\sigma}_{i,n}$	0.1934	-
Extracellular conductivity	$\tilde{\sigma}_{e,l}$	3.906	-
	$\tilde{\sigma}_{e,n}$	1.970	-
Torso conductivity	$\tilde{\sigma}_T$	2.2	-
Lung conductivity	$\tilde{\sigma}_L$	0.5	-
Heart cavity conductivity	$\tilde{\sigma}_C$	6.7	-

The heart is activated by setting the transmembrane potential equals to 0.8 in the activation zones shown in figure 4.15. The recovery variable is also set to 0.1 in the heart. The activation zones are defined to approach the early activation regions suggested by the isochrons of depolarization measured experimentally in [27]. Figure 4.17 shows isochrons of depolarization that can be compared with that of [27] in figure 4.16. The isochrons of repolarization are also presented. The solutions u , v and u_w are showed for selected time steps in figure 4.18 to see the propagation of the wave front through the tissue. The action potential in figure 4.20 is plotted with point values for all time steps. Remark on figure 4.19 that the solution variations during the depolarization are not well captured , the mesh being too coarse.

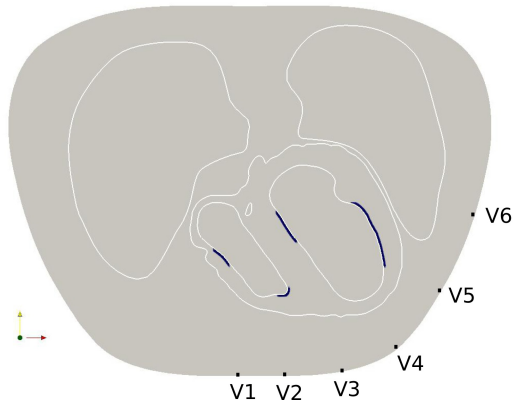


Figure 4.15: Computational domain of the heart-torso coupling problem with lungs and heart cavities. Activation zones are shown in black. The ECG can be plotted using probes $V1$ to $V6$.

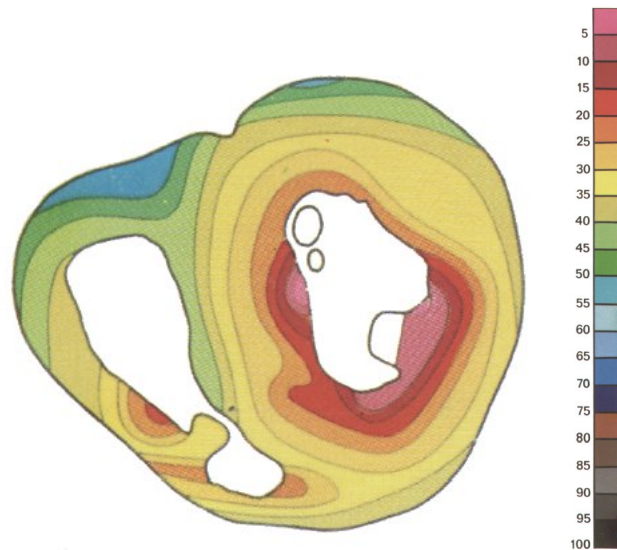


Figure 4.16: Isochrons of depolarization of an isolated human heart, based on measurements at 870 electrodes[27].

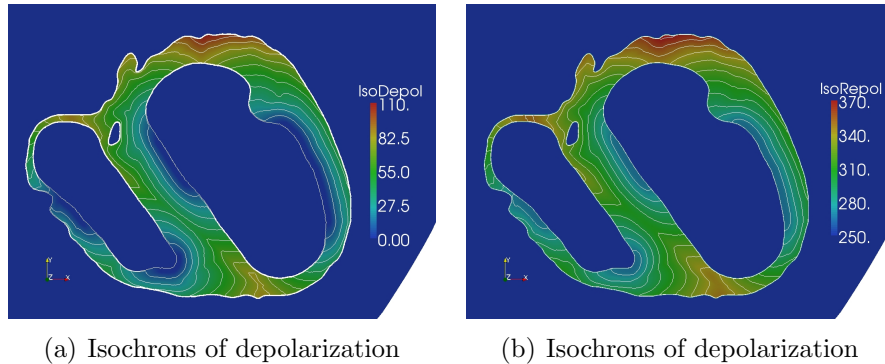


Figure 4.17: Isochrons of depolarization and repolarization.

In the following, we compare numerical simulations done over body and non body fitted meshes. We also want to see the effect of the extracardiac conductivity on the solution. We use isochrons of depolarization (figures 4.21 to 4.24)) and the ECG (figure 4.25) to measure the impact of both the type of meshes and the extracardiac conductivity. The ECG are plotted using probes $V1$ to $V6$, illustrated on figure 4.15.

Figure 4.21 indicates that when using the same body fitted mesh the isochrons of depolarization are only slightly modified ($<3\%$) if the extracardiac conductivity is composed of a single domain (torso) instead of multiple domains (heart cavities, lungs and torso). The extracardiac domain, even passive, can influence slightly the propagation inside the heart through the transmission conditions. This is also observed for non body fitted meshes (figure 4.22). In counterpart, the isochrons of depolarization are more modified if the extracardiac domain is the same but we rather compare body and non body fitted meshes. This is illustrated in figures 4.23 and 4.24 where a difference of at most 9% is observed (in the infinity norm). The geometrical description of the heart is thus more important than the extracardiac properties in order to simulate accurate isochrons (measured in the heart only).

If we are interested in simulating accurately ECGs, the conclusions are not the same (see figure 4.25). The extracardiac measures at the body surface are almost

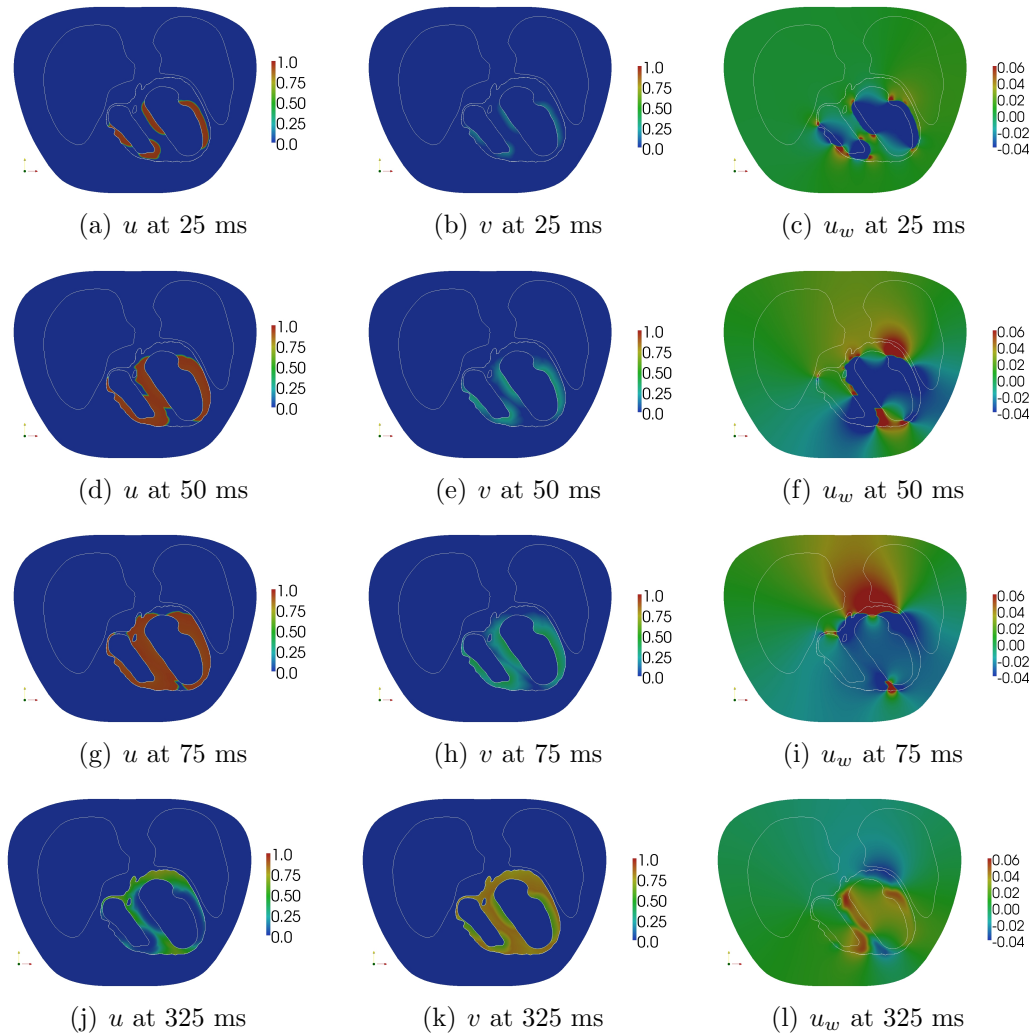


Figure 4.18: The transmembrane potential u , the recovery variable v and the extracellular/extracardiac potential u_w at selected time steps. Figures (a) to (i) show the depolarization phase, and figures (j) to (l) show the repolarization phase.

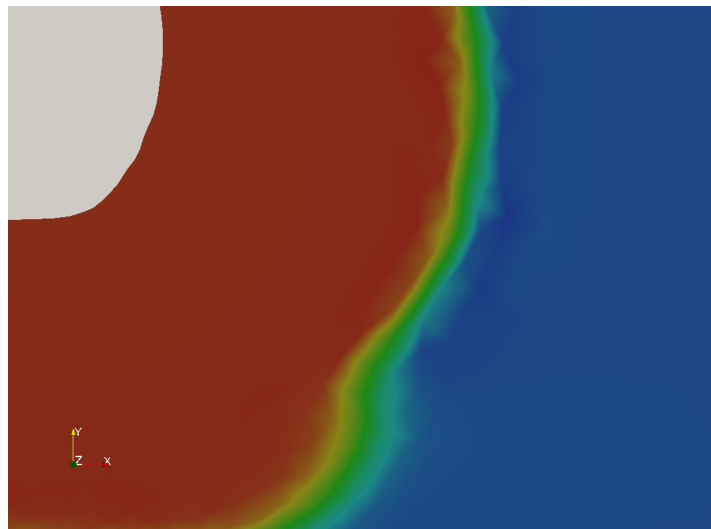
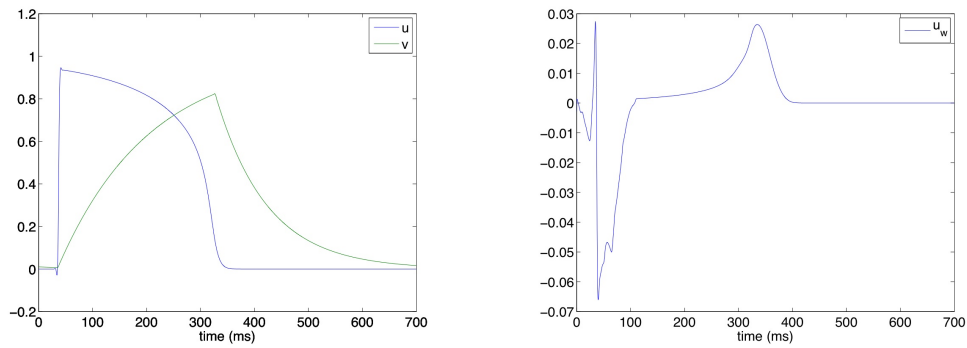


Figure 4.19: Zoom of the solution to see that the mesh does not capture very well the depolarization front. The region illustrated shows in grey the bottom of the left cavity.

superposed if the extracardiac domain is the same no matter the mesh is body or non body fitted. However, more obvious modifications occur if the extracardiac domain is not the same. An inaccurate geometrical description of the heart and extracardiac organs is then of second importance when simulating ECGs.

We finally put in perspective the use of an inaccurate geometrical description of the domains. It could be an important lack in situations of complex propagation behaviors, like spiral waves initiated by the propagation around subregion of highest conductivity (e.g. infarct scars). A possibly small subregion of highest conductivity could be defined with a level set function, and its shape could be under-resolved with a non body fitted mesh that is too coarse. The problem of remeshing is addressed in the next chapter, where mesh adaptation is used not only to remesh where an accurate geometrical description is needed, but also where the solution varies rapidly.

In conclusion, a numerical analysis of convergence and accuracy of the two proposed finite element methods approximating the heart-torso coupling problem was investigated. First, a purely diffusive problem with discontinuous conductivity on



(a) u and v

(b) u_w

Figure 4.20: The solutions u , v and u_w for all time steps at a given point of the septum. The small oscillations observed on the solution on both sides of the depolarisation front are likely coming from the fact that the time step 0.3 used in this simulation is too close to the critical time step for stability. This is an illustration of the loss of monotonicity of the solution discussed in section 3.1 for time steps just below the critical value.

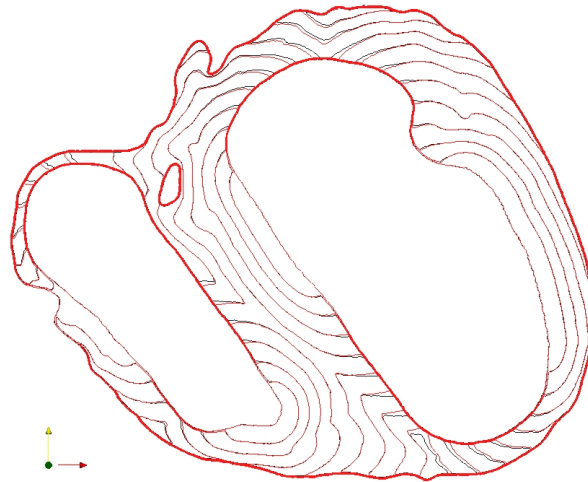


Figure 4.21: Isochrons of depolarization for the body fitted mesh. Contours are separated by 10 ms. There is a maximal difference of 3 ms between the geometry containing the heart, the lungs, the heart cavities and the torso (black contours) and the heart and the torso only (red contours).

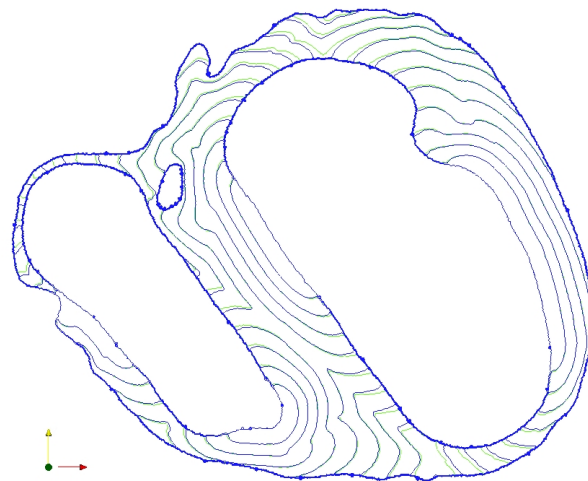


Figure 4.22: Isochrons of depolarization for the non-body fitted mesh. Contours are separated by 10 ms. There is a maximal difference of 3 ms between the geometry containing the heart, the lungs, the heart cavities and the torso (blue contours) and the heart and the torso only (green contours).

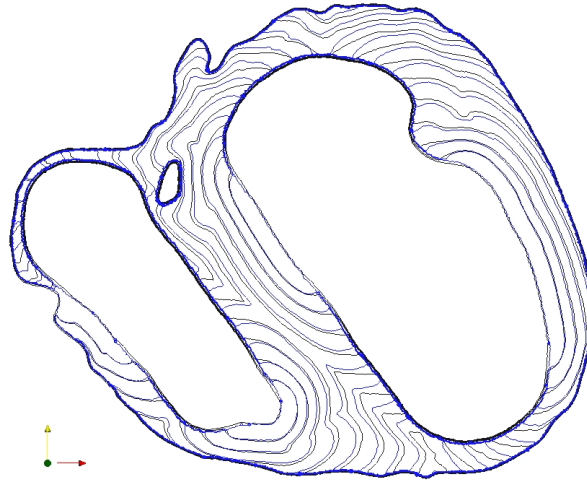


Figure 4.23: Isochrons of depolarization of the geometry containing the heart, the lungs, the heart cavities and the torso. Contours are separated by 10 ms. There is a maximal difference of 10 ms between the body and the non body fitted meshes (black and blue contours, resp.).

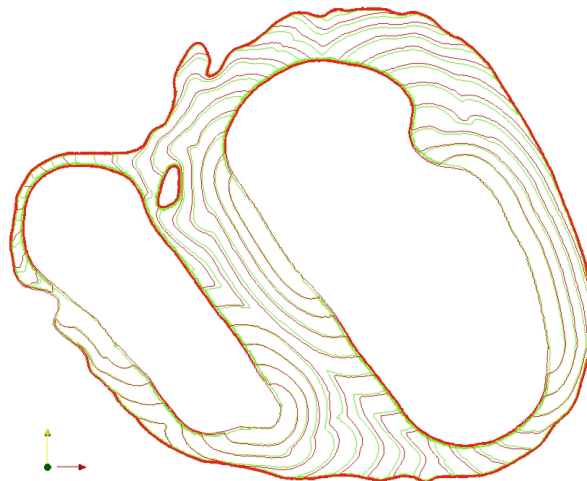


Figure 4.24: Isochrons of depolarization of the geometry containing the heart and the torso only. Contours are separated by 10 ms. There is a maximal difference of 5 ms between the body and the non body fitted meshes (red and green contours, resp.).

4. On the convergence of the heart-torso coupling problem using non-body fitted meshes.

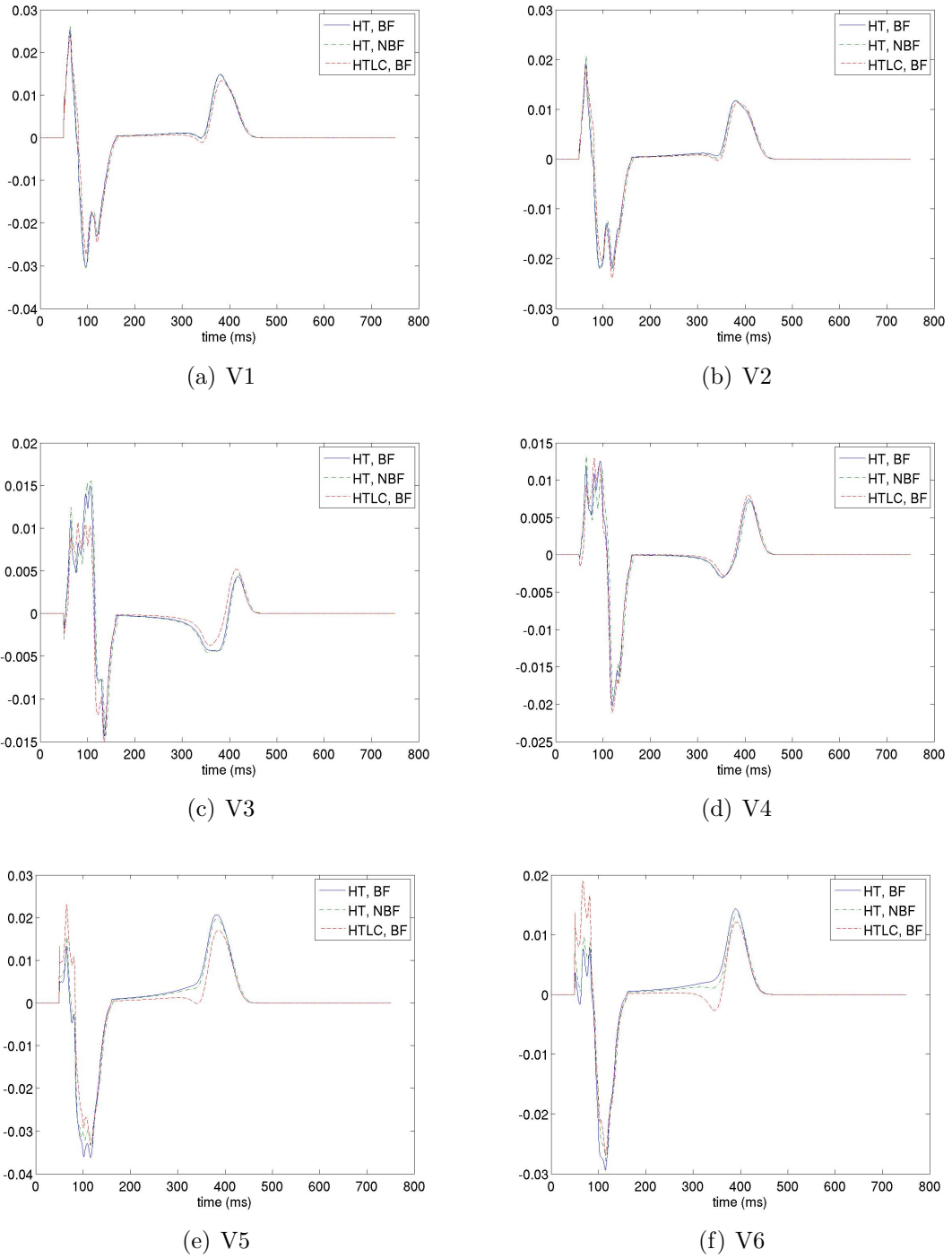


Figure 4.25: ECG with probes $V1$ to $V6$ (illustrated in figure 4.15). Blue: Heart-torso with a body fitted mesh. Green dash-dot: Heart-torso with a non body fitted mesh. Red dash: Heart-lungs-cavities-torso with a body fitted mesh.

a square was proposed as a benchmark to study the order of convergence for non body fitted meshes and recover analytical convergence for body fitted meshes. First order accuracy is obtained for numerical solutions using linear and quadratic finite elements on non body fitted meshes. The convergence of numerical solutions for the general bidomain model was considered in a simplified geometry. The error is calculated on the depolarization isochrons, as opposed to the diffusion problem where the error is calculated directly on the solution. Orders of convergence less than one (approximately between 0.4 and 0.7) are obtained on non body fitted meshes. Our results show that the accuracy and convergence of isochrons is a limitation that would eventually have to be addressed.

Chapter 5

Mesh Adaptation

5.1 Introduction: the need for mesh adaptation

In this chapter, a time-dependent mesh adaptation strategy is used for numerical simulations of traveling cardiac APs in the heart and propagating electrical potential throughout the body. Cardiac AP waves have sharp depolarization and repolarization fronts. They propagate across the myocardium leading to the requirements of uniformly fine meshes over the whole heart domain. When using very complicated ionic models and realistic geometries, the complexity and the size of the problem make its resolution a challenge, even with the increasing availability of computational resources. It is now well established that coarse meshes lead to wrong propagation speed and wave trajectories [15]. Moreover, the anisotropic nature of conductivities in the human heart leads to differences in wave speed and front width depending on the direction of propagation. For strongly anisotropic conductivities, achieving an adequate spatial resolution is important to prevent distorted wavefronts during propagation (see [7], [68] and [18]).

To address these difficulties, many authors use uniformly fine meshes and parallel computing to reduce the computational time (see [61] and [70] for instance).

Mesh adaptation is another avenue that has been introduced in finite element based simulations to improve the accuracy of the solutions as well as to capture the behavior of physical phenomena. The technique consists in maintaining the extremely fine resolution only where it is needed while coarsening elsewhere. It results in faster calculations (much smaller number of degrees of freedom) and a lower memory requirement. For post-processing there are smaller output files that are analyzed in order to extract the important information. The efficiency of this strategy has also been proved for cardiac electrophysiology (see [6], [7] for spatial adaptivity and [78] for spatiotemporal adaptivity), where the mesh adaptation strategy is used in the heart only. To our knowledge, there is no work for the heart-torso coupling problem using any unstructured mesh adaptation method.

The originality of this work results first from the use of an anisotropic adaptive remeshing method to efficiently capture solution variations within complex, realistic geometries for the heart-torso coupling problem; and second from the reduction of the frequency at which the mesh is adapted to reduce the computational burden caused by remeshing and reinterpolation operations.

Section 5.2 reviews briefly the basis of metric error estimation that is used in our mesh adaptation strategy. The mesh adaptation step is integrated in a resolution-adaptation loop for solving the whole heart-torso coupling problem. In section 5.3.1, two different resolution-adaptation loops are presented. The integration of level set based geometry and myocardial fiber arrangement as well as computing isochrons can cause some difficulties that are discussed and addressed. Then the mesh adaptation strategies are tested and optimized in section 5.3.6 with a 2D heart-torso simulation. We finally test our mesh adaptation strategy in section 5.4 on a more complex system, i.e. when the heart geometry moves during the propagation of the potential.

5.2 Overview of techniques and algorithms used in mesh adaptation

In addition to the discretization methods, computational mesh quality is crucial, in order to have an accurate representation of the dynamic phenomena simulated. In our approach, unstructured mesh adaptation is achieved through a geometrical *a posteriori* error estimator based on a discrete approximation of the Hessian of the solution. There are several types of error estimator that could be used to control the error made on the solution. For instance, a hierarchical error estimator can be used, where information from higher order reinterpolations of the solution is exploited (see [35] for details). Metric error estimation is another method that is briefly described in the following section. Note that a remeshing method based on such an error estimator has already been used for obtaining 2D numerical solutions in cardiac electrophysiology [6].

Optimization of the mesh progresses by improving the elements through a series of local operations in an attempt to equidistribute the solution error and hence improve the overall quality of the mesh. By repeating this procedure, an optimal mesh is obtained that leads to a numerical solution with the desired accuracy.

5.2.1 Metric error estimation

The problem consists in computing the approximation error $e_h = u - u_h$ between the exact and the numerical solutions on the mesh \mathcal{T}_h . Using this error, a new mesh \mathcal{T}'_h is generated on which the error is bounded by a given tolerance value tol . The dynamic mesh optimization is achieved through the construction of discrete metric (defined at the mesh nodes), which is itself dependent on the computed solution. This metric relies on an error estimate which is derived from the interpolation error. For elliptic problems, Céa's lemma shows that the error e on the finite element solution

is bounded by the interpolation error in the energy norm $\|\cdot\|$:

$$\|e\| \leq c \|u - \Pi_h u\|,$$

where the function u is approximated by its interpolant $\Pi_h u$ (e.g. piecewise linear Lagrange interpolant) and c is a constant independent of the mesh \mathcal{T} . In practice, minimizing the interpolation error in this manner has been found to be a reasonable way to control the discretization error, even for non-elliptic problems (see for instance [35]).

We next bound the interpolation error using the second derivatives, as it is done for *a priori* error estimation. For instance, the interpolation error over a linear element is bounded by the second derivative of the function. For a sufficiently smooth function u approximated by its piecewise linear Lagrange interpolant $\Pi_h u$, the interpolation error on element K satisfies[3]

$$\|u - \Pi_h u\|_{\infty, K} \leq c \max_{v \in \mathcal{E}_K} v^T |H| v,$$

with c a constant independent of the mesh, \mathcal{E}_K the set of edges of K , and $|H|$ is an element-valued Hessian defined such that the above inequality holds. $|H|$ denotes the positive definite metric formed by taking the absolute value of the eigenvalues of H and reflects the fact that it is the magnitude of the curvature that is of interest, rather than the sign of the curvature. As the Hessian describes the curvature of the solution at each point in every direction, the use of the Hessian for the error metric is ideal to guide anisotropic mesh adaptivity and place resolution in zones of high solution curvature. The local anisotropic features in a solution are made isotropic in a warped domain through a coordinate transformation specified by means of a Hessian based

metric. The optimized mesh is expected to satisfy

$$v^T |H| v = tol,$$

for every edge v of every element of the mesh. This allows a description of the ideal element sizing and orientation at every point in space. The goal of this adaptive method is then to build a mesh with nearly equilateral tetrahedra in a Riemannian metric space, where the error is equidistributed.

5.2.2 Pre-intersection of metrics

In this work, the metric was designed to resolve efficiently not only the transmembrane potential but also the recovery variable in the heart, as well as the extracellular potential in the heart and the torso. When several metrics are specified at the same mesh node, a single metric tensor must be defined taking into account all given metrics. To this end, a metric intersection procedure is used so that the interpolation error for each variable is bounded by the given tolerance value. The details of the method are given in [3].

In practice, metric intersection is obtained by the simultaneous reduction of two quadratic forms corresponding to the two metrics M_1 and M_2 . This is possible as both metrics are positive definite. The idea is to find a basis (e_1, e_2, e_3) , not necessarily orthogonal, such that M_1 and M_2 are diagonal in this basis. The next step is to deduce the intersected metric. Terms of the diagonal matrix associated to the metrics M_1 and M_2 are given by

$$\lambda_i = e_i^T M_1 e_i, \text{ for } i = 1, 2, 3$$

and

$$\mu_i = e_i^T M_2 e_i, \text{ for } i = 1, 2, 3.$$

Let P be the matrix having for column vectors e_1 , e_2 , and e_3 . P is invertible

since (e_1, e_2, e_3) is a basis in \mathbb{R}^3 . We have

$$M_1 = (P^{-1})^T \begin{pmatrix} \lambda_1 & 0 & 0 \\ 0 & \lambda_2 & 0 \\ 0 & 0 & \lambda_3 \end{pmatrix} P^{-1}$$

and

$$M_2 = (P^{-1})^T \begin{pmatrix} \mu_1 & 0 & 0 \\ 0 & \mu_2 & 0 \\ 0 & 0 & \mu_3 \end{pmatrix} P^{-1}.$$

The metric intersection $M = M_1 \cap M_2$ is then given by

$$M = M_1 \cap M_2 = (P^{-1})^T \begin{pmatrix} \max(\lambda_1, \mu_1) & 0 & 0 \\ 0 & \max(\lambda_2, \mu_2) & 0 \\ 0 & 0 & \max(\lambda_3, \mu_3) \end{pmatrix} P^{-1}.$$

In the mesh adaptation framework, metrics allow to compute lengths h . Recall that the interpolation error on a element K is estimated by $\max_{v \in \mathcal{E}_K} v^T |H| v$. If a metric M such that

$$\max_{x \in K} v^T |H(x)| v \leq v^T M(K) v, \text{ for all } v \in \mathcal{E}_K$$

can be found, then the interpolation error on that element K is proportional to the square of the highest edge length of K in the metric M . Imposing $v^T M(K) v = tol$ on any adapted element consists then in imposing the element to be of size $h_i = \sqrt{tol/\lambda_i}$ along direction e_i . Consequently, controlling the length of the element edges allows to control the interpolation error on the mesh.

5.2.3 Error estimation for piecewise continuous functions

The transmembrane potential and the recovery variable are defined only in the heart. Moreover, with the imposition of the condition of the total current continuity, it introduces a discontinuity in the first derivative of the extracellular potential any time there is a discontinuity in the conductivities. These discontinuities arise at the internal interfaces, where the error estimation cannot be performed properly. To address this difficulty and avoid spurious mesh refinement near the interfaces, the error was estimated in subregions of constant conductivities. For instance, the error on the transmembrane potential is evaluated only in the heart, where the error on the extracellular/extracardiac potential is evaluated separately on the heart and the torso. The error estimation is based on the estimation of first and second derivatives by a superconvergent method described in [8], where the error estimation at boundaries is also treated.

5.3 Numerical results in 2D with mesh adaptation

This section shows the details of how the adaptation is integrated to the resolution process, using the finite element code MEF++ [2] together with its mesh adaptation library. Indeed, the mesh adaptation is based on the solution and this necessitates the use of a resolution-adaptation loop. In the following, two loops are presented under the form of pseudo-code, where the details are skipped for simplicity. These supplementary specifications will be detailed in sections 5.3.2 to 5.3.4. Note that both loops carefully avoid reinterpolation of interpolated quantities.

5.3.1 Pseudo-code for the resolution-adaptation loop

Let us start with Loop 1, where the adaptation strategy is used at every time step. The index t runs over the time steps from 1 to N , as well as the index m runs over

the resolution-adaptation steps from 1 to M . The solution (u, v, u_w) for the bidomain model or (u, v) for the monodomain model is represented by U . More precisely, $U_{t,m}(\mathcal{T})$ stands for the solution U at the time step t calculated at the m^{th} adaptation step (i.e. calculated on the mesh $\mathcal{T}_{t,m}$), and U exists on the mesh \mathcal{T} . The mesh \mathcal{T} on which the solution exists could be different from the mesh $\mathcal{T}_{t,m}$ where it was calculated.

Loop 1: Adaptation at every time step.

$t = 0$

while ($t < N$: number of time steps)

I: Solution of prevision: $\rightarrow U_{t+1,0}(\mathcal{T}_{t,M})$

Resolution($\mathcal{T}_{t+1,0}=\mathcal{T}_{t,M}$) using Crank-Nicholson ($t = 1$) or Gear ($t > 1$)

I.C.: $U_t = U_{t,M}(\mathcal{T}_{t,M})$, if $t > 1$, $U_{t-1} = U_{t-1,M}(\mathcal{T}_{t,M})$

First Newton guess: $U_{t,M}(\mathcal{T}_{t,M})$

$m = 1$

Resolution-adaptation loop:

while ($m < M$: number of resolution-adaptation steps)

If $m = 1$, $\mathcal{T}_{t+1,m-1} = \mathcal{T}_{t,M}$.

II: Adaptation on the solution $\rightarrow \mathcal{T}_{t+1,m}$

- on $U_{t+1,m-1}(\mathcal{T}_{t+1,m-1})$,

and

- on $U_{t,M}(\mathcal{T}_{t+1,m-1})$,

and if $t > 1$,

- on $U_{t-1,M}(\mathcal{T}_{t+1,m-1})$.

III: Reinterpolation of the first guess of the Newton iterations:

reinterpole $U_{t+1,m-1}(\mathcal{T}_{t+1,m-1}) \rightarrow U_{t+1,m-1}(\mathcal{T}_{t+1,m})$

IV: Reinterpolation of the IC of the next resolution:

if $t > 1$, reinterpole $U_{t,M}(\mathcal{T}_{t,M}) \rightarrow U_{t,M}(\mathcal{T}_{t+1,m})$

if $t > 2$, reinterpole $U_{t-1,M}(\mathcal{T}_{t-1,M}) \rightarrow U_{t-1,M}(\mathcal{T}_{t+1,m})$

V: Resolution $\rightarrow U_{t+1,m}(\mathcal{T}_{t+1,m})$

IC: $U_t = U_{t,M}(\mathcal{T}_{t+1,m})$

if $t > 1$, $U_{t-1} = U_{t-1,M}(\mathcal{T}_{t+1,m})$

1st Newton guess: $U_{t+1,m-1}(\mathcal{T}_{t+1,m})$

resolution($\mathcal{T}_{t+1,m}$) using Crank-Nicholson ($t = 1$) or Gear ($t > 1$)

$m = m + 1$

end

end

It is worth mentioning a few words about this strategy. The first step of a loop iteration consists in calculating a solution of prevision on the last mesh, i.e. the mesh resulting from the previous iteration. This mesh is obviously not suitable for solving the current time step. However, this solution of prevision provides what is needed for the mesh adaptation at the current time step. The mesh adaptation is based on metric error estimation of the solution. As the solution is calculated with an implicit Gear time-stepping scheme, calculating precisely a solution U_{t+1} requires a precise representation of solutions of the two previous time steps U_t and U_{t-1} . The metric for error estimation is then the intersection of metrics for the three solutions, and other variables for which the details are explained in section 5.3.4. The mesh adaptation procedure is based on a number of local operations (described in [8]) on the initial mesh:

1. Edge refinement,
2. Edge swapping,
3. Vertex suppression,
4. Vertex displacement.

After the calculation of the solution of prevision, the adaptation-resolution steps are repeated M times at each loop iteration.

In order to have a good mesh for the first iteration, many iterations of the internal resolution-adaptation loop are required at the first time step. Starting from a regular grid, five to ten iterations are imposed to obtain a stabilized mesh well-adapted according to the initial conditions. The time step is so small (0.1 to 0.5 ms) that the solution barely changes in one time step. For the other time steps, only one adaptation-resolution iteration is needed at each time step.

To date, almost all papers report remeshing strategies that re-adapt the mesh at

each time step (for instance in [18], [6] and [7]). It turns out that this is unnecessary as the solution does not change very much from one time step to the next, the time step being limited for accuracy. The computation of the error and matrix re-assembling are a significant part of the overall computational work. For example in [7], a factor of 43 of reduction in the number of degrees of freedom corresponds to a computational speedup of 6.4 on a cubic geometry. The work of Southern and al.[78] shows that a speedup factor of 11.2 can be obtained for a realistic heart geometry. In general, reducing the number of degrees of freedom reduces the memory requirements. However, the reduction factor in the number of degrees of freedom is considerably higher than the reduction factor for the CPU requirements. Here, our work is focussed on an effective way of representing the geometry (with level sets) combined with an attempt at reducing the number of nodes in an embedded complex geometry: the heart in the torso. The following mesh adaptation strategy (Loop 2) does not update the mesh every time step, i.e. less time is spent for adaptation and reinterpolation. The mesh is adapted when the solution changes significantly, i.e. at every S time steps. The index n is the iteration number of Loop 2, not the time step as for Loop 1.

If there is any region of the heart undergoing a depolarization, Loop 2 can be used only for a number S of time steps between two consecutive mesh adaptations, such that the refined mesh region containing the depolarization front at time step $nS + 1$ overlaps the depolarization front at time step $(n - 1)S + 1$. Remark that the mesh is adapted according to the initial conditions of iteration n , i.e. $U_{t,M}$ for $t = (n - 1)S - 1$ and $(n - 1)S$, and the solution of prevision $U_{t,M}$ for $t = nS + 1$. This way, the mesh is assumed to be good for all the S time steps of iteration n , only because the refined region covers all points in the depolarization front. For large S which does not satisfy this condition, another strategy should be used, for instance, using solutions of intermediate time steps. When there is no region in depolarization (cells in repolarization and at rest only), a larger S can be used while keeping the

same accuracy.

Loop 2: Adaptation at every S time steps.

$n = 0$: 1 iteration of Loop 1.

$n = 1$

while ($n < N$: maximal number of iterations)

I: Solution of prevision ($t + 1$ runs from $(n - 1)S + 2$ to $nS + 1$):

Resolution($\mathcal{T}_{n,0} = \mathcal{T}_{n-1,M}$) using Gear

I.C. ($t = (n - 1)S + 1$): $U_t = U_{t,M}(\mathcal{T}_{n,0})$ and $U_{t-1} = U_{t-1,M}(\mathcal{T}_{n,0})$

First Newton guess ($t = (n - 1)S + 1$): $U_{t,M}(\mathcal{T}_{n,0})$

→ Gives the solution $U_{t+1,0}(\mathcal{T}_{n,0})$

$m = 1$

Resolution-adaptation loop:

while ($m < M$: number of resolution-adaptation steps)

If $m = 1$, $\mathcal{T}_{n,m-1} = \mathcal{T}_{n-1,M}$.

II: Adaptation on

• $U_{t+1,m-1}(\mathcal{T}_{n,m-1})$, the first Newton guess of time step $t + 1 = (n - 1)S + 2$,

• $U_{t,M}(\mathcal{T}_{n,m-1})$ and $U_{t-1,M}(\mathcal{T}_{n,m-1})$, the I.C. of time step $t + 1 = (n - 1)S + 2$,

and

• $U_{t+1,M}(\mathcal{T}_{n,m-1})$, the solution of prevision of time step $t + 1 = nS + 1$.

→ Gives the mesh $\mathcal{T}_{n,m}$

III: Reinterpolation of the first Newton guess and the I.C. of the next resolution:

reinterpolate $U_{t+1,m-1}(\mathcal{T}_{n,m-1}) \rightarrow U_{t+1,m-1}(\mathcal{T}_{n,m})$

reinterpolate $U_{t,M}(\mathcal{T}_{n-1,M}) \rightarrow U_{t,M}(\mathcal{T}_{n,m})$

reinterpolate $U_{t-1,M}(\mathcal{T}_{n-1,M}) \rightarrow U_{t-1,M}(\mathcal{T}_{n,m})$

IV: Resolution

I.C.: $U_t = U_{t,M}(\mathcal{T}_{n,m})$ and $U_{t-1} = U_{t-1,M}(\mathcal{T}_{n,m})$

First Newton guess: $U_{t+1,m-1}(\mathcal{T}_{n,m})$

resolution($\mathcal{T}_{n,m}$) using Gear

→ Gives the solution $U_{t+1,m}(\mathcal{T}_{n,m})$

$m = m + 1$

end

end

5.3.2 Using level sets and fiber arrangement in a resolution-adaptation loop

The distance function originates from the segmentation process, so it exists on the first mesh generated on the medical image. For instance, it could be simply a regular grid with the nodes centered on the image pixels. Any time the mesh is adapted, the distance function has to be reinterpolated from the original mesh and not from the last mesh it was reinterpolated. This strategy is used in the resolution-adaptation loop in order to keep the best level set description of geometries and avoid reinterpolation errors.

Using either calculated vector field or data coming from diffusion tensor MRI, the fibers orientation is information which also exists on the original mesh. The reinterpolation procedure in the loop requires care. Figure 5.3.2 illustrates the problem of reinterpolating a vector field from the original mesh \mathcal{T}_0 (in black) to the destination mesh (in red). Suppose that there exists a vector field interpolated in $P_1(K)$, for $K \in \mathcal{T}_0$. In figure 5.3.2, there are two vectors illustrated on the end nodes of an edge of the original mesh. One points upward and the other, downward. Pointing upward or downward is not important, as the vertical eigendirection is as well represented. If this vector field is reinterpolated on the red mesh, all the components of the vector on the red node (on the same edge) could be zero, while this vector should be vertical.

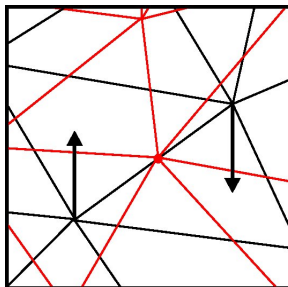
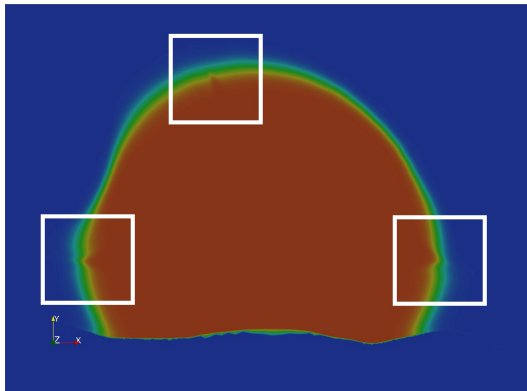


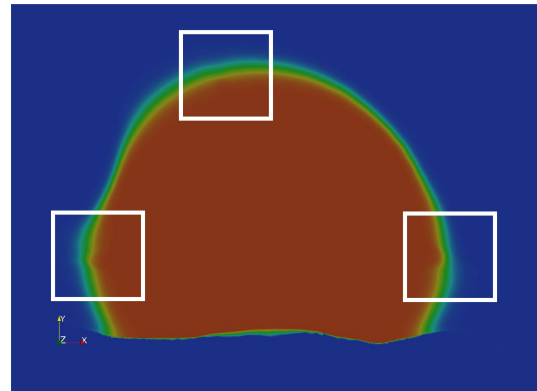
Figure 5.1: Problems in reinterpolating a vector field.

To address this problem, the conductivity tensor is built on the original mesh

using equation (1.2.17). Instead of reinterpolating the fiber vector field, this is the conductivity tensor (a 2×2 symmetric matrix in 2D) which is reinterpolated any time a new mesh results from the adaptation. Recall that equation (1.2.17) is used for transforming the conductivity tensor in a local system of coordinates given by the eigendirections of the fibers. Figure 5.2 illustrates that reinterpolating the conductivity tensor gives better results. The notches appearing in the depolarization front (figure 5.2(a)) caused by the error introduced by the reinterpolation of fibers vector field are attenuated when reinterpolating the conductivity tensor (figure 5.2(b)).



(a) Reinterpolation of fibers vector field in the adaptation loop.



(b) Reinterpolation of conductivity tensor in the adaptation loop.

Figure 5.2: The transmembrane potential propagating through the myocardium with a fiber arrangement. The notches (in boxes) appearing the depolarization front (figure 5.2(a)) caused by the error introduced by the reinterpolation of fibers vector field are attenuated when reinterpolating the conductivity tensor (figure 5.2(b)).

5.3.3 Calculating isochrons in a resolution-adaptation loop

The isochrons of depolarization, repolarization, etc. (see equation (3.2.1) for a definition) are very useful for summarizing a whole numerical simulation. They are updated at each time step. For obvious reasons, they have to be calculated on a different mesh from all adapted meshes. In fact, an adapted mesh at a given loop iteration minimizes

the error for the solution at that iteration loop, but can be very poor for solutions of other loop iterations. Moreover, information can be lost definitively by interpolating solutions of previous time steps, e.g. when the depolarization front existed on a region where the mesh is now coarse.

The support mesh for computing the isochrons is called the background mesh. It has to be fine enough that the isochrons satisfy a certain error tolerance. However, if the background mesh is too fine, i.e. the wave front passes more than one mesh element in a time step, then the resulting isochron function can be constant on a whole element. The background mesh used in the 2D simulations with a realistic geometry has 243, 039 nodes (see figure 5.3). The mesh is finer in the heart; the mesh size is about twenty times finer in the heart than in the torso and can be up to thirty times smaller near the boundary of the heart than in the torso. Precisely, the background meshsize is $h \sim 3$ mm and represents twice the front displacement during a time step of 0.3 ms.

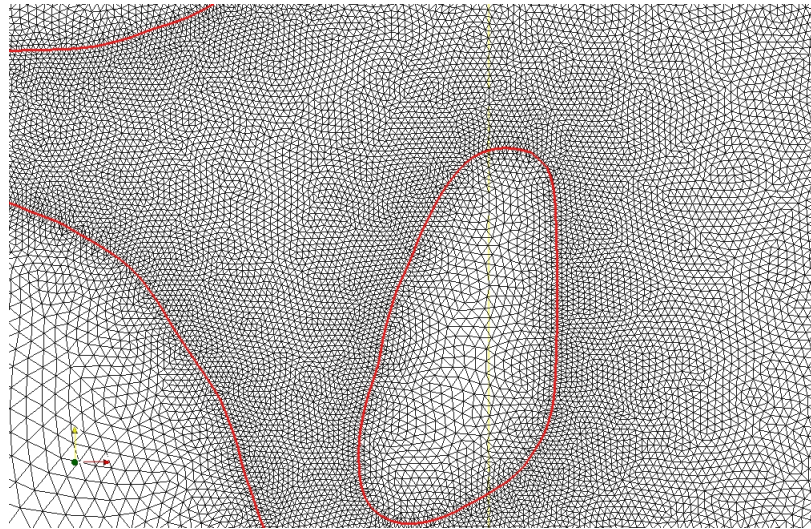


Figure 5.3: Background mesh used to calculate the isochrons. The figure is zoomed near the smallest cavity of the heart.

5.3.4 Refining the mesh near the internal interfaces

For simplicity, the pseudo-code of loops 1 and 2 does not take into account of the mesh adaptation on variables other than solutions, though it is done in the actual adaptation code. For instance, for the heart-torso coupling problem with non body fitted meshes, there is a mesh refinement in the neighborhood of the surface of the heart. A distance function φ is available directly from the segmentation of the medical image. It is a scalar function giving the signed distance from the surface of the heart. It is negative inside the heart and positive otherwise. The level set $\varphi = 0$ defines the surface of the heart (see section 1.3.2). The following function, built from the distance function, is used with various values of δ to refine the mesh near the surface of the heart. Most of the simulations used two functions to refine the mesh near the interface, one with $\delta = 1.2$ mm and another with $\delta = 2.4$ mm. Both functions are considered in the metric intersection.

$$f(\varphi) = \begin{cases} \cos\left(\frac{\pi\varphi}{\delta}\right) & -\delta < \varphi < \delta, \\ -1 & \text{otherwise.} \end{cases}$$

5.3.5 First numerical solutions with mesh adaptation

We now present the action potential computed on the 2D realistic geometry illustrated on figure 4.2(b). The parameters of the models are all given in section 4.4. The action potential is initiated with localized super-threshold regions showed in figure 4.15, and evolves throughout the cardiac tissue as in figure 4.18. Loop 1 is used so the mesh is adapted every time step. The number of nodes is limited to 20,000. Figures 5.4 and 5.5 clearly demonstrate that solution variations are efficiently captured by the remeshing method. During depolarization, the solution varies from 0 to 1 in 8 ms, a very sudden variation compared to the repolarization where solution varies from 0.5 to 0 in 30 ms. This can be seen directly in the mesh, where no obvious refinement is

necessary during repolarization.

Anisotropic mesh adaptation provides means to control and mitigate the loss of accuracy for non body fitted meshes, by refining and aligning the elements along the interface. This is illustrated on figure 5.6 where mesh elements follow very precisely the interface even in regions with high curvature.

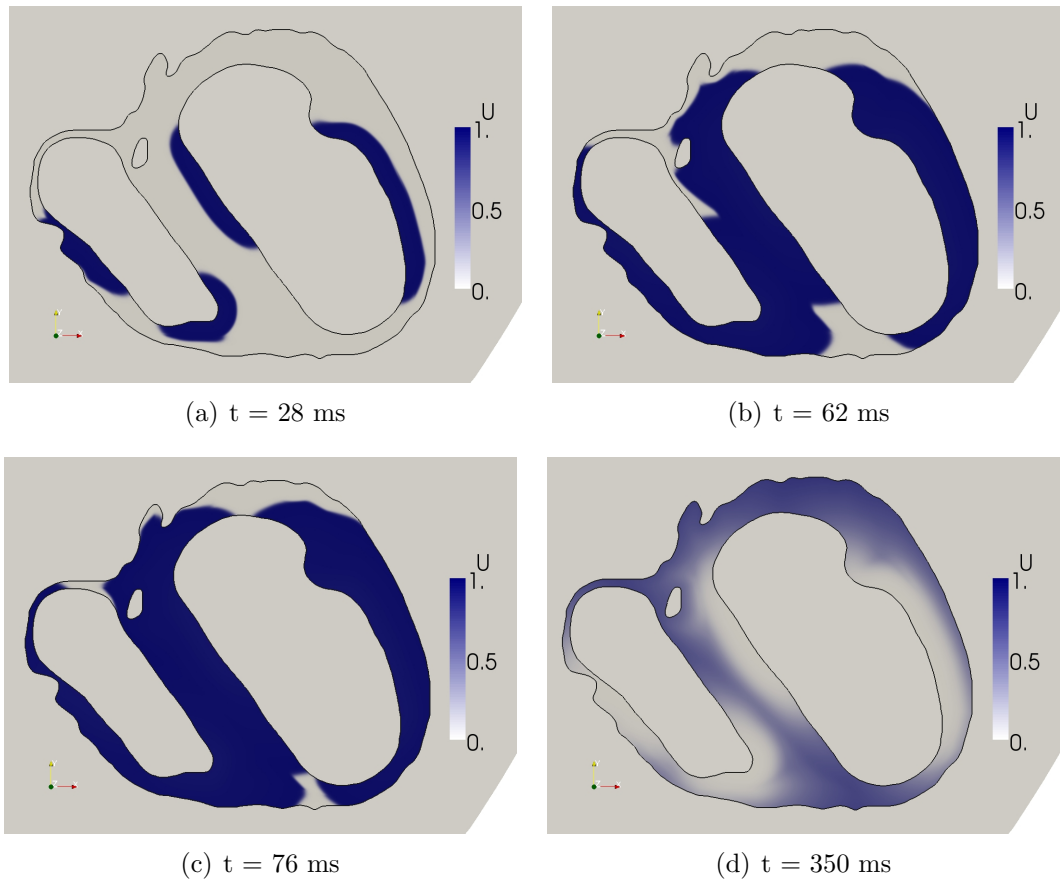


Figure 5.4: The solution at selected times for the non body fitted simulation with the adaptive strategy.

Whether or not the mesh is body fitted, it is worth verifying if adapting the mesh near the interface improves the accuracy of the solution. By comparing two simulations on body-fitted meshes (with one using adaptation according to the functions described above), one can note a slight difference between the isochrons of depolar-

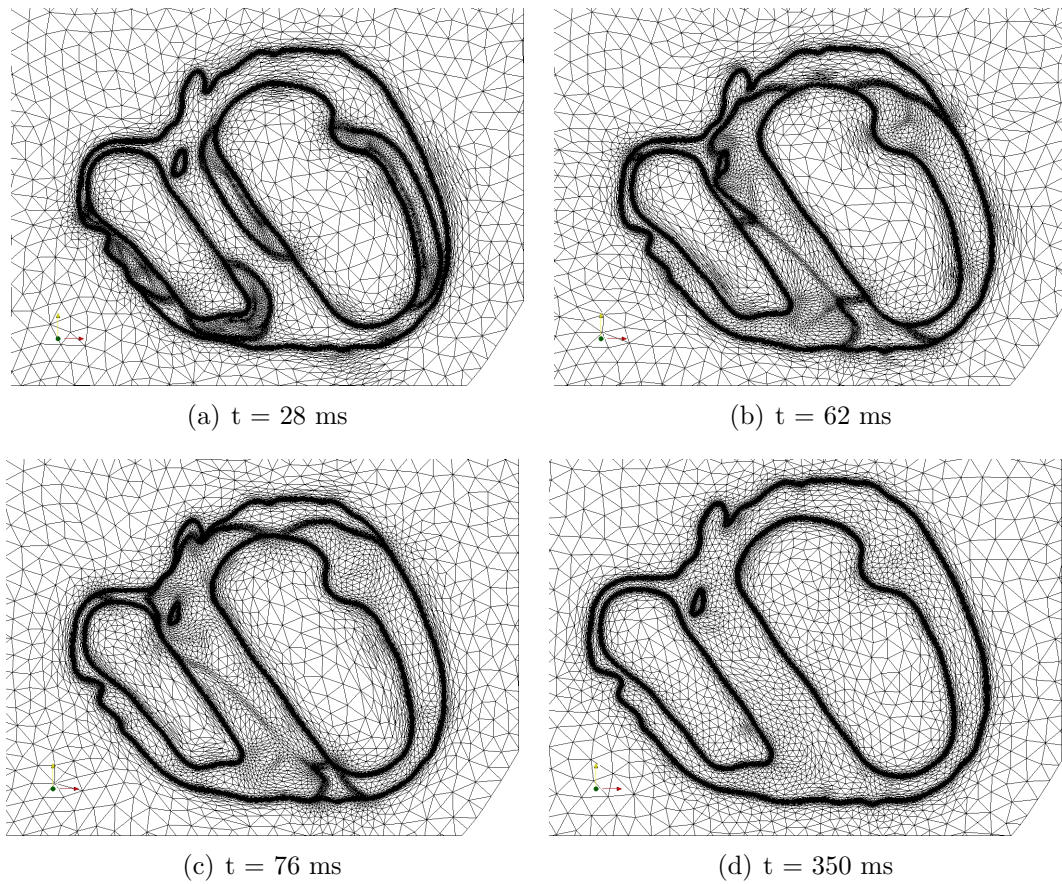


Figure 5.5: The adapted mesh at selected times for the non body fitted simulation. During the repolarization (d), solution variations are smoother than in depolarization (a), (b) and (c). The mesh is refined where the solution gradient is high, i.e. in the depolarization front.

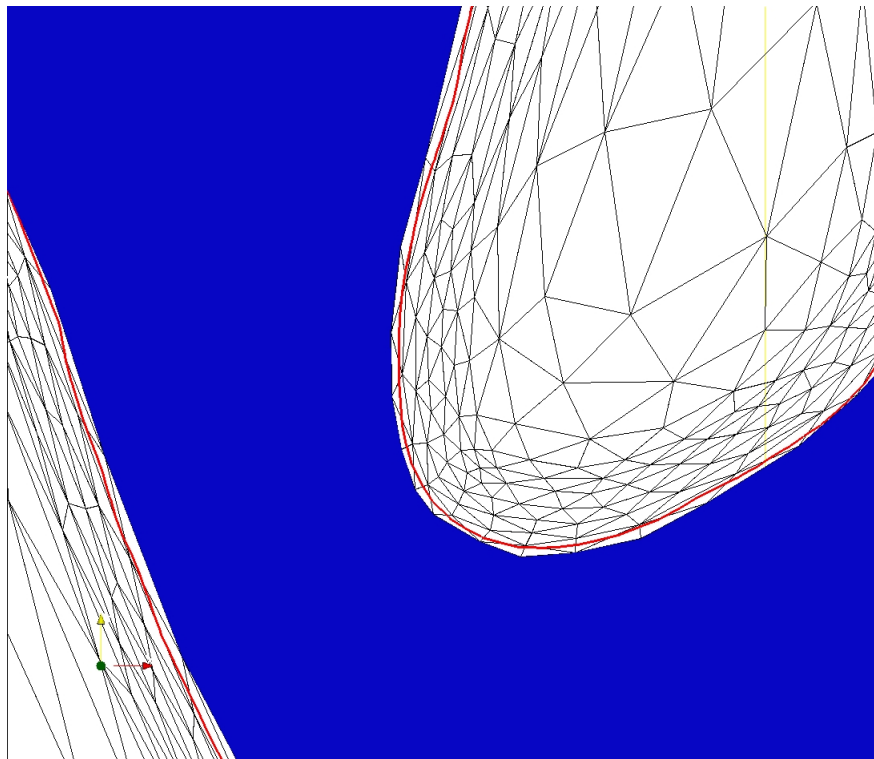


Figure 5.6: The anisotropic mesh is refined near internal interfaces. The red curve represents the level set $\varphi = 0$ of the distance function φ from the surface of the heart. The domain of the heart (colored in blue) is defined as the largest set of elements completely inside $\varphi \leq 0$. This figure shows a portion of the heart cavity with the largest interface curvature.

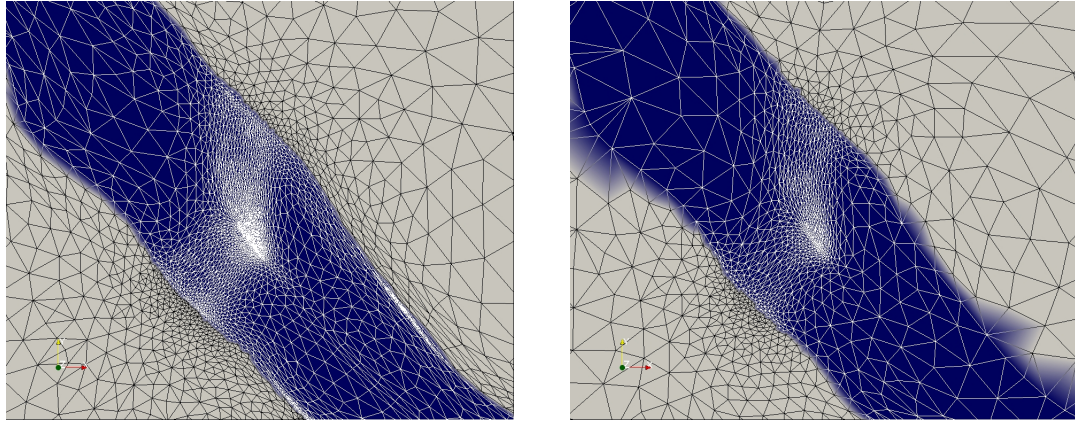
ization. The maximal difference between the isochrons of depolarization is about 0.5 ms when limiting the number of nodes to 20,000 (figure 5.7). The shift between two contours after 80 ms is comparable to the mesh size of the background mesh used for computing isochrons. Note that the wavefront of the simulation without adaptation near the interface is in advance (of 0.5 ms for a simulation of 80 ms) compared to the solution with adaptation near the interface.

5.3.6 Optimization of the adaptation-resolution loop

Adapting every time step or not

Using Loop 1 is not very efficient in terms of CPU time. The mesh is adapted each time step and if the time step is very small, the solution barely changes from one time step to another. The operations performed in pre- and post-processing (reading and writing data, assembling matrices, etc.), and for the adaptation (error estimation, reinterpolation, reading and writing data, etc.) are computationally intensive. Using Loop 1 to analyze the influence of the time discretization is inadequate. For example, simulating a whole cycle of 1000 ms can take about 18 days when using Loop 1 with a time step of 0.3 ms, when imposing a maximal number of 20,000 mesh nodes. The gain is then of 6.3 when imposing a maximal number of mesh nodes at 20,000 with Loop 2.

Table 5.1 summarizes the results obtained with Loop 2. The notation “/20” means that the WC (Wall Clock) or CPU time is the total time for 20 occurrences of the process mentioned in the first column. The simulation with time steps of 1 ms is then equivalent to a simulation performed with Loop 1 as adaptation is done every ms. The gain of using Loop 2 is estimated in the last row. For instance, the gain of using Loop 2 instead of Loop 1 for a time step of 0.05 ms is obtained by factoring out the jobs in Loop 2 that are repeated every iterations of Loop 1, i.e. the assembling and the whole adaptation process. The CPU times associated with these jobs in one



(a) Mesh refined along the internal interfaces.

(b) Mesh NOT refined along the internal interfaces.

(c) Isovalue $u = 0.13$ at $t=80$ ms for both adaptation strategies (a) in red and (b) in black.

Figure 5.7: Body fitted mesh at time 80 ms using different adaptation strategies: (a) refining along the internal interfaces, and (b) not refining along the internal interfaces. Isovalue $u = 0.13$ at $t=80$ ms are shown in (c) for both adaptation strategies (a) and (b). The isovalue for the strategy without adaptation along the internal interfaces is ahead with about 0.5 ms compared to the isovalue for the strategy with adaptation along the internal interfaces.

iteration of Loop 2 are then estimated with 20 times the CPU time using Loop 1 with a time step of 1 ms (last column). Finally, a whole iteration with time step 0.05 ms using Loop 1 is estimated with $(281 - 227 + 20 \times 20) + (20 \times 70) + (289 - 232 + 20 \times 17)$ which gives 2251 ms.

Time step (ms)	0.05	0.1	0.5	1
Solution of prevision				
Resolution (WC)	330/20	185/10	61/2	37
Resolution (CPU)	281/20	156/10	51/2	28
Assembling (CPU)	227/20	123/10	38/2	20
Newton's iterations (CPU)	28/20	18/10	9/2	6
Adaptation				
Total (WC)	122	117	93	80
Total (CPU)	101	93	83	70
Error estimation (CPU)	13	13	13	9.5
Adaptation (CPU)	54	43	41	30
Solution				
Resolution (WC)	336/20	196/10	63/2	30
Resolution (CPU)	289/20	167/10	54/2	25
Assembling (CPU)	232/20	133/10	39/2	17
Newton's iterations (CPU)	31/20	19/10	10/2	6
Total (CPU)	671	416	188	123
Estimated gain when using Loop 2 instead of Loop 1	3.35	2.73	1.29	1

Table 5.1: Wall clock (WC) and CPU times (s) for a typical iteration of Loop 2 for simulations with various time steps during the depolarization.

A more systematic way of determining when it is necessary to adapt should be investigated, rather than simply adapting every n steps. For example, unnecessary mesh adaptations during the recovery phase could be avoided.

Influence of the time discretization

We use Loop 2 with an adaptation procedure limiting the number of nodes to 20,000 in order to analyze the effect of the time step on the solution accuracy during the

depolarization. Remark that the following results are valid only for the MS model with the parameters proposed in section 2.4, giving an AP with an upstroke duration of about 8 ms. We also use body fitted meshes to make sure that there is no error introduced by boundary effects. Then we shorten the time step until the isochrons of depolarization are converged, for instance with less than a certain percentage of error. The reference solution is calculated with a time step of 0.01 ms with 40,000 elements. Table 5.2 illustrates the gain in CPU time and the associated maximal error on the isochrons of depolarization when using various time steps. The simulations are performed for a time interval of 80 ms, and the relative CPU time (second column) is calculated with a ratio of the total CPU time of the whole simulation to the total CPU time of the whole reference simulation. Positive values of delays (third column)

Time step (ms)	Relative CPU time	Maximal delay in iso_{depol} (ms)	Relative error on iso_{depol} (%)	Relative error on the speed (%)
0.01	1	0	0	0
0.02	0.543	<0.5	<0.625	<0.63
0.05	0.248	<0.5	<0.625	<0.63
0.1	0.188	0.5	0.625	0.63
0.5	0.102	+1	1.25	1.27
1	0.091	+5	6.25	6.67
2	0.048	+19	23.75	31.15

Table 5.2: Accuracy of the solution during the depolarization.

mean that the solution has a higher speed than the reference solution (with a time step of 0.01 ms). The values ”< 0.5 ms” mean that the background mesh used to compute the isochrons of depolarization was not fine enough to detect delays of less than 0.5 ms.

We decided to afford an error of propagation of about 1.25% for the further simulations by taking a time step of 0.5 ms. Taking the largest time step to reach this error is important also because of the CPU time taken for the calculation. For this error threshold, doubling the number of time step roughly doubles the amount

of work (see the second column). Remark that this time step may not be appropriate for an other set of model's parameters.

A delay on the isochrons of depolarization is translated in an error on the speed of the depolarization wavefront (see the third and last columns). The isochrons of maximal depolarization iso_{max} were also computed so that the upstroke duration could be analyzed. It turns out that the upstroke duration is not affected by the time discretization. This is also observed in section 3.2 when the time steps are far from the valued indicated for instability (see Table 3.4).

The next step is to analyze the effect of the time discretization on the solution accuracy right after the heart depolarization, while cells start repolarizing. Again, body fitted meshes and Loop 2 are used together with an adaptation procedure limiting the number of nodes to 20,000. Using the same model parameters as for the depolarization gives an AP with a downstroke duration of about 32 ms. For the initial conditions, we use the result of a numerical simulation previously calculated up to 280 ms with a time step of 0.3 ms. At 280 ms, there is already a repolarization front forming in the region of the activation zone. We then perform simulations for a supplementary 80 ms with various time steps and measure the CPU times and solution accuracies with the isochrons of repolarization (see table 5.3).

Time step (ms)	Relative CPU time	Maximal delay in iso_{repol} (ms)
0.5	1	0
1	0.437	<0.5
2	0.232	+2
5	0.110	+5
10	0.058	+11

Table 5.3: Accuracy of the solution during the repolarization.

For the same error threshold as in depolarization, we can use a time step up to 1 ms. Taking a time step of 1 ms in the repolarization instead of 0.5 ms (used for the

depolarization) gives a considerable gain of 50% in CPU time. For a rule of thumb, we could say that in order to study a phenomena 4 times longer (repolarization vs depolarization), we can use a time step which is roughly twice longer. Note that again, the speed of the repolarization front is obviously altered by the time discretization though the downstroke duration is not.

Influence of the space discretization

To analyze the influence of the space discretization in the depolarization phase (the first 80 ms), we use a time step of 0.1 ms and Loop 2 with an adaptation procedure limiting the number of nodes to different values. The mesh is adapted every 1 ms, so S is equal to 10. Table 5.4 gather the WC and CPU times while using Loop 2 with a single step of adaptation-resolution after the calculation of the solution of prevision.

Nb of nodes	5,000	10,000	20,000
Solution of prevision			
Resolution (WC)	87	126	185
Resolution (CPU)	54	86	156
Assembling (CPU)	23	36	123
Newton's iterations (CPU)	4	8	18
Adaptation			
Total (WC)	55	76	117
Total (CPU)	34	55	93
Error estimation (CPU)	5	9	13
Adaptation (CPU)	16	25	43
Solution			
Resolution (WC)	88	121	196
Resolution (CPU)	54	83	167
Assembling (CPU)	23	35	133
Newton's iterations (CPU)	4	8	19
Total (CPU)	192	224	416

Table 5.4: Wall clock (WC) and CPU times (s) for a typical iteration of Loop 2 for simulations with various number of nodes (imposed at the adaptation step) during the depolarization. The time step is 0.1 ms.

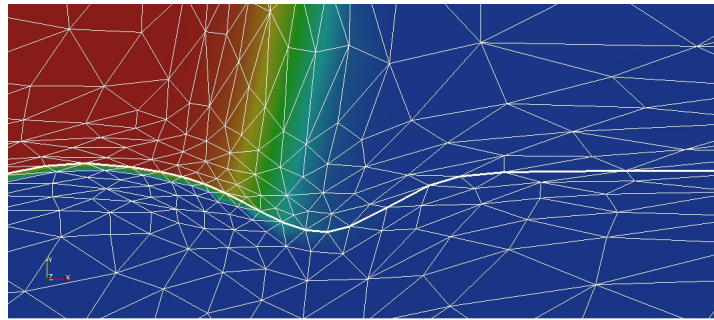
It is not clear that using less nodes is better. In fact, the adaptation is rather unstable with 5,000 nodes, stable with 10,000 nodes and very stable and reliable with 20,000 nodes. With 5,000 nodes for instance, it is difficult to manage the adjustment of the error threshold on several variables, while keeping the number of nodes this low. This is why the remeshing strategy does not capture very well either the solution variations or the heart surface. See figure 5.8 for a comparison of the meshes at a given time of the simulations presented in table 5.4. One way to stabilize the adaptation is by doing several resolution-adaptation iterations at each loop iteration. However, we may lose all the gain of using less nodes as we solve and adapt more than once every iteration.

Estimating the error on the isochrons of depolarization by comparing with isochrons calculated when limiting the number of nodes to 40,000, we find that:

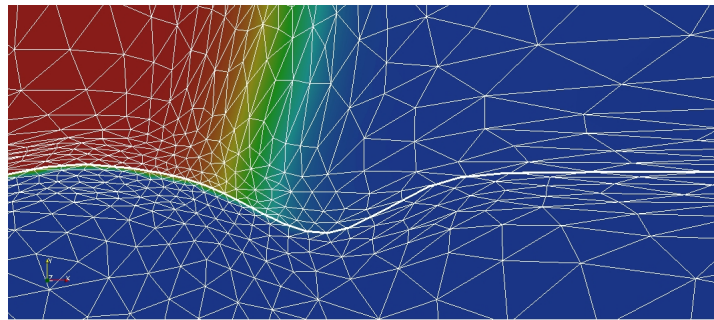
- if limiting the number of nodes to 5,000, the wavefront is in advance of 5 ms after a simulation of 80 ms,
- if limiting the number of nodes to 10,000, the wavefront is in advance of 0.5 ms after a simulation of 80 ms,
- if limiting the number of nodes to 20,000, the wavefront is in late of 0.5 ms after a simulation of 80 ms.

This means that using 10,000 nodes is about the minimal number of nodes that we can afford to have an error of less than 1% in the isochrons of depolarization. We mention finally that the analysis of the convergence of the method with adaptation cannot be performed correctly using the isochrons as these are calculated on a background mesh of constant meshsize.

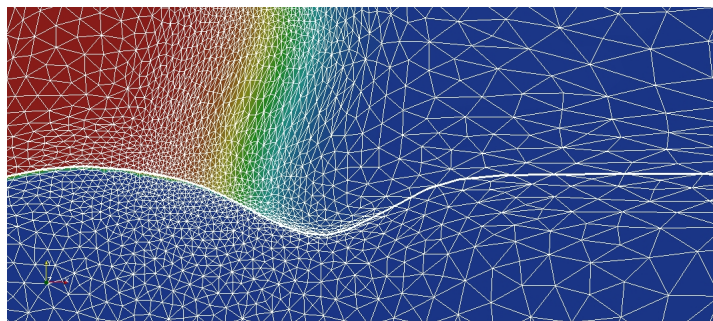
Remark 14 (Comparison with uniform meshes) *Using uniform meshes is necessary to evaluate the precision of simulations with adaptation, as well as to estimate the real gain of using mesh adaptation. However, this has already been proved in [7]*



(a) 5,000 nodes



(b) 10,000 nodes



(c) 20,000

Figure 5.8: Zoom of the adapted meshes along an internal interface. The region illustrated is near the bottom of the heart. Meshes at time $t = 62$ ms with a number of nodes limited to 5,000 (a), 10,000 (b) and 20,000 (c). The background color is the magnitude of u with $u = 1$ in red and $u = 0$ in dark blue.

for a mesh adaptation strategy with a remeshing every time step. The depolarization time of the solution of the adaptive method was compared with the asymptotic value computed on uniform meshes as if we were keeping refining these uniform meshes. As obtaining the asymptotic solution was not even possible with the available computational resources, the depolarization time on the finer uniform meshes was obtained using Richardson extrapolation. The asymptotic solution recovered from Richardson formula were found to be close to the values computed on adapted meshes. We decided to prevent from doing this laborious study as it was not necessary to validate our adaptation strategy.

5.4 Simulating the movement of the heart embedded in the torso

Level set methods turn out to be very efficient methods when considering moving geometries. This section demonstrates the application of level set methods in cardiac electrophysiology when moving domains with complex geometries are involved. We first briefly review the considerations to take when modeling and solving the conduction contraction coupling, and then bring an alternative way of solving the problem when using a level set description of the domains.

5.4.1 Deforming the heart geometry using small/large deformations

The conduction contraction coupling can be modeled with different approaches. See [45] for a good review. We present here the idea of a model where the electrical simulation is used as an input in the mechanical model without mechano-electrical feedback. The work of Chapelle and al. [17] is an example of this type of model. The model includes mainly three mechanical components: transmembrane potential

propagation, active contraction forces, and passive biomechanics. The evolution of the displacement λ of each mesh node is governed by the following equation:

$$M\ddot{\lambda} + C\dot{\lambda} + K\lambda = F_b + F_c,$$

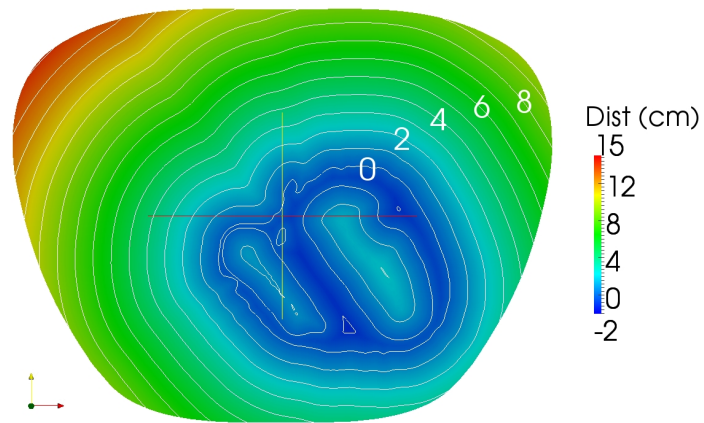
where M , C , and K are the mass, damping, and stiffness matrices, respectively, F_b is the external load from boundary conditions (blood pressure, valves), F_c is the force vector for active contraction. This contraction force is applied along a local fiber orientation and is controlled by the transmembrane potential u and several other parameters. Remark that the segmentation of time series of medical images can be integrated in the model equations. We voluntarily avoid the details for simplicity and we refer the reader to [77].

In this method, the displacement vector field λ is calculated and the mesh nodes are displaced accordingly. In the following section, we introduce a method that connects the level set using a velocity vector field. We attempt to use such a method in the perspective of using, in addition, mesh adaptation and non-body fitted meshes.

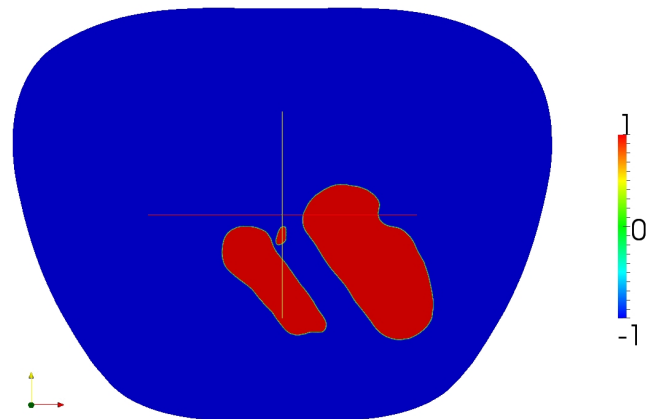
5.4.2 Deforming the heart geometry using non-body fitted meshes and level sets

The aim of the simulation presented here is to prove the use of a time sequence of segmented medical images for defining the motion of cardiac geometries. No model of electromechanical coupling is explicitly used here. The computational mesh could be eventually built from time interpolation of patient-specific anatomical data based on medical image segmentations. In the lack of these time series, we build a fictitious time dependent level set description of the heart based on the same level set description as in section 4.4. In the simulations, the initial conditions and the parameters of the equations are also the same.

The distance function from the heart surface $\varphi(x)$ and the sign function for the cavities $s_c(x)$ are used for defining the heart domain H . The function $s_c(x)$ is a piecewise constant function illustrated in figure 5.9, that is equal to 1 in the heart cavities, and -1 elsewhere.



(a) The distance function from the heart surface $\varphi(x)$.



(b) The sign function for the cavities $s_c(x)$, a piecewise constant function obtained from segmentation of a medical image.

Figure 5.9: The data coming from a segmented CT scan used to build the fictitious moving heart.

$$H = \{x \in \Omega | \varphi(x) < endo(t) \text{ and } s_c(x) > 0\} \cup \{x \in \Omega | \varphi(x) < epi(t) \text{ and } s_c(x) < 0\},$$

where $endo(t)$ and $epi(t)$ are the time varying thresholds, respectively, for the endocardium and the epicardium,

$$endo(t) = endo_i + (endo_f - endo_i) \zeta(t)$$

with $endo_i = 0.5$ cm and $endo_f = 6$ cm, and

$$epi(t) = epi_i + (epi_f - epi_i) \zeta(t)$$

with $epi_i = 10$ and $epi_f = 1$. Both threshold functions are defined with the following piecewise sigmoid function $\zeta(t)$:

$$\zeta(t) = \begin{cases} \frac{KP_0e^{r_s t}}{K+P_0(e^{r_s t}-1)} - P_0 & \text{if } t \leq 300 \text{ ms,} \\ \zeta(300)e^{-r_d(t-300)} & \text{if } t > 300 \text{ ms,} \end{cases}$$

with $P_0 = 0.0002$, $K = 1 + P_0$, $r_s = 0.05$ and $r_d = 0.03$. Figure 5.10 shows that the function $\zeta(t)$ is chosen so that it approaches qualitatively experimental measures performed on cardiac cells of a carp[66].

Figures 5.11 to 5.14 show selected time steps of a numerical simulation with mesh adaptation of a moving heart described by level sets. The heart depolarizes (a) and when it is completely depolarized (b), muscle contraction has already been initiated. Just before repolarizing (c), the heart reaches maximal contraction resulting in muscle thickening in the cross section illustrated in (d) and (e). The muscle progressively returns to its rest state in terms of potential and force contraction after a certain portion of the heart is repolarized (f).

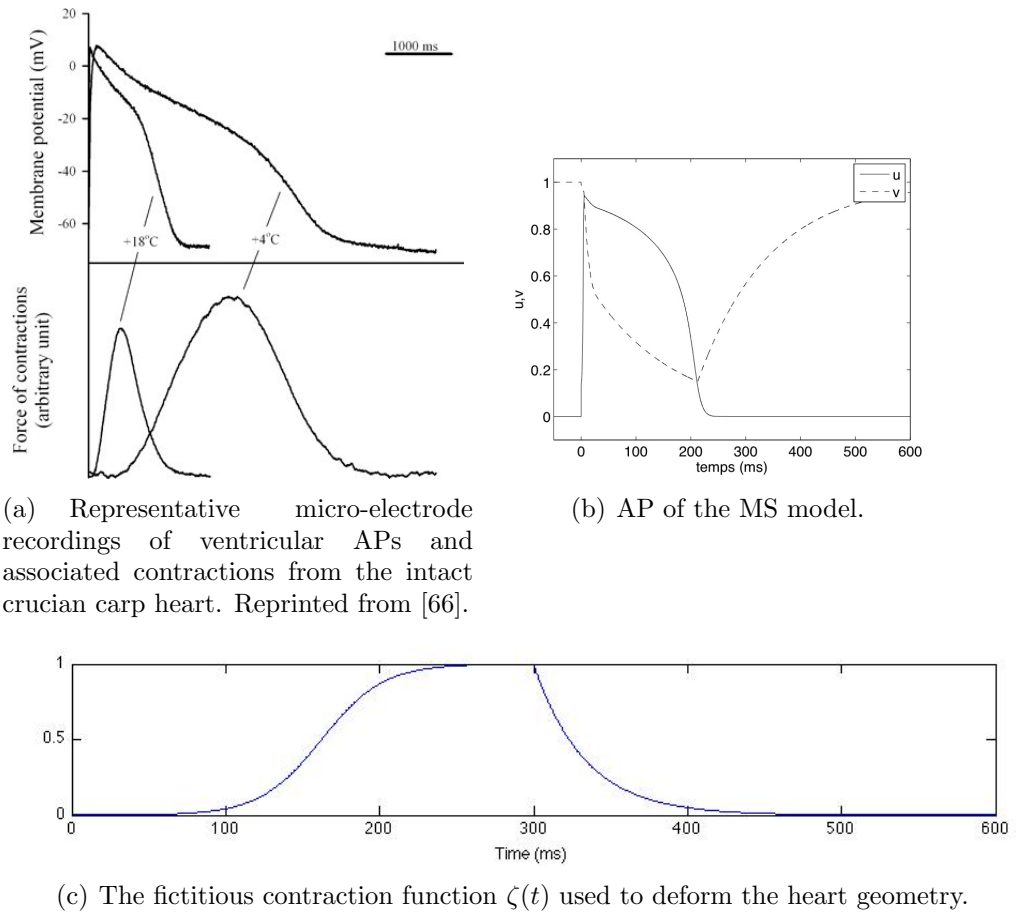


Figure 5.10: Comparison of experimental measures and our model for the relation between the transmembrane potential and the force of contraction.

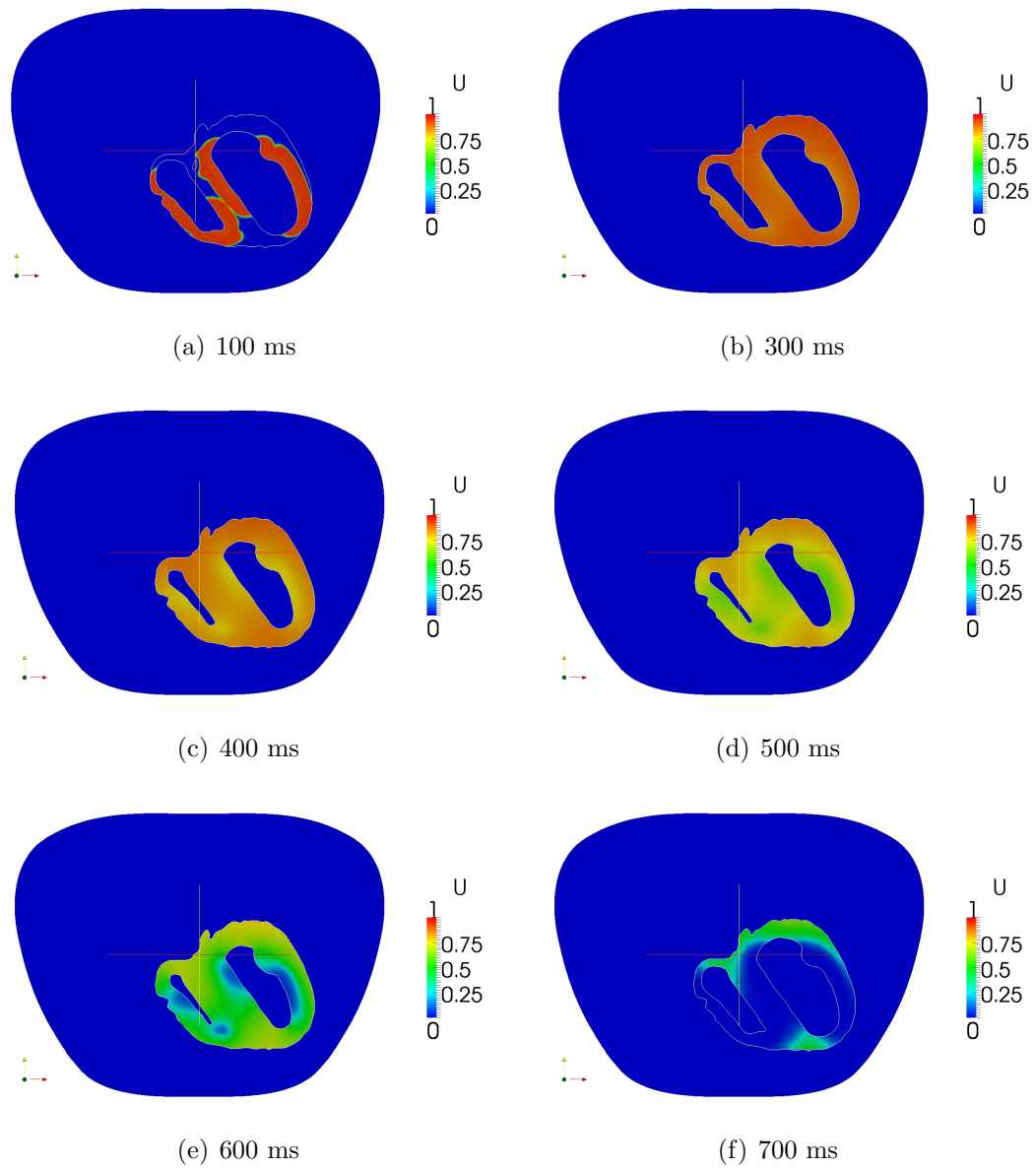


Figure 5.11: The transmembrane potential u calculated on an adapted non body fitted mesh of a moving level set based geometry.

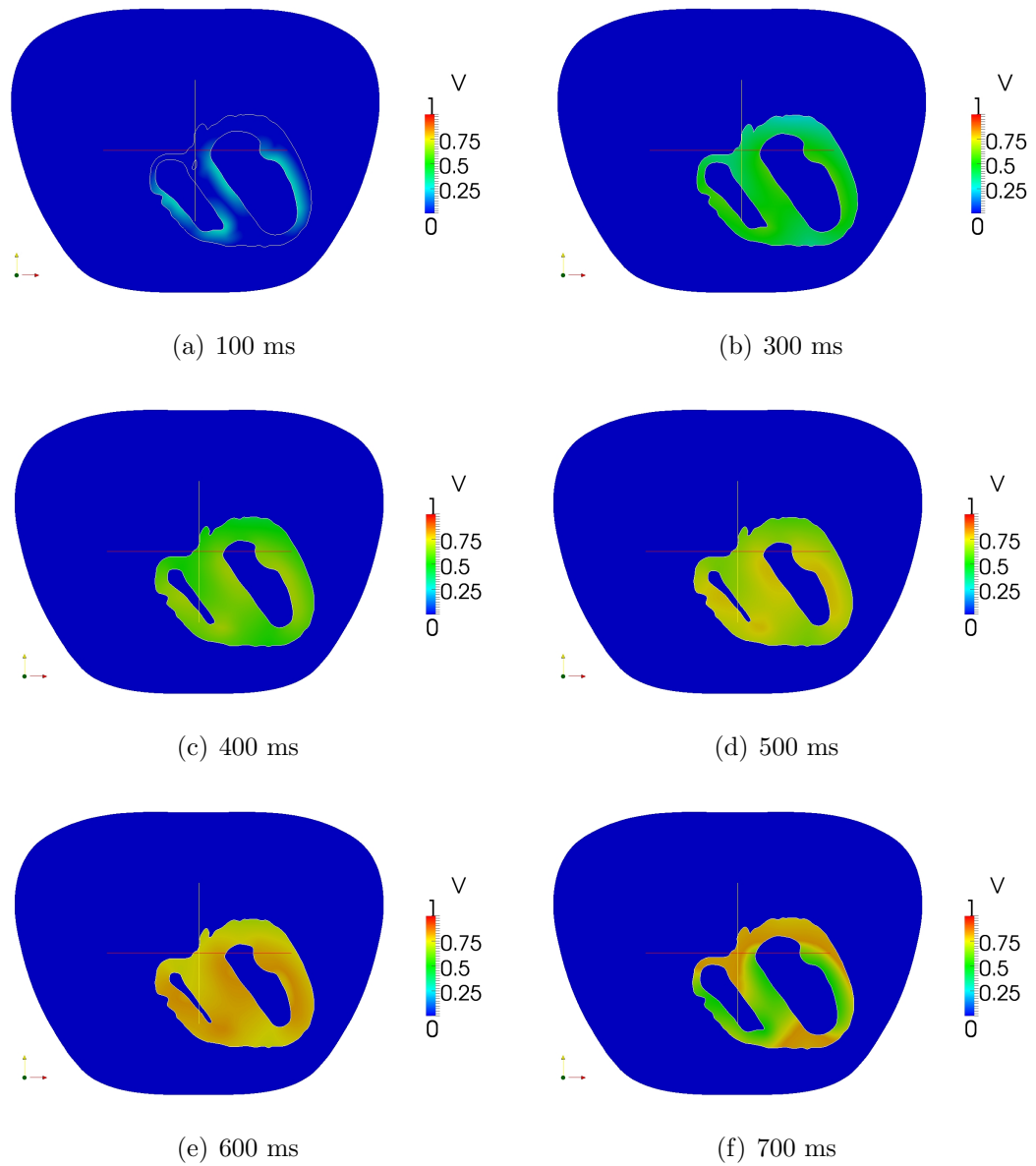


Figure 5.12: The recovery variable v of the MS model calculated on an adapted non body fitted mesh of a moving level set based geometry.

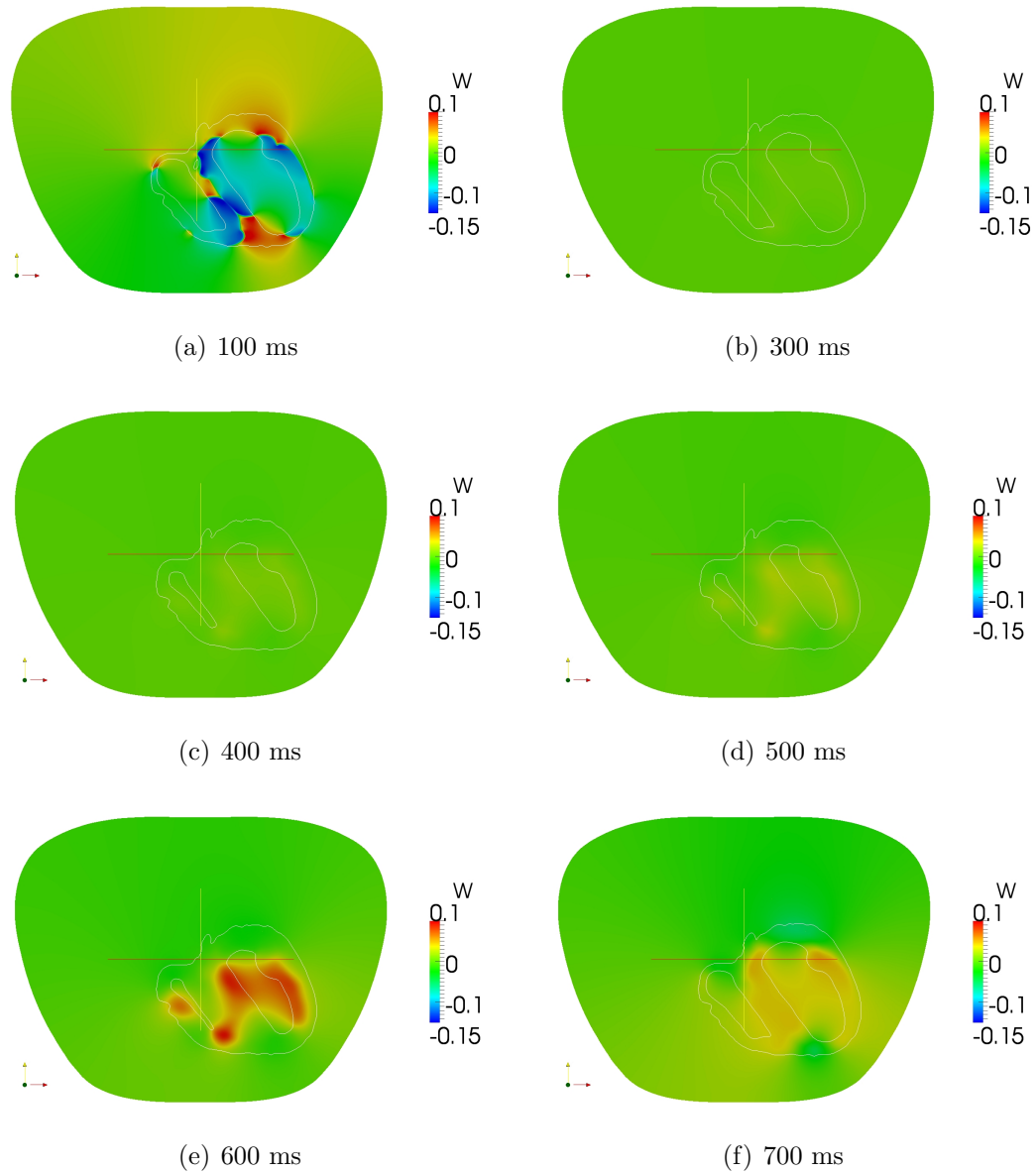


Figure 5.13: The extracellular/extracardiac potential u_w calculated on an adapted non body fitted mesh of a moving level set based geometry.

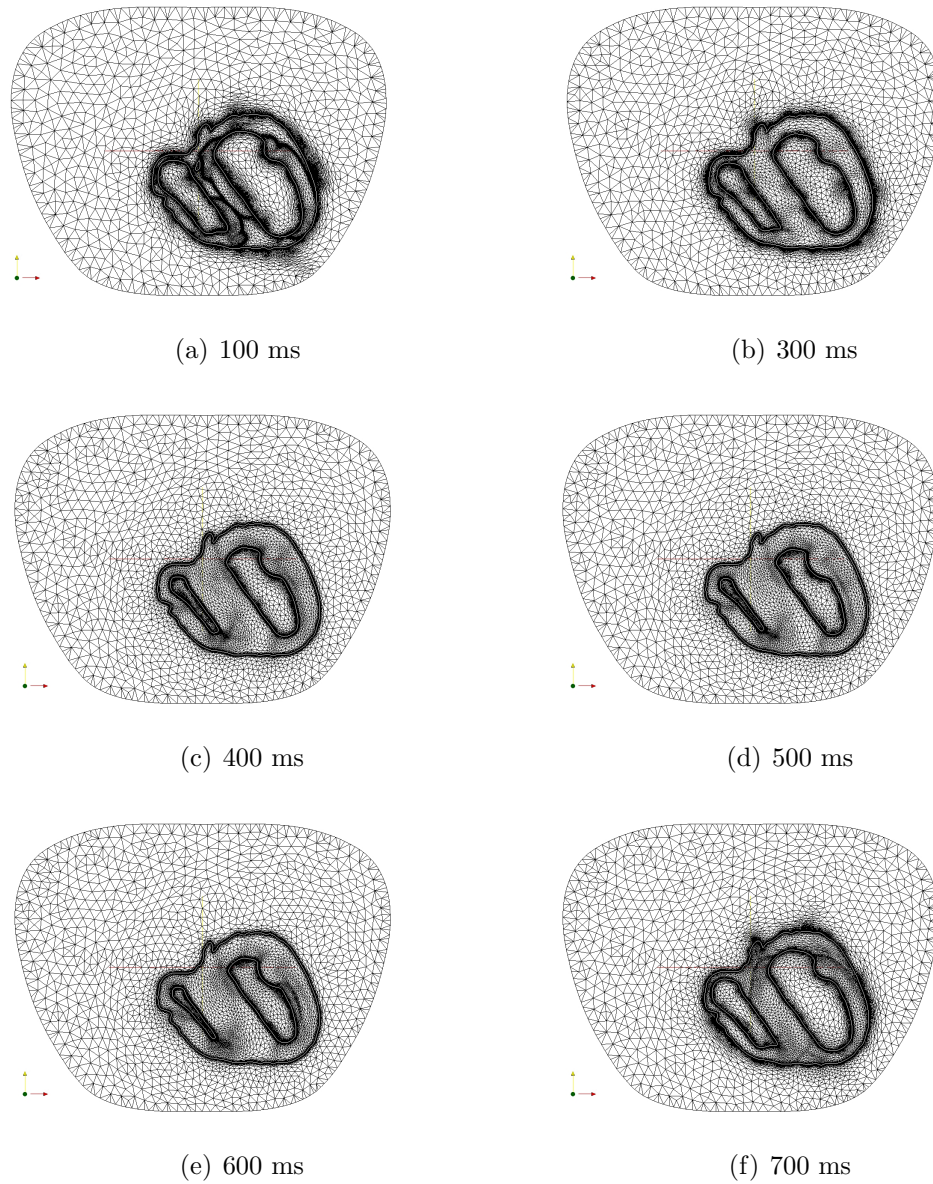


Figure 5.14: The non body fitted mesh adapted every 1 ms (every 10 time steps) of a moving level set based geometry.

A major drawback of this simplified method comes from solution reinterpolations between two different heart geometries. Suppose that the heart domain H at a given time t is different from the heart domain H' at the next time step. The solution is reinterpolated from H to H' in this simplified method. Recall that the transmembrane potential u and the recovery variable v are solutions that exist only in the heart. At the time $t + \Delta t$, these solutions $u_{t+\Delta t}$ and $v_{t+\Delta t}$ are computed on H' using solutions of previous time steps, for instance u_t that exists on H . The time steps are so small ($\Delta t \leq 0.5$ ms required for the resolution of the ionic model) that the domain moves only slightly. The solutions u and v have to be transported in some way from H to H' . In this method, the solutions are simply reinterpolated for regions common to both domains. If the heart enlarges in a certain neighborhood of the interface, then the solution at a point x'_1 of H' outside H is taken as the solution at the nearest point x_1 of H via a projection. Problems arise when doing both reinterpolation and projection if the heart gets smaller or bigger, respectively (see figure 5.15). On the one hand, when the heart gets smaller with a given displacement $\lambda = \vec{d}$, the solution calculated on $H \setminus H'$ is lost in the reinterpolation. On the other hand, when the heart enlarges in a given region, the solution calculated at the point x'_1 of H' uses the solution state at the point x_1 of H through a projection, while it should use the state at a point, e.g. x_2 , of H displaced at a point, e.g. x'_2 , of H' using the displacement \vec{d} .

This simplified method is not suitable for computing the conduction contraction problem with level sets in realistic conditions. It rather proves the use of level sets, non body fitted meshes and moving geometries in a context of mesh adaptation.

Moving (convecting) level sets is done very often for instance in numerical simulations of free surface fluids and fluid-structure coupling. The displacement or velocity vector field is calculated with continuum mechanics models e.g. Navier-Stokes equations and equation of section 5.4.1. Provided a velocity vector field given by $\dot{\lambda}$, the

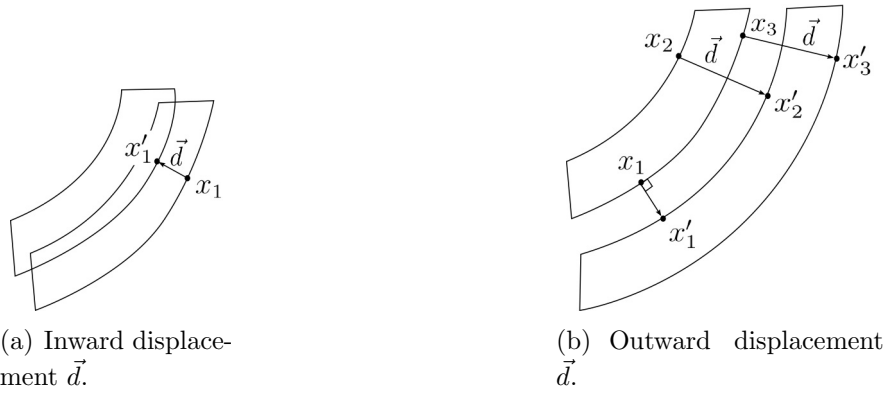


Figure 5.15: For inward displacements (a), a part of the solution may be lost. For outward displacements (b), the solution may be misdiplaced with a projection (e.g. x_1 to x'_1). It should have to be displaced with \vec{d} (e.g. x_2 to x'_2).

level set equation is

$$\frac{\partial \varphi}{\partial t} = \dot{\lambda} \cdot \nabla \varphi.$$

This equation could be solved eventually in an improved version of our moving geometrical model.

Conclusion

This thesis makes contributions to the following two aspects of cardiac electrophysiology: predicting the shape of a propagated action potential wave, simulated with the MS model, is made possible with a dimensional and asymptotic analysis, and a numerical method involving unstructured mesh adaptation is proved to be efficient for solving the heart-torso coupling problem on domains described by level sets.

The dimensional asymptotic analysis gives the steps to predict the solution shape and propagation in a local region of constant conductivity. The application of the method was done successfully on two very different tissues of the heart, the ventricle and the Purkinje fibers. Even when time scales differ by many orders of magnitude in the same AP, the reliability of the method with the MS phenomenological model has been demonstrated. This method proves that using a single simple model for the membrane potential is possible and replaces the use of complicated combinations of tissue-specific ionic models. This remains true only when the phenomena under study involves no complicated dynamics other than the four AP phases: depolarization, excitation, repolarization and recovery. For example, if an electrocardiogram is used together with numerical simulations, studying very short scale AP manifestations is probably useless because these details would not appear on the electrocardiogram. Our method would then open the door to many applications like the inverse problem, at least diagnosing propagation problems like infarct scars, and hopefully much more. Testing the predictions using realistic patient data would be a great advance.

In this thesis, we have also discussed and tested the new capability of an anisotropic adaptive remeshing method applied to the heart-torso coupling problem with realistic and complex computational domains. Not only does the method allow to capture the rapid variations of the solution, but it also allows to solve accurately and efficiently the heart-torso coupling problem on non body fitted meshes. We have also demonstrated the application of the method to moving domains. It then opens the door to combine the electrocardiology problem to other problems like the electromechanical coupling and blood flow in the heart cavities, problems for which the efficiency of level sets methods have already been proven.

Finally, it would be very interesting to apply our asymptotic analysis combined with our adaptive strategy to the bidomain model on 3D regional domains (defined by level sets and using non body fitted meshes) with specific and realistic patient conditions. These problems occur for instance in situations of complex propagation behaviors, like spiral waves initiated by the propagation around subregions of lowest conductivity (e.g. infarct scars). This would be a perfect occasion to test the efficiency and the predictive capability of our method for such problems at the heart of computational therapy planning.

Appendix A

Solving the Neumann problem with a finite element method

When the problem is solved with Dirichlet BCs, the problem 1.3.6 is naturally well-posed for $u|_K \in P_k$ and $u \in C^0(\Omega)$. When the problem is solved with Neumann BCs, the problem is not necessarily well-posed, depending on the choice of the function space in which we seek u . In fact, using V (see section 1.3.3 for definition), the problem is well-posed because $\int_{\partial\Omega} \nabla u_{exact} \cdot n = \int_{\Omega} f = 0$. However, using the same space as the one used for the Dirichlet problem, the problem is no longer well-posed. Many approaches can be used to solve this problem¹. The approach that we finally retain consists first in modifying the problem so that it becomes well-posed and we solve it in correction. The algorithm is the following:

¹1) Imposing a Dirichlet BC at one point. 2) Perturbing A with a small mass matrix, solving it once with a CG and adjusting the average (the initial guess for the CG was not necessarily good).

With the initial guess U_0 , solve

For $n = 0$ to a maximal number of iterations

$$(A + \epsilon M)\delta U_n = F - AU_n$$

$$U_{n+1} = U_n + \delta U_n$$

If $\delta U_n < \text{stopping criteria (small)}$,
break.

End of the loop

with $\phi \in P_k$, $A_{ij} = \int_{\Omega} \sigma \nabla \phi_j \cdot \nabla \phi_i$, $M = \int_{\Omega} \phi_j \cdot \phi_i$, $F = \int_{\Omega} f \phi$ and ϵ a constant. At each step, the solution $u = \sum_j U_j \phi_j$ is obviously not the solution of the original problem, but $A + \epsilon M$ is symmetric positive definite. To get the solution of the original problem, we had to impose an initial guess U_0 which has the same average than the exact solution, i.e. $\overline{U_0} = 1/\pi^2(1 - \sigma^-/\sigma^+)$. Indeed, the solution δU_n of the linear problem $(A + \epsilon M)\delta U_n = F - AU_n$ is of zero mean. The following remark is devoted to the demonstration of the last assertion. We actually want to prove that the solution of the approximate problem leads asymptotically to a solution with a zero mean. We start with a solution with a non zero mean and we will prove that the mean is asymptotically zero.

Remark 15 *Suppose that we have the solution $\widetilde{\delta u}_{h,n} = \delta u_{h,n} + \lambda_n$ of the problem which arise at each step n of the iterative process, with h the mesh size and λ_n an arbitrary constant. We know that constant functions are in $\ker A$. For any h (then also when h tends to zero), this modified problem has a unique solution.*

As we have $\widetilde{\delta u}_{h,n}$ in P_k , it is at least twice differentiable on every element K and the divergence theorem can be used on every element. Up to a consistency error due

to the integration of f , $\widetilde{\delta u}_{h,n}$ is the solution of variational problem

$$\sum_{K \in \Omega_h} \left\{ \int_K \sigma \nabla \widetilde{\delta u}_{h,n} \cdot \nabla v + \epsilon \int_K \widetilde{\delta u}_{h,n} v \right\} = \quad (\text{A.0.1})$$

$$\sum_{K \in \Omega_h} \left\{ \int_K f v - \int_K \sigma \nabla u_{h,n} \cdot \nabla v \right\} \quad \forall v \in H^1(\Omega). \quad (\text{A.0.2})$$

Without any consistency error (integrals calculated exactly), integrating the last equation over the whole domain Ω we get the exact compatibility condition

$$\int_{\partial\Omega} \nabla \widetilde{\delta u}_{h,n} \cdot n + \epsilon \overline{\delta u}_{h,n} = \bar{f} + \int_{\partial\Omega} \nabla \widetilde{u}_{h,n} \cdot n. \quad (\text{A.0.3})$$

Both $\widetilde{\delta u}$ and \widetilde{u}_n satisfy the homogeneous Neumann boundary condition and for this problem f is of zero mean. Then $\widetilde{\delta u}$ is necessarily of zero mean.

Let us come back to the consistency error. This consistency error is important because it can be accumulated through the iterative process (problem solved in correction). When h is still large, we make sure that integral involved in $\overline{\delta u}_{h,n}$ is calculated exactly. Indeed, the quadrature is chosen properly so that integrals of polynomials of order $2k$ (product of $\widetilde{\delta u}_{h,n}$ and v in the mass term) are exact. The only integral which is not exact is $\int_{\Omega} f$. This introduces a consistency error that is $O(h^k)$ [20]. Let us see what could be the order of magnitude of the mean of the final solution.

As A.0.2 is true for all $v \in H^1(\Omega)$, it is true for $v = 1$ and so we get the following discrete compatibility condition

$$\overline{\delta u}_{h,n} + \lambda_n = \frac{1}{\epsilon |\Omega|} \int_{\Omega} f.$$

By assumption $\delta u_{h,n}$ is of zero mean, then

$$\lambda_n = \frac{1}{\epsilon |\Omega|} \int_{\Omega} f = O(h^k).$$

In the limit $h \rightarrow 0$, we have $\widetilde{\delta u}_{h,n} \rightarrow \delta u_n$ with δu_n solution of $-\Delta \delta u_n + \epsilon \delta u_n = f + \Delta u_n$. As $h \rightarrow 0$, the integrals are calculated exactly and so the consistency error vanishes, meaning that the problem is asymptotically consistent. Though λ_n is never calculated explicitly, it is estimated to be $O(h^k)$ and it tends to zero as $h \rightarrow 0$.

In correction, one solves the problem until the residue be less than the stopping criteria, i.e. $\int_{\Omega} f v - \int_{\Omega} \sigma \nabla u_{h,n} \cdot \nabla v < \text{stopping criteria}$. Because of the gradient of $u_{h,n}$, no matter the average of $u_{h,n}$, the last condition can be satisfied and the numerical solution is up to a constant to the exact solution. If $\overline{u_{h,0}} = 0$, $\overline{u_{h,n}} = \sum_{i=1}^n \lambda_i$ and if the number of iterations in correction is significantly less than the number of the degrees of freedom, one can say that the mean of the final numerical solution $\overline{u_{h,n}}$ is $O(h^k)$ too.

◇

Note that the method described before is explained for f in $L_0^2(\Omega)$. But the remark remains valid for f in $L^2(\Omega)$ as long as the compatibility condition is satisfied. Suppose that we want to solve the homogeneous Neumann problem and we have a given f in $L_0^2(\Omega)$. In practice, the source term f is computed in floating point arithmetic via quadrature. As a result, the linear system to solve may become numerically inconsistent and the conjugate gradient could diverge. To restore the consistency, one can use a projection operator for the discrete source term have a zero mean to machine precision. Such a projection operator is proposed in [10]. It is considered as the unconstrained optimization setting of the problem, i.e.

$$\min_{v \in H^1(\Omega)/\mathbb{R}} J(v, f) \quad \text{with} \quad J(v, f) = \frac{1}{2} \int_{\Omega} |\nabla v|^2 - \int_{\Omega} f v$$

and f in $L_0^2(\Omega)$.

A.0.3 Other ways to solve the Neumann problem [10]

The constrained optimization setting is also discussed and a vanishing w -mean is imposed. The problem considered is the following

$$\min_{v \in H^1(\Omega)/\mathbb{R}} J(v, f) \quad \text{subject to} \quad u_w = \frac{(u, w)_{L^2(\Omega)}}{(1, w)_{L^2(\Omega)}} = 0,$$

The choice of w and the handling of the constraint provide a template for many finite element methods for the Neumann problem.

Saddle-point formulation

With a Lagrange multiplier $\tau \in \mathbb{R}$, the saddle-point formulation can be written as

$$\inf_{u \in H^1(\Omega)} \sup_{\tau \in \mathbb{R}} (J(u, f) + \tau u_w).$$

The saddle-point solves the first-order optimality condition: Find $(u, \tau) \in H^1(\Omega) \times \mathbb{R}$ such that

$$\begin{aligned} a(u, v) + \tau v_w &= f(v) \quad \forall v \in H^1(\Omega) \\ \sigma u_w &= 0 \quad \forall \sigma \in \mathbb{R} \end{aligned}$$

which is equivalent to the reduced problem: Find $u \in H_w^1(\Omega) = \{u \in H^1(\Omega) | (u, w) = 0\}$ such that

$$a(u, v) = f(v) \quad \forall v \in H_w^1(\Omega).$$

For any $f \in L^2(\Omega)$, existence and uniqueness of the solution can be proved. However, the solutions of the reduced problem does not solve the original exact problem unless $f \in L_0^2(\Omega)$.

The choice of w is crucial. If w approaches a delta function as $h \rightarrow 0$, the method corresponds to the one of specifying a solution value at a node. For the singular $N \times N$ matrix A (for the original ill-posed problem) with ordered eigenvalues $0 = \lambda_1 \leq \lambda_2 \leq \dots \leq \lambda_N$, the rate of convergence of the conjugate gradient algorithm depends on the ratio $\kappa(A) = \lambda_N(A)/\lambda_2(A)$ or the effective condition number. For this particular choice of w , the condition numbers of the resulting matrices are larger than the effective condition number of the singular matrix. Moreover, as the delta function is in the dual of $H^1(\Omega)$ in one dimension only, the constraint $(u, w) = 0$ becomes ill-posed in two or three dimensions as $h \rightarrow 0$. *Specifying the solution at a node leads to an ill-posed variational problem in 2D and 3D and so impacts the resulting linear system.*

Stabilized saddle-point formulation

With a Lagrange multiplier $\tau \in \mathbb{R}$, the saddle-point formulation can be written as

$$\inf_{u \in H^1(\Omega)} \sup_{\tau \in \mathbb{R}} \left(J(u, f) + \tau u_w - \frac{1}{2\rho} \tau^2 \right).$$

The saddle-point solves the first-order optimality condition: Find $(u, \tau) \in H^1(\Omega) \times \mathbb{R}$ such that

$$\begin{aligned} a(u, v) + \tau v_w &= f(v) \quad \forall v \in H^1(\Omega) \\ \sigma u_w &= \frac{1}{\rho} \sigma \tau \quad \forall \sigma \in \mathbb{R} \end{aligned}$$

which is equivalent to the reduced problem: Find $u \in H_w^1(\Omega) = \{u \in H^1(\Omega) | (u, w) = 0\}$ such that

$$a_\rho(u, v) = a(u, v) + \rho u_w v_w = f(v) \quad \forall v \in H_w^1(\Omega).$$

Remark that the last problem can be seen as the first-order optimality system for the unconstrained minimization of the penalized energy functional

$$\min_{u \in H^1(\Omega)} \left(J(u, f) + \frac{\rho}{2} u_w^2 \right).$$

For any $f \in L^2(\Omega)$, existence and uniqueness of the solution can be proved. However, the solutions of the reduced problem do not solve the original exact problem unless $f \in L_0^2(\Omega)$. An advantage of such a method is that the discretized version of $a_\rho(u, v)$ is symmetric positive definite and its sparsity can be controlled so as to match the sparsity of the singular matrix by taking w with the appropriate support. For instance, if $w = 1$, a_ρ is dense, but with an appropriate choice of ρ , the number of CG iterations is less than when we specify a solution value at a node. *The choice of w and ρ seems to be not necessarily obvious. This is why we choose the method of the modified problem solved in correction.*

Remark 16 *Because the overall problem was solved iteratively, we had to impose that the initial guess u_0 be such that $\int_\Omega u_0 = \int_\Omega u_{exact}$, for the final solution (once converged) have the right mean. If we do not do that, the final solution is up to a constant to the exact solution.*

Appendix B

Complement on the Conjugate Gradient (CG)

With Neumann boundary conditions, the stiffness matrix A is symmetric positive *semi*-definite. This comes from the fact that we find our solution in P_k , the space of piecewise polynomials of order k , where the constant functions are possible. The problem is then ill-posed. For the conjugacy be well-defined, one absolutely needs a positive definite matrix. We slightly modified the approximate problem by adding a mass matrix of order ϵ small, and we solve it in correction (set $u = u_0 + \delta u$, u_0 is the initial guess and δu the correction). Note that the new problem is well-posed because $\int_{\partial\Omega} \nabla u_{exact} \cdot n + \epsilon \int_{\Omega} u_{exact} = \int_{\Omega} f = 0$ (each term is zero). The new approximate problem becomes:

Find $\delta u \in P_k$ s.t.

$$A\delta u + M\delta u = F - Au_0,$$

where

$$A_{ij} = \sum_K \int_K \nabla \phi_j \cdot \nabla \phi_i$$

$$M_{ij} = \epsilon \sum_K \int_K \phi_j \phi_i$$

with $\delta u = \sum \delta u_j \phi_j$, ϕ are basis functions in P_k and K represents the elements in the mesh. Working in correction implies that we solve for δu and update u_0 until the right hand side becomes zero. Once converged, the residual of the non modified approximate problem (without the mass matrix) is zero and we have a solution to $Au = F$. In each iteration, we solve this linear problem using a CG solver, which is described below (d_i are the search directions, r_i are the residuals and $B = A + M$).

Algorithm

Set $d_0 = r_0 = F - Au_0 - B\delta u_0$

For i equals 0 to size(δu)

$$\alpha_i = \frac{r_i^T r_i}{d_i^T B d_i}$$

$$\delta u_{i+1} = \delta u_i + \alpha_i d_i$$

$$r_{i+1} = r_i - \alpha_i B d_i$$

if r_{i+1} is less than the stopping criteria, break.

$$\beta_i = \frac{r_{i+1}^T r_{i+1}}{r_i^T r_i}$$

$$d_{i+1} = r_{i+1} - \beta_{i+1} d_i$$

End of the for loop.

The search directions are built (via a Gram-Schmith process using the B -conjugacy) with a set of linearly independent vectors, which are here the gradients $g_i = -r_i$. In consequence, we have $d_i \in \text{span}\{r_0, r_1, r_2, \dots, r_{i-1}\} = \text{span}\{d_0, B d_0, B^2 d_0, \dots, B^{i-1} d_0\} = \text{span}\{r_0, B r_0, B^2 r_0, \dots, B^{i-1} r_0\}$. The before last equality comes from the fact that r_i is just a linear combination of the previous residual and $B d_{i-1}$. The last equality holds from the initial choice of d_0 . If the conjugacy is good, the solution stays in this Krylov space through the CG iterations. We would like to have an algorithm which preserves the average of the initial guess through the iterations. If we write the initial guess as an orthogonal decomposition, we have $\widetilde{\delta u}_0 = \delta u_0 + \lambda w$ with $\delta u_0 \in \ker A^\perp$, $w \in \ker A$

and λ is a constant. Note that the kernel of A is the set of constant functions, but the kernel of B is zero. For guesses $\widetilde{\delta u}_0$ and δu_0 , we have the following first directions.

$$\begin{aligned}\widetilde{r}_0 &= F - Au_0 - B\widetilde{\delta u}_0 = F - Au_0 - A\delta u_0 - M\widetilde{\delta u}_0 \\ r_0 &= F - Au_0 - B\delta u_0 = F - Au_0 - A\delta u_0 - M\delta u_0\end{aligned}$$

The results are not the same and an error could grow up through the iterations, even if ϵ is small. It means that using the CG to solve this equation is not suitable to preserve the average of the initial guess.

Appendix C

Definitions and theorems [20]

Hypothesis 1 *Let h_K be the diameter of element K of the triangulation. We consider a regular family of triangulations \mathcal{T}_h in the following sense:*

- *There exists a constant σ such that*

$$\forall K \in \bigcup_h \mathcal{T}_h, \frac{h_K}{\rho_K} \leq \sigma.$$

- *The quantity $h = \max_{K \in \mathcal{T}_h} h_K$ approaches zero.*

Hypothesis 2 *All the finite elements (K, P_K, Σ_K) , $K \in \bigcup_h \mathcal{T}_h$, are affine equivalent to a single reference finite element $(\hat{K}, \hat{P}, \hat{\Sigma})$.*

Hypothesis 3 *All the finite elements (K, P_K, Σ_K) , $K \in \bigcup_h \mathcal{T}_h$, are of class C^0 .*

Theorem C.0.1 *Consider the hypothesis 1, 2 and 3. Assume that there exists an integer $k \geq 1$ such that the following inclusions are satisfied:*

$$\begin{aligned} P_k(\hat{K}) &\subset \hat{P} \subset H^1(\hat{K}), \\ H^{k+1}(\hat{K}) &\hookrightarrow C^s(\hat{K}), \end{aligned}$$

where s is the maximal order of partial derivatives occurring in the definition of the set $\widehat{\Sigma}$.

Then if the solution $u \in V$ of the variational problem is also in the space $H^{k+1}(\Omega)$, then there exists a constant C independent of h such that

$$\|u - u_h\|_{1,\Omega} \leq Ch^k |u|_{k+1,\Omega} \quad (\text{C.0.1})$$

Remark 17 *The last theorem assumes that u is sufficiently smooth, i.e. in $H^{k+1}(\Omega)$ for some $k \geq 1$. If u does not satisfy this regularity condition, i.e. $u \in H^r(\Omega)$ with $d/2 < r \leq k + 1$, the estimate becomes*

$$\|u - u_h\|_{1,\Omega} \leq Ch^{r-1} |u|_{r,\Omega}$$

Moreover, the assumption $H^{k+1}(\widehat{K}) \hookrightarrow C^s(\widehat{K})$ is valid if $d/2 + s < k + 1$. If this condition is not satisfied, it is still possible to prove the convergence of the method with an appropriate choice of the space in which we seek u and with a density argument [20].

Theorem C.0.2 *Consider the hypothesis 1, 2 and 3. Assume that $d \leq 3$, and that there exists an integer $k \geq 1$ such that the solution $u \in H^{k+1}(\Omega)$ and such that the inclusions hold:*

$$P_k(\widehat{K}) \subset \widehat{P} \subset H^1(\widehat{K}).$$

Moreover, if the adjoint problem is regular, there exists a constant C independent of h such that

$$|u - u_h|_{0,\Omega} \leq Ch^{k+1} |u|_{k+1,\Omega} \quad (\text{C.0.2})$$

Lemma C.0.3 *(Inverse Inequality) With notation defined in hypothesis 1, suppose*

that the finite element space $V_h \subset C^0 \cap H^1(\Omega)$ and that the triangulation \mathcal{T} satisfies the following regularity condition[20]:

$$\exists \nu \text{ such that } \frac{h}{h_K} < \nu$$

for ν independent of K . Then $\forall v_h \in V_h$

$$|v_h|_1 \leq \frac{\mathcal{C}}{h} \|v_h\|_0.$$

Bibliography

- [1] <http://cvphysiology.com/arrhythmias/a003.htm>.
- [2] <http://giref.ulaval.ca/mef.html>.
- [3] F. Alauzet. Estimateur d'erreur géométrique et métriques anisotropes pour l'adaptation de maillage. Partie I: aspects théoriques. Rapport de recherche INRIA no. 4759, 10 mars 2003.
- [4] R.R. Aliev and A.V. Panfilov. A simple two-variable model of cardiac excitation. *Chaos Soliton. Fract.*, 7:293–301, 1996.
- [5] G. W. Beeler and H. Reuter. Reconstruction of the action potential of ventricular myocardial fibres. *J. Physiol.*, 268:177–210, June 1977.
- [6] Y. Belhamadia. A time dependent adaptive remeshing for electrical waves of the heart. *IEEE Trans. Biomed. Eng.*, 55(2):443–452, 2008.
- [7] Y. Belhamadia, A. Fortin, and Y. Bourgault. Towards accurate numerical method for monodomain models using a realistic heart geometry. *Math. Biosci.*, 220(2):89–101, 2009.
- [8] Y. Belhamadia, A. Fortin, and É. Chamberland. Anisotropic mesh adaptation for the solution of the Stefan problem. *J. of Comput. Phys.*, 194(1):233–255, 2004.

- [9] M.J. Bishop and G. Plank. Representing cardiac bidomain bath-loading effects by an augmented monodomain approach: application to complex ventricular models. *IEEE Trans. Biomed. Eng.*, 58(4):1066–1075, 2011.
- [10] P. Bochev and R. B. Lehoucq. On finite element solution of the pure Neumann problem. *SIAM Rev*, 47:50–66, 2001.
- [11] M. Boulakia, M. Fernández, J.-F. Gerbeau, and N. Zenzemi. Towards the numerical simulation of electrocardiograms. In Frank Sachse and Gunnar Seemann, editors, *Functional Imaging and Modeling of the Heart*, volume 4466 of *Lect. Notes Comput. Sci.*, pages 240–249. Springer Berlin / Heidelberg, 2007.
- [12] M. Boulakia and J-F. Gerbeau. Parameter identification in cardiac electrophysiology using proper orthogonal decomposition method. In Dimitris Metaxas and Leon Axel, editors, *Functional Imaging and Modeling of the Heart*, volume 6666 of *Lecture Notes in Computer Science*, pages 315–322. Springer Berlin / Heidelberg, 2011.
- [13] M. Boulakia, J.-F. Gerbeau M. Fernández, and N. Zenzemi. Analysis of a coupled system of PDEs and ODEs arising in the numerical simulation of electrocardiograms. *Appl. Math. Res. Express*, 2:Art. ID abn002, 2008.
- [14] Y. Bourgault, Y. Coudière, and C. Pierre. Existence and uniqueness of the solution for the bidomain model used in cardiac electrophysiology. *Nonlinear Anal.: Real World Appl.*, 10:458–482, February 2009.
- [15] Y. Bourgault, M. Ethier, and V.G. LeBlanc. Simulation of electrophysiological waves with an unstructured finite element method. *Math. Model. Numer. Anal.*, 37(4):649–661, 2003.
- [16] N. F. Britton. *Essential Mathematical Biology*. Springer Undergrad. Math. Series, 2005.

- [17] D. Chapelle, M. A. Fernández, J.-F. Gerbeau, P. Moireau, J. Sainte-Marie, and N. Zemzemi. Numerical simulation of the electromechanical activity of the heart. In *FIMH'09*, pages 357–365, 2009.
- [18] E. M. Cherry, H. S. Greenside, and C. S. Henriquez. Efficient simulation of three-dimensional anisotropic cardiac tissue using an adaptive mesh refinement method. *Chaos: An Interdiscipl. J. of Nonlin. Sci.*, 13(3):853–865, 2003.
- [19] C. Chicone. *Ordinary Differential Equations with Applications*. Springer, 2006.
- [20] P. G. Ciarlet. *Finite Element Method for Elliptic Problems*. Soc. Ind. Appl. Math., Philadelphia, PA, USA, 2002.
- [21] R.H. Clayton, O. Bernus, E.M. Cherry, H. Dierckx, F.H. Fenton, L. Mirabella, A.V. Panfilov, F.B. Sachse, G. Seemann, and H. Zhang. Models of cardiac tissue electrophysiology: Progress, challenges and open questions. *Prog. Biophys. Mol. Bio.*, 104:22 – 48, 2011.
- [22] R.H. Clayton and A.V. Panfilov. A guide to modelling cardiac electrical activity in anatomically detailed ventricles. *Prog. Biophys. Mol. Bio.*, 96(1-3):19 – 43, 2008.
- [23] Y. Coudière and C. Pierre. Stability and convergence of a finite volume method for two systems of reaction-diffusion equations in electrocardiology. *Nonlinear Anal.: Real World Appl.*, 7:916–935, 2006.
- [24] H. Delingette, F. Billet, K. C. L. Wong, M. Sermesant, K. Rhode, M. Ginks, C. A. Rinaldi, R. Razavi, and N. Ayache. Personalization of cardiac motion and contractility from images using variational data assimilation. *IEEE Trans. Biomed. Eng. Lett.*, December 2011.
- [25] B. Deng. The existence of infinitely many traveling front and back waves in the Fitzhugh - Nagumo equations. *SIAM J. Math. Anal.*, 22:1631–1650, 1991.

- [26] K. Djabella, M. Landau, and M. Sorine. A two-variable model of cardiac action potential with controlled pacemaker activity and ionic current interpretation. *46th IEEE Conf. Decis. Control*, pages 5186–5191, 2007.
- [27] D. Durrer, R. TH. Van Dam, G. E. Freud, M. J. Janse, F. L. Meijler, and R. C. Arzbaecher. Total excitation of the isolated human heart. *Circulation*, 41(6):899–912, 1970.
- [28] I. R. Efimov, R. A. Gray, and B. J. Roth. Virtual electrodes and deexcitation: New insights into fibrillation induction and defibrillation. *J. of Cardiovasc. Electrophysiol.*, 11(3):339–353, 2000.
- [29] R. E. Ten Eick, C. M. Baumgarten, and D. H. Singer. Ventricular dysrhythmia: Membrane basis or of currents, channels, gates, and cables. *Prog. Cardiovasc. Dis.*, 24:157–188, 1981.
- [30] M. Ethier and Y. Bourgault. Semi-implicit time-discretization schemes for the bidomain model. *SIAM J. Numer. Anal.*, 46(5):2443–2468, 2008.
- [31] F. Fenton and A. Karma. Vortex dynamics in three-dimensional continuous myocardium with fiber rotation: Filament instability and fibrillation. *Chaos*, 8:20–47, March 1998.
- [32] R. FitzHugh. Impulses and physiological states in theoretical models of nerve membrane. *Biophys. J.*, 1:445–466, July 1961.
- [33] R.A. FitzHugh. Impulses and physiological states in theoretical models of nerve membrane. *Biophys. J.*, 1:445–466, 1961.
- [34] A. Fortin and K. Benmoussa. An adaptive remeshing strategy for free-surface fluid flow problems. part II: the three-dimensional case. *J. Polym. Eng.*, 26(1):59–86, 2006.

- [35] M. Fortin. Scientific computing and applications. chapter Anisotropic mesh adaptation through hierarchical error estimators, pages 53–65. Nova Science Publishers, Inc., Commack, NY, USA, 2001.
- [36] P. Colli Franzone, L. Guerri, and S. Tentoni. Mathematical modeling of the excitation process in myocardial tissue: influence of fiber rotation on wavefront propagation and potential field. *Math. Biosci.*, 101:155–235, 1990.
- [37] P. Colli Franzone, L.F. Pavarino, and B. Taccardi. Simulating patterns of excitation, repolarization and action potential duration with cardiac bidomain and monodomain models. *Math. Biosci.*, 197(1):35–66, 2005.
- [38] R. Glowinski, T.-W. Pan, and J. Periaux. A fictitious domain method for Dirichlet problem and applications. *Comput. Meth. Appl. Mech. Eng.*, 111:283–303, 1994.
- [39] Y. Gong, B. Li, and Z. Li. Immersed-interface finite-element methods for elliptic interface problems with nonhomogeneous jump conditions. *SIAM J. on Numer. Anal.*, 46(1):472–495, 2008.
- [40] S. Hastings. Single and multiple pulse waves for the Fitzhugh–Nagumo equations. *SIAM J. Appl. Math.*, 42:247–260, 1982.
- [41] A. L. Hodgkin and A. F. Huxley. A quantitative description of membrane current and its application to conduction and excitation in nerve. *J. Physiol.*, 117:500–544, August 1952.
- [42] M. Kass, A. Witkin, and D. Terzopoulos. Snakes: Active contour models. *International Journal of Computer Vision*, 1(4):259–268, 1987.
- [43] J. Keener and J. Sneyd. *Mathematical Physiology*. Springer, 2004.

- [44] J. P. Keener. Modeling electrical activity of cardiac cells, Two variable models, Mitchell-Schaeffer revised. www.math.utah.edu/~keener/lectures/ionic_models/Two_variable_models.
- [45] R.C.P. Kerckhoffs, S.N. Healy, T.P. Usyk, and A.D. McCulloch. Computational methods for modeling cardiac electromechanics. In *Proc. IEEE*, pages 769–783, 2006.
- [46] Ten Tusscher K.H., Noble D., Noble P.J., and Panfilov A.V. A model for human ventricular tissue. *Am. J. Physiol. Heart Circ. Physiol.*, 286:H1973–H1589, April 2004.
- [47] R. Killmann, P. Wach, and F. Dienstl. Three-dimensional computer model of the entire human heart for simulation of reentry and tachycardia: gap phenomenon and Wolff-Parkinson-White syndrome. *Basic Res. Cardiol.*, 86:485–501, 1991.
- [48] D. L. King, L. El-Khoury Coffin, and M. S. Maurer. Noncompressibility of myocardium during systole with freehand three-dimensional echocardiography. *J. Am. Soc. Echocardiograph.*, 15(12):1503 – 1506, 2002.
- [49] Z. Li. The immersed interface method using a finite element formulation. *Appl. Numer. Math.*, 27(3):253–267, 1998.
- [50] Z. Li. An overview of the immersed interface method and its applications. *Taiwanese J. Math.*, 7(1):1–49, 2003.
- [51] Z. Li, T. Lin, and X. Wu. New cartesian grid methods for interface problems using the finite element formulation. *Numer. Math.*, 96:61–98, 2003.
- [52] G. T. Lines, P. Grottum, A. J. Pullan, J. Sundes, and A. Tveito. Mathematical models and numerical methods for the forward problem in cardiac electrophysiology. *Comput. Visual. Sci.*, 5:215–239, 2002.

- [53] A. Loubenets. *An Immersed Finite Element Method and its Application to Multiphase Problems*. PhD thesis, KTH Royal Institute of Technology, 2007.
- [54] C.H. Luo and Y. Rudy. A dynamic model of the cardiac ventricular action potential: I. simulations of ionic currents and concentration changes. *Circ. Res.*, 74:1071–1096, June 1994.
- [55] V. Mihalef, R. I. Ionasec, P. Sharma, B. Georgescu, I. Voigt, M. Suehling, and D. Comaniciu. Patient-specific modelling of whole heart anatomy, dynamics and haemodynamics from four-dimensional cardiac CT images. *Interf. Focus*, 1(3):286–296, 2011.
- [56] C. Mitchell and D. Schaeffer. A two-current model for the dynamics of cardiac membrane. *Bulletin Math. Bio.*, 65(5):767–793, September 2003.
- [57] B. R. Munson, D. F. Young, and T. H. Okiishi. *Fundamentals of Fluid Mechanics*. Wiley and Sons, 2001.
- [58] J. Nagumo, S. Arimoto, and S. Yoshizawa. An active pulse transmission line simulating nerve axon. *Proc. IRE.*, 50:20612070, 1962.
- [59] J. S. Nagumo, S. Arimoto, and S. Yoshizawa. An active pulse transmission line simulating nerve axon. *Proc. IRE*, 50:2061–2071, 1962.
- [60] J.C. Neu and W. Krassowska. Homogenization of syncytial tissues. *Crit. Rev. Biomed. Eng.*, 21(2):137–199, 1993.
- [61] S. Niederer, L. Mitchell, N. Smith, and G. Plank. Simulating human cardiac electrophysiology on clinical time-scales. *Front. Physiol.*, 2(0), 2011.
- [62] P.M. Nielsen, I.J. Le Grice, B.H. Smaill, and P.J. Hunter. Mathematical model of geometry and fibrous structure of the heart. *Am. J. of Phys. - Heart and Circ. Phys.*, 260:1365–1378, 1991.

- [63] D. Noble. A modification of the Hodgkin-Huxley equations applicable to purkinje fibre action and pacemaker potentials. *J. Physiol.*, 160:317–352, February 1962.
- [64] S. Osher and R. P. Fedkiw. Level set methods: An overview and some recent results. *J. of Comput. Phys.*, 169(2):463–502, May 2001.
- [65] S. Osher and J. A. Sethian. Fronts propagating with curvature-dependent speed: Algorithms based on hamilton-Jacobi formulations. *J. of Comput. Phys.*, 79:12–49, 1988.
- [66] V. Paaanen and M. Vornanen. Regulation of action potential duration under acute heat stress by $i(k,atp)$ and $i(k1)$ in fish cardiac myocytes. *Am. J. Physiol. Regul. Integr. Comput. Physiol.*, 286(2):405–415, 2004.
- [67] G. H. Peichl and R. Touzani. An accurate finite element method for elliptic interface problems. *Submitted to Numer. Math.*, 2007.
- [68] C. Pierre. *Modélisation et simulation de l'activité électrique du coeur dans le thorax, analyse numérique et méthodes de volumes finis*. PhD thesis, University of Nantes, 2005.
- [69] C. Pierre, O. Rousseau, and Y. Bourgault. Segmented medical images based simulations of cardiac electrical activity and electrocardiogram: a model comparison. *hal Preprints*, 2009.
- [70] M. Potse, B. Dube, J. Richer, A. Vinet, and R. M Gulrajani. A comparison of monodomain and bidomain reaction-diffusion models for action potential propagation in the human heart. *IEEE Trans. Biomed. Eng.*, 53:2425–2435, 2006.
- [71] J. Relan, M. Sermesant, H. Delingette, M. Pop, G. A. Wright, and N. Ayache. Quantitative comparison of two cardiac electrophysiology models using personalisation to optical and mr data. In *Proc. Sixth IEEE Int. Symp. Biomed. Imaging 2009 (ISBI'09)*, July 2009.

- [72] J. Relan, M. Sermesant, M. Pop, H. Delingette, M. Sorine, G. A. Wright, and Nicholas Ayache. Parameter estimation of a 3d cardiac electrophysiology model including the restitution curve using optical and MR data. In *World Congr. on Med. Phys. and Biomed. Eng., WC 2009, München*, September 2009.
- [73] O. Rousseau. Geometrical modeling of the heart/meshes. <http://www.mathstat.uottawa.ca/orous272/>.
- [74] O. Rousseau. *Geometrical Modeling of the Heart*. PhD thesis, University of Ottawa, 2009.
- [75] D. Schaeffer, J. Cain, D. Gauthier, S. Kalb, R. Oliver, E. Tolkacheva, W. Ying, and W. Krassowska. An ionically based mapping model with memory for cardiac restitution. *Bulletin Math. Bio.*, 69:459–482, 2007. 10.1007/s11538-006-9116-6.
- [76] D. Schaeffer, W. Ying, and X. Zhao. Asymptotic approximation of an ionic model for cardiac restitution. *Nonlinear Dyn.*, 51:189–198, 2008. 10.1007/s11071-007-9202-9.
- [77] M. Sermesant, H. Delingette, and N. Ayache. An electromechanical model of the heart for image analysis and simulation. *IEEE Trans. Med. Im.*, 25:612–625, 2006.
- [78] J. Southern, G.J. Gorman, M.D. Piggott, P.E. Farrell, M.O. Bernabeu, and J. Pitt-Francis. Anisotropic mesh adaptivity for cardiac electrophysiology. *Proc. Comput. Sci.*, 1(1):935 – 944, 2010. ICCS 2010.
- [79] G. Strang and G. J. Fix. *An analysis of the finite element method*. Prentice-Hall, 1973.
- [80] S. H. Strogatz. *Nonlinear Dynamics and Chaos (With Applications to Physics, Biology, Chemistry, and Engineering)*. Addison-Wesley Publishing Company, 1994.

- [81] J. Sundnes, G. T. Lines, X. Cai, B. F. Nielsen, K.-A. Mardal, and A. Tveito. *Computing the Electrical Activity in the Heart*, volume 1 of *Monogr. Comput. Sci. Eng.* Springer, September 2006.
- [82] M. Sussman, P. Smereka, and S. Osher. A level set approach for computing solutions to incompressible two-phase flow. *J. of Comput. Phys.*, 114(1):146–159, September 1994.
- [83] E.G. Tolkacheva, D.G. Schaeffer, D.J. Gauthier, and C.C. Mitchell. Analysis of the Fenton-Karma model through an approximation by a one-dimensional map. *Chaos*, 12:1034–1042, December 2002.
- [84] N. Trayanova, J. C. Eason, and F. Aguel. Computer simulations of cardiac defibrillation: a look inside the heart. *Comput. Visualiz. Sci.*, 4:259–270, 2002.
- [85] N. A. Trayanova. Whole-Heart Modeling: Applications to Cardiac Electrophysiology and Electromechanics. *Circ. Res.*, 108(1):113–128, January 2011.
- [86] M.L. Trew, B.H. Smaill, D.P. Bullivant, P.J. Hunter, and A. J. Pullan. A generalized finite difference method for modeling cardiac electrical activation on arbitrary, irregular computational meshes. *Math. Biosci.*, 198:169–189, 2005.
- [87] F.J. Vetter and A.D. McCulloch. Three-dimensional analysis of regional cardiac function: a model of rabbit ventricular anatomy. *Prog. Biophys. Mol. Biol.*, 69(2-3):157–183, 1998.
- [88] E. Vigmond, F. Vadakkumpadan, H. Arevalo V. Gurev, M. Deo, G. Plank, and N. Trayanova. Defibrillation of the heart: insights into mechanisms from modelling studies. *Exp. Phys.*, 91(2):323–337, 2006.
- [89] E. Vigmond, F. Vadakkumpadan, H. Arevalo V. Gurev, M. Deo, G. Plank, and N. Trayanova. Towards predictive modelling of the electrophysiology of the heart. *Exp. Physiol.*, 94:563–577, 2009.

-
- [90] E.J. Vigmond, F. Aguel, and N.A. Trayanova. Computational techniques for solving the bidomain equations in three dimensions. *Biomed. Eng., IEEE Trans.*, 49(11):1260–1269, nov. 2002.
- [91] A. I. Volpert, V. A. Volpert, and V. A. Volpert. *Traveling wave solutions of parabolic systems*, 1994.
- [92] J.P. Wikswo, S.F. Lin, and R.A. Abbas. Virtual electrodes in cardiac tissue: a common mechanism for anodal and cathodal stimulation. *Biophys. J.*, 68(6):2195–2210, 1995.
- [93] A. A. Young and A. F. Frangi. Computational cardiac atlases: from patient to population and back. *Exp. Physiol.*, 94:578–596, 2009.